Investigating Low-Strain GaAs/AlGaAs Quantum Dots with Nuclear Magnetic Resonance

Peter Millington-Hotze

A thesis presented for the degree of
Doctor of Philosophy

Supervisor: Dr. Evgeny A. Chekhovich

December 2024

Low Dimensional Structures and Devices Group
Department of Physics and Astronomy
The University of Sheffield
United Kingdom

Abstract

The contents of this thesis present experimental measurements performed on III-V, predominantly GaAs/AlGaAs, nanohole infilled quantum dots. Through the use of optically detected nuclear magnetic resonance the nuclear spin system is investigated. The results of these investigations are presented across three interconnected chapters, each highlighting distinctive insights on the elimination of decoherence and the enhancement of the longevity and initialisation of nuclear spins.

The first experimental chapter discusses the inherent strain within quantum dot samples. GaAs, InGaAs, and $Al_xGa_{1-x}As$ quantum dots embedded in $Al_yGa_{1-y}As$ barriers are studied using optically detected nuclear magnetic resonance techniques with nanometre scale resolution. These spectra are then reproduced using a Monte-Carlo method; the simulation parameters are optimised through a differential evolution algorithm, which show the presence of atomic scale strain. The evaluated results of these atomic scale strain magnitudes, in a pristine crystal lattice, were found to differ considerably from previous studies which used powderised samples. The breadth of the quadrupolar splitting was determined to increase from ~ 55 kHz to ~ 300 kHz due to the addition of 10% Al into pure GaAs quantum dots.

Nuclear spin dynamics are studied in the second set of experiments. The Knight-field-gradient barrier, hypothesised to occur due to the introduction of an electron into a quantum dot, is shown not to be applicable in the case of GaAs/AlGaAs epitaxial quantum dots. In fact, the presence of an electron is found to increase nuclear spin diffusion at a large range of magnetic fields due to electron mediated nuclear spin flip-flops.

In the final experimental chapter, we achieve levels of nuclear spin polarisation that, for nearly two decades, were met with theoretical scepticism regarding their attainability. We reliably achieve polarisations well above 95% in a statistically significant set of randomly chosen individual quantum dots. The process for reaching these levels only requires time scales of the order of one minute and can be applied/is compatible with standard quantum dot designs. Within this chapter the underlying mechanism behind this process is both understood and explained.

Acknowledgments

The work in this thesis would not have been possible without the support of many individuals. I would, therefore, like to start the thesis by thanking these people.

Firstly, I would like to thank **EPSRC** for the funding for the PhD, without which the project would not have been possible. My supervisor, **Evgeny Chekhovich** also has my gratitude for the countless hours of assistance he provided, ensuring I learnt the skills possible to develop as a researcher. Ever present throughout the PhD, his determination and drive for experimental work is something to be admired. **Chris Vickers** and **Thomas Ball** also deserve some recognition. The thirst for liquid helium in the department is never ending, but through their efforts we were able to run multiple bath cryostats as well as perform flow-cryostat measurements in the C11 lab. Without their contribution to the recycling/reliquefaction of helium none of the work in this thesis would have happened.

Many thanks go to my colleagues within the C11 lab. Firstly to **George Gillard**, who I could always ask any physics questions to without feeling like a complete fool, as well in aiding with my many queries about *Wolfram Mathematica*. Secondly thanks go to **Harry Dyte**, who ran parallel measurements in C11, and was always there to bat ideas off/sympathise with experimental challenges. With respect to this, I would like to thank everyone in the E46 office who had to listen to my many incoherent ramblings and or frustrations with malfunctioning code.

Outside of the academic life, a broader thank you goes to my friends who supported me during these last three and a half years of research. Unquestionably, I would not have been able to reach this level of physics without the encouragement of my family. My parents, **Mil Millington** and **Margret Hotze** and my brother, **Jonathan Millington-Hotze** have all helped me reach this point. I hope through all the 'learning via proxy' that now whenever you watch a movie and a character technobabbles with the justification of *quantum* you can now sigh with me. Lastly, I would like to thank my husband, **Toby Major-Seager**. Your unwavering support made all the difference, this would not have been possible without you.

Publications and Conferences

Papers

P. Millington-Hotze, S. Manna, S. F. Covre da Silva, A. Rastelli, E. A. Chekhovich. "Nuclear spin diffusion in the central spin system of a GaAs/AlGaAs quantum dot". *Nat Commun* **14**, 2677 (2023). doi: 10.1038/s41467-023-38349-0.

P. Millington-Hotze, H. E. Dyte, S. Manna, S. F. Covre da Silva, A. Rastelli, E. A. Chekhovich. "Approaching a fully-polarized state of nuclear spins in a solid". *Nat Commun* **15**, 985 (2024). doi: 10.1038/s41467-024-45364-2.

Conference Talks

P. Millington-Hotze, S. Manna, S. F. Covre da Silva, A. Rastelli, E. A. Chekhovich. "Nuclear Spin Diffusion in the Central Spin System of a GaAs/AlGaAs Quantum Dot". *Quantum Dot Day*. London, UK. March 2022.

P. Millington-Hotze, S. Manna, S. F. Covre da Silva, A. Rastelli, E. A. Chekhovich. "Intrinsic atomic-scale strains in GaAs QDs probed by NMR". *GaAs Workshop*. Oxford, UK. May 2023.

P. Millington-Hotze, S. Manna, S. F. Covre da Silva, A. Rastelli, E. A. Chekhovich "Approaching a Fully-Polarized State of Nuclear Spins in a Semiconductor Quantum Dot". *Quantum Dot Day 2023*. Manchester, UK; September 2023.

Posters

P. Millington-Hotze, S. Manna, S. F. Covre da Silva, A. Rastelli, E. A. Chekhovich. "The Effect of Alloying Disorder and Nanoscale Strains in $Al_xGa_{1-x}As/Al_yGa_{1-y}As$ Quantum Dots". *International Conference on Optics of Excitons in Confined Systems (OECS 18)*. Lecce, Italy; June 2023.

P. Millington-Hotze, S. Manna, S. F. Covre da Silva, A. Rastelli, E. A. Chekhovich. "Strain and Disorder Effects in AlGaAs". *Quantum Dot Day 2023*. Manchester, UK; September 2023.

P. Millington-Hotze, S. Manna, S. F. Covre da Silva, A. Rastelli, E. A. Chekhovich. "The Effect of Alloying Disorder and Nanoscale Strains in $Al_xGa_{1-x}As/Al_yGa_{1-y}As$ Quantum Dots". *Materials for Quantum Network - Horizon Scanning UK Conference (M4QN)*. Cambridge, UK; November 2023.

P. Millington-Hotze, S. Manna, S. F. Covre da Silva, A. Rastelli, E. A. Chekhovich. "The Effect of Alloying Disorder and Nanoscale Strains in $Al_xGa_{1-x}As/Al_yGa_{1-y}As$ Quantum Dots". *QD2024*. Munich, Germany; March 2024.

List of Acronyms

AC Alternating Current

AFM Atomic Force Microscopy

BE Bright Exciton

BNC Bayonet Neill-Concelman

BS Beam Splitter

CB Conduction Band

CCD Charge Coupled Device

CCTV Closed-Circuit Television

CGS Crystal Ground State

CHASE Combined Hahn and Solid Echo

CT Central Transition

CW Continuous Wave

DBR Distributed Bragg Reflector

DE Dark Exciton

DFT Density Functional Theory

DNP Dynamic Nuclear Polarisation

EFG Electric-Field Gradient

EST Elastic-Strain Tensor

GET Gradient-Elastic Tensor

HGH Hartwigsen-Goedeker-Hutter

HH Heavy Hole

HWP Half-Wave Plate

InvNMR Inverse Nuclear Magnetic Resonance

LDE Local Droplet Etching

LH Light Hole

LP Linear Polariser

MAS Magic Angle Spectroscopy

MBE Molecular Beam Epitaxy

MOVPE Metal Organic Vapour Phase Epitaxy

ND Neutral Density

NMR Nuclear Magnetic Resonance

NSD Nuclear Spin Diffusion

NSR Nuclear Spin Relaxation

NV Nitrogen Vacancy

ODNMR Optically Detected Nuclear Magnetic Resonance

OHS Overhauser shift

PL Photoluminescence

QCSE Quantum Confined Stark Effect

QD Quantum Dot

QM Quantum Mechanics

QWP Quarter-Wave Plate

RF Radiofrequency

SM Single Mode

SMU Source/Measure Unit

SO Split-Off

ST Satellite Transition

VB Valence Band

Contents

List of Figures

List of Tables

Chapter 1

Introduction

Quantum Mechanics (QM) is said, by many, to have been 'discovered' by Planck on 14^{th} December 1900 when he explained black body radiation by discretising energy levels [1–3]. 124 years later this 'new' approach to physics has become a pillar of modern day life. A notable innovation that has stemmed from QM is quantum computing. The rationale behind a quantum computer, as stated by [4–9], is the need to simulate quantum systems that classical computing techniques are *realistically* unable to handle. This led to the development of quantum algorithms, such as the eponymous Shor's, Deustch-Jozsa's and Grover's algorithms, which demonstrated the exponential computational time savings that could be utilised through quantum computing.

For all of these algorithms to work, however, one must not use a classical bit which has the logical values of $|1\rangle$ and $|0\rangle$, but a qubit. A qubit relies upon the QM property of a wavefunction; more precisely, it is dependent on the superposition of the pure two-level binary state, so that the wavefunction, ψ, can be defined as:

$$|\psi\rangle = \alpha\,|0\rangle + \beta\,|1\rangle\,. \tag{1.1}$$

In Equation 1.1, binary states of 0 and 1 have probability amplitudes α and β. These represent the likelihood that when the wavefunction collapses the observable state will be either $|0\rangle$ or $|1\rangle$. Ideal qubits can be set in any arbitrary superposition state and entangled with other qubits to form quantum gates, which can then be used for a quantum computer [10]. For these qubits to be useful in quantum computing, the system which they are within must be able to meet certain criteria. Some of these requirements were initially stated by DiVincenzo in 2000 [11], but these were then rephrased by Ladd et al. in 2010 [12], which we will state here:

Scalability The computer should be able to be scaled exponentially without there being an exponential increase to the resources required to run the system (energy, time, space, et cetera).

Universal logic The system needs to be accessible using a set and finite number of control operations, whose resources should also not grow exponentially, to perform all necessary

computations.

Correctability The entropy of the computer must be extractable, i.e. the system must be able to be effectively initialised, manipulated and measured.

The question arises as to what the qubits can be created from, the answer to which is a variety of materials. A few examples being: ions trapped within an electric field [13–17], defects in crystals [18–20], Nitrogen Vacancy (NV) centres in diamond [21, 22], superconducting qubits [23–28], and Quantum Dots (QDs) [12, 29–31]. By no means is this an exhaustive list, but its shows the diversity of techniques that physicists are using. A more detailed comparison of qubit sources can be found in the aforementioned paper by Ladd et al. [12]. In this thesis the work focuses on III-V semiconductor nanohole infilled QDs; I will provide a brief introduction to the pros and cons of these dots, as to enhance the overall understanding of the field for the reader.

The semiconductors used for growing QDs have a direct bandgap, which allows for efficient/strong light matter interactions (strong optical dipole moment [32]). In addition to this, QDs have also been found to be an excellent source for single-photon sources [33–36]. This enables the photon to be used as a, so-called, 'flying' qubit, where information can be transported between 'stationary' QD qubits. These stationary qubits can be created due to the spin degrees of freedom, and the confinement of an electron, within QDs. These QDs can be grown within cavities/waveguides to enhance their properties [36–42], which also paves the way forward for on-chip integration of the qubits. However, there are issues with QDs, some of which are non-trivial. Firstly, the placement of QDs is random; there are techniques for registration of the locations of QDs prior to any optical cavities/waveguides et cetera being fabricated, however these methods have not yet been developed enough for high success rates of registered QDs with the same optical properties as randomly located dots.

Another difficulty with solid-state QDs is when a confined spin, such as an electron, is utilised as a qubit within a QD. This structure is an example of a central spin system, where the electron is not isolated from its environment of approximately 10^5 neighbouring nuclei, which all have fluctuating quadrupolar nuclear spins (explained in Section 2.4.1.3). This raises a potential inherent issue with QDs, as there are not only strong light-matter interaction but also matter-matter interactions. The central spin of an electron interacts with the nuclear spins of a QD adding to their decoherence (more details in Chapter 5). To add to this, there are phonons present which can interact with the crystal lattice, which can add another layer of 'noise' into the system [43].

The work in this thesis can be summarised as an investigation into the longevity of nuclear spins and improving the initialisation of QD states. This is to improve the "correctability" factor as previously mentioned, so that one could utilise nuclear spins as quantum memories, registers and logic devices [31, 44–47]. This is, predominantly, achieved through the use of Nuclear Magnetic Resonance (NMR) techniques to non-invasively probe both the dynamics and spectral-domain properties occurring within the QD. A brief outline of the thesis chapters are as follows:

Chapter 2 introduces the basics of QD growth. It then discusses the optical selection rules and spin system of QDs. These are then considered with the specific application of the measurements used in the thesis.

Chapter 3 outlines the experimental techniques and equipment required. The pump-probe technique is explained along with a description of how it is incorporated into NMR measurements.

Chapter 4 presents the investigation into the strain within QDs with different chemical compositions. Altering the isotopes within the QDs resulted in distinct NMR spectra. The spectral broadening of these spectra was used to analyse internal (nanoscale) strain within QDs.

Chapter 5 exposes the nature of the nuclear spin ensemble dynamics when an electron is introduced in the QD. Nuclear spin diffusion is studied with and without an electron being present and a conclusion on the Knight-field-gradient barrier is made.

Chapter 6 contains experimental findings that show, for the first time in III-V semiconductor QDs, nuclear spin polarisations $\geq 95\%$ being reached.

Chapter 7 summaries the work contained within the thesis, as well as future directions that could be studied for advancements in the field.

Chapter 2

Background

2.1 History of Confined Heterostructures

The electron's de Broglie wavelength, λ_D, as defined in Equation 2.1 can be, very broadly, used to describe the electron's ability to travel. Where h is Planck's constant, m_e^* is the electron's effective mass, k_B is the Boltzmann constant and T is the temperature. By creating a semiconductor structure with confined dimensions, for example through heteroepitaxy, it is possible for the confinement length to be similar to the electron wavelength. For context if one takes $m_e^* = 0.067m_e$ [48], m_e being the classical mass of an electron, then the de Broglie wavelength of an electron is 42 nm/350 nm at room temperature/liquid helium temperatures. The result of this is the quantisation of the electron's motion, i.e. the confinement of its ability to travel. As can be seen in Figure 2.1, in bulk material there is no confinement and the density of states, $D(E)$, for the conduction band is continuous, after the bandgap, E_g, of the semiconductor. If one restricts a dimension, say the z axis, then the smooth $D(E)$ has a step-like form; if the confinement is in all dimensions then the result is a density function consisting of δ peaks. With this δ distribution the electron/hole movement within the structure is essentially stopped.

$$\lambda_D \sim \frac{h}{\sqrt{m_e^* k_B T}} \tag{2.1}$$

Experimental evidence for this three-dimensional confinement effect was not found until less than a century ago. In 1981 Ekimov and Onushchenko discovered that there was a shift of absorption lines of excitons which they attributed to this "quantum size effect"[1] [52]. It was later found by Goldstein et al. in strained-layer superlatices that these δ distributions were possible. These works then spurred on further research into reduced dimensionality systems with the prospects of discovering a variety of new physical properties [53].

[1] In 2023 Ekimov, would receive a Nobel prize due to this work along with Brus and Bawendi for "the discovery and synthesis of quantum dots" [49–51].

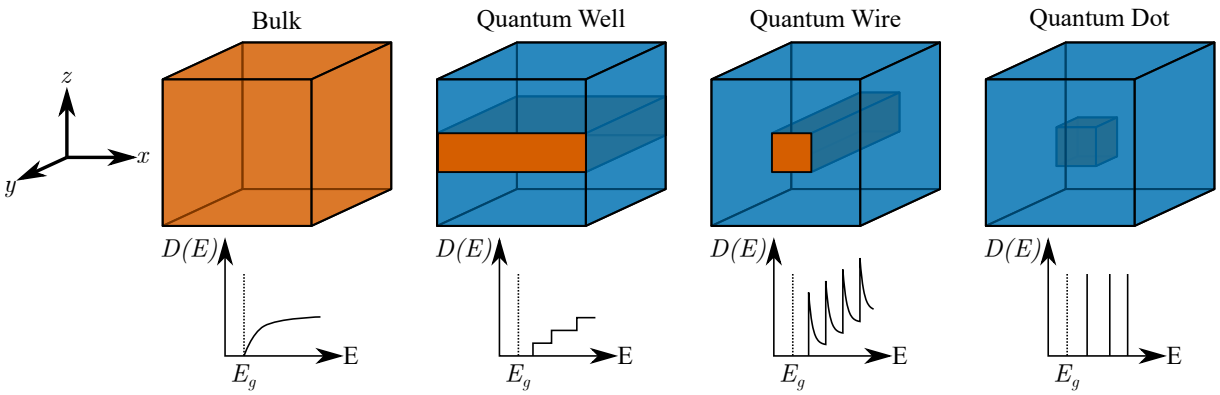

Figure 2.1: Comparison of the density of states as the level of confinement of the system changes. In a bulk system there is no dimensionality constraint, resulting in a smooth $D(E)$. For quantum wells one dimension, chosen to be z axis here, has been confined which leads to a step-like form of $D(E)$. In a quantum wire two dimensions are confined, here in z and x, leading to a $D(E)$ that has an inverse square root relationship. Finally, the QD has three-dimensional confinement and has a $D(E)$ that is a series of δ distributions. This figure has been adapted from [54].

2.2 States of Optically Active Quantum Dots

2.2.1 Quantum Dot Growth

The growth techniques used for the generation of QDs vary depending on the materials and properties that the QD is made from/for. Typically for group III-V semiconductors, such as: GaAs, InAs, InP, and GaN, the preferred methods for growth are either Molecular Beam Epitaxy (MBE) or Metal Organic Vapour Phase Epitaxy (MOVPE). MBE was first established by Günther, further developed by Davey and Pankey, and then majorly advanced by Cho and Arthur [55–57]. It can be defined as the "epitaxial growth of compound semiconductor films by a process involving the reaction of one or more thermal molecular beams with a crystalline surface under ultra-high vacuum conditions" [57]. MOVPE, on the other hand, results in the growth of structures due to chemical reactions rather than physical deposition, importantly the process also does not happen in vacuum but in a gaseous atmosphere with pressures ranging between $0.01 - 1$ atm. This lack of vacuum allows for the quicker growth of samples, however it can lead to more *dirty* samples, due to impurities being present. All the samples in this thesis were created using the MBE technique so that these contaminations are not present when conducting measurements, this is especially important for the findings of Chapter 4 where the strain of QDs is being researched.

There are different growth mechanisms one can use to create the QDs once the fabrication technique has been chosen, as shown in Figure 2.2. Apart from the nanohole infilling technique, all these methods require a small amount of strain at the interface of each layer[2].

[2]There is a threshold amount of strain required which is on the scale of %. In the case of GaAs/AlGaAs QDs, for example, Stranski-Krastanov can not be used as the growth technique as the lattice mismatch is too small.

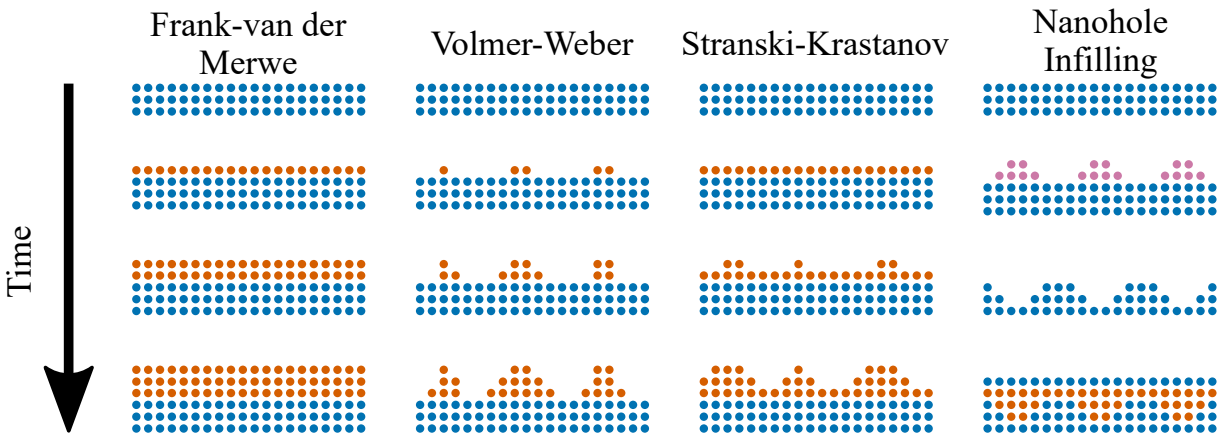

Figure 2.2: The three primiary forms of heteroepitaxy are shown along with the nanohole infilling technique used for QDs in this thesis. This has been adapted from [58].

The first form of hetreoepitaxy we shall discuss is Frank-Van Der Merwe growth. This is also known as monolayer by monolayer growth and, as the name implies, complete layers of differing material can be added to a substrate. This is possible due to the sum of both the surface energy of the film being added and the substrate/film interface being smaller than the initial substrate's surface energy (surface energy is reduced with the addition of the film) [59]. This contrasts with the second growth mechanism where the surface energy of the substrate is larger than the sum (the lattice constant mismatch is higher) [60]. This is called Volmer-Weber growth; rather than perfect monolayers being grown, due to surface energy minimisation, islands are formed. The formation of these islands occurs to maximize the proximity of matching atoms within the system, by reducing the presence of atoms from a differing material at the interface. Probably the most well known type of growth is called Stranski-Krastanov, which resembles the combination of these two techniques. The lattice mismatch of the substrate and the additive are still significant, however they are lower than in the Volmer-Weber growth [61]. This results in a couple of monolayers forming on the surface of the substrate (wetting layer) and after a critical thickness is reached the transition to islands growth begins [53]. This 'critical thickness' is due to the elastic energy accumulating in the strained layers before the self-assembly of QDs forms due to the crystal minimising its total energy [53, 62].

In an ideal world there would be no wetting layer present as the interaction of this with the QD states increases the sources of decoherence as well as causing broadening of Photoluminescence (PL) lines [63, 64]. This brings us onto the growth technique used for the QDs in this thesis, nanohole infilling through Local Droplet Etching (LDE). LDE, initially referred to as nanodrilling [65], works by preparing the substrate similarly to the other techniques discussed. A small flux of Ga (Al is used for the QDs in this thesis, but we shall proceed with the example case of Ga) is deposited onto the sample; the growth pattern of the Ga follows that of the Volmer-Weber mechanism, where small droplets form on the surface.

After the formation of these droplets there is some desorption of the underlying GaAs substrate, as shown in Figure 2.3, due to GaAs being unstable in Ga-rich environments [57]. This Ga can then be removed through an annealing process, leaving the etched nanohole behind. The size and depth of these holes will be dependent on the temperatures/concentrations/timings used during the deposition phase. The result of this LDE can be seen in Figure 2.4. The QD material can then be added to the vacuum chamber, to deposit onto the substrate, filling in the nanoholes. As no strain mechanics are used to create the QD, this is an excellent technique for creating high quality/uniform QDs which have low internal strain (see Chapter 4 for more details on this) with narrow PL linewidths [66–69].

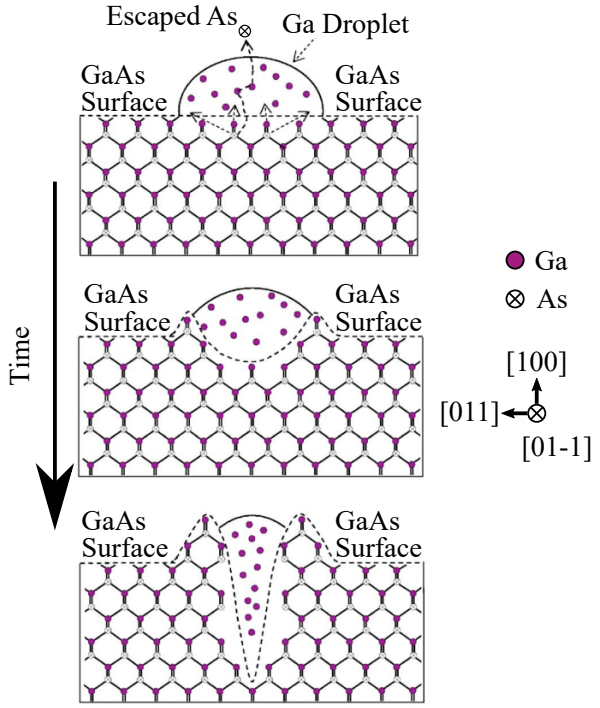

Figure 2.3: The proposed model as to why LDE occurs according to [65]. As time passes, the Ga droplet desorb the GaAs substrate thereby etching a hole. Used with permission from [65].

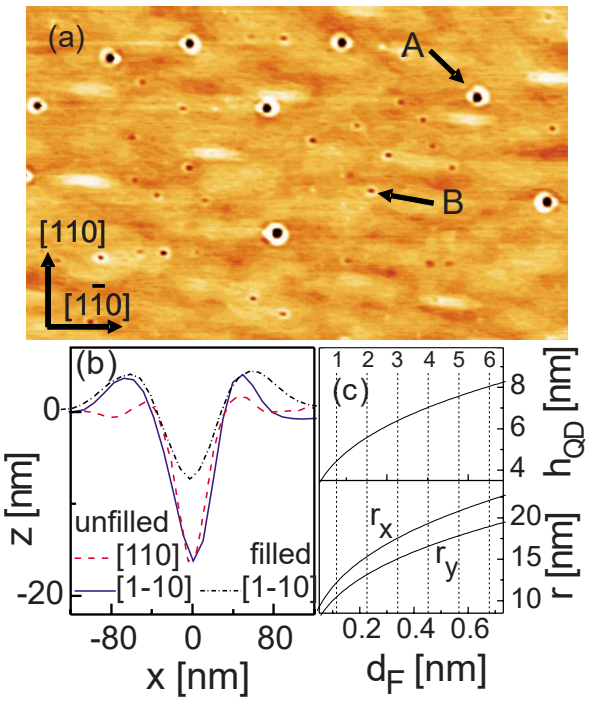

Figure 2.4: a) $42.5 \times 2.5\ \mu m^2$ Atomic Force Microscopy (AFM) image of an AlGaAs surface after LDE. Arrows A/B show the location of a deep/shallow hole respectively. Location A would be the precursor to a QD. b) Profiles of the deep hole marked by arrow A and of a deep hole after a pulsed-mode deposition of thin GaAs layer ($d_F = 0.45$ nm). c) Calculated height h_{QD} of a QD inside a deep hole as a function of the d_F and calculated radii of the elliptical QD base area. The dashed lines indicate the number n_p of GaAs filling pulses. Used with permission from [66].

2.2.1.1 Distributed Bragg Reflector

While on the topic of growing QDs it is useful to discuss Distributed Bragg Reflectors (DBRs). A schematic of a DBR can be seen in Figure 2.5. The physics behind this structure is fairly simple; alternating layers of semiconductor, in this case AlAs and GaAs, with differing refractive indices are grown on top of one another. The optical reflectivity, R, of the DBR, at the centre of the stopband, is given by Equation 2.2, as derived in [70]. In this equation, n_0 and n_s are the refractive indices of the originating and terminating layers respectively, n_1 and n_2 refer to the alternating semiconductor substrate refractive indices and N is the number of repeated pairs. In Figure 2.5 the originating, terminating and one of the alternating layers is GaAs, so $n_0 = n_s = n_2$. The assumption with this equation is that the repeated pair layers all have a thickness which is one quarter of the incident light wavelength. If one was using 700 nm light, at room temperature for simplicity, then the reflectivity from 15 pairs of AlAs/GaAs would be 98.5% [71, 72]. As to not trap the light between the two Bragg reflectors, a smaller number of pairs are grown above the dots. With 4 pairs of AlAs/GaAs the reflectivity would be 40.2%, therefore causing more light to be transmitted through the top of the sample, allowing for the PL collection necessary for Optically Detected Nuclear Magnetic Resonance (ODNMR).

$$R = \left(\frac{n_0 \left(n_2\right)^{2N} - n_s \left(n_1\right)^{2N}}{n_0 \left(n_2\right)^{2N} + n_s \left(n_1\right)^{2N}} \right)^2 \tag{2.2}$$

2.2.2 Discretised Energy States within a Quantum Dot

The III-V semiconductors used for creating the QDs in this thesis form a zinc-blende structure, which can be seen in Figure 2.6. In this configuration, the bulk state exhibits a parabolic-like band structure in the Conduction Band (CB) and Valence Band (VB) near the Γ ($\boldsymbol{k} = 0$) point in reciprocal space. The form of the energy dispersions, $E_{c/v}\left(\boldsymbol{k}\right)$, for the CB and VB follow Equation 2.3, where: E_g is the bandgap, $\hbar$ is the reduced Planck constant, $\boldsymbol{k}$ is the crystal momentum, and m^*_{carr} is the effective mass of the relevant charge carrier.

$$E_c\left(\boldsymbol{k}\right) \approx E_g + \frac{\hbar^2 \boldsymbol{k}^2}{2m^*_{\text{carr}}} \qquad \text{and} \qquad E_v\left(\boldsymbol{k}\right) \approx -\frac{\hbar^2 \boldsymbol{k}^2}{2m^*_{\text{carr}}} \tag{2.3}$$

The bandgap arises from the absence of permissible electron states between the CB and VB. In the case of GaAs this is a direct bandgap, i.e. it occurs at the centre of the Brillouin zone (Γ point); this means that no phonons are required to optically excite charge carriers. The band structure for GaAs, which can be simulated using Density Functional Theory (DFT), is shown as a function of the wavevector $\boldsymbol{k}$ in Figure 2.7. The Kohn-Sham form of DFT used here underestimates the bandgap[3], however the line shape reflects that of reality. There is a 1.81 eV

[3] A so-called *scissor function* is often used to correct this, as it will not change the form of the band structure.

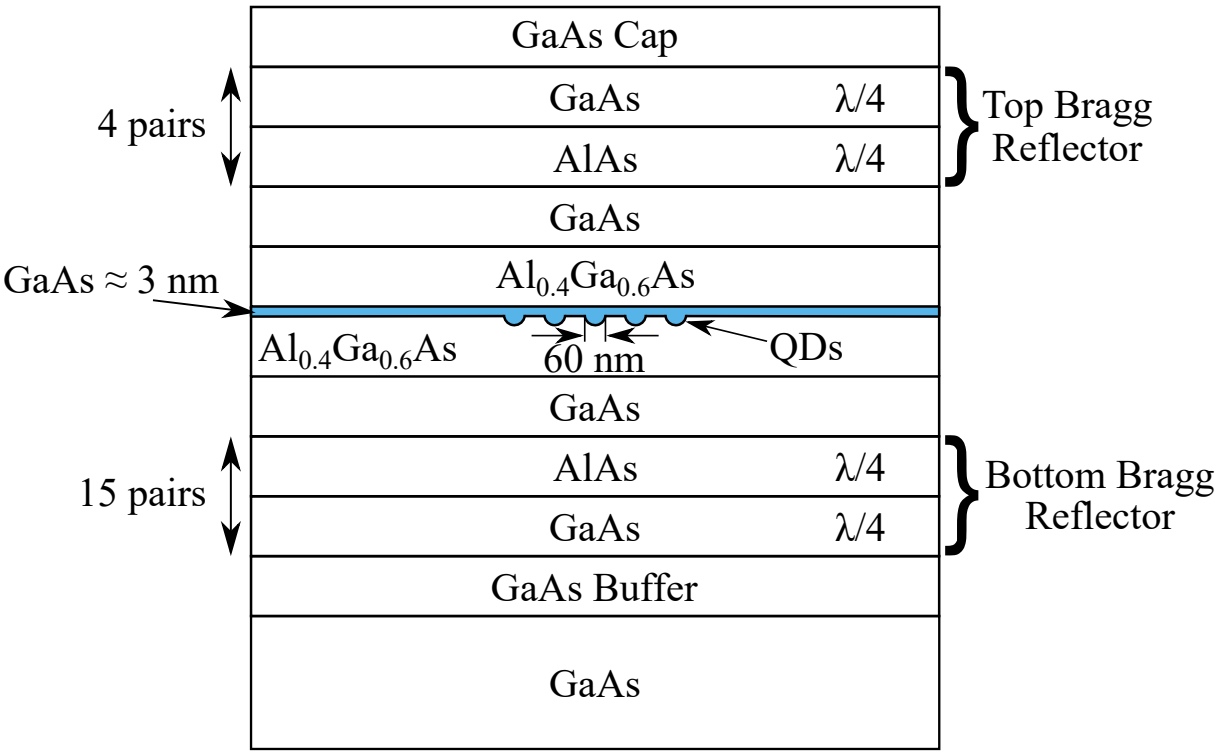

Figure 2.5: Structure of a GaAs QD sample, with DBR structures grown within the sample. The bottom/top Bragg reflector has 15/4 GaAs/AlAs layer pairs.

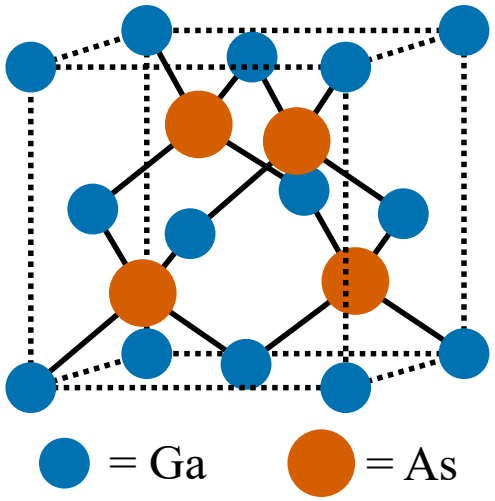

Figure 2.6: The zinc-blende structure of GaAs.

bandgap present for $Al_{0.3}Ga_{0.7}As$[4] and a 1.42 eV for GaAs, at 300 K [74]. These bandgaps change as the temperature of the sample decreases; at liquid helium temperatures there is a bandgap of 1.88 eV and 1.52 eV for $Al_{0.3}Ga_{0.7}As$ and GaAs respectively [73, 75, 76]. As the work in this thesis focuses on improving quantum computation using electron spin qubits, it is useful to consider electron/hole confinement. A free electron would have a single continuous

[4]The bandgap of $Al_xGa_{1-x}As$ depends on the concentration of Al in the sample [73]; a 30% concentration has been used as an example here as it is similar to the typical Al composition used in the barrier layers of the samples discussed across Chapters 4-6.

energy dispersion [76], however this is not useful for quantum computing where the electrons/holes need to be confined. For this reason QDs are made from semiconductors, such as GaAs embedded within AlGaAs. The three-dimensional confinement present in a QD suppresses spin-orbit interaction and makes for useful optical properties. The GaAs/AlGaAs semiconductor structure has a straddling gap (type I) alignment, which means that the CB within the QD region is lower (and the VB is higher) in potential than the surrounding bulk material (as seen in Figure 2.8). This results in excellent confinement of the electrons/holes within the QD.

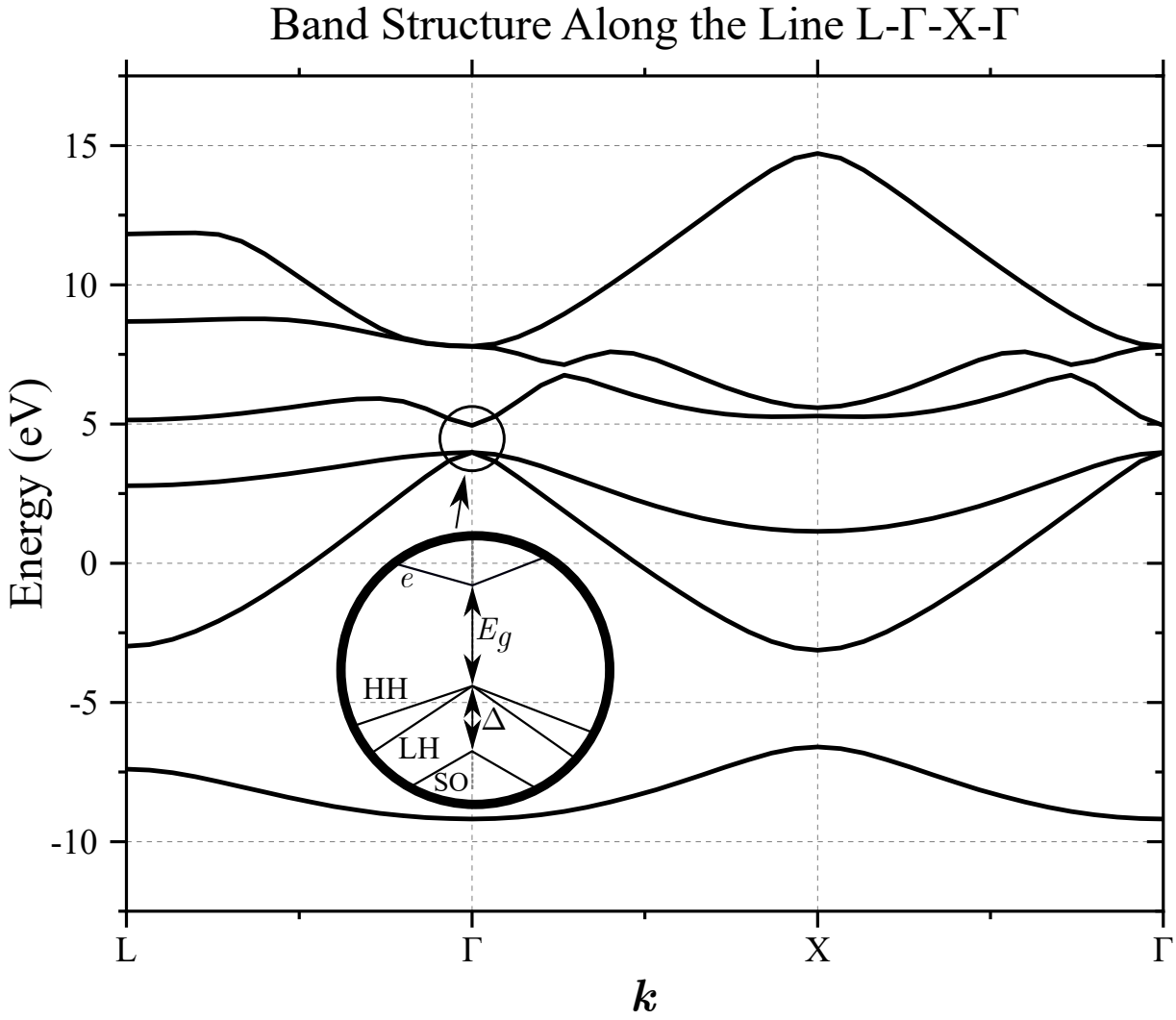

Figure 2.7: Band structure for unstrained GaAs along the line L-Γ-X-Γ in the Brillouin zone found with *ABINIT* software using Hartwigsen-Goedeker-Hutter (HGH) pseudopotentials [77]. The free-electrons would be in the CB, while holes are split in the VB, the separation of which is the bandgap E_g. There are three sub-bands in the VB which are, in decreasing energy, the: Heavy Hole (HH), Light Hole (LH) and Split-Off (SO) band. The HH and LH bands are degenerate at the Γ point, but as one travels along a line in $\boldsymbol{k}$-space the LH energy starts to decrease (at a faster rate) than the HH band. At $\boldsymbol{k} = 0$ the HH/LH and SO band are separated by a spin-orbit splitting Δ, which has been added to the plot in this magnification for clarity.

The CB is primarily composed of s-type atomic electron orbitals, which means that they

have no orbital angular momentum, $\hat{\boldsymbol{L}} = 0$. The VB, however, is primarily comprised of p-type electrons, meaning that $\hat{\boldsymbol{L}} = 1$. The total angular momentum, $\hat{\boldsymbol{J}}$ is simply the sum of $\hat{\boldsymbol{L}}$ and the spin angular momentum, $\hat{\boldsymbol{S}}$,

$$\hat{\boldsymbol{J}} = \hat{\boldsymbol{L}} + \hat{\boldsymbol{S}}. \tag{2.4}$$

Due to the motion of electrons within the potential of an atom (non-zero orbital angular momentum) there is some spin-orbit interaction. However if one temporarily neglects this, and with the knowledge of GaAs being a cubic crystal system, one can explain the two-fold degeneracy of the VB seen in Figure 2.7. For the CB the quasi-momentum of the electron would be $\boldsymbol{p} = 0$, as $\hat{\boldsymbol{L}} = 0$, but the VB is more complex due to the triple degeneracy of the orbital angular momentum, m_l, [78]. For simplicity, one can project m_l onto the QD growth axis, $\hat{e}_z$, as the basis for $\boldsymbol{p}$. This means we have the degenerate states of $m_l = [-1, 0, 1]$. Then using the Luttinger Hamiltonian, Equation 2.5, leads to the eigenvalues in Equation 2.6 [78]. In Equation 2.5: A and B are arbitrary constants, $\mathscr{I}$ is a unit 3×3 matrix, and we can use $\left(\boldsymbol{p} \cdot \hat{\boldsymbol{L}}\right)^2 = p^2 L_z^2$.

$$\mathscr{H}_{\text{Lutt}} = Ap^2\mathscr{I} + B\left(\boldsymbol{p} \cdot \hat{\boldsymbol{L}}\right)^2 \tag{2.5}$$

$$\begin{gathered} E_h(p) = (A+B)p^2 \text{ for } L_z = \pm 1,\ E_l(p) = Ap^2 \text{ for } L_z = 0 \\ A + B = \frac{1}{2m^*_{HH}},\ A = \frac{1}{2m^*_{LH}} \end{gathered} \tag{2.6}$$

As in Equation 2.3, here we have introduced the effective mass of charge carriers. This 'effective mass' is a mathematical contraption that arises as the charge carriers response to forces when interacting with other particles differs from the bare electron mass. The effective mass ascribed to the carriers is the mass that the particle *appears* to have in response to these forces. Here m^*_{HH} and m^*_{LH} are the effective masses for the HH and LH respectively. The descriptive words *heavy* and *light* come from $B = \frac{m^*_{LH} - m^*_{HH}}{m^*_{LH} m^*_{HH}} < 0$, which therefore means $m^*_{LH} < m^*_{HH}$. It can be noted that the HH has two-fold degeneracy itself due to $L_z = \pm 1$.

If one includes the effect of spin, all the energy states are essentially doubled (both in the VB and CB). However, the spin-orbit interaction results in an extra energy which is proportional to $\hat{\boldsymbol{L}} \cdot \hat{\boldsymbol{S}}$. The momenta $\hat{\boldsymbol{L}}$ and $\hat{\boldsymbol{S}}$ are no longer conserved quantities, but the total angular momentum, $\hat{\boldsymbol{J}}$ from Equation 2.4, is. The eigenvalues for J^2 are $j(j+1)$ where $|l - s| \leq j \leq l + s$ [78]. For holes, in GaAs, this results in two bands with $j_h = \frac{3}{2}$ and $j_h = \frac{1}{2}$. When these are projected onto the direction of growth, $\hat{e}_z$, the values are $m_{j,h} = \left[+\frac{3}{2}, +\frac{1}{2}, -\frac{1}{2}, -\frac{3}{2}\right]$ for the $j_h = \frac{3}{2}$ band and $m_{j,h} = \left[+\frac{1}{2}, -\frac{1}{2}\right]$ for the $j_h = \frac{1}{2}$ band. This latter band is referred to as the SO band, and is separated by an energy difference $\Delta \approx 0.34$ eV (in GaAs) compared to that of the $j = \frac{3}{2}$ band [78, 79]. The holes with $m_{j,h} = \pm\frac{3}{2}$ are referred to as HHs while those with $m_{j,h} = \pm\frac{1}{2}$ are LHs. A visualisation of the energy levels is shown

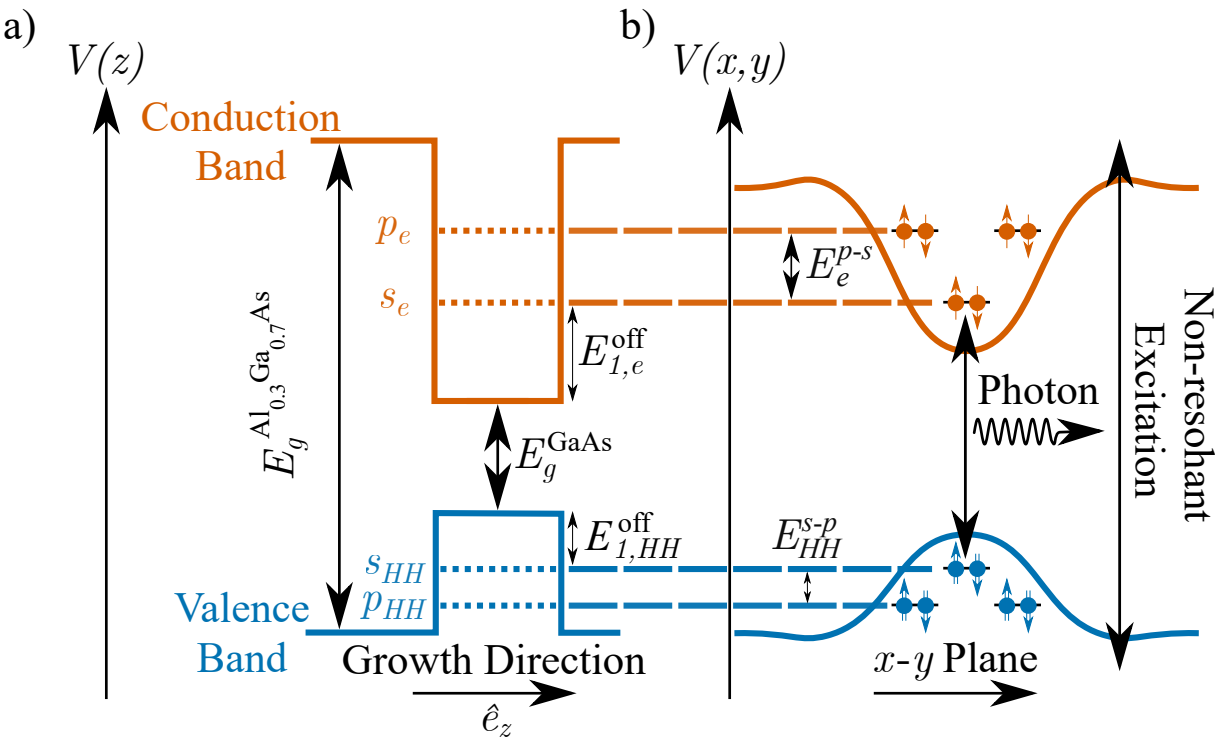

Figure 2.8: a) There is strong confinement for the QD in the growth direction $\hat{e}_z$, it can be treated as a finite quantum well. b) The weaker confinement in the $x-y$ plane can be treated as a 2D harmonic potential, with an atom-like structure in the valence and conduction band. When non-resonant excitation occurs to the wetting layer electrons will be excited into the conduction band, leaving a hole in its place. Nearby carriers will be quickly carried into higher shells in the QD, which then relax non-radiatively. The electron/hole then recombine to emit a photon, which can then be detected optically. ⇑ and ⇓ are the spin up and down heavy holes respectively while ↑ and ↓ are the spin up/down states of the electron respectively. These are often shown as ⇑⇓ for HHs and ↑↓ for electrons.

in Figure 2.8, where the different shells of the electrons/holes are denoted by $s_e/s_{HH}, p_e/p_{HH}$ (which would continue in the same manner with $d, f, ...$ shells)[5].

Considering the three-dimensional confinement of a QD, as illustrated in Figure 2.1, the energy levels can be approximated using a very simplified model: the infinite potential quantum box. In this model, the potential inside the box is assumed to be zero, while outside the box, it is infinite. The side lengths of the box are L_x, L_y, and L_z. The time-independent Schrödinger equation for this system is shown in Equation 2.7, where $\hbar$ is the reduced Planck constant, ψ is the electron wavefunction, m_e^* is the effective mass of the electron, and $E_{x,y,z}$ represents the total energy, which is the sum of E_x, E_y, and E_z. Solving for $E_{x,y,z}$, as shown in Equation 2.8, reveals that the energy levels of the electron are quantised with respect to the quantum numbers n_x, n_y, and n_z [80].

[5]It should be noted that the energy levels in this figure are not identical to those atomic sub-orbitals in 3D. In Figure 2.8b, for example, the potential has been defined in only 2D, with there being a fixed energy offset (due to the z axis confinement), which will naturally distort the energy levels.

$$-\frac{\hbar^2}{2m_e^*}\left(\frac{\partial^2}{\partial x^2}+\frac{\partial^2}{\partial y^2}+\frac{\partial^2}{\partial z^2}\right)\psi\left(x,y,z\right)=E_{x,y,z}\psi\left(x,y,z\right) \tag{2.7}$$

$$E_{x,y,z}=\frac{\hbar^2\pi^2}{2m_e^*}\left(\frac{n_x^2}{L_x^2}+\frac{n_y^2}{L_y^2}+\frac{n_z^2}{L_z^2}\right) \tag{2.8}$$

A more refined approach to this model incorporates specific characteristics of the QD system and relaxes the assumption of an infinite potential. As can be determined from Figure 2.5, the potentials for in-plane and out-of-plane confinement differ significantly due to the higher degree of confinement in the growth direction [81]. Figure 2.8 shows the potential modelled as a finite square well in the $\hat{e}_z$ direction[6]. The energy, E_j of an electron in state j is given by Equation 2.9 [86], where: d is the dot height, V_0 is the potential outside the well, the potential $V(z)$ inside the well is zero, and $m^*_{\text{dot}}/m^*_{\text{bulk}}$ being the effective mass in the QD/surrounding bulk material. The solutions to this equation are symmetric/antisymmetric wavefunctions, when values of j are even/odd.

$$\sqrt{\frac{m^*_{\text{bulk}}\left(V_0-E_j\right)}{m^*_{\text{dot}}E_j}}=\tan\left(\frac{d}{2}\sqrt{\frac{2m^*_{\text{dot}}E_j}{\hbar^2}}+\frac{\pi}{2}\bmod\left(j+1,2\right)\right) \tag{2.9}$$

For the $x-y$ plane the confinement is weaker, causing a broadening of the potential, which is modelled as a parabola in Equation 2.10 [80]. ω_{carr} is a constant energy separation frequency and, once again, m^*_{carr} refers to the effective mass of the charge carrier (electron or hole).

$$V\left(x,y\right)=\frac{1}{2}m^*_{\text{carr}}\omega^2_{\text{carr}}\left(x^2+y^2\right) \tag{2.10}$$

The eigenvalues for Equation 2.10 are:

$$E^{\text{carr}}_{m,n}=\hbar\omega_{\text{carr}}\left(k+l+1\right). \tag{2.11}$$

Here one can see the quantised shell-like states, which are called s, p, d, f, ... with quantum number values $n=l+k=0,1,2,3,...$ [53]. These shells have degeneracy values of $(2n+1)$. The energy splitting for adjacent shells would be $E^{p-s}_{\text{carr}}=\hbar\omega^{p-s}_{\text{carr}}$, which for electrons/HHs the values are $\sim 55/20$ meV [87]. From Figure 2.8 one can also see that there is an offset from the bottom/top of the CB/VB to the first shell, these offsets are approximately $E^{\text{off}}_{1,e}\approx 190$ meV and $E^{\text{off}}_{1,HH}\approx 130$ meV [88, 89]. However, all these values vary significantly between QDs as they are determined by the dot's geometry as well as the composition of the dot and its surroundings.

[6]There are other considerations/assumptions that can go into the the modelling of the potentials based upon the geometry of the QD. There exist different theoretical models for these e.g. for lens/disc/pyramid QDs there are [81, 82]/[83]/[84, 85].

2.2.3 Charge Tuning

If QDs are grown in a *p-i-n* diode structure, then it becomes possible to tune the energy levels of the system. The *n*-doped layer, as shown in Figure 2.9a, acts as the Fermi sea (a reservoir of electrons existing under the Fermi energy, E_F). As a bias voltage, V_b, is applied across the sample, the energy level of the *n*-doped layer shifts relative to E_F (the direction of the shift depends on the polarity of the applied electric field). The strength of the electric field that couples to the QD is dependent on the thickness of the tunnelling barrier, t_B that separates dot layer from the *n*-doped substrate. At large reverse biases E_F is lower than the first charging state within the QD. As is shown in Figure 2.9b, as one increases V_b the difference between E_F and the $1e$ state decreases until an electron can tunnel into the QD at a bias of V_{1e}. This effect can be seen in Figure 2.10, which is where a single electron has tunnelled in at ~ 0.43 V. There is a separation of energy levels due to the Coulomb blockade, which is due to the Coulomb repulsion between electrons [90]. This is why there exist plateaus between the filling of electrons in Figure 2.10. The middle of this plateau (0.517 V in Figure 2.10) can then be used to deterministically fill a QD with a single electron, which can be seen as an on-demand electron spin qubit. The filling of the QD with electrons continues for n electrons (at biases V_{2e}, V_{3e}, ...), however the 'length' of the plateaus decreases as one increases the number of electrons, as the separation between energy levels decreases. Building on Figure 2.10, Figure 2.14 shows the effect of varying the bias on exciton states, as observed through their PL spectra. In Chapter 5 the filling of a dot with an electron was used in order to determine whether a Knight-field-gradient barrier exists.

2.3 Excitons and Optical Selection Rules

While QDs do have discrete energy levels, for this to be of any practical use, the temperature of the sample needs to be lowered. This is because thermal excitations, which are governed by phonons, can occur promoting electrons to higher energy levels. To reduce these unwanted excitations, one can cool down the sample to lower the phonon's thermal energy, k_BT (k_B being the Boltzmann constant and T the temperature in Kelvin). By doing this one ensures that the separation of discrete energy levels in the QD is larger than the thermal energy of electrons. This is why most work with QDs is performed in cryogenic temperatures (< 50 K), to ensure that discrete energy levels are present and any electron/holes that are generated only occupy the lowest energy state. In Sections 5 and 6 the selective control of electron occupancy was crucial for the work, so it was essential low temperatures were used to ensure electrons/holes were not able to escape the QD entirely.

GaAs and $Al_xGa_{1-x}As$ both have direct bandgaps, i.e. the smallest separation of the VB and CB occur at the Γ point in the Brillouin zone[7]. This results in the trivial conservation of crystal momentum; QDs interact strongly with photons as they do not require the absorption of

[7]The direct bandgap for $Al_xGa_{1-x}As$ is true when $x < 0.4$, as is the case for QDs used in this thesis [93].

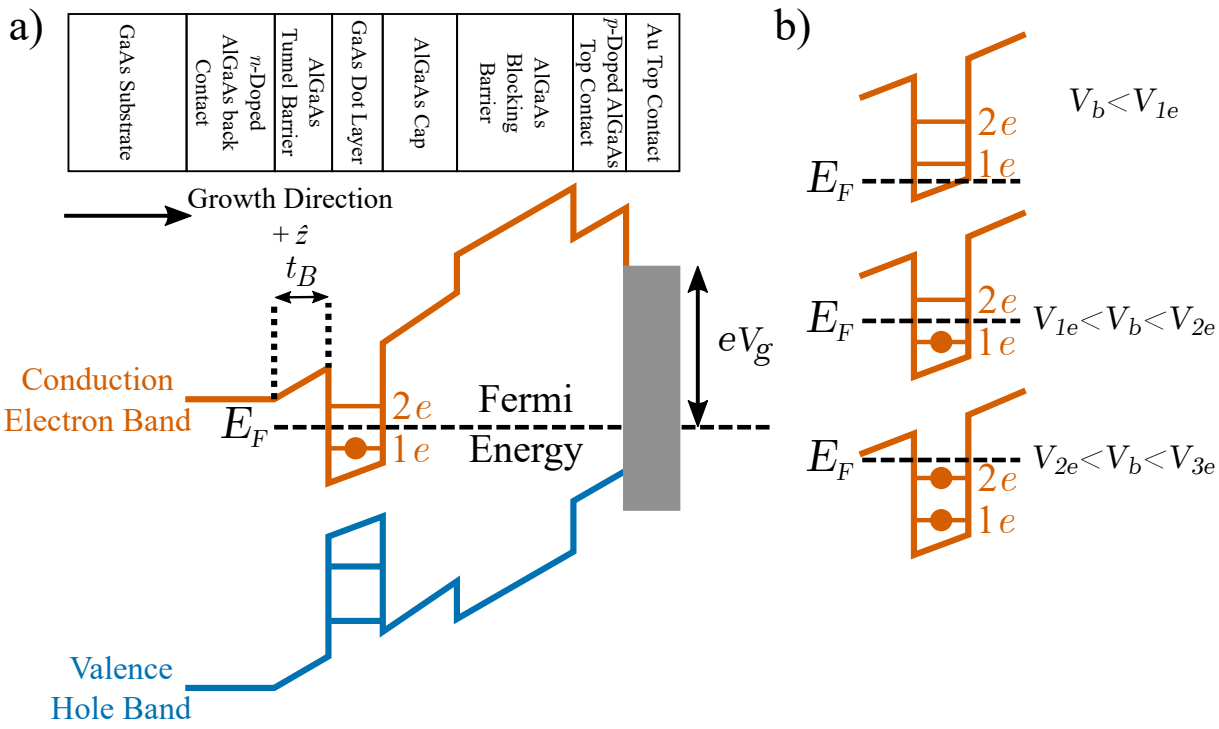

Figure 2.9: a) The energy levels of a QD within a *p-i-n* diode structure, with the applied bias allowing for one electron to have tunnelled into the QD. Adapted from [91]. b) The variation of applied bias determines the how many electrons to tunnel into the QD.

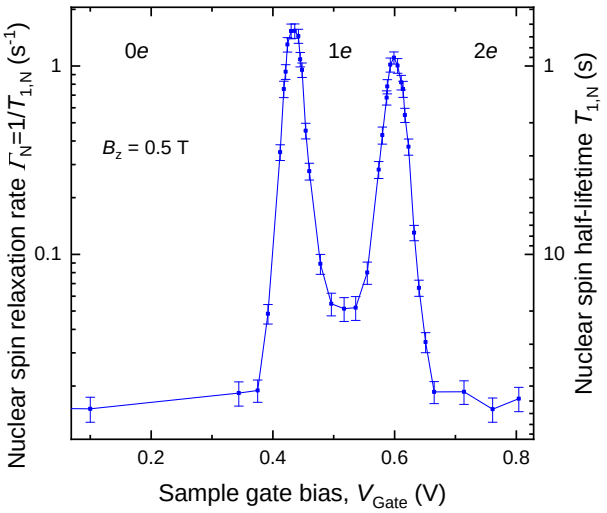

Figure 2.10: Bias dependency of the nuclear spin relaxation rate for a QD with an external field of 0.5 T while at 4.2 K. The centre of the $1e$ plateau is at 0.517 V, where a single electron has tunnelled into the QD. The Coulomb blockade is preventing a second electron from tunnelling into the QD. Figure is reproduced with permission from Springer Nature and is from the publication [92], which is used for Chapter 5.

extra phonons. Under optical excitation, where the photon energy, $\hbar\omega$, is greater than or equal to $E_g^{\text{GaAs}} + \left(E_{1,e}^{\text{off}} + E_{1,HH}^{\text{off}}\right)$, an electron is promoted from the VB into the CB, and a hole is left behind. Equally, an electron can recombine with a hole to emit a photon with that same energy. The bound pair of electron and hole is called an exciton, which can be treated as a

quasi-particle. This exciton forms due to the Coulomb interaction between oppositely charged (spatially separated) particles. In semiconductor nanostructures this interaction is enhanced due to the confinement of the electron/holes, which increases their wavefunction overlap [94]. The binding energy between an electron in a state $\psi_i^e(\mathbf{r})$ and hole in state $\psi_j^h(\mathbf{r})$ is [95]:

$$E_{ij}^{eh} = \frac{e^2}{4\pi\epsilon_0\epsilon_r}\int\int \frac{\left|\psi_i^e\left(\mathbf{r}_e\right)\right|^2\left|\psi_j^h\left(\mathbf{r}_h\right)\right|^2}{\left|\mathbf{r}_e - \mathbf{r}_h\right|} d\mathbf{r}_e d\mathbf{r}_h, \tag{2.12}$$

where ϵ_0 is the vacuum permittivity, ϵ_r is the relative static permittivity in the QD and $\mathbf{r}_e/\mathbf{r}_h$ are the positions of the electron/hole respectively. The optical transition energy is lowered by this excitonic binding energy, which will vary based upon the size of the QD [95]. In bulk GaAs, the excitonic binding energy is 4.2 meV [96], which is significantly lower than that observed in a QD. Specifically, the binding energy in a QD is roughly half of that found in bulk GaAs, owing to the enhancement resulting from the confinement within the QD [95–97].

When a photon is absorbed that has an energy larger than the QD resonance, non-resonant excitation occurs. This results in electron-hole pairs being created at higher energy levels (e.g. p/d levels) in the QD or perhaps even the wetting layer. These pairs are captured by the QD on a picosecond timescale, much faster than the radiative lifetime of the ground state QD exciton (on the order of nanoseconds [98]). When the exciton recombines to emit a photon, the energy will be equal to that exciton's resonant energy. This means that if one uses a different wavelength of light to that of the emitted photon it is easy to distinguish the emission spectra of the QD. While not required for the work in this thesis, one could however use a resonant energy photon for excitation to get resonant PL. One would then need to suppress scattered light from the sample, in order to *truly* observe the emission lines of the QD. This can be achieved by cross polarisation and by using spatial filters, so that any scattered backscattered light is suppressed [99].

There are optical selection rules which determine which transitions are *allowed*. This is due to a photon carrying a net angular momentum, $J_{\gamma,z}$, of ± 1 and intrinsic parity, π_γ, of -1 [100]. The Bloch functions for the CB and VB have opposite parity, therefore only interband transitions are allowed (e.g. $s_e \leftrightarrow s_{HH}$ or $p_e \leftrightarrow p_{HH}$). For intraband transitions the Bloch states must be identical which only occurs when the change in orbital angular momentum, $\Delta\hat{\boldsymbol{L}}$, is ± 1 (e.g. $s_e \leftrightarrow p_e$). When an electron absorbs a photon, its angular momentum is altered by ± 1 dependent on the incident helicity of light (σ^+/σ^-). To describe this, the notation we shall use is $\uparrow/\downarrow$ for a spin up/down electron and $\Uparrow/\Downarrow$ for a spin up/down HH. As the angular momentum of the photon is unity, only the states $|\uparrow\Downarrow\rangle$ (where $J_{ex} = 1$) and $|\downarrow\Uparrow\rangle$ (where $J_{ex} = -1$) are optically active, as shown in Figure 2.11a. The optically forbidden states would have parallel spins for the hole and electron ($|\downarrow\Downarrow\rangle$ and $|\uparrow\Uparrow\rangle$); this is not optically active as it would require the photon to have an angular momentum of ± 2. The states that are optically active are called *bright* excitons, X_b, and those that are not are called *dark* excitons, X_d . In Figure 2.11a one can not distinguish the forbidden states for the trions (a trion consisting of three charged particles

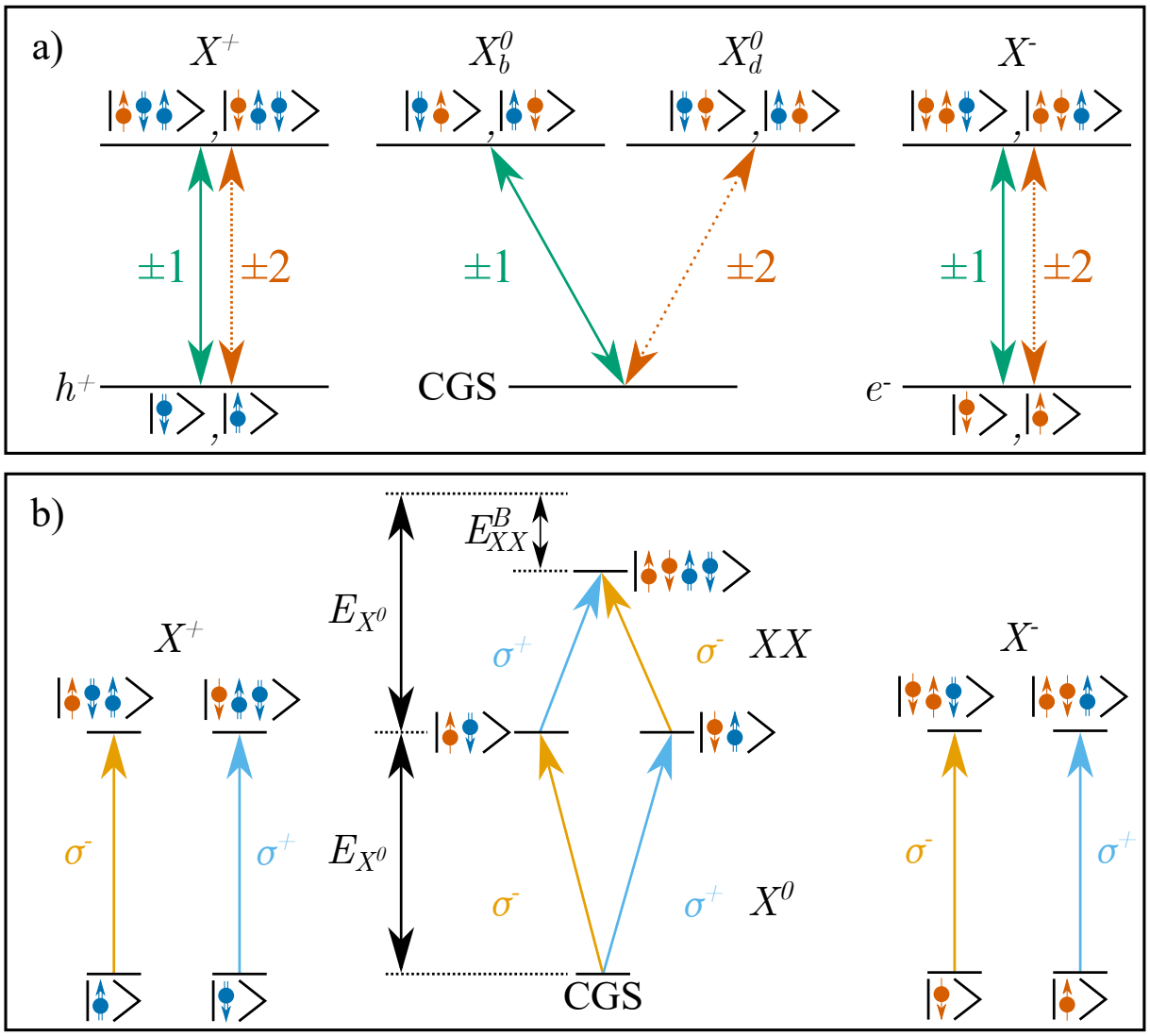

Figure 2.11: a) Positive and negative trions (X^+/X^-) have two possible spin configurations. The neutral exciton (X^0) has two possible states, bright and dark (X_b^0/X_d^0). Only X_b^0 is allowed; X_d^0 if optically forbidden. The Crystal Ground State (CGS) is sometimes labelled as $|0\rangle$. b) The states here are shown in the case of Faraday geometry with a large magnetic field. Each spin state, for the trions, is coupled to a particular circular polarisation of light, which allows for set spin states to be prepared. Energies shown are not to scale, and the transitions of the trion states are shifted in energy with respect to the X^0 transition.

bound together rather than two), without the presence of a magnetic field, since the initial and final spin states are degenerate. In GaAs QDs the Dark Exciton (DE) is lower in energy than the Bright Exciton (BE) due to the form of exchange interaction between the hole and electron, resulting in its protection from a separate spin flip of one of its constituents and longer lifetimes [101, 102]. Asymmetries present in the QD at the atomic scale also affect DE more strongly than for the BE, as discussed in [103]. If the symmetry of a QD is broken there is mixing of the eigenstates for the BE and DE, allowing for the DE to become partially optically active [103]. Due to the hyperfine interaction mixing of exciton states and/or a tilted dot quantisation axis, it is possible to see, experimentally, the DEs when using PL spectroscopy under low-power

optical excitation, due to some finite coupling to the $\Delta J = \pm 2$ transitions [104], as shown in Figure 2.12.

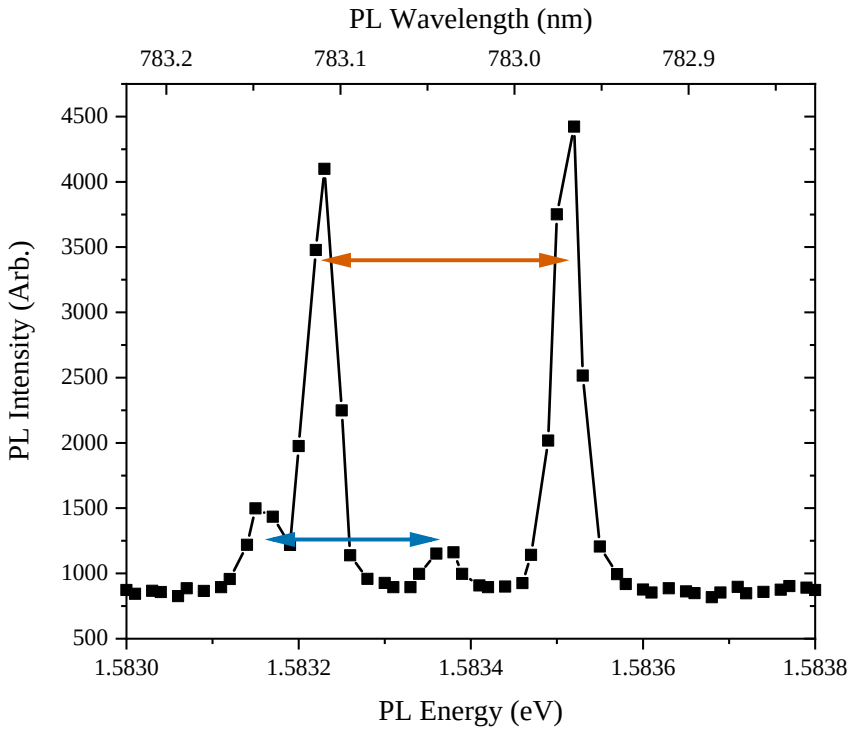

Figure 2.12: PL spectra of a QD showing the splitting of a BE with an orange arrow and a DE with a blue arrow. This data was taken while the QD was within an external field of 4.5 T in Faraday geometry and taken with a 0.2 μW 690 nm excitation laser.

2.3.1 Heavy Hole-Light Hole Mixing

When there is asymmetry in the QD, for example due to elongation, then there will be some degree of HH-LH mixing. This mixing can be observed through the polarisation of exciton emission, as shown in Fig. 2.13. When a conduction electron recombines with a HH one would get a perfectly circular polar diagram. However, if an electron recombines with a LH instead of a HH a photon with the exact opposite polarisation is produced [105]. When two opposite polarisations interfere with each other, from HH and LH recombination, the resultant superposition is elliptically polarised. The exact polarisation state depends on the amplitude and phase of the two components. If there is tensile strain added to the QD, either due to the growth or as implemented in [106], then HH and LH states become energetically closer. This can lead to mixing of the HH-LH states, required for the anisotropic hyperfine interaction discussed in Section 2.4.1.1. The mixing of these states will also reduce the efficiency of optical spin pumping, discussed in Section 3.2.2 as additional, previously forbidden, optical transitions become allowed.

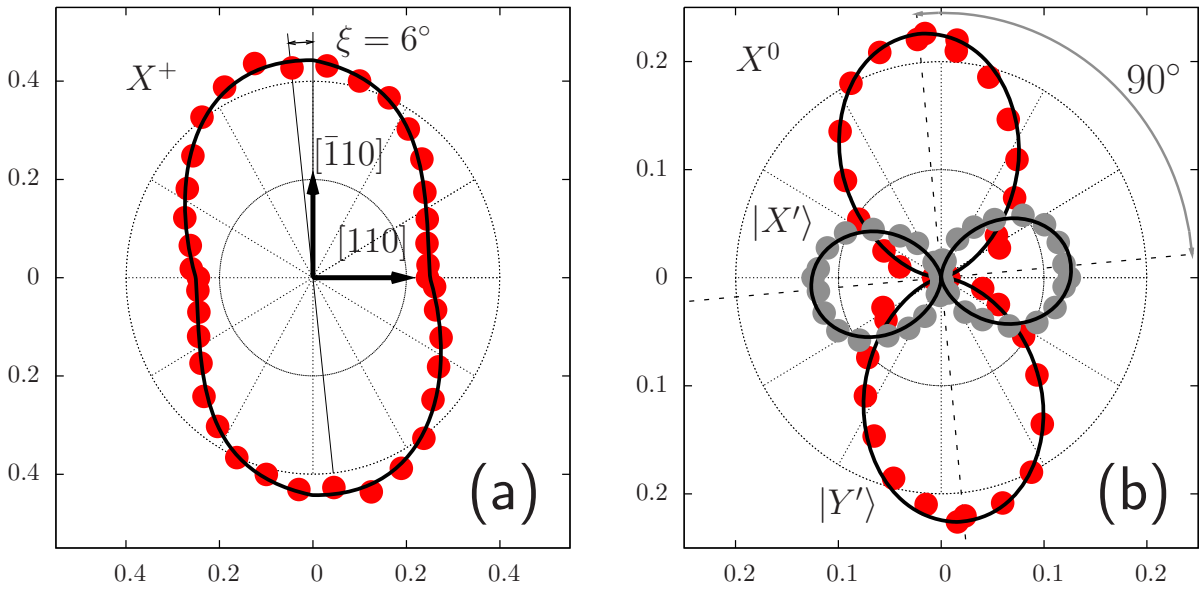

Figure 2.13: a) Polar plot of the X^+ exciton emission intensity for different positions of a linear polarisation analyser relative to $[110]$ crystallographic direction in a GaAs/AlGaAs QD. b) Neutral excitons X' grey and Y' red. The theoretical calculation is shown by the solid black lines. Used with permission from [105].

2.3.2 Charged Excitons

If an extra hole or electron is present within the QD, different types of excitons can be produced. This can be exploited if one uses a charge tunable sample, as one can tune the voltage across the sample to change the Fermi level (sea of electrons) relative to the differences in QD energy states (charging energy). This behaviour is shown in Figure 2.14, which depicts the PL spectra of a QD measured at various gate biases. These different species of excitons are shown in Figure 2.11. If the QD has an extra electron the negative trion, X^-, can form, if there is an extra hole the positive trion, X^+, can form. As can be seen in Figure 2.11b, different circular polarisations of light can be used to *pump* a QD deterministically to a particular spin state. When looking at the PL spectra of a QD, one would tend to find $X^-(X^+)$ at lower (higher) energies when compared to X^0. This difference exists due to differences in magnitude of the Coulomb interaction. The X^+ and X^0 excitons will also be present at a larger reverse bias than X^-. X^0 and X^- will have a fairly static PL emission energy as one changes the bias, while the X^+ would have its emission energy vary. These factors allow for identification of the excitons from a QD. It is also possible for a 4-particle biexciton (XX or occasionally $2X$) to form which will consist of a pair of the lowest energy transitions (being comprised of two carriers with opposite spin projection). This biexciton will have a total angular momentum of zero, however it will not have double the energy of X^0. This is because there also exists a binding energy E^B_{XX}, caused by the Coulomb interaction, which increases the energy of this exciton.

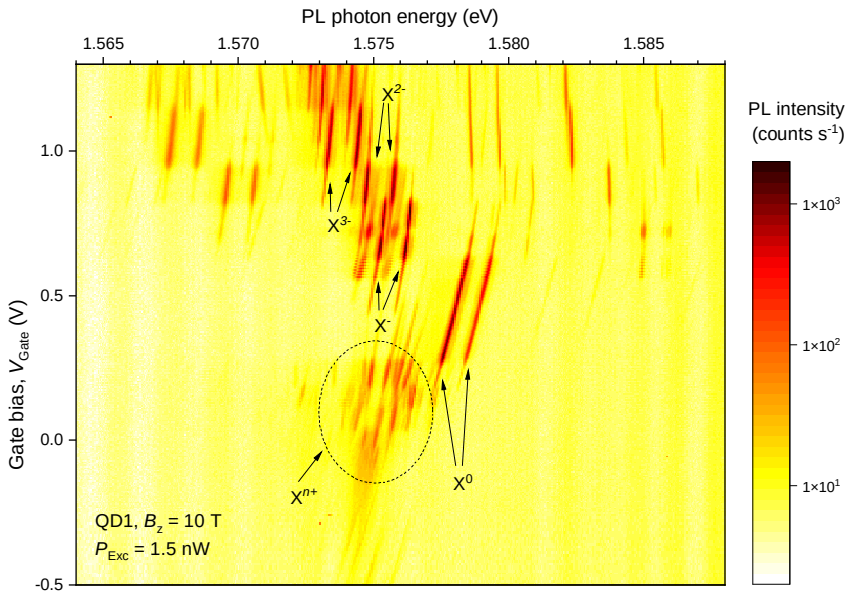

Figure 2.14: Bias dependent PL spectra of a QD with an external field of 10 T in Faraday geometry, measured with a 1.5 nW 632.8 nm laser. Figure is reproduced with permission from Springer Nature and is from the publication [107], which is used for Chapter 6.

2.3.3 Fine Structure for Excitons

Due to the electron-hole exchange interaction, there is a structure in the exciton energy spectrum. These spin interactions are mediated by the Coulomb interaction, and can be split into short and long range couplings. Both of these couplings, however, will be sensitive to anisotropy or strain present in the QD [108]. An example is in [109], where QDs were grown in anisotropic/imperfect nanoholes, leading to asymmetry along the $[1\bar{1}0]$ axis. The consequence of this is the mixing of the two bright and two dark excitons [108].

The electron-hole exchange interaction, for a confined exciton formed by an electron with spin $\boldsymbol{S}_e$ and a hole with spin $\boldsymbol{J}_h$, is given by Equation 2.13 [53, 111, 112].

$$\mathscr{H}_{exch} = -\sum_{i=x,y,z} \left(a_i J_{h,i} S_{e,i} + b_i J_{h,i}^3 S_{e,i} \right) \tag{2.13}$$

In Equation 2.13, a_i and b_i are the spin-spin coupling constants and $J_{h,i}$ is the spin projection of the hole in the i direction. Equally, the Hamiltonian can be expressed in terms of the BE and DE states as in Equation 2.14, through substitution of the electron and hole spin matrices into Equation 2.13. This would follow along from Figure 2.11a, where the BE has the eigenstates of $|+1\rangle$ and $|-1\rangle$, while the DE is $|+2\rangle$ and $|-2\rangle$. In this BE/DE description the exciton splittings, which would be: $\delta_0 = 1.5(a_z + 2.25b_z)$, $\delta_b = 0.75(b_x - b_y)$ and $\delta_d = 0.75(b_x + b_y)$, form Equation 2.14 [112]. These splittings are present within all QDs and can be seen within Figure 2.15.

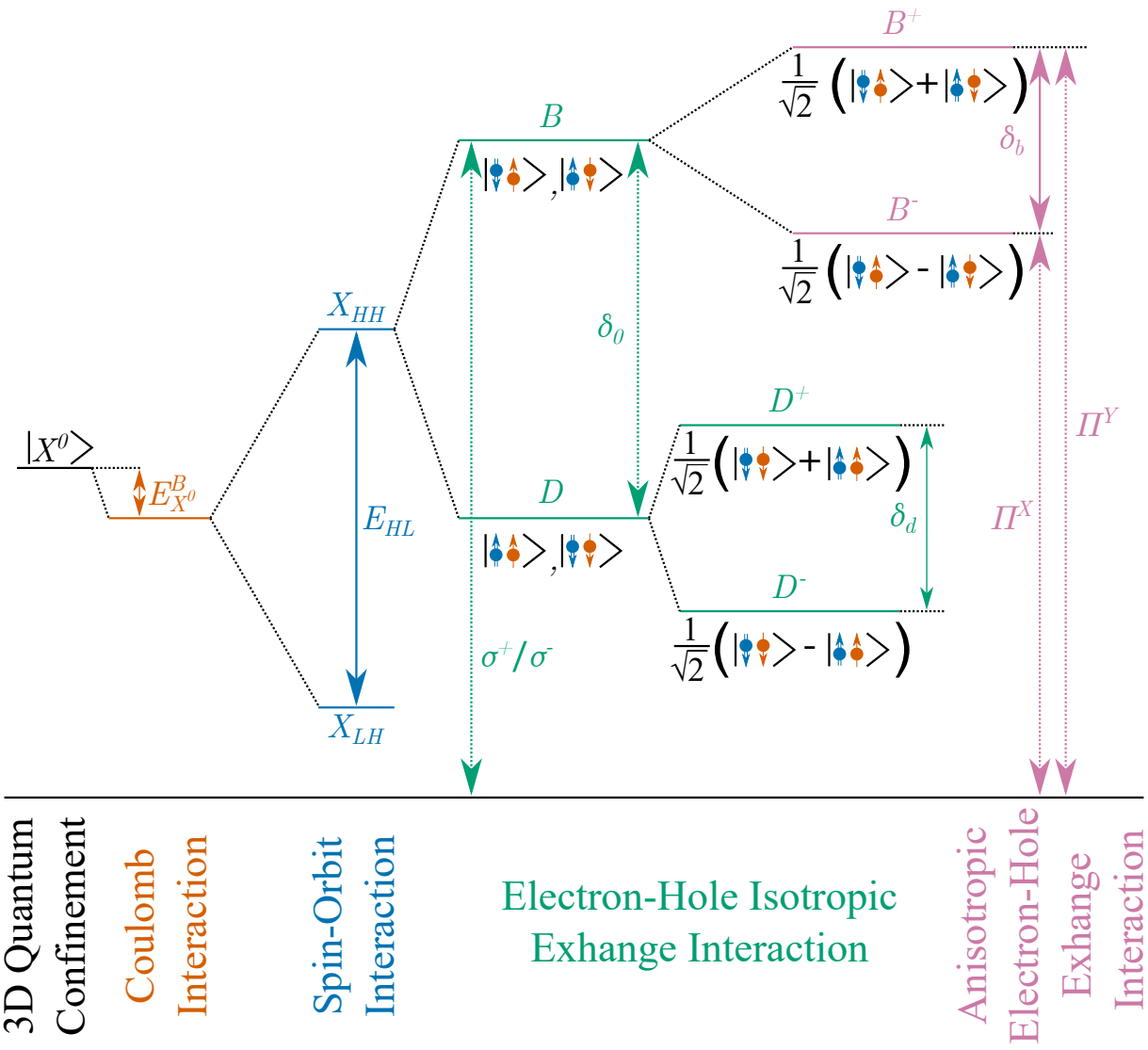

Figure 2.15: The spin-independent Coulomb interaction reduces the transition energy of the neutral exciton by $E^B_{X^0}$ (orange). Reduced symmetry causes the p-type hole band splitting between the HH and LH by E_{HL} (blue). The isotropic part of the exchange interaction lifts the spin degeneracy between the bright and darks states by δ_0 and mixes the dark states by δ_d (green). The transitions of the bright exciton are circularly polarised (σ^+/σ^-), while the dark states are optically forbidden. The anisotropic part of the exchange interaction then further splits the bright states by δ_b (pink). The fine structure of splitting of the bright states results in changed eigenstates leading to, at zero external magnetic field, the linearly polarised Π^X and Π^Y. Adapted from [110].

$$\mathscr{H}_{exch} = \frac{1}{2}\begin{pmatrix} \delta_0 & \delta_b & 0 & 0 \\ \delta_b & \delta_0 & 0 & 0 \\ 0 & 0 & -\delta_0 & \delta_d \\ 0 & 0 & \delta_d & -\delta_0 \end{pmatrix} \tag{2.14}$$

Within Equation 2.14, δ_0 is the splitting between the bright and dark states $B \leftrightarrow D$. This is a short range interaction which is characterised by the probability of an electron and hole being

found in the same space. Its value can range between $150-230$ μeV in GaAs QDs [108]. There is also a smaller splitting, δ_d, which splits the dark states by $\sim 10-25$ μeV [108]. Both δ_0 and δ_d occur due to the isotropic part of the exchange interaction. In contrast, δ_b exists due to the anisotropic exchange interaction (pink in Figure 2.15), and will vary strongly from dot to dot. To be more precise, this interaction occurs due to the lack of full rotational symmetry in the $x-y$ plane and $b_x \neq b_y$ [86]. For exciton doublets $\delta_d > \delta_b$ ($\delta_b \approx 3-13$ μeV [113]), but generally both δ_b and δ_d are small when compared to δ_0, as they are coupling coefficients proportional to J_h^3 [112]. The effect of δ_b is the mixing of bright states, affecting optical selection rules. Due to this mixing the total exciton angular momentum, $J_{ex} = \pm 1$, will no longer be a *good* quantum number; this results in the two split states no longer being able to be selected with circularly polarised light. Instead, when no magnetic field applied, these two states would be observed to be linearly polarised (Π^x/Π^y) [112].

2.3.4 Excitons in an Electric Field

Due to the nature of an exciton being a bound state between an electron and hole, there is an intrinsic permanent electric dipole. The associated moment, for the case of X^0 say, is $\boldsymbol{p}_{d,0} = e \cdot \boldsymbol{r}$, e being elementary charge and $\boldsymbol{r}$ being the displacement vector for the hole wavefunction relative to the centre of the electron wavefunction. When a static electric field, $\boldsymbol{F}$, is applied this separation can be further shifted, introducing an additional dipole moment whose magnitude will be dependent on the electric polarisability, α, of the exciton.

$$\boldsymbol{p}_d = e \cdot \boldsymbol{r} + \alpha \cdot \boldsymbol{F} \tag{2.15}$$

For a diode sample, $\boldsymbol{F} = -\frac{V_{bi}-V_{bias}}{d}$ where: V_{bi} is the built-in bias for the diode, V_{bias} is the applied bias, and d is the thickness of the intrinsic layer . A coupling then exists between this electric dipole and the field, which acts to shift the excitonic transition energies. The shifts can be much larger than in bulk material and even exceed that of the exciton binding energy due to quantum confinement [114, 115]. Denoting the transistion energy with no applied field as E_0, the change in energy is:

$$\Delta E_{QCSE} = E_0 - \boldsymbol{p}_d \cdot \boldsymbol{F} = E_0 - \boldsymbol{p}_{d,0} \cdot \boldsymbol{F} - \alpha \cdot \boldsymbol{F}^2 \tag{2.16}$$

This shift is called the Quantum Confined Stark Effect (QCSE) and contains both linear and quadratic terms. Using the QCSE, one can tune two QDs of similar wavelengths into resonance with one another [116] or an optical cavity [117]. If one uses an oscillating electric field another type of Stark shift occurs. Due to time-varying nature of the electric field resembling Alternating Current (AC) in conventional electronics, this effect is called the AC Stark effect. This often uses high-power optical excitation to shift one of the eigenstates, therefore removing the fine structure splitting [118, 119]. The shift is related to the frequency of field produced by the

incident optical signal. As the AC Stark effect is not used for work in this thesis the details of its principles are not discussed, but they can be found in [120–122].

2.3.5 Excitons in a Magnetic Field

There are two geometries commonly used to apply an external magnetic field. The first type is called *Faraday* geometry, which is where the applied field is oriented parallel to the optical axis ($+z$). This is the geometry mainly used for the work in this thesis. The alternative is *Voigt* geometry, where the magnetic field is applied perpendicular to the optical axis ($x-y$ plane). A summary of exciton selection rules in a magnetic field in these two configurations can be seen in Figure 2.16. The external field transforms the initially linear polarised components of $B^{\pm}$ into circularly polarised components, as the Zeeman splitting becomes larger than the fine structure splitting, i.e. $\Delta E_{\text{Zeeman}} > \delta_b$.

The general Zeeman Hamiltonian in an external field, $\boldsymbol{B}$, between an electron, $\boldsymbol{S}_e$, and a hole, $\boldsymbol{J}_h$, spin in an arbitrary direction is given by Equation 2.17 [111, 123].

$$\mathscr{H}_{\text{Zeeman}} = \mu_B \sum_{i=x,y,z} \left(g_{e,i} S_{e,i} - g_{h,i} J_{h,i}\right) B_i \tag{2.17}$$

In Equation 2.17, μ_B is the Bohr magneton and g_e and g_h are the electron and hole g-factors. There is a linear dependence with respect to the magnetic field for this interaction, as would be expected for a Zeeman splitting. There is also some *squeezing* of the wavefunction due the strong geometrical confinement of the exciton in the QD, which can be characterised by a diamagnetic coefficient, γ_2, defined in [124]. This spin-independent mechanism shifts exciton energies to higher levels in a quadratic manner, with increasing magnetic field. As the work in this thesis is in Faraday geometry, one can simplify Equation 2.17 by using $\boldsymbol{B} = (0, 0, B_z)$, to give Equation 2.18.

$$\mathscr{H}_{\text{Zeeman}} = \mu_B \left(g_{e,z} S_{e,z} - g_{h,z} J_{h,z}\right) B_z \tag{2.18}$$

One can find the total of the exchange and Zeeman interaction of the exciton (Equation 2.14 + Equation 2.18) and diagonalise this Hamiltonian. This allows for the the effect of the exchange and Zeeman interactions on the exciton energy levels to be seen, as shown in Table 2.1.

At high external magnetic fields, where $\beta_{b/d} \gg \delta_{b/d}$, the usually quadratic splitting of the excitonic states, becomes linear. At strong magnetic fields, there is also coupling between the circularly polarised light and bright excitons, which breaks the linear polarisation basis caused by the exchange interaction [112].

In the Voigt configuration there is in-plane mixing between the bright and dark states, allowing the dark states to be observed. This occurs due to the lack of rotational symmetry that

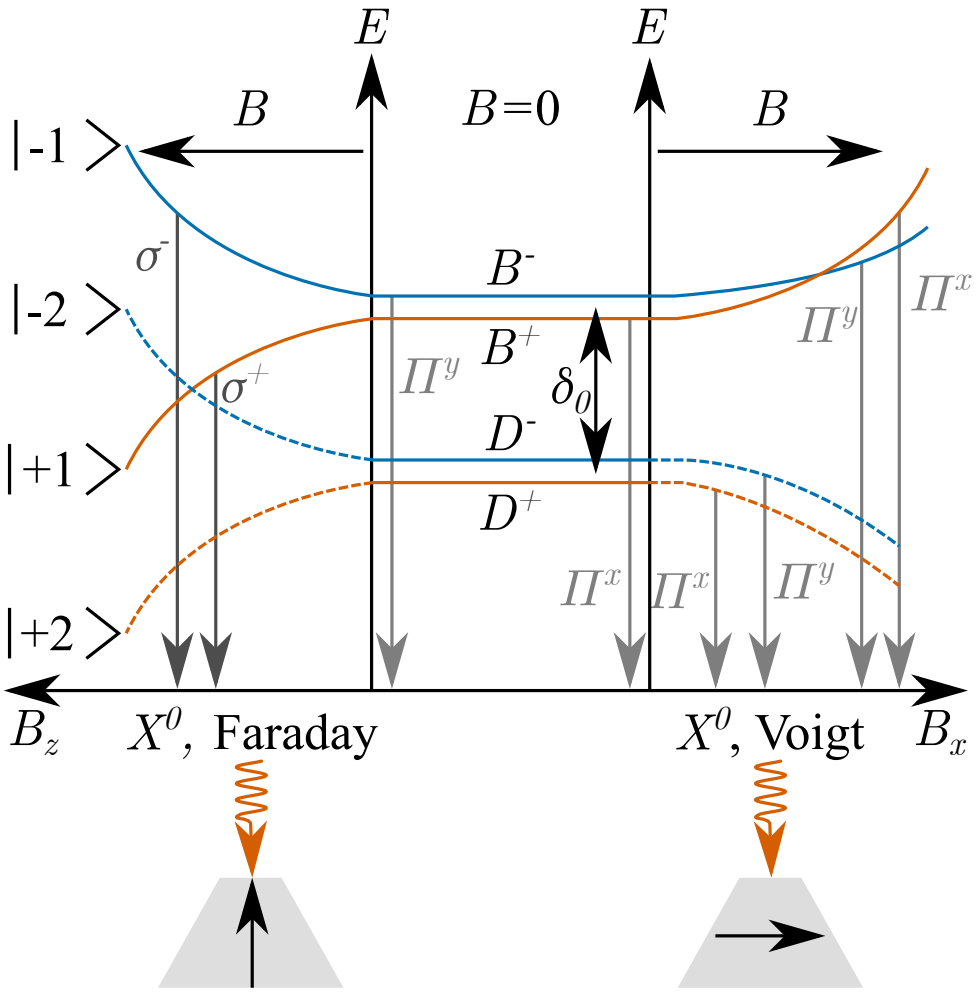

Figure 2.16: Schematic illustrating the effect of an external magnetic field, B, on the neutral exciton fine structure. With no external field the splitting of the $B^{\pm}$ to the $D^{\pm}$ states is δ_0 (isotropic exchange interaction). The eigenstates of the bright excitons are linearly polarised (Π^x, Π^y). In Faraday geometry when a large external field is applied, the bright states transition into circularly polarised states (σ^+, σ^-). However for the Voigt configuration both the bright and dark states (which become optically active) remain linearly polarised. The orange arrows at the bottom of the figure show the incident photon on the sample with black arrow being the external B field for both configurations. Adapted from [110].

occurs, as mentioned in Section 2.3.3. This leads to four linearly polarised carrier states; The bright and dark states lose their distinguishability, making it inappropriate to categorise them as such.

2.4 Quantum Dot Spin System

2.4.1 Interactions with Nuclear Spins in Quantum Dots

The wavefunction of a trapped electron within a QD can penetrate into the surrounding barrier material. There are approximately 10^5 nuclei in a single QD, all of which will have

State	Eigenstate	Energy Shift	Total Energy
$B^{\pm}$	$\|\pm 1\rangle$	$+\frac{1}{2}\left(\delta_0 \pm \sqrt{\delta_b^2+\beta_b^2}\right)$	$E_B = E_0 + \frac{1}{2}\left(\delta_0 \pm \sqrt{\delta_b^2+\beta_b^2}\right) + \gamma_2 B_z^2$
$D^{\pm}$	$\|\pm 2\rangle$	$-\frac{1}{2}\left(\delta_0 \pm \sqrt{\delta_d^2+\beta_d^2}\right)$	$E_D = E_0 - \frac{1}{2}\left(\delta_0 \pm \sqrt{\delta_d^2+\beta_d^2}\right) + \gamma_2 B_z^2$

Table 2.1: Energy shift and total energy for excitons (in an anisotropic QD) in an external magnetic field $B_z > 0$ setup in a Faraday configuration. This combines the QD bandgap energy, E_0, at zero field, diamagnetic shift, exchange interaction and Zeeman interactions. $\beta_b = \mu_B\left(g_{e,z} + g_{h,z}\right)B_z$ and $\beta_d = \mu_B\left(g_{e,z} - g_{h,z}\right)B_z$ [112].

an associated quadrupolar nuclear spin, (explained in Section 2.4.1.3), a schematic of which is shown in Figure 2.17. This results in the central spin problem[8], where the electron spin is linked to the mesoscopic (and fluctuating) nuclear spin bath [125]. The collection of interactions for nuclear spins within a solid can be combined into a single Hamiltonian, $\mathscr{H}$, described in Equation 2.19 [126].

$$\mathscr{H} = \mathscr{H}_Z + \mathscr{H}_{hf} + \mathscr{H}_{orb} + \mathscr{H}_{dd} + \mathscr{H}_Q \tag{2.19}$$

In Equation 2.19, $\mathscr{H}_Z$ describes the Zeeman energy of the nuclei, when in a magnetic field B_z. For a sum of i nuclear spins, I_z, this Zeeman term is written explicitly in Equation 2.20.

$$\mathscr{H}_Z = -\sum_i \hbar\gamma_{N_i} B_z I_{z,i} \tag{2.20}$$

This Zeeman Hamiltonian will be dependent on the gyromagnetic ratios of the nuclear spin species in the system. The gyromagnetic ratio is also related to the nuclear g-factor, $\gamma_N = \frac{g_N \mu_N}{\hbar}$. Due to the nuclear magneton, μ_N, (which is defined by fundamental constants) being smaller than the equivalent Bohr magneton, μ_B, for the electron, the energy splitting of the nuclear states is significantly smaller than the Zeeman splitting of the electron [125]. The second term, $\mathscr{H}_{hf}$, in Equation 2.19 is the hyperfine interaction. $\mathscr{H}_{orb}$ describes the coupling between the nuclear spin and electron orbital angular momentum. $\mathscr{H}_{dd}$ and $\mathscr{H}_Q$ are the nuclear-nuclear and quadrupolar interactions respectively.

2.4.1.1 Hyperfine Interaction

The hyperfine interaction describes how the magnetic field produced, due to the electron's orbital and spin angular momentum, affects the energy of the nuclear spin magnetic moment, as well as the reverse interaction. It can be split into three constituent parts: isotropic Fermi-contact, anisotropic, and orbital, denoted as $\mathscr{H}_{hf}^{fc}$, $\mathscr{H}_{hf}^{an}$, and $\mathscr{H}_{hf}^{orb}$ respectively, so that $\mathscr{H}_{hf} = \mathscr{H}_{hf}^{fc} + \mathscr{H}_{hf}^{an} + \mathscr{H}_{hf}^{orb}$.

The Fermi-contact hyperfine interaction relates the electron spin $S_z^e = \frac{\sigma^e}{2}$, where σ^e is the

[8]The central spin problem is an approximation of the QD spin system.

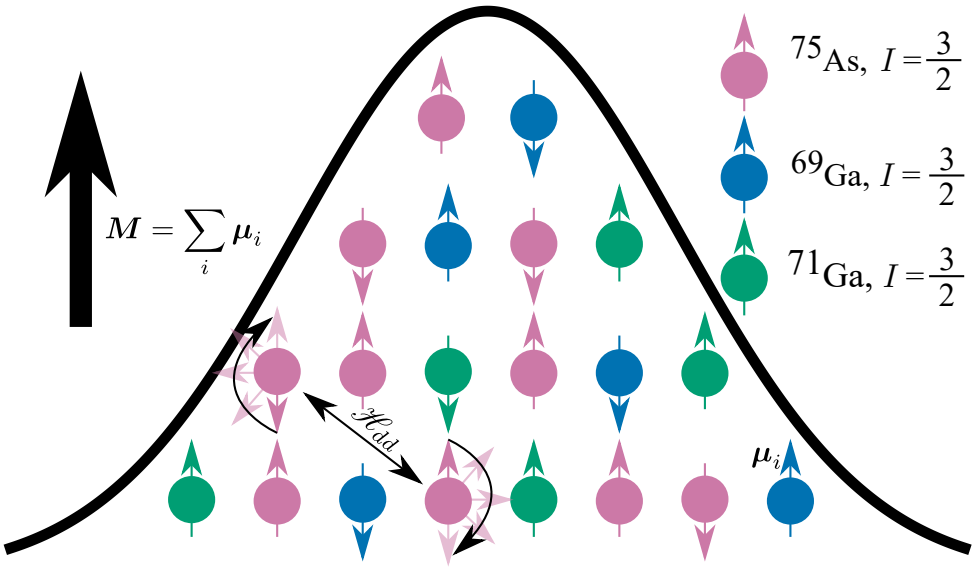

Figure 2.17: Nuclear spin bath for a GaAs QD. Each isotope in GaAs has a nuclear spin I=$\frac{3}{2}$, which have magnetic moments $\boldsymbol{\mu}_i$ associated with them. These magnetic moments are summed to form an overall magnetisation $\boldsymbol{M}$ of the QD. There are nuclear dipole-dipole interactions which induce spin flips across the QD, as shown through $\mathscr{H}_{dd}$. While the envelope wavefunction is depicted here, it is important to remember the periodic Bloch wavefunction, which has the shell-like properties, e.g. s, p, et cetera.

Pauli matrix operator, to the nuclei in a QD, and is written in Equation 2.21 [127–129].

$$\mathscr{H}_{hf}^{fc} = \frac{\nu_0}{2} \sum_j A_j |\psi(\boldsymbol{r}_j)|^2 \left(2I_z^j S_z^e + \left[I_+^j S_-^e + I_-^j S_+^e\right]\right) \tag{2.21}$$

In Equation 2.21, $\nu_0 = a_0^3$ is the volume of the unit cell with lattice constant a_0, A_j is the hyperfine coupling constant, I^j and $\boldsymbol{r}_j$ refer to the nuclear spin and position of the j^{th} nucleus respectively and finally ψ is the normalised electron envelope wavefunction. The first term in Equation 2.21 is the Overhauser shift (OHS), which acts as an effective field shifting the energy of the electron spin. The Knight field is this process in reverse, where the average electron spin acts as an effective field upon each nucleus. The second term acts leads to so-called *flip-flops*, where polarisation is transferred between an electron and a nucleus. This transfer can lead to Dynamic Nuclear Polarisation (DNP) as well as Nuclear Spin Diffusion (NSD) [130], see Chapter 5 for details on this. A_j is defined as [131]:

$$A_j = \frac{2\mu_0}{3} \hbar \gamma_{N,j} g_e \mu_B |\psi(0)|^2, \tag{2.22}$$

where μ_0 is the vacuum permeability and g_e is the free electron g-factor, which will be approximately equal to two. The electron density at the nucleus, $\boldsymbol{r}_j = 0$ (hence the zero in $|\psi(0)|^2$), varies between materials, which is a reason why A_j varies for different elements. Table 2.2 shows the values for this parameter for arsenic and the gallium isotopes along with other parameters required for the NMR work in this thesis.

Isotope	Nuclear Spin, I	Nuclear Magnetic Moment, $\boldsymbol{\mu}_i$	Hyperfine Constant, A_j (μeV)	Quadrupolar Moment (Q fm^{-2})	Gyromagnetic Ratio, $\gamma/2\pi$ (MHz T^{-1})	Natural Abundance (%)
^{27}Al	5/2	3.64	- [9]	14.7	11.103	100
^{75}As	3/2	1.44	46	31.4	7.315	100
^{69}Ga	3/2	2.01	43	17.1	10.248	60.1
^{71}Ga	3/2	2.56	54	10.7	13.021	39.9

Table 2.2: Properties of nuclear spin for ^{27}Al, ^{75}As, ^{69}Ga, and ^{71}Ga isotopes within a QD which are fundamental to NMR. Nuclear magnetic moments were taken from [132], hyperfine constants were taken from [125, 131] and quadrupolar moments/gyromagnetic ratios were taken from [133].

The spin of both the hole and the electron in QDs is more robust than in bulk or quantum well structures, due to the discrete energy states and strong confinement. The anisotropic term in the hyperfine interaction acts similarly to a dipole-dipole interaction, but between nuclear spins and p-type hole spins, S^h. For this interaction to occur some mixing between the LH and HH states is required, as otherwise it would be energetically forbidden (as a consequence of the HH-LH splitting) [125, 135–137]. This mixing can be denoted by β, where $|\beta|$ is much smaller than unity and typically below 0.3 [105, 125, 138]. The mixed state spin is considered in Equation 2.23 [125].

$$\widetilde{\left|\pm\frac{3}{2}\right\rangle} = \frac{1}{\sqrt{1+|\beta|^2}}\left(\left|\pm\frac{3}{2}\right\rangle + \beta\left|\mp\frac{1}{2}\right\rangle\right) \tag{2.23}$$

For bands that are mainly composed of p-orbitals, as opposed to the s-orbitals in contact interaction, the wavefunction 'vanishes' at the nuclear sites, which is where the anisotropic interaction has its largest influence [139]. This anisotropic term of the Hamiltonian can then be written as:

$$\mathscr{H}_{hf}^{an} = \nu_0 \sum_j \frac{A_j^h}{1+\beta^2}|\psi(\boldsymbol{r_j})|^2\left(I_z^j S_z^h + \frac{|\beta|}{\sqrt{3}}\left[I_+^j S_-^h + I_-^j S_+^h\right]\right), \tag{2.24}$$

where A_j^h is the hole dipole-dipole hyperfine constant, which has a similar form as A_j in the contact hyperfine interaction [140]. Hidden (for simplicity) within the form that Equation 2.24 is written in is the anisotropy factor, which is $\alpha = 2|\beta|/\sqrt{3}$.

A Hamiltonian can be written using the Pauli exclusion principle for an electron with a momentum $\boldsymbol{p}$ in a vector potential $\boldsymbol{A}$. This is under the assumption that $\boldsymbol{A}$ is being generated by the magnetic moments of the nuclear spins $\boldsymbol{I}_k$ which are located throughout the crystal [126].

[9] There is no literature value of the hyperfine constant for ^{27}Al, however it can be estimated by scaling the hyperfine constant for ^{69}Ga, as done in [134].

$$\mathscr{H}_{orb} = -\frac{\mu_0}{4\pi}\sum_k \gamma_S\gamma_{jk}\frac{\boldsymbol{L}_k\cdot\boldsymbol{I}_k}{|\boldsymbol{r}-\boldsymbol{r}_k|^3} \tag{2.25}$$

In Equation 2.25, $\boldsymbol{L}_k$ is the operator for the total electron orbital angular momentum about the nuclear site $\boldsymbol{r}_k$, and $\boldsymbol{r}$ is simply the electron position operator. γ_S and γ_j refer to the gyromagnetic ratios for the free electron (which is always negative) and the nucleon (which can be positive or negative) respectively. The combination of Equations 2.24 and 2.25 is useful in the description of electrons in the p-type valence band of III-V semiconductors (i.e., for holes) [139], for example in experiments such as in [140, 141].

2.4.1.2 Nuclear Dipolar Interaction

The dipolar interaction relates to the coupling between magnetic moments. Mutual cross-relaxation (spin flips) occur due to dipolar interactions, resulting in proton-proton OHSs [142]. The OHS is "a direct measure of the magnetization transferred from one nucleus to another," [143], i.e. the diffusion of spin polarisation from 'spin-active' nuclei to another [144]. The process of NSD in the central spin system of a GaAs QD is described within Chapter 5.

The Hamiltonian for the nuclear dipolar interaction for nuclei i and j, separated by a displacement vector $\boldsymbol{r}_{ij,}$ is given by [127]:

$$\mathscr{H}_{dd} = \frac{\mu_N^2}{2}\sum_{i\neq j}\frac{g_i g_j}{r_{ij}^3}\left(\boldsymbol{I}^i\cdot\boldsymbol{I}^j - 3\frac{\left(\boldsymbol{I}^i\cdot\boldsymbol{r}_{ij}\right)\left(\boldsymbol{I}^j\cdot\boldsymbol{r}_{ij}\right)}{r_{ij}^2}\right) \tag{2.26}$$

Within Equation 2.26 is the dipolar coupling constant expressed as its equivalent value of rather than using its symbol R, which is a measure of the strength of the interaction. The dipolar coupling strength, which is proportional to $\frac{1}{r^3}$, is significantly influenced by the spatial separation between nuclei. As a result, the interaction is weak for nuclei that are spatially distant. In Equation 2.26, for moderate magnetic fields (larger than 10^{-4} T) only the secular (spin-conserving) part of the interaction contributes to nuclear spin dynamics [126]. This is as it commutes with the Zeeman term, $\mathscr{H}_Z$. This results in the static part $\propto I^iI^j$ and the nuclear flip-flop term $\propto \left[I_+^iI_-^j + I_-^iI_+^j\right]$ acting on nuclei of the same isotope.

2.4.1.3 Nuclear Quadrupolar Interaction

The intrinsic electric dipole moment of a nucleus is usually assumed to be zero [127], and if non-zero it must be very small (a nice collective table of electric dipole moments from different sources is shown in [145]). This means that nuclei are insensitive to a homogeneous electric field, however a nucleus with $I > \frac{1}{2}$ (a prolate charge distribution) can interact through an Electric-Field Gradient (EFG) due to its electric quadrupole moment. Figure 2.18 shows what such a distribution would look like.

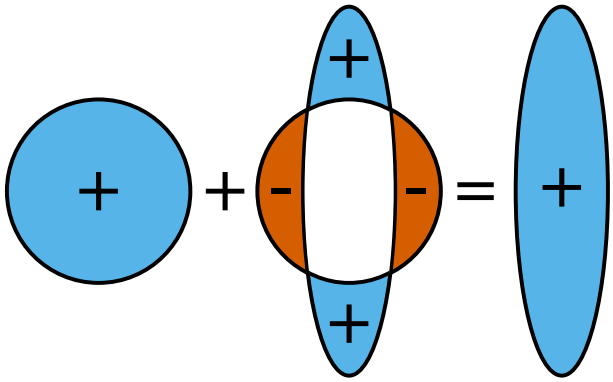

Figure 2.18: A non-spherical (prolate) charge distribution is equivalent to a spherical charge distribution plus a charge distribution with positive polar charge and negative equatorial charge, adapted from [146].

In the process of making a GaAs QD, there will be inherent strain due to the lattice mismatch, which breaks the cubic symmetry found in bulk GaAs [125]. The local Elastic-Strain Tensor (EST), ϵ_{ij}, is then linked to the traceless EFG, V_{ij}, by the Gradient-Elastic Tensor (GET), S_{ijkl}, as shown in Equation 2.27 [147], where V is the electrostatic crystal field potential.

$$V_{ij} = \frac{\partial^2 V}{\partial x_i \partial x_j} = \sum_{k,l=1}^{3} S_{ijkl}\epsilon_{kl} \tag{2.27}$$

In Equation 2.27, the x, y, and z components are chosen to be over the crystallographic axes, which in the case of GaAs is cubic, with the z axis being aligned with the direction of QD growth, $[001]$. The zincblende lattice (cubic crystal) of GaAs results in only two independent components for the GET. These are S_{11} and S_{44}, as $S_{12} = -\frac{S_{11}}{2}$, due to the traceless property of V_{ij}. These relate the diagonal and off-diagonal components of the strain and EFG respectively, e.g. $V_{zz} = S_{11}\epsilon_B$, $V_{xy} = 2S_{44}\epsilon_{xy}$, et cetera, where the biaxial strain, ϵ_B, is defined as, $\epsilon_B = \epsilon_{zz} - \frac{\epsilon_{xx}+\epsilon_{yy}}{2}$ [148].

If one assumes cylindrical (axial) symmetry for the EFG in a QD then one can use Equation 2.28, which describes the secular (spin-conserving) term of $\mathscr{H}_Q$ [126].

$$\mathscr{H}_Q^{sec} = \frac{1}{4}\sum_k \nu_Q^k f(\theta)\left((I_k^z)^2 - \frac{1}{3}I^{j_k}\left(I^{j_k}+1\right)\right) \tag{2.28}$$

In Equation 2.28: ν_Q^k is the quadrupolar coupling strength (dependent on the EFG), $f(\theta) = (3\cos^2\theta - 1)$, and θ is the angle between the unit vector $\hat{n}$ and the applied magnetic field in the z direction. Solving $f(\theta) = 0$ results in $\theta \approx 54.7°$, which is commonly known as the *Magic Angle* in NMR. At this angle the angular dependence of $\mathscr{H}_Q^{sec}$ goes to zero, resulting in an NMR spectrum where only the Central Transition (CT) is present. This magic angle is used in Magic Angle Spectroscopy (MAS).

The total Hamiltonian for the quadrupolar interaction is shown in Equation 2.29 [127, 149].

$$\begin{gathered}\mathscr{H}_Q = \frac{eQ}{4I(2I-1)}\left(3I_{z'}^2 - I^2 + \eta(I_{x'}^2 - I_{y'}^2)\right), \\ \eta = \frac{V_{x'x'} - V_{y'y'}}{V_{z'z'}}.\end{gathered} \tag{2.29}$$

In Equation 2.29: η is the asymmetry parameter, Q is the quadrupolar moment for a particular nucleus , and $\{\hat{e}_{x'}, \hat{e}_{y'}, \hat{e}_{z'}\}$ are the principal axes of the symmetric tensor V_{ij} (note these axes should not be confused with the crystallographic axis used in Equation 2.27). η has the constraints of $0 \leq \eta \leq 1$ and the EFG components satisfy $|V_{z'z'}| \geq |V_{x'x'}| \geq |V_{y'y'}|$.

When in a high magnetic field, the quadrupolar effect can be treated as a perturbation to the Zeeman part of the Hamiltonian. If one again assumes cylindrical symmetry of the EFG, as to cause η to vanish, one can also introduce the Larmor frequency, ω_L[10], as:

$$\omega_L = -\gamma B_z, \tag{2.30}$$

where B_z is parallel to the O_z axis. Then using perturbation theory [127] the energy levels of a state m from Equation 2.29 can be written, as in Equation 2.31.

$$E_m = E_m^{(0)} + E_m^{(1)} + E_m^{(2)} + ... \tag{2.31}$$

We can then define the terms $E_m^{(n)}$ in Equation 2.31 upto the second order, $n = 2$, [127].

$$E_m^{(0)} = \hbar\omega_L m \tag{2.32}$$

$$E_m^{(1)} = -\frac{h\omega_Q}{12}\left(I\left(I+1\right) - 3m^2\right)\left(3\cos^2\left(\theta\right) - 1\right) \tag{2.33}$$

$$E_m^{(2)} = -\frac{hm\pi\omega_Q^2}{16\omega_L}\sin^2(\theta)\begin{pmatrix}1 - 2I(I+1) + 2m^2 + \\ \left(18I(I+1) - 34m^2 - 5\right)\cos^2(\theta)\end{pmatrix} \tag{2.34}$$

Here we have introduced the quadrupolar coupling strength, $\omega_Q = \frac{3e^2qQ}{2hI(2I-1)}$ [127], which is sometimes shown within Equation 2.29. Within this coupling strength is the field gradient parameter q, where $q = \frac{V_{z'z'}}{e}$. From these one can now determine the energy difference between adjacent energy levels for given spin states, e.g. when $m = I_z$ and $I_z + 1$.

$$\Delta E^{(0)} = E_{I_z+1}^{(0)} - E_{I_z}^{(0)} = \hbar\omega_L \tag{2.35}$$

$$\Delta E^{(1)} = E_{I_z+1}^{(1)} - E_{I_z}^{(1)} = \frac{h\omega_Q}{4}(2I_z + 1)\left(3\cos^2(\theta) - 1\right) \tag{2.36}$$

[10]Note that for Equations 2.32 to 2.37 we have changed the notation from what Abraham used in [127], where they defined $\omega_L = \frac{\gamma B_z}{2\pi}$. This is to keep the notation used in this thesis consistent, but will result in a factor of -2π difference (which can be absorbed into the reduced Planck constant $\hbar$).

$$\Delta E^{(2)} = E^{(2)}_{I_z+1} - E^{(2)}_{I_z} = \frac{h\pi\omega_Q^2}{16\omega_L}\sin^2(\theta)\begin{pmatrix}2I(I+1) - 6I_z(I_z+1) - 3 + \\ 3\cos^2(\theta)\left(34I_z(I_z+1) - 6I(I+1) + 13\right)\end{pmatrix} \quad (2.37)$$

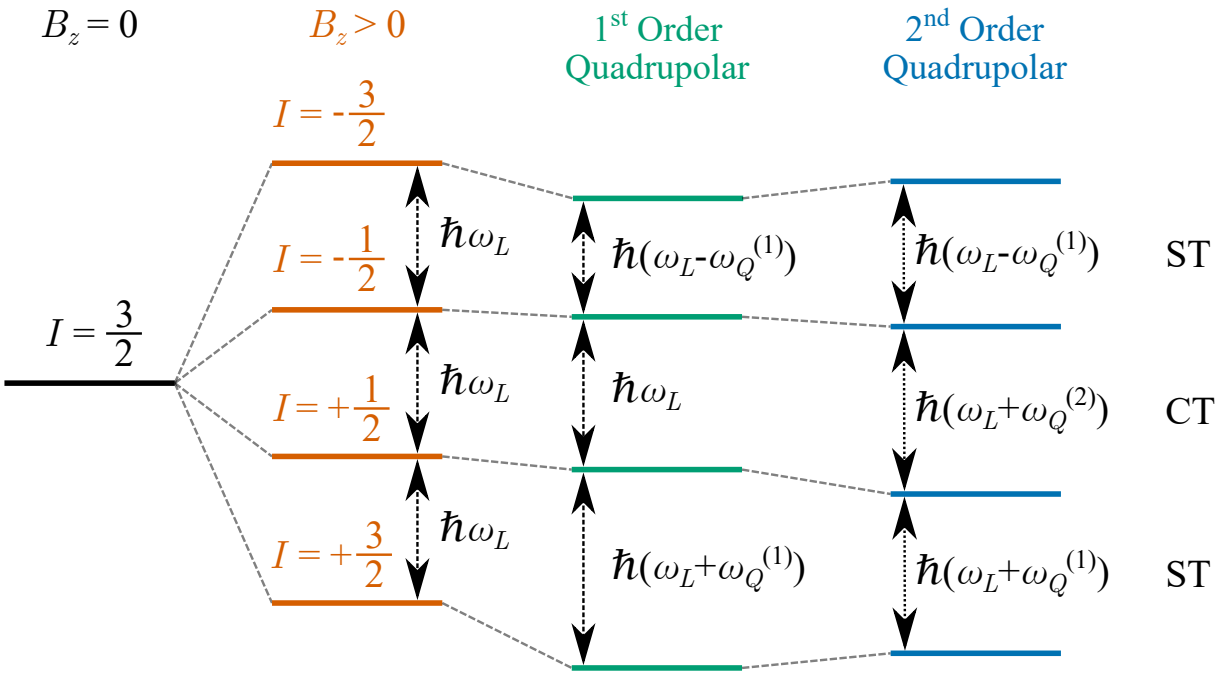

Figure 2.19: Energy diagram of a single nucleus with spin $I = 3/2$. Under a magnetic field of B_Z, to the zeroth order of quadrupolar interactions, the degeneracy of $I = 3/2$ is lifted, resulting in four equally spaced states, separated by the Larmor frequency (ω_L). Under first order perturbation the CT is unaffected, whereas the Satellite Transitions (STs) are strongly perturbed by $\omega_Q^{(1)}$. Including second order effects, the CT is affected weakly by $\omega_Q^{(2)}$. The effect of $\omega_Q^{(2)}$ has not been included for the STs as $\omega_Q^{(1)} \gg \omega_Q^{(2)}$. Note that this diagram is true for the Ga isotopes; for ^{75}As the $\pm\frac{3}{2} \leftrightarrow \pm\frac{1}{2}$ transition would have the sign of $\omega_Q^{(1)}$ switched, for our QD samples.

As before, if one uses $\theta \approx 54.7°$ the first order perturbation vanishes. It can also be noted that in the first order when $I_z = -1/2$, as would be the case for the CT, $\Delta E^{(1)} = 0$; the CT is insensitive to first order quadrupolar interactions. If the EFG major axis is parallel to the magnetic field, $\theta = 0°$, then similarly the second order perturbation vanishes. Generally this second order effect can be neglected for the STs due to $\omega_Q^{(1)} \gg \omega_Q^{(2)}$ $\left(\text{where } \omega_Q^{(1)} = \Delta E^{(1)}/\hbar \text{ and } \omega_Q^{(2)} = \Delta E^{(2)}/\hbar\right)$.

All isotopes in GaAs contain nuclei with $I = 3/2$, so one may, naively, assume that for the initial state with $I_z = -3/2$ ($I_z = 1/2$) the value of $\omega_Q^{(1)}$ is negative (positive). This is would also result in the ST transition $-\frac{3}{2} \leftrightarrow -\frac{1}{2}$ $\left(\frac{1}{2} \leftrightarrow +\frac{3}{2}\right)$, appearing on the lower (higher) frequency side of the CT. However, this is not always correct. While the statement is true for Ga isotopes under compressive strain, the opposite holds true for As isotopes or under dilation conditions. The spectral positions of the STs are determined by the sign of the values in the GET, S_{ijkl}, and by the type of strain the QD is under.

2.5 Manipulation of the Nuclear Spin Ensemble

2.5.1 Initialising Nuclear Spin

For QD nuclear spin to be useful for a qubit, it must be possible to initialise a desired polarisation state, which can be achieved by using circularly polarised light. Figure 2.20 shows the process one would use to to initialise and manipulate nuclear spins. The different colours show the different elements/isotopes (only 2 shown for simplicity). Initially, the nuclear spins are randomly fluctuating with no net polarisation. One can then shine a high-power circularly polarised laser onto the QD. Depending on the wavelength of the laser, there are two pathways that both lead to the same outcome. The generation of spin-polarised electron-hole pairs occurs either within the QD, as explained through resonant excitation in Figure 2.11, thanks to the optical selection rules in III-V semiconductors. Alternatively, the pairs can also form in the wetting layer of the QD, from where they are subsequently captured into the dot. This process is further explained in Section 3.2.2. As the electron (the hole too but it affect is much weaker) relaxes it interacts with the nuclear spin ensemble through the flip-flop term in the hyperfine interaction. This occurs for all nuclei that are within the wavefunction of the electron in the QD. The electron-nuclear spin interaction occurs as a result of the non-zero hyperfine constants (see Table 2.2) for all the elements within the QD. This transfer of spin aligns the nuclei spin, i.e. increases nuclear spin polarisation, which is shown in Figure 2.20 as all the arrows being in the same direction. It should be noted that not 100% of the nuclei would be polarised using this technique alone, a more realistic polarisation degree that is commonly attainable would be around 60% [150]. The polarisation of the pump laser (σ^+/σ^-) will change the sign of the polarisation degree of the nuclei. The pump laser wavelength can be varied as shown in Figure 3.6, and different degrees of DNP are reached. This is mentioned in greater depth within Section 3.2.5 and Chapter 6.

Once optical pumping has occurred, a Radiofrequency (RF) pulse with a set spectral shape can be used. Within this thesis a range of RF spectral and temporal shapes have been used, which are discussed within Section 3.3.1. The RF pulse will selectively depolarise nuclei based on the frequencies it is composed off. In Figure 2.20 this is shown by the pink nuclei no longer being aligned in the same direction.

2.5.2 Measuring Nuclear Spin

Once the nuclear spin state of the ensemble has been initialised it can be readout using optical spectroscopy. For the nuclear system this is done using the OHS. When the ensemble is polarised there will be an additional shift (in addition to the Zeeman effect) to the spectral splitting of an exciton doublet. This shift is directly related to the polarisation degree of the nuclear spin bath [152]. For a GaAs QD, the maximum additional splitting that one can expect to see, i.e. 100% nuclear polarisation, is $\gtrsim$ 110 μeV, but this is dependent on the chemical composition, e.g.

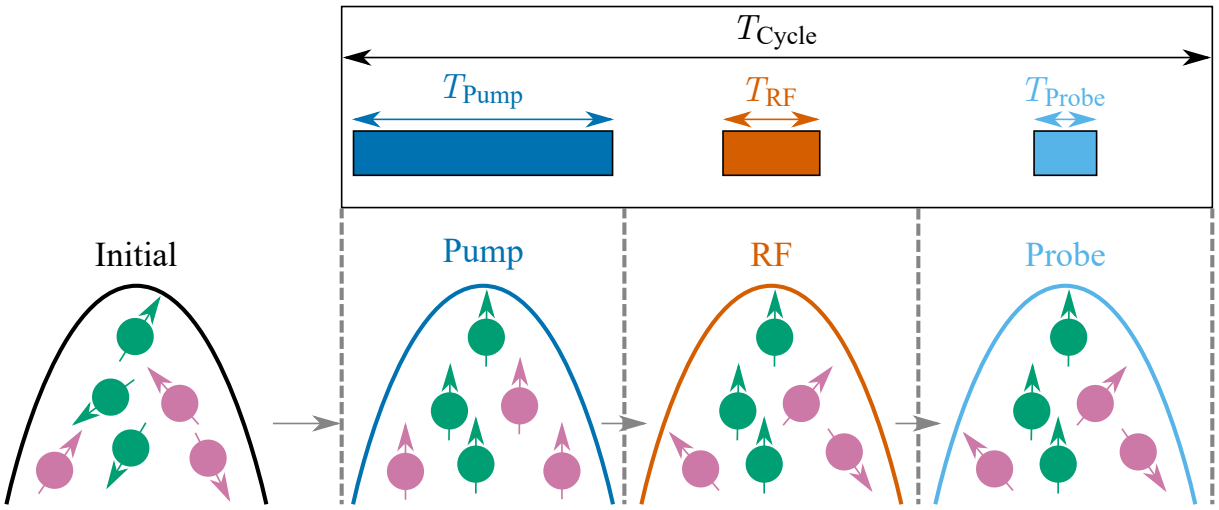

Figure 2.20: A template timing diagram for the pump-RF-probe cycle, for initialising then measuring nuclear spin. In the initial state distribution of nuclear spins is uniform/randomly orientated. A polarised pump laser is then used to align all the nuclear spins. A RF burst can then be used to selectively depolarise nuclei of a set isotope, here the pink nuclei are depolarised. The final net spin polarisation can then be measured using a low power probe laser. Figure is based from [125, 151].

Ga/Al ratio, of the QD [126, 153, 154]. An increase of DNP is useful in multiple ways, for example it will aid in: techniques such as NMR, increasing electron spin qubit coherence times [155, 156], and quantum memory operations [156, 157]; but, there are limits to reaching such a high polarisation due to several loss rate, e.g. NSD and Nuclear Spin Relaxation (NSR) [126]. These factors are discussed in the context of measurements within Chapters 5 and 6.

2.5.3 Nuclear Spin Relaxation

A qubit would have to be isolated from its environment, otherwise information may be lost [11, 12]. Therefore in order to use QDs as spin qubit devices, one must understand the relaxation mechanisms that result in shorter spin lifetime/coherence times. There are three main parameters which are used to describe the effect of spin relaxation, which can be seen Figure 2.22.

The *Bloch equations of motion*, named after Felix Bloch's work in the 1940s [159], describe the general exponential relaxation behaviour of the magnetisation vector $\boldsymbol{M}$. Let us consider a spin system in which the spin has been initialised in a spin up state, $|\uparrow\rangle$, parallel to the external magnetic field, $\boldsymbol{B}_0$, in Faraday geometry (see Section 2.3.5 for an explanation on this). As shown in Figure 2.17, $\boldsymbol{M}$ is the summation of all the nuclear spins in the ensemble[11]. From this initialised situation, $\boldsymbol{M}_y$ and $\boldsymbol{M}_x$ would decay to zero and $\boldsymbol{M}_z$ would decay to the equilibrium value M_0. The equations governing this are Equations 2.38 and 2.39 [161].

[11] In reality $\boldsymbol{M}$ would be weighted by the electron wavefunction density [160]. This treatment of the magnetisation vector is based on the simplest approximation, called the box model.

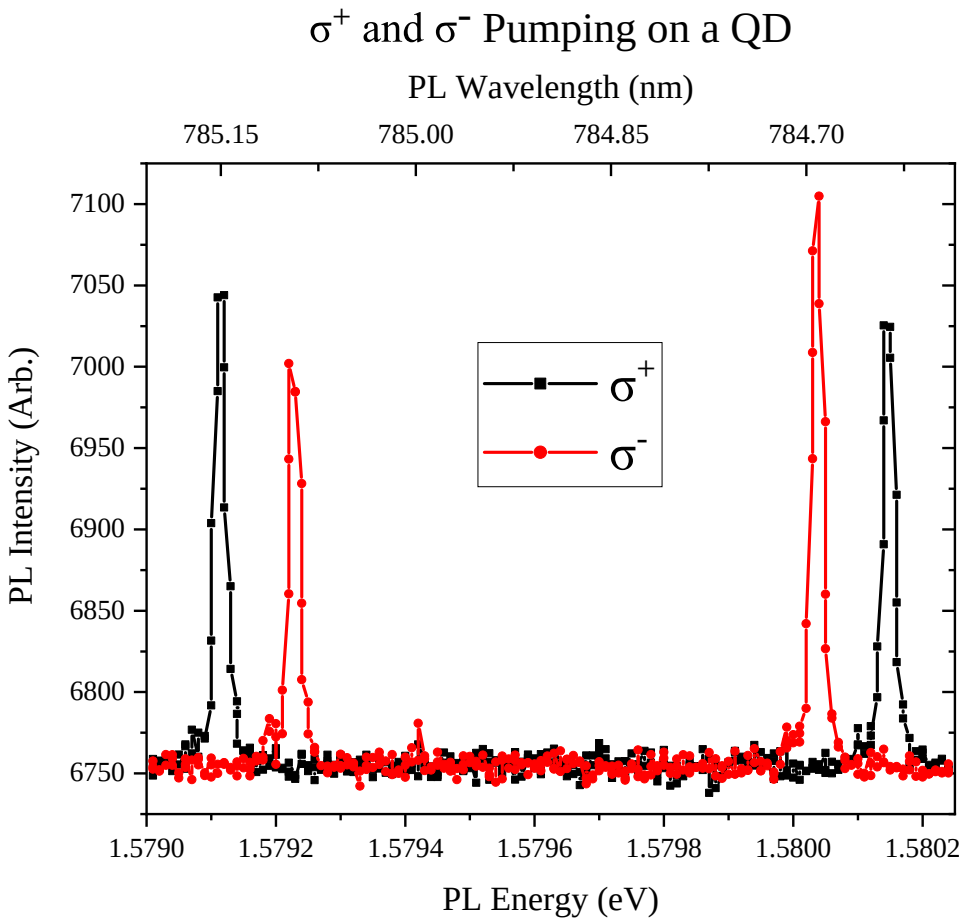

Figure 2.21: PL spectra using both σ^+ and σ^- pumping of an X^- exciton in a GaAs QD at 10 T. The spectral splitting of the σ^+/σ^- components is 1033.2/809.7 μeV leading to a total difference ($\sigma^+ - \sigma^-$) in splitting of 223.5 μeV. The zero-DNP level is at 920.5 μeV and, through NMR spin thermometry, it has been shown that the spin polarisation of the QD is over 90% (see Chapter 6 for details).

$$\dot{\boldsymbol{M}}_{x,y} = \gamma |\boldsymbol{M} \times \boldsymbol{B}|_{x,y} - \frac{M_{x,y}}{T_2} \tag{2.38}$$

$$\dot{\boldsymbol{M}}_{z} = \gamma |\boldsymbol{M} \times \boldsymbol{B}|_{z} + \frac{M_0 - M_z}{T_1} \tag{2.39}$$

In Equations 2.38 and 2.39, $\dot{\boldsymbol{M}}$ is the derivative of $\boldsymbol{M}$ with respect to time. Solving these two equations, one arrives at Equations 2.40 and 2.41.

$$M_{x,y}(t) = M_{x,y}(0) e^{-\frac{t}{T_2}} \tag{2.40}$$

$$M_z(t) = M_0 - (M_0 - M_z(0))\, e^{-\frac{t}{T_1}} \tag{2.41}$$

The longitudinal, sometimes called *spin-lattice*, relaxation time is denoted by T_1 and characterises the likelihood of a spin flip along the $\hat{\boldsymbol{e}}_z$ axis. The initial polarised state along $\hat{\boldsymbol{e}}_z$ decays back to its equilibrium value in a characteristic time T_1; after a time T_1 the magnitude

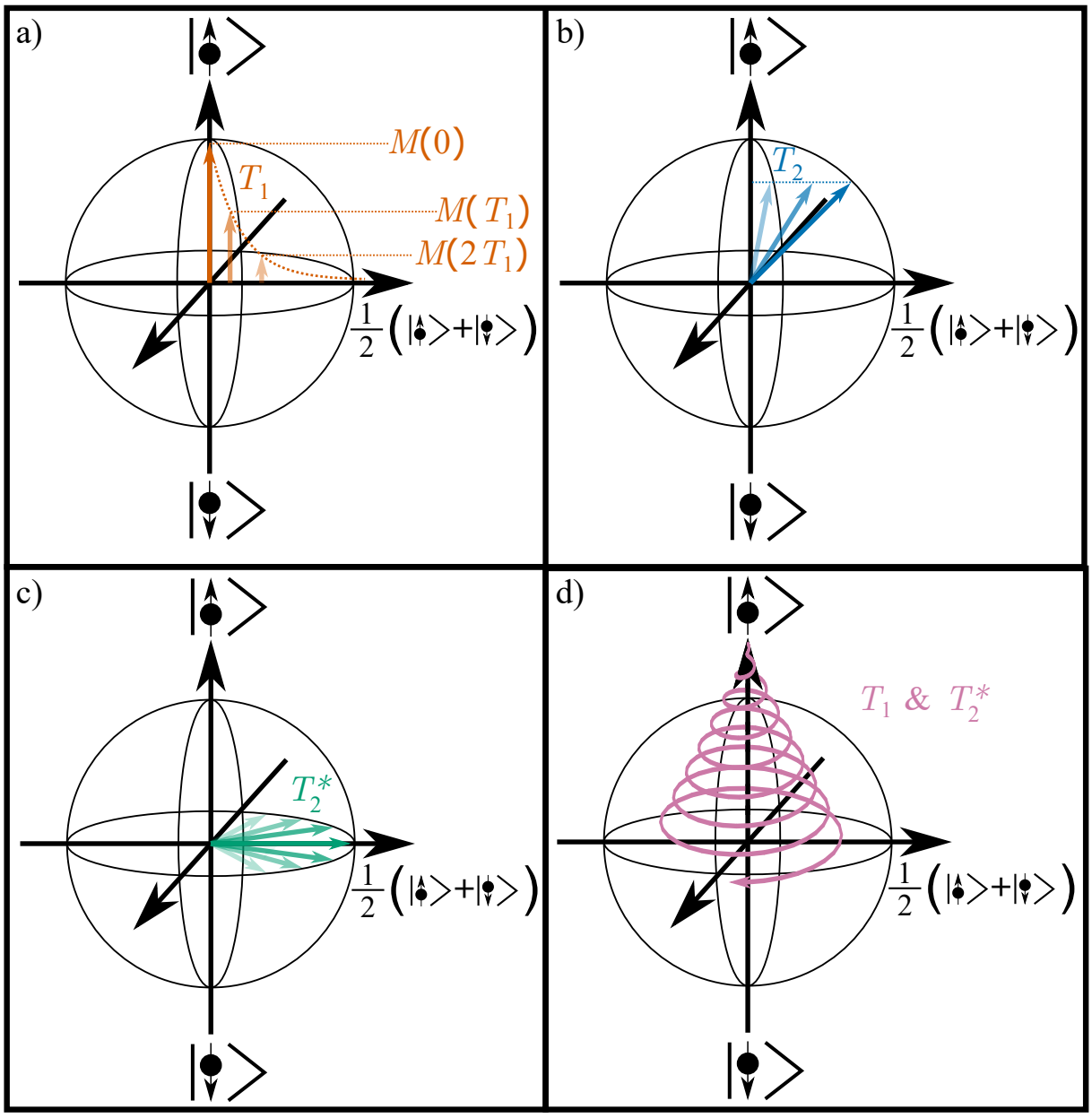

Figure 2.22: Spin relaxation and dephasing times T_1, T_2 and T_2^* represented on a Bloch sphere. a) T_1 is the longitudinal relaxation time describing the decay of spin polarisation. Note the horizontal axis is not indicative of time; rather, it is presented in this manner to aid comprehension and visualisation. b) T_2 is the transversal decay time, measuring the loss of the magnetisation vector due to spin-spin interactions. It occurs due to *intrinsic* magnetic field inhomogeneities. It does *not* change the polarisation along the longitudinal direction. c) T_2^* is the *pure* dephasing of phase information due to local variations in the magnetic field, which includes random T_2 effects as well as non-random effects, e.g. field inhomogeneities [158]. This accelerates the decay of the magnetisation vector in the $x-y$ plane. d) The effect when both T_1 and T_2^* are combined. There is both a loss of magnitude of the magnetisation vector and dephasing. The radius at a given point of the spiral signifies the increase in dephasing, rather than the phase itself.

of the magnetisation vector will be 63% of its initial value. T_2 is the transverse component related to NSR, sometimes called coherence time. Unlike T_1 it is not related to the transfer of

energy, but rather a loss of phase information, in the $x - y$ plane due to random spin-spin interactions. T_2 describes the loss of phase coherence of the nuclear spins precessing around $\hat{\boldsymbol{e}}_z$. When using an ensemble of nuclear spins, as in a QD, there is another timescale related to the dephasing of spin along the $x - y$ plane. This is the T_2^* time, sometimes called purely the dephasing time. In some protocols for using electron spin qubits, e.g. [31], RF pulses are used to address/initialise nuclear spin states. However, after the RF has been applied nuclei in the spin ensemble will precess at varying speeds, due to local fluctuations in the magnetic field. These varying precession speeds will cause dephasing. This dephasing need not be permanently lost, and can be recovered using spin echo techniques [162] or with specific pulses of RF [163]. The relation between all three timescales is shown in Equation 2.42.

$$\frac{1}{T_2} = \frac{1}{2T_1} + \frac{1}{T_2^*} \tag{2.42}$$

It can be deduced from this equation that $T_2 \leq 2T_1$, it should also be noted though that T_2^* is always less than T_2 as it includes both the random and non-random mechanisms for dephasing [158].

2.5.4 Radiofrequency Induced Depolarisation

One can use a RF pulse to systematically depolarise nuclei in the ensemble. When the nuclei are subjected to a magnetic field, with a frequency resonant with the nuclear Larmor frequency ($I_z \leftrightarrow I_z + 1$ transition), Rabi rotations of nuclear spins occur. This is where the field drives rotation of the spin state of the nuclei polarisation back and forth (parallel/antiparallel to the external magnetic field) [164]. The nuclear-nuclear dipolar interactions (see Section 2.4.1.2) mean that each nucleus will be subject to a local field. The randomness of the local fields causes ensemble dephasing as the Rabi precession frequencies are perturbed by the local fields. After a long pulse of resonant RF, the ensemble of nuclei will become depolarised (randomly orientated with respect to the external magnetic field) as the populations of each spin state are equalised. This has been done in many experiments, and is explained in more detail in [151], where they use the energy from the applied RF field to depolarise the nuclei into the surrounding lattice [158].

Chapter 3

Experimental Techniques

The majority of the experiments within this thesis involve a combination of optical excitation of QDs and RF depolarisation of nuclei. The overall aim of these experiments is to investigate the nuclear spin system in epitaxial semiconductor QDs. The experimental setup includes a bath cryostat to maintain the low-temperature environment, lasers for optical excitation of the QDs and for measuring the degree of nuclear spin polarisation, and a RF system designed to selectively depolarise the nuclear spins. A carefully timed sequence of laser pulses and tailored RF waveforms allows us to manipulate the spin states of nuclei within the QDs. These operations are performed to probe the underlying physics, particularly the mechanisms behind nuclear spin polarisation and its interaction with electron spins.

3.1 Bath Cryostat

The main housing for the majority of measurements in this thesis is an Oxford Instruments Teslatron liquid helium bath cryostat. However, for some initial sample characterisation a continuous flow cryostat system was used[1]. The flow cryostat requires constant pumping of liquid helium to cool the sample, which leads to instabilities due mechanical vibrations. For our setup, this results in frequent optical realignment being necessary, typically required every minute. Additionally, our flow cryostat lacks a magnet, whereas the bath cryostat can reach fields of up to 10 T. As the majority of experiments in this thesis require measurements to run over the course of days and high magnetic fields, a flow system is not often appropriate. As explained in Section 2.3, the separation of QD energy levels must be larger than the thermal energy, which is why the work in this thesis uses liquid helium as a coolant.

The bath cryostat is shown in Figure 3.1. The sample is housed within a cage-like structure comprised of four non-magnetic stainless steel rods held in place by aluminium blocks. This cage system, which is depicted as black lines in Figure 3.1, is inserted into an ‘insert’. On top

[1] The setup of our flow cryostat is very similar to our bath setup, hence I will not discuss its construction in depth here. However, it is described in detail within Chapter 3 in [58], where it was used to characterise self assembled QDs.

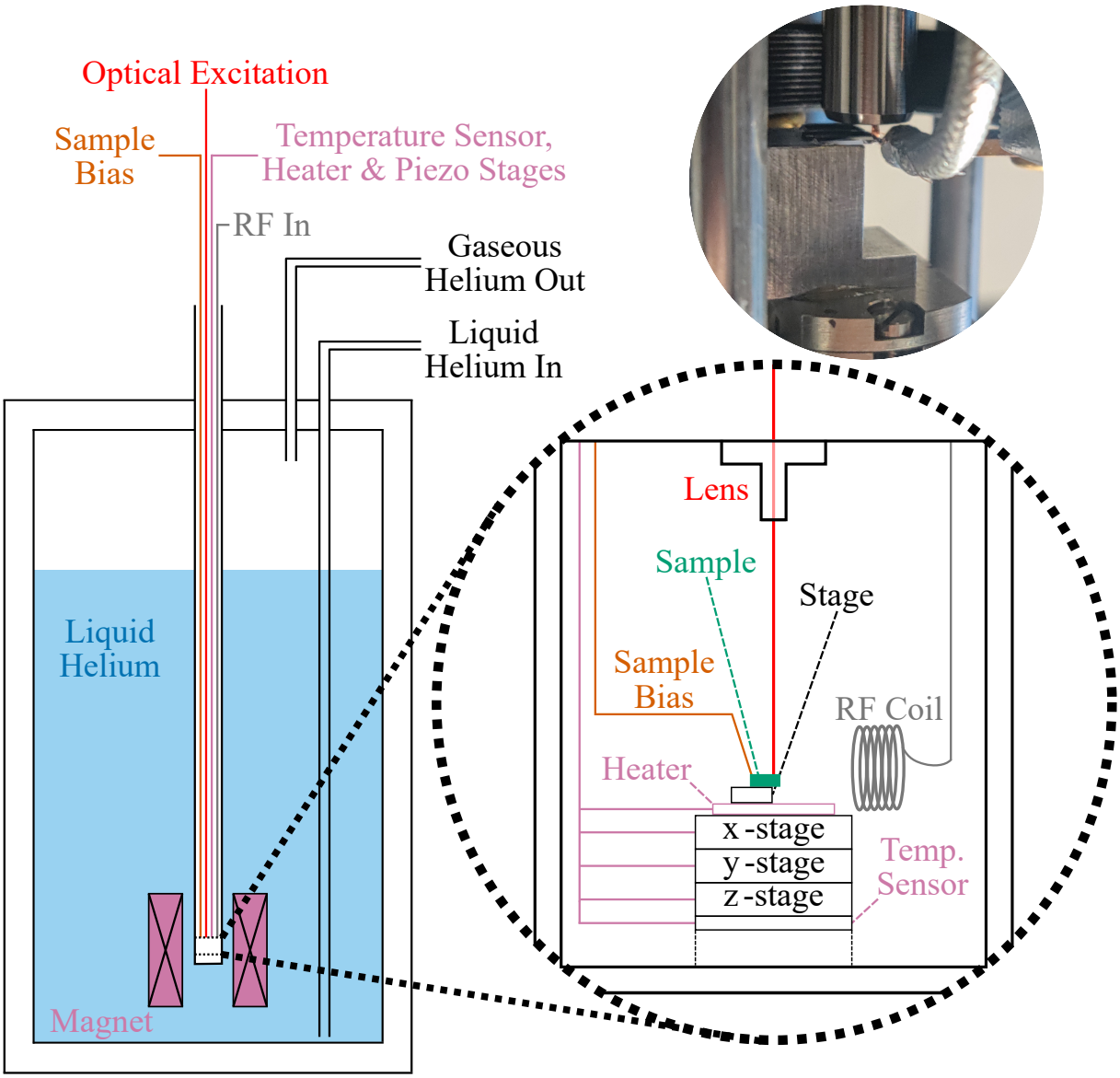

Figure 3.1: Schematic illustrating the bath cryostat. The cryostat is filled with liquid helium which keeps the sample at a temperature of approximately 4.2 K. The laser used for optical excitation travels, through a glass window at the top of the cryostat, into a sealed insert (which contains a small amount of helium exchange gas) before travelling through a lens to focus onto the sample. RF signals are carried through a coaxial cable to a copper coil located close to the sample. The sample is mounted on an aluminium pedestal which is attached to the piezo stages. The piezo stages and temperature sensor are linked through a 12-pin connection to a Bayonet Neill-Concelman (BNC) line. This setup allows for the piezo stages, and hence the sample, to be moved and the temperature of the sample to be recorded. If the sample is charge tunable it is connected to a sample bias line made from a coaxial cable, where this is again connected to a BNC line outside of the cryostat.

of this insert there is a glass window, allowing for optical spectroscopy to be performed on the sample. There is no direct contact of liquid helium with the sample. Instead, the 1.55 m long insert, with a diameter of $\approx$ 50 mm, is pumped to $<$ 1 mbar and then $\sim$ 6 cm^3 of helium exchange gas is added. The pressure within the insert, at room temperature, is then $\approx$ 3 mbar.

This enables the sample to cool down gently, via conduction. If too little He gas is added then the sample will not cool down to/maintain the required 4.2 K, if too much is added then the liquid helium reservoir will be consumed at a faster rate. The aforementioned ~ 6 cm^3 of He gas is a compromise of these two variables. The advantage of using an insert to house the sample rather than an immersion cryostat is that, the optical path (see Figure 3.2) required for spectroscopy travels through a low pressure gas rather than the boiling liquid He. This again aids in the stability of the setup. The insert, once inserted into the cryostat, passes through a bore of a superconducting magnet that is controlled by an Oxford Instruments IPS120-10 power supply, allowing for a maximal static field, B_z, of 10 T.

Along the length of the cage system there exists cabling to allow for the connection of devices near the sample to outside the cryostat. One of these cables is used to transmit the RF produced by the generators (see Section 3.3.1) to a small copper coil. This coil is made of 10 turns of a 0.1 mm diameter enamelled copper wire which has been wound on a ≈ 0.4 mm spool in 5 layers, with 2 turns in each layer. This coil is aligned ≈ 0.5 mm from the sample and is used to generate the required oscillating magnetic field perpendicular to B_z, which depolarises nuclei. The sample is located near the end of this cage system, at the end of the optical path, and positioned underneath the sample are piezo stages. These are controlled through an Attocube ANC350 Piezo Motion Controller allowing for submicron accuracy of the sample position. As there are mechanical vibrations that cannot be stopped in the building, these piezo stages allow for the adjustment of the position of the sample, i.e. to realign a QD with the optical path of incident light. For some experiments in this thesis (Chapter 5) the temperature of the sample was also adjusted. To achieve this, a heater plate was fabricated in-house. This was made from a titanium plate which had ≈ 8 m of 63 μm diameter enamelled copper solderable wire dual wrapped around it. Through adjustment of the voltage across the heater coil one can deliver power (dissipated as heat) to the sample. The temperature is monitored using a Cernox CX-1050-SD-HT-1.4L Resistor, where the resistive sensor is located underneath the sample, which is connected to a Keithley 2000 Bench Multimeter.

3.2 Optical Spectroscopy

To investigate the energy level transitions of the QD system we employ confocal optical spectroscopy. The ODNMR techniques described in Section 2.5 require a pump-probe process to initialise and measure the nuclear spin states of a QD. Therefore, an optical breadboard setup is essential, and in this section this experimental setup is described.

3.2.1 Optical Breadboard

A diagram of the optical setup is shown in Figure 3.2, which comprises two ‘arms’: the pump arm and the probe arm. The pump laser is a Matisse 2 tunable ring laser, which has a

15 W Millennia eV 532 nm laser as its optical power supply. The Matisse laser's wavelength can be set between 670 nm to 1050 nm. While the spectral range that QDs are visible at changes from sample to sample, the typical range of wavelengths is from 740 nm to 800 nm. Therefore, the pump arm's wavelength range is well above and below the optical range that the QDs used in this thesis require, meaning resonant excitation is possible. The probe arm's laser can be chosen according to the experiment, the rationale for which is explained in Section 3.2.5.4. Both the pump and probe arms pass through Neutral Density (ND) filters (which have an exponential gradient) as to control the power of the beam. The probe arm's laser passes through a manually set filter wheel, as to ensure the laser power is below the saturation point (defined in Section 3.2.5.4) for the QD; importantly, the filter wheel remains fixed once a measurement begins, as to not alter the power. However, the pump arm's laser passes through a ND filter, which is attached to a linear translation stage. This stage is attached to a stepper motor and a KST101 K-Cube Stepper Motor Controller, which allows the power of the beam to be varied all while ensuring that the beam path remains unaltered. A feedback loop is then created, through the addition of a Fieldmaster GS power meter later in the arm that monitors the power of the laser. Through user-created LabVIEW programs running on a master computer, the desired power of the pump arm can be set through this stepper motor-power meter combination. The two laser beams pass through mechanical optical shutters which have switching times on the order of a few milliseconds. This allows for the timings shown in Figure 2.20 to be designated to a high degree of accuracy.

After these filters and optical shutters, both arms are coupled into Single Mode (SM) fibres. Up to this point all of the optical setup has been located on an optical bench near the bath cryostat, rather than on top of the cryostat. This is due to both the limited space available and weight consideration of the equipment on top of the cryostat. The pump laser passes through a Linear Polariser (LP) and then a Half-Wave Plate (HWP), allowing for any arbitrary orientation of linear polarised light to be produced. The pellicle BS allows the pump/probe laser power to be monitored, but due to short probe times (explained in Section 3.2.5.4) during measurements the probe power cannot be recorded. However, if the probe shutter is manually opened, the probe power can be measured using the power meter. This can be done before, during (by pausing) and after measurements to ensure that the probe power remains constant. The now combined laser paths then travel through a 70:30 (70 for QD PL) cube BS before passing through a Quarter-Wave Plate (QWP). The QWP is installed last to allow for a high degree of circular polarisation to be generated, as here it can compensate any polarisation imperfections introduced by the cube BS.

The laser path then travels through a glass window on top of the bath cryostat and into the insert. For Chapters 4 and 5 an aspheric lens with a focal distance of 1.45 mm and a numerical aperture of 0.58 was used as an objective for optical excitation of the QD and for PL collection. For Chapter 6 this was changed to be a cryo-compatible apochromatic objective with

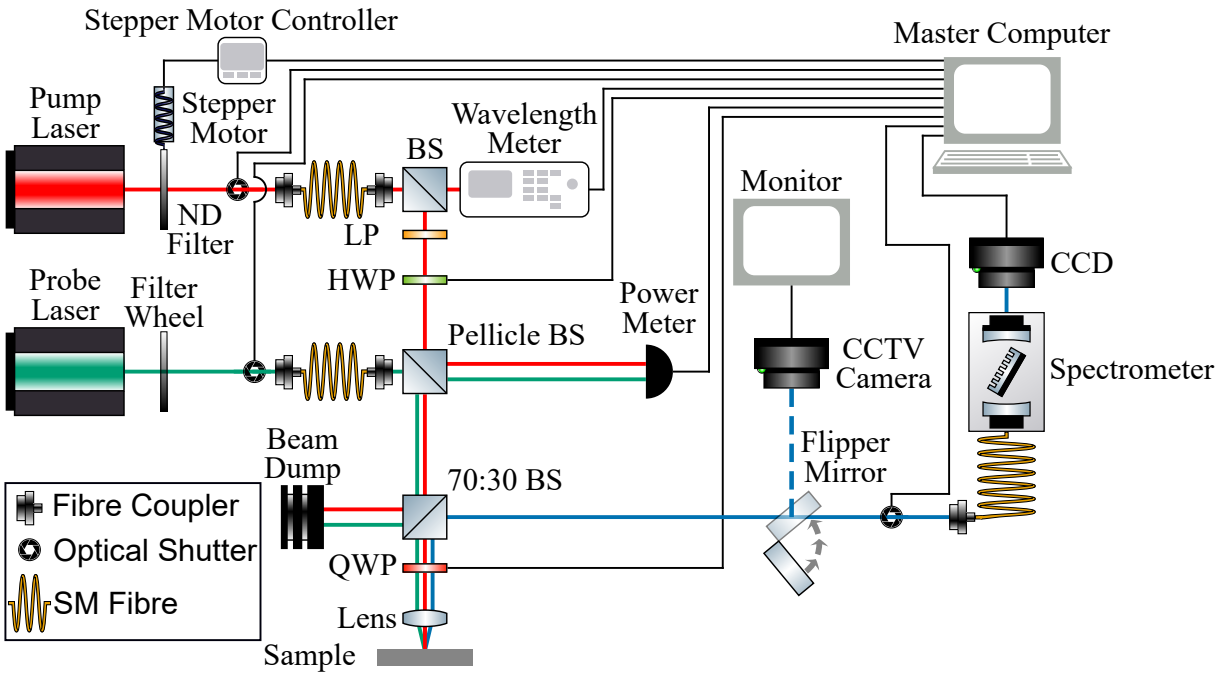

Figure 3.2: Schematic of the optical setup used for optical PL spectroscopy in this thesis. The pump/probe arms are shown by the red/green paths and the PL path is shown by the blue path, note the colours are not representative of the wavelength of light. These paths travel through a series of filters, shutters, Beam Splitters (BSs), and wave plates in order to create circularly polarised light that is then used in a pump-probe cycle. The PL from a QD is directed through a shutter, into a double spectrometer and then recorded by a Charge Coupled Device (CCD). Figure was made with aid from [165].

a focal distance of 2.89 mm and a numerical aperture of 0.81. The 70:30 cube BS then allows the PL to be transmitted into a fibre coupler, which passes the light through an optical shutter into the SPEX1404 double spectrometer (located on the optical bench). This spectrometer has a resolution of approximately 10 μeV. The optical shutter, immediately before to the spectrometer, is essential to ensure that the CCD is only exposed to PL from the QD during the pump-RF-probe cycle. The position of the SM fibre leading to the spectrometer can be adjusted to ensure that both cross-polarised components of PL, for an exciton in a magnetic field (see Figure 2.21), have equal optical signal, as not to hinder any fitting occurring in data analysis. A CCD is used to record the light. The exposure set for this CCD can be set to any arbitrary value, which varies for differing measurements. For the experiments within Chapter 6 a pair of doublet lenses, with a magnification of 3.75, were put between the spectrometer and the CCD allowing for a greater resolution, however it limited the spectral window. This is not included in Figure 3.2 as it was not present for all experiments. A flipper mirror is present, offering the option to reflect the laser beam away from the spectrometer and towards a Closed-Circuit Television (CCTV) camera and monitor. This is a useful tool for looking at the reflectance of the pump/probe laser off the sample. This gives one the ability to: check that there are no surface defects, perform initial PL alignment, and to map the borders of the sample within the cryostat.

3.2.2 Optical Spin Pumping

Optical spin pumping is a method used for initialising the spin state of the QD with high fidelity [166]. Figure 3.3 shows the mechanism of spin pumping. In units of $\hbar$, the electron's projected spin angular momentum, m_S, has values of $\pm\frac{1}{2}$ ($\uparrow$ or $\downarrow$), reflecting the electron's nature as a lepton with half-integer spin.

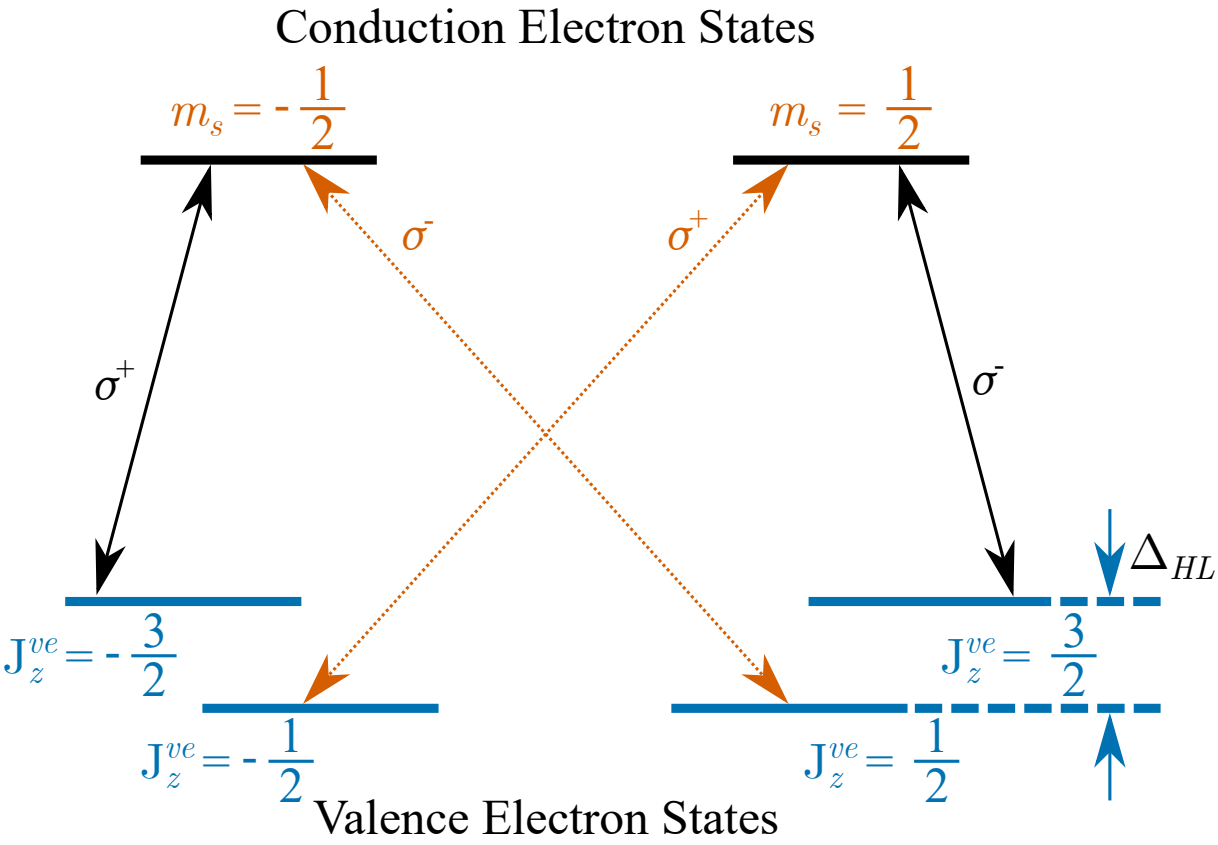

Figure 3.3: A simplified version of Figure. 2.11 showing optical selection rules for interband transitions involving valence band electrons with total angular momentum $J^{ve} = \frac{3}{2}$ in units of $\hbar$, the corresponding photon polarisation σ^+ or σ^- is indicated. Adapted from [125].

Light can be circularly polarised, so the electric and magnetic components rotate clockwise (σ^+) or anti-clockwise (σ^-) from the point of view of the source. An interesting phenomenon occurs when circularly polarised light is incident on the QD, due to the structure of the valence band in III-V semiconductors, such as GaAs. As there is no centre of inversion (inversion symmetry) there is an energy splitting between energy bands, and the spin and orbit degrees of freedom mix [167, 168]. In addition to this, the two helicities of light have angular momenta $L = \pm 1$, in units of $\hbar$, which leads to optical selection rules. By changing the helicity of the absorbed photons, one can pump electrons to certain states within a QD. For example, Figure 3.3 shows a σ^+ photon being absorbed by a valence electron with a projected angular momentum $J_z^{ve} = -\frac{3}{2}$. This results in the electron being promoted to the conduction state, $m_S = -\frac{1}{2}$, and a HH forming in the valence band. The hole is described as *heavy* as it has a higher effective mass, m_e^*, than the LH at the Γ point in the Brillouin zone (see Section 2.2.2). The projection of

total angular momentum of a HH is $J_z = \pm\frac{3}{2}$ ($\Uparrow$ or $\Downarrow$); a LH would be described with a projected total angular momentum of $J_z = \pm\frac{1}{2}$ ($\uparrow$ or $\downarrow$)[2]. The absorption of the photon has caused the creation of a neutral exciton, X^0, which is a bound state of the electron-hole pair, governed by the electrostatic Coulomb force. These excitons can then be used to investigate the spin-carrier mechanisms that occur within the QD.

3.2.3 Selecting a Suitable QD

Before conducting any experiments, a suitable QD must be selected. In our setup, we follow a specific procedure to achieve this. First, once the sample is loaded into the cryostat, has cooled down to 4.2 K, and the pump/probe lasers are focused on the sample, we map out the edge of the sample. This can be done using several methods. For example, a CCTV camera can be used to detect reflections from the sample surface, or if a diode sample is used, one can employ the pump laser and a Source/Measure Unit (SMU) to measure the photocurrent generated by the QDs in the sample.

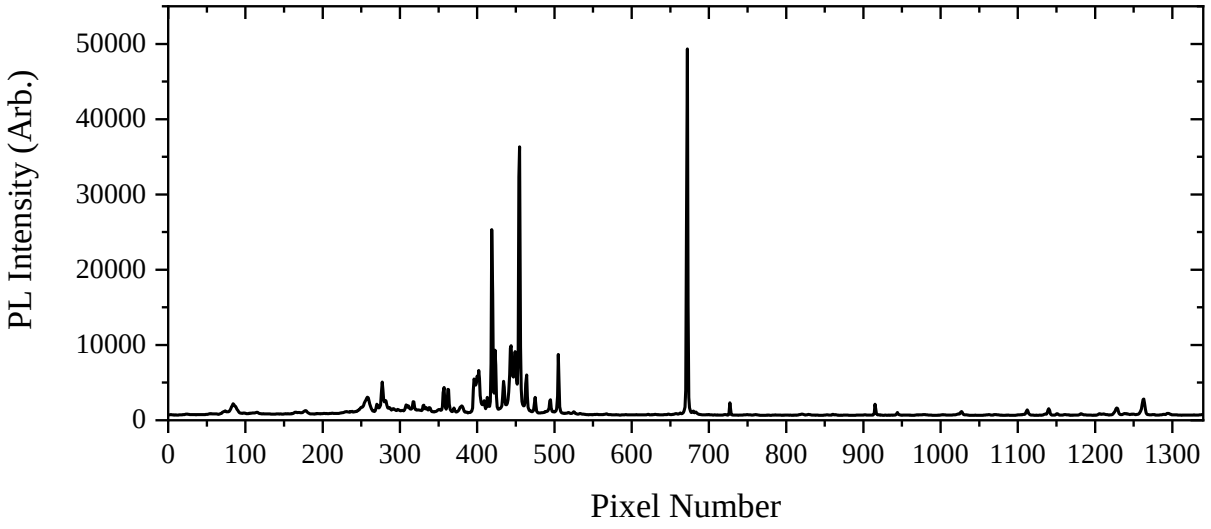

Figure 3.4: PL spectrum of a suitable QD for measurements at 0 T. The X^- exciton is visible at pixel ~ 672 and multi-charged states are visible between pixels 250-520.

After determining the boundaries of the sample, the next step is to move at least 15 μm inward to avoid any potential edge effects. The back reflection from the sample, viewed through the CCTV camera, is also used to check for surface defects in the region where QDs will be searched for. If there is a possibility that the sample will be remeasured in the future, selecting a QD near a well-defined feature, such as the corner of the sample, is advisable. This sharp feature can help in relocating the QD later. However, it is essential not to restrict measurements to one

[2]Note there is a difference in notation for the arrows of HHs and LHs. Frustratingly, the notation for a LH is often the same as an electron, which can add to confusion when reading literature. Fortunately, due to the energy splitting Δ_{HL} between the two states, typically several tens of meV, the LH states can often be ignored as they are not used for optical excitation [125]. This is unless there is: a break in rotational symmetry, strain, and or shape anisotropy which introduces HH-LH coupling [105, 112, 169, 170].

location on the sample. For a statistically significant set of data, QDs should be selected from various regions across the sample. Once a potential QD candidate is found, its suitability for measurement is assessed by measuring its PL using a probe laser. At 0 T a sharp exciton line should be visible, as shown in Figure 3.4 ,where the full width at half maximum of this line is 1.45 ± 0.06 pixels, as well as some multi-charged states.

The QD must be spectrally and physically isolated from nearby dots. This can be checked by tuning the spectrometer range and scanning a region of approximately 15 μm^2 around the QD to ensure no other QDs are detected. If the QD is confirmed to be spatially and spectrally isolated, located in a suitable part of the sample, and exhibits sharp exciton lines, the next criterion is the brightness of its PL. To determine this, several other QDs that also meet the aforementioned criteria are identified, and their locations and maximum PL intensities are recorded. The brightest QD is then chosen for further measurements.

3.2.4 Measuring Hyperfine Shifts

The spectral splitting of an exciton doublet can be optically measured using a PL spectrum, as shown in Figure 3.5. In this figure, the QD is optically pumped with a circularly polarised laser to generate DNP. As the pump time increases, the degree of nuclear spin polarisation rises, resulting in a larger hyperfine shift of the exciton. To quantify this shift, one can measure the exciton's spectral splitting when the QD nuclei are completely depolarised, and take the difference between this baseline and the splitting observed after optical pumping. The spectral splitting, and consequently the hyperfine shift, is obtained by fitting the exciton doublet. The precision of this fit is influenced by the resolution of the spectrometer, along with other factors such as signal to noise ratio, spectral linewidth, et cetera. These combined factors typically result in a fitting accuracy on the order of 1 μeV. In NMR measurements using an RF erase pulse, the spectral splitting can be measured both with and without the RF applied. The difference in exciton doublet splittings in the presence and absence of RF is known as the NMR signal.

3.2.5 Optimising Dynamic Nuclear Polarisation

In order to perform the NMR measurements that this thesis relies upon it is important that one can reliably create DNP. Without this, there would be no contrast to the spectral splitting of an exciton doublet under varying conditions of RF application, as explained in Section 2.5. There are numerous variables to consider, described in the sections below, all of which must be optimised to maximise DNP. Ideally this multidimensional search for finding the global optimum of variables would be done in parallel, i.e. a single measurement where all parameters are changed (as there may be some interdependency between them)[3]. However, it

[3]This methodology is to some extent used in Chapter 6 where the pump laser's power, wavelength, and the bias applied during pumping are all varied at the same time. It was performed in this way as, the aim here was to reach higher degrees of nuclear spin polarisation than previously attained.

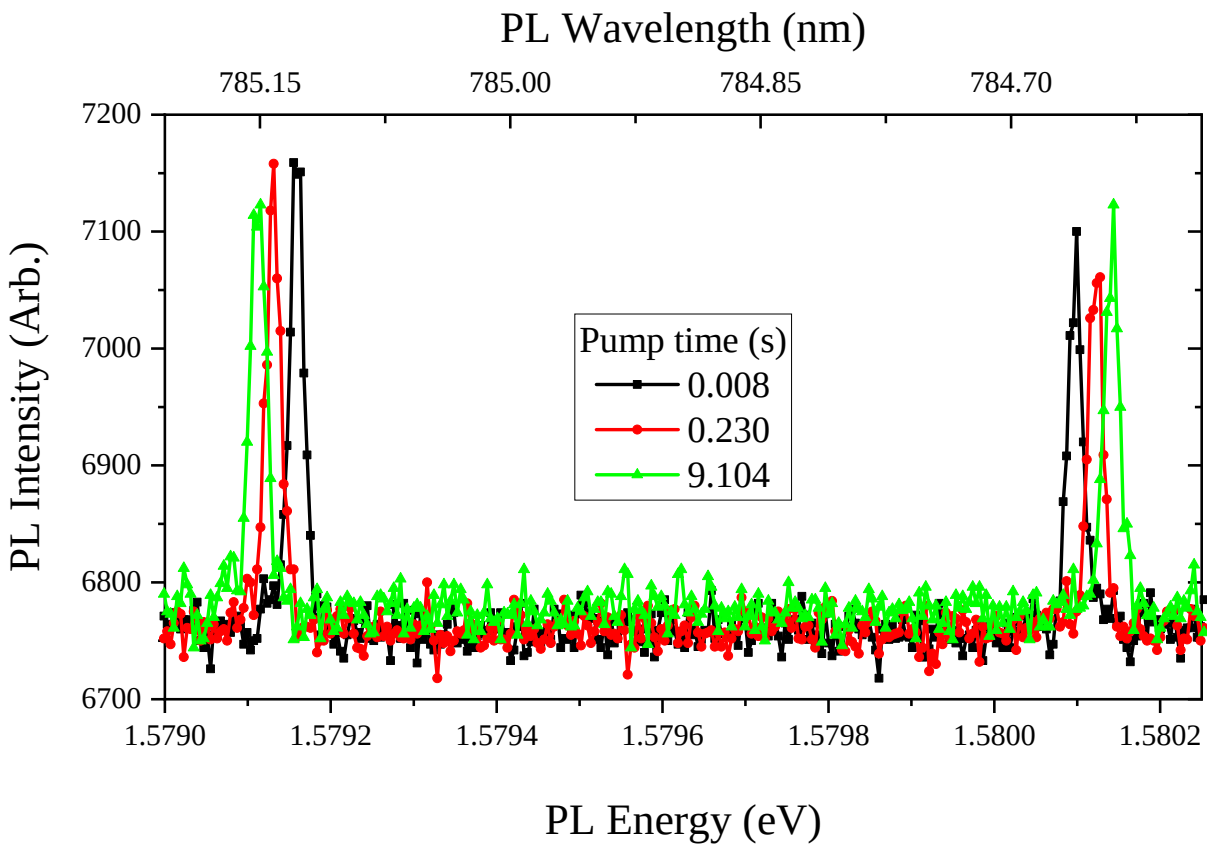

Figure 3.5: PL spectra of a X^- exciton for a QD at 10 T after optical pumping with a σ^+ polarised laser, shown for different pumping durations. As the pumping time increases, the spectral splitting of the exciton doublet increases due to the hyperfine shift.

is significantly simpler to do a line search for a single parameter, and then use the optima of all of these parameters in substantive measurements. Utilising this framework, nuclear spin polarisation degrees ranging from $60 - 80\%$ have been demonstrated [131]. However, in Chapter 6, we present the our ability to generate polarisation degrees $\geq 95\%$.

3.2.5.1 Pump Laser

For the pumping of the QD there are a few variables that need to be optimised in order to increase DNP. The first that is usually optimised is the wavelength of laser used. The pump laser used is a Matisse 2 Tunable Ring Laser. This allows for a broad range of laser wavelengths which can also be at high powers, however the lasing power usually is heavily attenuated as it would cause damage to the SM optical fibres. A wavelength calibration measurement can be run, as shown in Figure 3.6, using the method outlined in Section 2.5.2. In Figure 3.6, it is shown that a pump wavelength of ~ 791 nm yields the highest degree of DNP for this QD. For QDs on the same sample there is usually some variation of optimum pump wavelength, however as the optimal DNP is via s-shell exciton excitation, one would not expect it to fluctuate by more than a couple of nanometres. This has two advantages, it makes pumping with diode lasers possible as the peaks of DNP will occur in similar spectral locations from QD to QD. It also means that

when changing QDs after a measurement set has been completed, a smaller spectral range can be probed, as to save experimental time. The power and time that one pumps for also have an effect on the DNP of the QD and its surrounding area through nuclear spin diffusion. For details on the way power affects the DNP see Chapter 6 and for nuclear spin diffusion see Section 2.5.3 and Chapter 5.

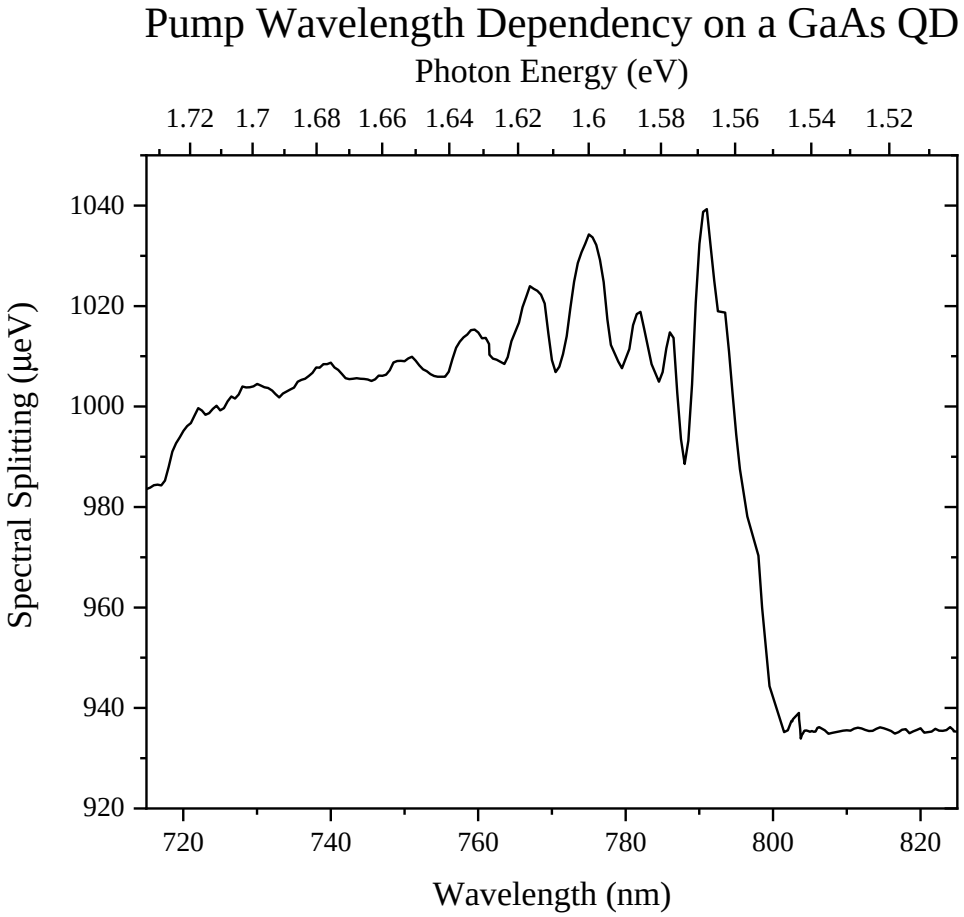

Figure 3.6: Pump wavelength dependency on the spectral splitting of an X^- exciton for a QD at 10 T using a σ^+ polarised laser. The peak DNP occurs at ~ 791 nm, which creates a spectral splitting that is ~ 105 μeV above the zero DNP level.

3.2.5.2 Radiofrequency Excitation

When applying a RF pulse during the pump-RF-probe cycle within a measurement, the centre of the RF's bandwidth often needs to be centred on the CT frequency, near the Larmor frequency, for an isotope within the QD. When applying a RF burst, it is important not to apply too high an amplitude wave, as it may cause heating of the sample and/or damage the RF coil inside the cryostat. If the duration of the RF pulse is too short (less than a couple of milliseconds) then Rabi oscillations may be induced, resulting in not all of the nuclei being depolarised. If the RF time is long, one could ensure that the majority of the nuclei are depolarised. However, due to the exponential decay of polarisation, there are diminishing

returns with this and it uses more experimental time. If one does desires a shorter RF pulse time, a faster depolarisation rate can be achieved by increasing the amplitude of the RF waveform. From Figure 3.7 one can see the effect of varying the RF depolarisation time for differing isotopes, where the RF frequency has been centred on each isotope individually. From this, an exponential function can be fitted to determine the decay constant for each isotope, with a characteristic decay time of ≈ 30 ms usually desired. A RF pulse combining frequencies from different isotopes is then generated, with each isotope's decay factor employed to weigh its respective contribution. This waveform is then used for multi-isotope depolarisation, as shown by the blue line in Figure 3.7. By using this method one can ensure that all the isotopes decay at the same rate. The combined multi-isotope depolarisation rate can then be measured and fitted. Five times the decay constant, from this fit, is then used as the total depolarisation time in experiments. This will ensure that the nuclear spin polarisation of all isotopes has fully decayed without wasting experimental time.

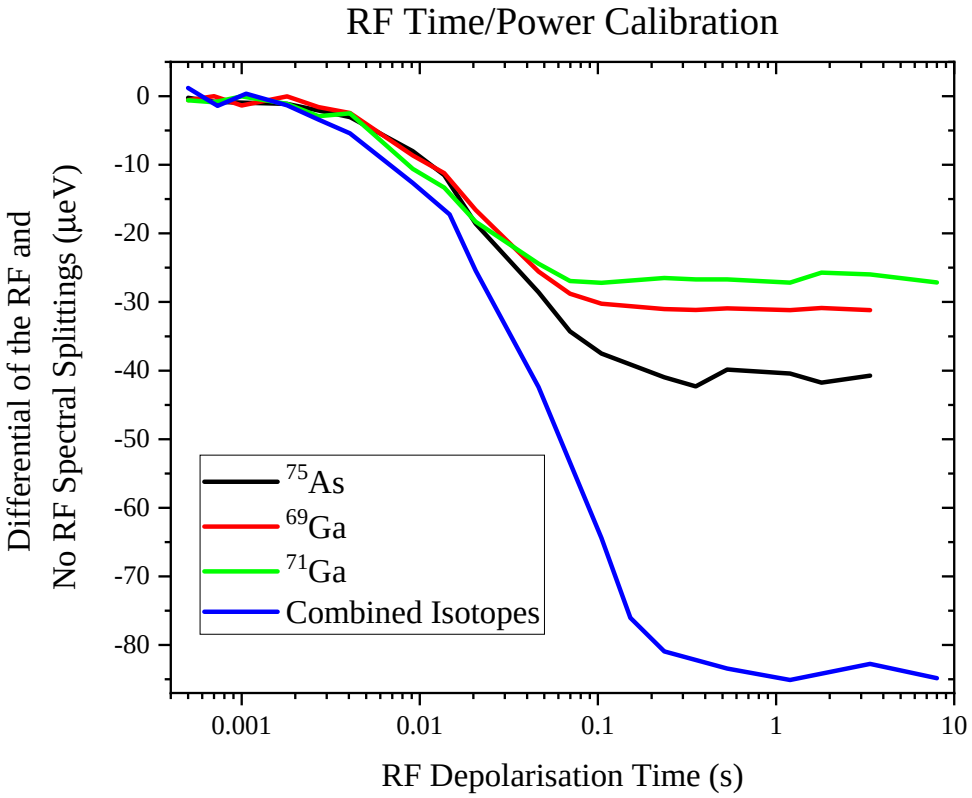

Figure 3.7: RF time/power calibration on a QD at 1 T. The spectral splitting of a reference spectra, where the RF is gated off, is subtracted from the splitting in a spectrum where the RF has been enabled. As the RF time increases, a greater difference emerges between the reference spectrum, where minimal depolarisation has occurred, and the spectrum obtained with the RF enabled. As to not complicate the plot, the RF amplitudes for all three individual isotopes are the same; the combined isotope waveform has had its power increased, from the single isotope waveforms, as to depolarise the nuclei with a characteristic decay time of 64 ms. In calibration measurements these powers may be changed to try to obtain a ≈ 30 ms decay constant.

3.2.5.3 Half and Quarter-Wave Plates

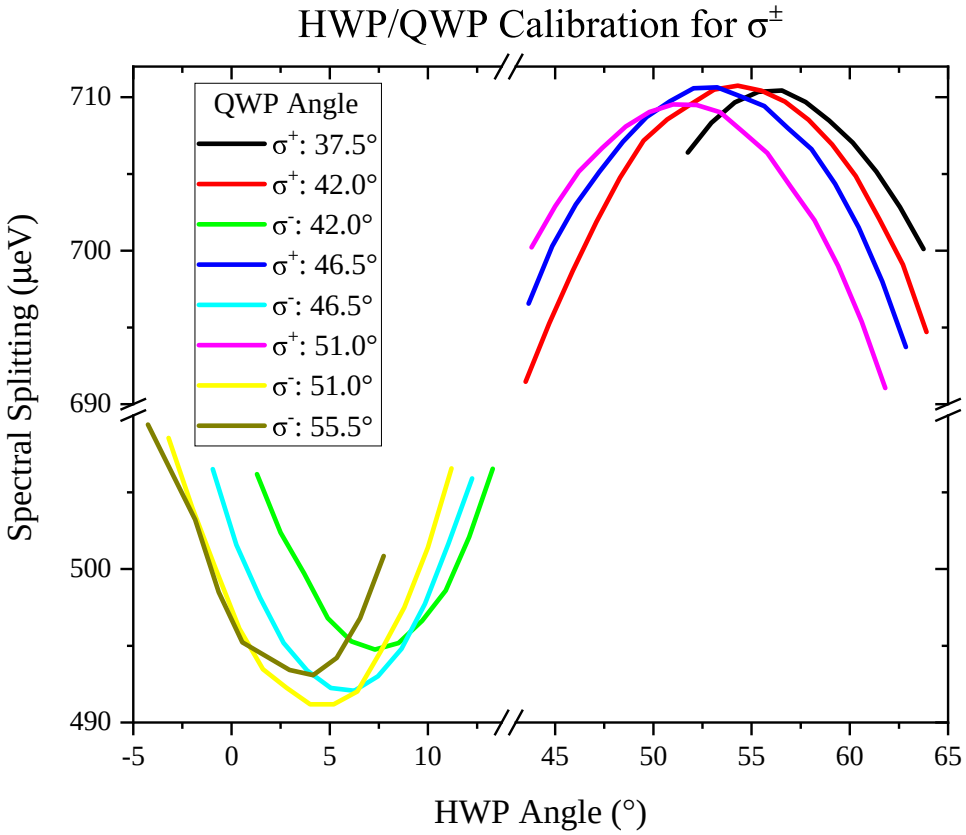

Figure 3.8: Calibration of the HWP/QWP angles for both $\sigma^{\pm}$ for a QD at 10 T.

The degree of circular polarisation for the pump laser can be optimised for each QD studied, as shown in Figure 3.8. While in Figure 2.15 the formation of excitons are described as a consequence of a purely circular polarised excitation, in reality when elliptically polarised light is used higher values of DNP can be obtained. The reasoning for this is due to the anisotropy of the QD shape, as explained in Section 2.3.3 and Chapter 6. The pump arm laser initially goes through a LP to ensure that the laser is linearly polarised before passing through the HWP, see Figure 3.3 for reference. The HWP can be adjusted to arbitrarily orientate the polarisation direction of the lineally polarised light. The pump and probe laser both then pass through the QWP which converts the linearly polarised light into circularly polarised light. By adjusting the angles for these wave plates one changes the degree of linear polarisation of the lasers, allowing for a more helical polarisation of light. In HWP/QWP calibration measurements one can fit the data with a $\sin$ function. For σ^+/σ^- one usually desires the maximal/minimal splitting of the exciton doublet (signifying larger DNP), in GaAs QDs in external magnetic fields above $\approx$ 0.5 T. For Figure 3.8 this would mean a QWP angle of $42/51°$ and a HWP angle of $54.0/4.6°$ for σ^+/σ^-.

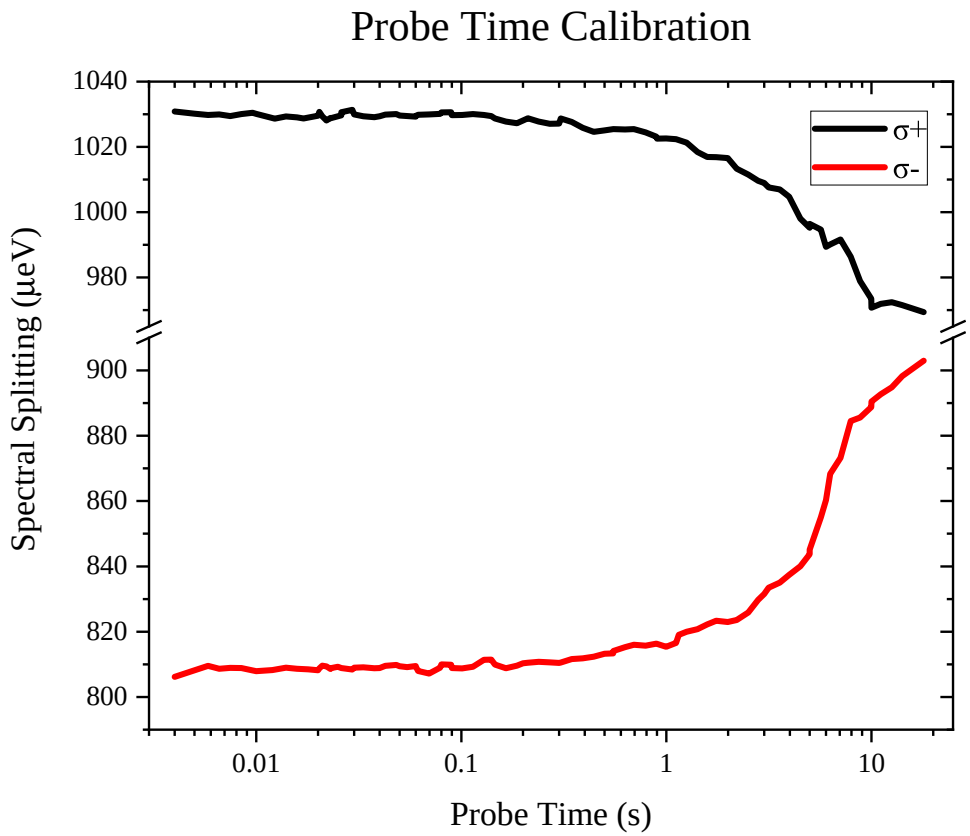

Figure 3.9: Probe time calibration for a QD at 10 T. The two data sets show the decay of nuclear spin polarisation for a QD pumped using σ^+/σ^- light in black/red.

3.2.5.4 Probe Laser

The initial optimisation for the probe laser involves selecting an excitation wavelength with which the PL from a QD sample can be seen. There are a selection of diode lasers in the laboratory that we can use, for example 532/690/710/730 nm as well as a HeNe laser that produces 632 nm. When probing a QD with a laser it is important to optimise the power of the laser and time that you probe for. If the power is too high then the PL from the exciton doublet being investigated will be saturated, leading to a less sensitive measurement of its splitting. Saturation is where the PL intensity of the exciton doublet no longer increases linearly as the power increases. However, if the power is too low then the signal to noise ratio of the PL from the QD will become difficult to fit. The optimum probe power used for QDs in this thesis, unless stated otherwise, is with a power that is just below where the QD saturates. A quick optimisation process is manually performed for several probe lasers, where the power of each laser is chosen to be just below saturation, as to determine which laser generates the brightest PL for the exciton. Figure 3.9 shows how varying the probe laser duration affects the measured DNP of the QD, as seen by the change in the spectral splitting of the exciton. As the probe time increases, the probe laser induces a decay of the DNP that was created by the pumping process. In other words, the probe laser causes a parasitic depolarisation which

returns the nuclear polarisation degree back to the depolarised state. A similar issue arises in optimising probe time as it did for probe power; if the pulse is too short the PL signal to noise ratio is poor, too long and the detected DNP is distorted. Throughout this thesis most measurements were conducted so that the probe time only caused a total decrease of DNP of $\approx 2\%$. A decaying exponential model, of the form $\propto Ae^{-\left(\frac{t}{\tau}\right)}$, was used to fit the curves in order to determine said probe time. In Figure 3.9, the decay times are $0.168/0.288$ s for σ^+/σ^- respectively. As these values differ, a probe time not exceeding the shorter time of 0.168 s would be used, to ensure that the 2% loss of DNP was not surpassed. To combat short probe times, leading to low PL signal intensities, multiple exposures can sometimes be taken for experiments. To do this several pump-RF-probe cycles can be run, with the CCD having one continuous exposure. In the optical path preceding the CCD, there is an optical shutter which is timed to open/close by a master computer. This ensures the CCD is solely exposed to QD PL emission induced by the probe laser, and not the pump laser.

3.2.5.5 Bias

When using a sample that is charge tunable, one can use the bias across the sample to increase the DNP achievable. This is not a direct relation, rather the bias changes the electric field and charge states which affect DNP. The peaks one can see in Figure 3.6 are shifted when different biases are applied, during the pumping process. Optimum DNP occurs when the QD is pumped under a large reverse bias. This quickly ionises electron-hole pairs that have been optically generated, before they can recombine to emit a photon (optical recombination times are appropriately 300 ps in GaAs QDs [171, 172]). However to achieve high DNP with large reverse biases, it is essential that a high pump power is used. This is to generate a sufficient number of spin-polarised electrons capable of undergoing a spin flip to polarise the nuclei before their ionisation (see Chapter 6 for information on this process). In addition to this, the bias shifts the spectral position of the DNP peaks seen in Figure 3.6, therefore one must optimise the bias, pump power, and pump wavelength simultaneously.

3.2.5.6 Bistability of Nuclear Polarisation

To build up the DNP, as described in Subsection 2.4.1.1, electron spin flips need to occur. The rate that these spin flips occur is proportional to the ratio of the absolute square of the electron hyperfine coupling to the electron spin state energy splitting $\left(w_{ff} \propto \left(\frac{|A_j|}{\Delta E_e}\right)^2\right)$ [125][4]. The QD samples discussed in the thesis are subjected to an external magnetic field B_z. The Overhauser field, generated by nuclei with DNP, can align either parallel or antiparallel to this external magnetic field. This in turn will either increase/decrease ΔE_e, altering the rate of

[4]This is a highly simplified equation, in the perturbative regime, that assumes an electron wavefunction is uniform over the ensemble of nuclei within a III-V semiconductor QD. This is why A_j is a constant here; a precise description of the electron spin dynamics is beyond the scope of this thesis.

electron flip-flops, and change the rate of nuclear spin polarisation for the QD. This leads to non-linearities within the, usually, pure exponential curves seen in Figure 3.9. These non-linearities can be occasionally eluded by adjusting the pump/probe/RF power as to alter the rate of electron flips that are occurring. However as noted in the literature, the prevalence of these non-linearities is, in part, determined by the external magnetic field, which can make these non-linearities harder to evade when a designated external field is required [86, 173–175]. In measurements using adiabatic RF sweeps and where a large variation of hyperfine shifts are required for fitting, as performed in Chapter 6, these non-linearities are a potential source of irritation.

3.3 Nuclear Magnetic Resonance

In this thesis, the focus is solely on Continuous Wave (CW) ODNMR, in contrast to the pulsed NMR techniques utilised in similar experimental setups [163, 176, 177]. Unlike pulsed NMR, which operates in the time domain, CW ODNMR operates in the frequency domain. The underlying principles of NMR spectroscopy via nuclear spin manipulation are discussed in Section 2.5; this chapter focuses on detailing the experimental implementation of the technique.

3.3.1 Generation of Radiofrequencies for Nuclear Magnetic Resonance

In order to use NMR as a form of spectroscopy it must be possible to create the RF signals that selectively depolarise nuclei, the hardware to do so is shown in Figure 3.10. The total frequency bandwidth of any one isotope in our GaAs/AlGaAs QD samples, without external strain, is usually < 1.5 MHz. This is due to the inhomogeneous broadening of nuclear spin transitions (see Chapter 4 for a comparison of nuclear spin transition broadening for QDs with differing chemical compositions). To approximate this frequency range with digital devices a RF comb can be employed, as illustrated in Figure 3.13. This comb is first generated, through direct synthesis of a waveform, and then mixed with a carrier waveform to shift it in the spectral domain. Typically, the carrier signal's frequency is selected to be near resonance with the Larmor frequency of a specific isotope. The comb signal is an arbitrary waveform consisting of a linearly spaced series of discrete modes, with the mode spacing, w_m, typically set to be 125 Hz. This mode spacing is chosen to be smaller than the homogenous NMR linewidth of the isotopes within the QD. This ensures that all nuclear spin transitions within the RF bandwidth are depolarised by multiple modes, leading to an exponential decay in nuclear spin polarisation [178], as shown in Figure 3.7. If the RF waveform is for the Inverse Nuclear Magnetic Resonance (InvNMR) technique, discussed in Section 3.3.2.3, then the generator internally modulates the carrier signal, to create an upper and lower sideband (two-toned signal), while also suppressing the carrier frequency. In either case, the carrier and envelope signals are mixed together resulting in a linearly spaced series of modes around the carrier frequency.

The frequency comb is then amplified using an amplifier rated up to a maximum power

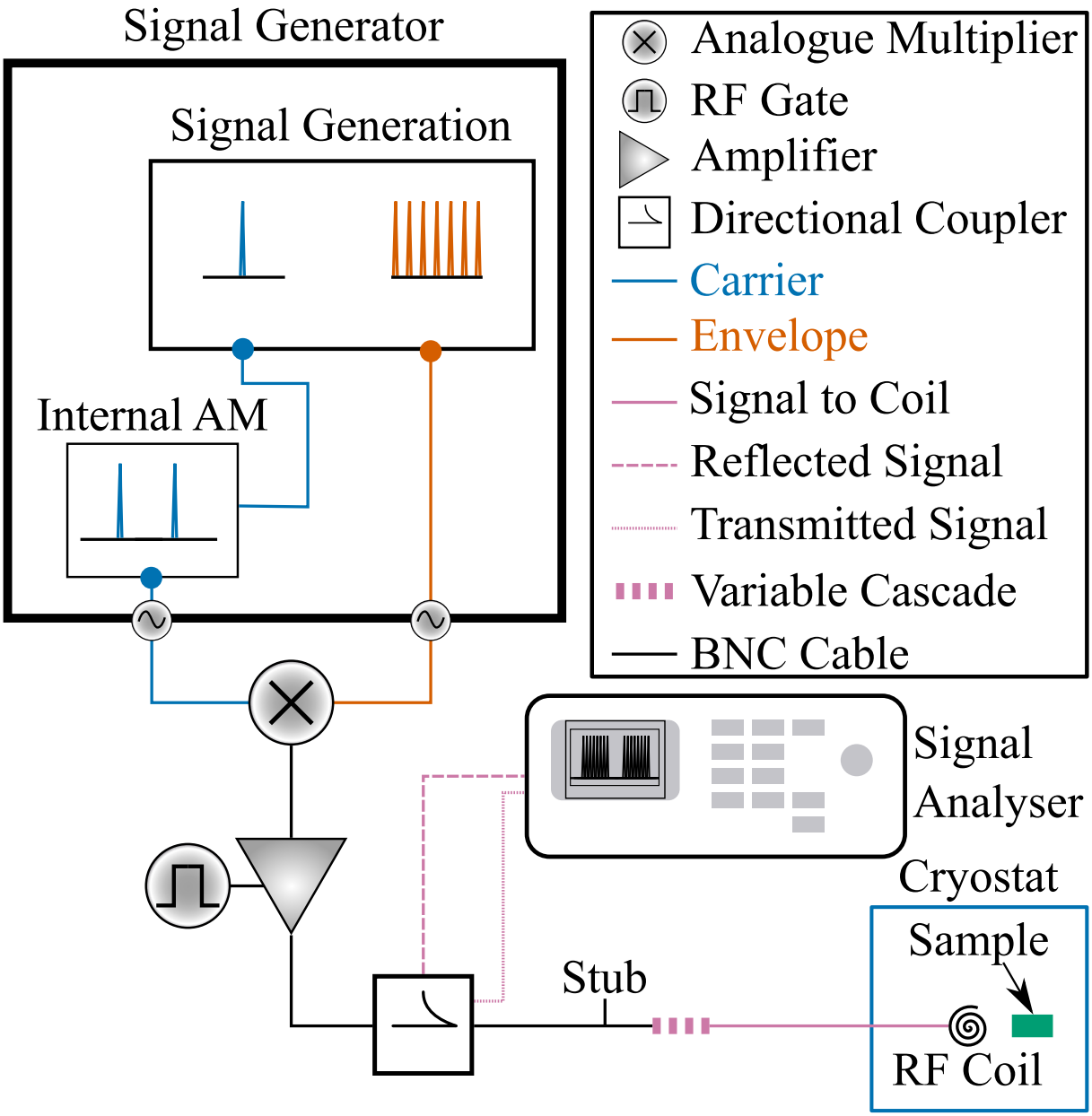

Figure 3.10: Circuitry required for InvNMR measurements. A carrier (blue) waveform and an envelope (orange) arbitrary waveform are mixed together to create the required RF waveform. A gated amplifier is then used to amplify the signal, which can be monitored using the directional coupler and signal analyser, before passing through a RF cascade. This cascade then connects to a coil within the cryostat which transmits the RF to the sample.

of 20 W (100 W) for Chapters 4 and 5 (Chapter 6). The amplification is gated, so it can be switched on/off via an external signal. The benefit of this gated amplification is that when no RF is required in the pump-RF-probe cycle, the amplifier can be gated off to prevent any noise being amplified. The amplified comb first passes through a directional coupler, then progresses into a RF cascade, before ultimately entering the cryostat and reaching the RF coil. Using the directional coupler and a signal analyser, the reflected and transmitted signals are measured, as shown in Figure 3.11. In order to produce a magnetic field at the coil, the RF signal must be

transmitted; however, the load impedance of the coil, due to being an inductor, is frequency dependent as $Z_L \approx i\omega L_C$, where L_C is the inductance. Due to the imaginary component of the impedance, it will never match that of the RF coaxial delay line (completely real $Z_0 = 50\Omega$), constructed from BNC cables. To compensate for this, a variable length cascade and shunt stub are implemented, in order to match the impedance of the coil to the $50\ \Omega$ impedance of the RF source and amplifier. The fully analytical approach to determining the length required for the cascade/stub is given in Chapter 5 of [179], however in practise we use an empirical approach.

For this procedure one must choose a set magnetic field, from which one can estimate the Larmor frequency for a given isotope using its gyromagnetic ratio, before any measurement is performed. For example, at 8 T the frequencies of ^{75}As, ^{69}Ga and ^{71}Ga would be 58.5 MHz, 82.1 MHz and 104 MHz respectively, as shown in Figure 3.11. A broadband (120 MHz bandwidth) white noise RF waveform is then generated on an arbitrary waveform generator. The forward and reverse ports of the directional coupler can then be used to monitor this RF signal, using a spectrum analyser, to see how the transmitted (forward) power differs from the reflected (reverse). The differential of the forward and reverse powers is shown by the green data in Figure 3.11. For InvNMR the difference between the transmitted and reflected powers need only be ≈ 3 dBm for a strong enough magnetic field to be produced at the coil. These non-zero differentials between forward and reverse power signify that some power from the RF signal has been transmitted by the RF coil, at that frequency. By changing the length of the cascade/stub one can change where the large differentials in power occur, in order to match the desired transmitted frequency. It is important that these differential power peaks, where transmission of the RF signal occurs, are not too narrow, as the quadrupolar shifts in QDs can span over hundreds of kHz. It is crucial to depolarise the spectrally broad components, thus necessitating the presence of a broadband peak. As well as this, while the magnetic field decays so will the frequency that needs to be generated to depolarise nuclei. Inevitably if enough time passed, the frequency necessary for depolarisation would shift away from a peak of transmission. This alteration would lead to a modified depolarisation rate for the nuclear spins, from that already determined in measurements such as the one shown in Figure 3.7.

An alternative approach is to use a broadband cascade, where no effort is made to get a high transmittance at set frequencies, as shown in Figure 3.12. With this setup, there is a relatively flat transmittance dependency for the transmittance against frequency, however the actual transmittance is significantly lower than for a resonant cascade, averaging about 0.5 dBm in Figure 3.12. One may question why such a cascade would be used, as it would both cause a greater reflection of power to the amplifier and be less efficient in transmitting power. However, due to the relatively frequency independent transmittance it allows the cascade to be used for a large range of magnetic fields. This means that one does not need to physically change the cascade each time a different magnetic field is used. Also, the power delivered to each isotope in the sample will be roughly equal, so their RF waveform

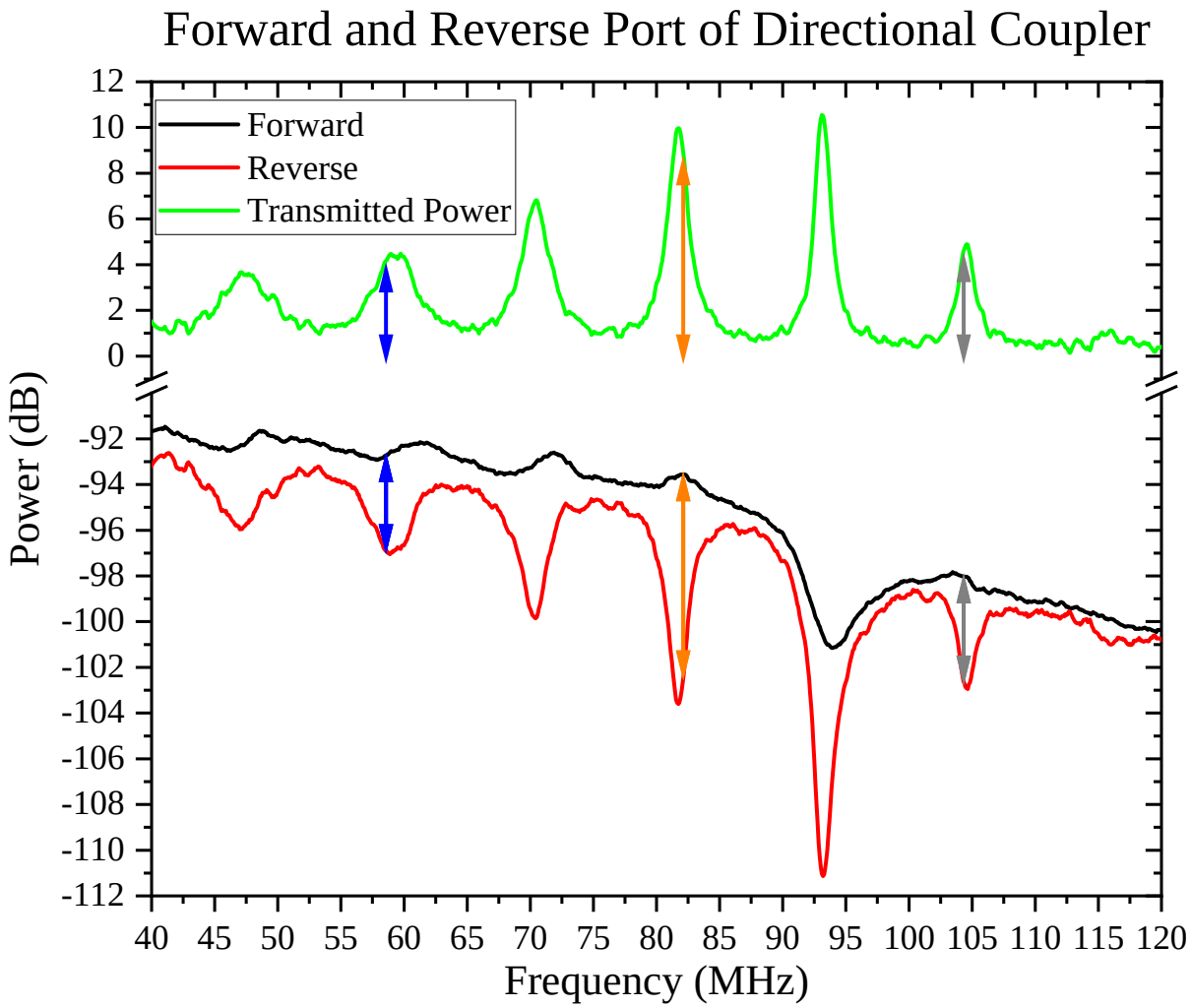

Figure 3.11: The signal from the forward and reverse ports of a directional coupler, as seen in a spectrum analyser. The RF being generated is a 120 MHz bandwidth white noise waveform. The cascade being used here has been designed for InvNMR measurements occurring at 8 T. The blue/orange/grey arrows represent the ^{75}As/^{69}Ga/^{71}Ga Larmor frequencies at a magnetic field strength of 8 T. The green signal is the calculated differential between the forward and reverse powers, which is the power transmitted by the RF coil.

amplitudes, governing the rate of nuclear spin depolarisation, are easier to equalise.

There are a few other factors that affect the magnetic field strength present at the QD due to the RF produced at the coil, including coil geometry and distance from the coil to the QD. The RF transmittance from the coil will have the most significant impact, although these other considerations are also important. The coil used in this thesis is made from 0.1 mm copper enamelled wire with 10 turns with an inner diameter of approximately 0.4 mm spooled in 5 layers with 2 turns in each layer. Equation 3.1, derived from the Biot-Savart law, describes the magnetic field strength, B_x, for a coil with N turns of radius R at distance x along the central axis with current I running through it, where μ_0 is the permittivity of free space. As this is not quite the geometry of our coil, and different turns will produce very different fields, we can use $N = 1$ to estimate the magnetic field strength. With: the coil values described above, a distance

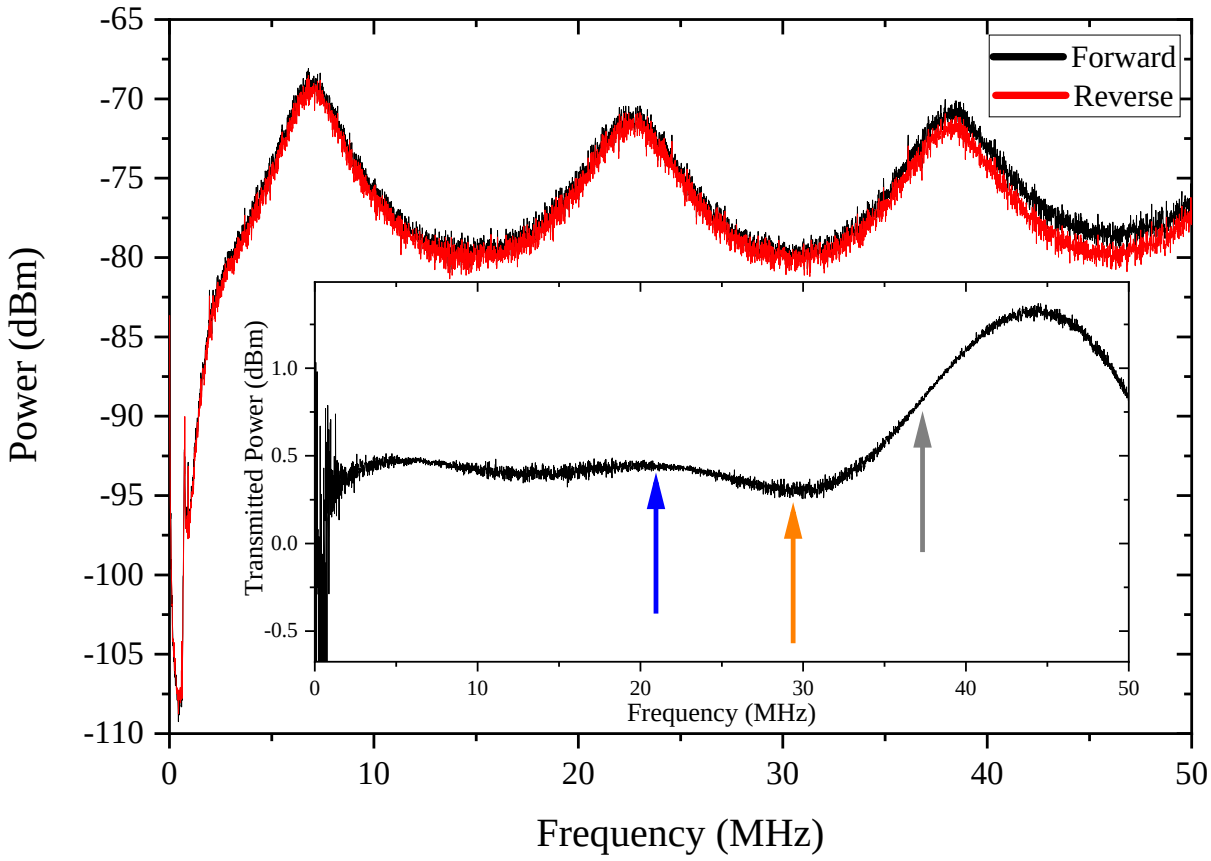

Figure 3.12: The forward and reverse port of a directional coupler attached to a broadband NMR cascade. The blue/orange/grey arrows represent the ^{75}As/^{69}Ga/^{71}Ga Larmor frequencies at a magnetic field strength of 2.87 T. The irregularities in power at low frequencies occur because they fall outside the amplifier's effective frequency range, specified as between 3 to 200 MHz.

of 0.2 mm from coil to the QD, an impedance matched cascade, and a 1 A current, the magnetic field magnitude at the QD would be ≈ 1 mT. Note, there must always be a non-zero distance between the coil and the sample to ensure that the coil does not get damaged when moving the sample in the cryostat, as well as to minimise any heating of the sample.

$$B_x = \frac{\mu_0}{4\pi} \frac{2NI\pi R^2}{(x^2 + R^2)^{\frac{3}{2}}} \tag{3.1}$$

3.3.2 Types of Nuclear Magnetic Resonance Spectroscopy

There are several types of NMR, however the research in this thesis focuses mainly on integral saturation NMR and InvNMR. The differences between these types of NMR are shown in Figure 3.13.

3.3.2.1 Optically Detected Nuclear Magnetic Resonance

Before discussing integral saturation NMR or InvNMR it is useful to understand how standard CW saturation ODNMR works. Some details of ODNMR have already been

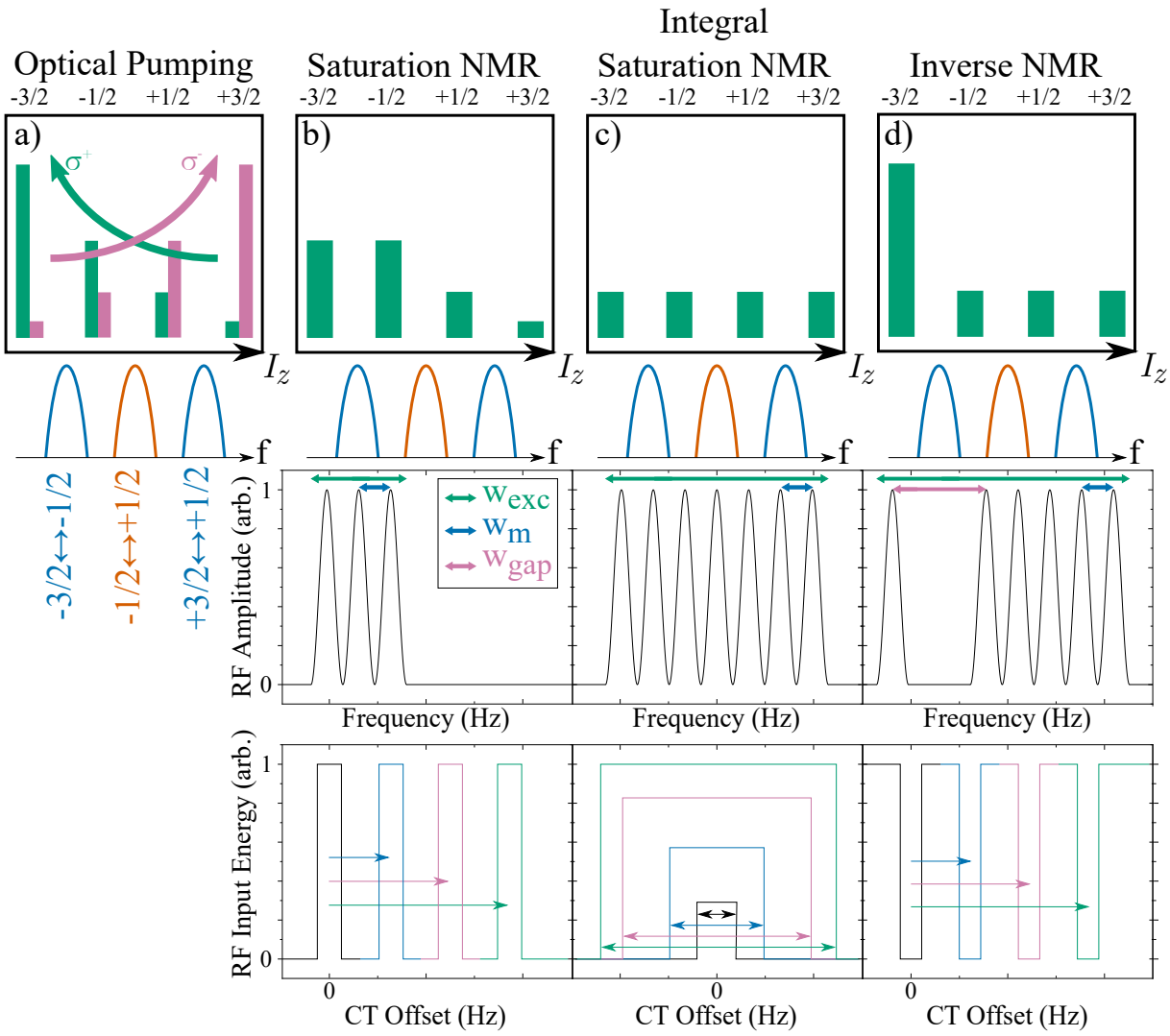

Figure 3.13: a) Depolarisation of nuclear spins after optically pumping nuclei with $3/2$ spin. Note as was the case for Figure 2.19, the $-\frac{3}{2} \leftrightarrow -\frac{1}{2}$ transition occurs at lower frequencies in the case of Ga isotopes, for ^{75}As this would be the higher frequency ST, in our QD samples. Nuclear spin depolarisation due to and spectral shapes of b) Saturation NMR, c) Integral saturation NMR, d) InvNMR. Beneath the nuclear spin depolarisation figures, the individual combs that form the RF waveform are shown. Underneath these combs the way these waveforms would be varied to collect data is shown. In the case of integral saturation NMR, the required RF input power increases as the bandwidth increases as to ensure the power density remains constant. To maintain clarity in the spectral shape of the InvNMR waveform, where a gap occurs for one measurement state the RF waveforms for the other states are not shown. For instance, at the 0 kHz CT offset, a gap is shown in the waveform of the black line. The RF waveforms for the blue, pink, and green lines are not shown here, but there would be no gap present. In reality, each measurement state would exhibit only one decrease in RF energy within its bandwidth. This figure is based on those in [151, 176].

discussed in Section 2.5, so a brief summary is provided here. This technique utilises the pump-RF-probe method as shown in Figure 2.20. A circularly polarised pump laser is used to create electron-hole pairs, which through the hyperfine interaction create nuclear spin polarisation. Figure 3.13 shows how the initial polarisation changes for $\sigma^{\pm}$ pump lasing. More

analytically, after pumping and before any application of RF, the population probabilities, p_m, of the levels of nuclear spin projections, m, for a $\frac{3}{2}$ nuclear spin QD, can be expressed as the canonical Boltzmann distribution [131, 151], as shown in Equation 3.2.

$$p_m = \frac{e^{m\beta}}{\sum_{m=-I}^{+I} e^{m\beta}} \tag{3.2}$$

In Equation 3.2, β is the inverse spin temperature defined as $\beta = \frac{\hbar\omega_L}{k_B T_e}$, k_B is the Boltzmann constant, $\hbar$ is the Planck constant, ω_L is the Larmor frequency and T_e is the spin temperature of the electron which has induced the DNP. The total nuclear spin polarisation, P_N, is then defined in Equation 3.3.

$$P_N = \sum_{m=-I}^{+I} \frac{m p_m}{I} \tag{3.3}$$

Through optically detecting the spectral splitting of an exciton's PL doublet, one can measure the nuclear spin polarisation. After this initialisation of nuclear spin polarisation, an excitation band, of width w_{exc}, of RF is applied via the coil, as described in Section 3.3.1, which depolarises nuclear spins. Physically, it causes the equalisation of population probabilities of nuclear spin states with different spin projections. As there is a frequency splitting of these nuclear spin states, one can scan this excitation band across a frequency range to selectively depolarise set transitions, shown in Figure 3.13, while having no effect on other transitions. The NMR signal from this measurement is proportional to the difference in population probabilities of the affected states, so in Figure 3.13 where the RF is applied to the $-\frac{3}{2} \leftrightarrow -\frac{1}{2}$ transition the signal would be $\propto p_{-\frac{3}{2}} - p_{-\frac{1}{2}}$.

3.3.2.2 Integral Saturation Nuclear Magnetic Resonance

Integral saturation NMR is similar in concept to frequency-swept saturation NMR spectroscopy, but it deviates from the latter by not employing a constant excitation bandwidth that scans across frequencies. Instead, this form of NMR usually remains centred on the CT frequency, at the $-\frac{1}{2} \leftrightarrow \frac{1}{2}$ transition, and varies the excitation bandwidth. By using a large number/range of excitation bandwidths one can *integrate* the change in nuclear spin polarisation over a span of frequencies. This technique is not useful for detecting sharp spectral features, however it is very practical when investigating broad components. With this integral technique one needs to keep the power density constant, so that the rate of nuclear spin depolarisation is kept constant. If one were to simply increase the RF waveform's bandwidth then the power of each mode in the comb would decrease. To remove this issue, the RF amplification needs to increase for broader waveforms. However, this means that as one increases the bandwidth the total power required increases too, which will increase any heating

effects occurring near the sample. This heating will cause unwanted depolarisation of nuclei within the sample and, if the power is too high, may even damage the RF coil itself. In order to prevent this occurring, when calibrating the RF amplitudes, as in Figure 3.7, one can use a low-power long ($\approx$ 6 s) RF pulse with a large (6 MHz) bandwidth. One can then slowly increase the power of the waveform, by increasing the voltage output of the RF waveform generator, and measure the temperature increase in the cryostat. The maximum increase in temperature that we wish to have, due to the RF coil, is 0.5 K. Once we have increased the power enough as to reach this temperature change we note down the voltage set on the generator. This will then be used to set the maximum amplification allowed for the RF waveforms. The RF duration in an experiment is usually between 10 ms $\leq T_{RF} \leq$ 0.5 s, so this maximum heating is never reached, however it is a useful benchmark to set. As a 6 MHz bandwidth comb is chosen, it is also unlikely that larger bandwidths are required to depolarise the nuclear spins.

3.3.2.3 Inverse Nuclear Magnetic Resonance

The most common form of NMR used in this thesis is InvNMR, which was developed by our research group in Sheffield in 2012 [151]. This novel approach uses a specialised RF waveform to significantly enhance the detectable change in nuclear spin polarisation for quadrupolar nuclei with large nuclear spin. Specifically, this improvement can be written as the ratio of the change in total polarisation for NMR using InvNMR and standard saturation ODNMR. If comparing these measurements for NMR on the CT of an isotope with $I \geq \frac{3}{2}$, this ratio is $\Delta P_N^{\text{InvNMR}}/\Delta P_N^{\text{Sat}} > \left(I+\frac{1}{2}\right)^3$ [151]. For the GaAs QDs mainly used in this thesis, all isotopes have a nuclear spin $I = 3/2$; this means the InvNMR would give eight times larger total change in total polarisation than ODNMR.

The InvNMR waveform has an 'inverse' shape to that of saturation NMR, as shown in Figure 3.13. Rather than a single excitation band which depolarises nuclei in a frequency span, w_{exc}, there are two excitation bands with a small gap, w_{gap}, in between. The total width of w_{exc} is large enough to fully depolarise all the nuclear spin transitions of a given isotope (usually $\approx$ 1.5 MHz in our GaAs QDs), when centred on its CT frequency. However, any nuclear transitions that occur within the gap of the RF waveform are left in their polarised state, thereby creating a large differential signal.

The width of the gap can be chosen to either maximise the InvNMR spectral resolution or the signal strength. This is shown in Figure 3.14. In this figure, the InvNMR data of the CT has been fitted with a unit box convolved with a Gaussian distribution. This form is chosen because, as the gap size increases the CT signal amplitude saturates, as all the nuclei within this $-\frac{1}{2} \leftrightarrow \frac{1}{2}$ transition are kept in a polarised state. The maximum InvNMR signal is a differential between two different nuclear polarisation states. The first of these is when the nuclei are in a polarised state, due to the optical pumping, with no RF applied. The second is when there has been RF

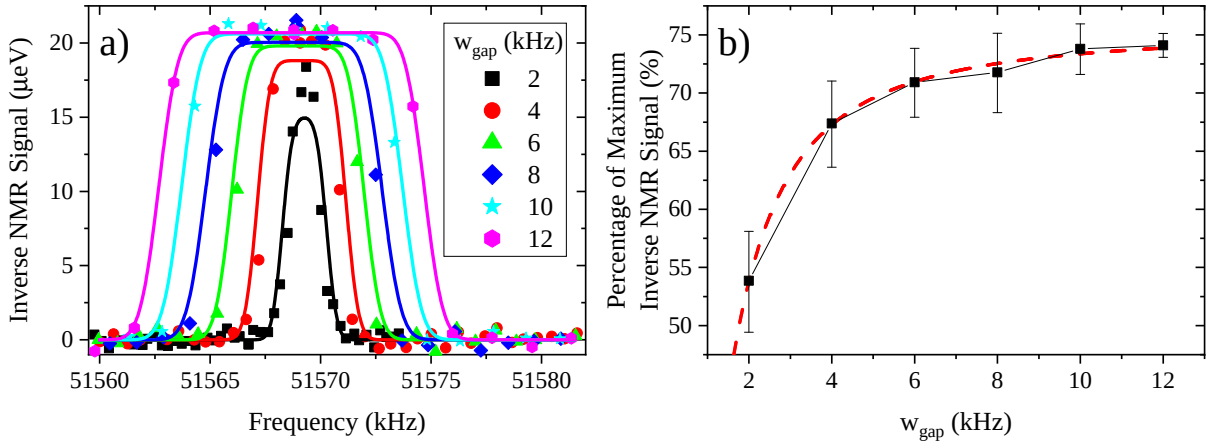

Figure 3.14: InvNMR data obtained by varying w_{gap} around the CT of ^{75}As nuclei in a QD at 4.2 K with an external field of 7.01244 T. These measurements were kindly performed by George Gillard on a separate experimental setup using an externally strained QD sample, as to not incorporate any broad components of STs, which was not used in this thesis. a) Convolution of a unit box with a Gaussian function to fit the InvNMR data. b) Percentage of the maximum InvNMR signal achieved for the varying gap sizes shown in (a). The dashed red line represents an empirical fit of the data.

saturation with a broadband signal and no gap, resulting in all the nuclei in the waveform's bandwidth depolarising. The differential of these two states describes the maximum possible signal in a measurement.

Let it be clear that this maximum possible NMR signal does not describe the maximum DNP possible or that there is a polarisation degree of ± 1, but simply the maximum InvNMR signal possible in the current configuration. If the pumping conditions, for example, were changed then this maximum NMR signal would also change. This percentage of the maximum signal is shown in Figure 3.14b as a function of w_{gap}. It can be seen that increasing the gap width increases the maximum signal possible, however it eventually plateaus out. The empirical fit shows that in order to reach 95% of the maximum signal, for the CT in this measurement, the value of w_{gap} should be 6.6 kHz. In reality a full calibration of gap width and maximal signal is rarely performed. Typical values of w_{gap} are chosen to be 6 kHz for measuring both the STs and CT in a single spectrum and then a higher resolution 2 kHz spectrum is taken for just the CT. However, in some measurements where the InvNMR signal itself is too weak, for example for a non-abundant isotope in the QD, the gap size must be increased, decreasing the maximal resolution possible.

Chapter 4

Strain and Disorder in AlGaAs

If one wanted to use electrons as spin qubits, it is imperative to ensure that their coherence times are sufficiently long for practical applications. To extend these electron spin qubit lifetimes, the strain inhomogeneity of the QD needs to be reduced. However, knowledge of the strain of the system is difficult to characterise. Inhomogeneous strain results in broadening of the nuclei precession rates, due to changes in the local fields. Through the hyperfine interaction between an electron and this broadened nuclear environment, there is a decrease in spin coherence times [30, 125, 131, 155, 163, 180–183]. It is therefore important to be able to characterise the strain within QDs, to understand whether it would be appropriate to use them as a source for spin qubits.

The following chapter examines a variety of QDs, with varying chemical compositions, to determine the appropriateness to electron spin qubits. All QDs are grown via nanohole infilling, as opposed to the Stranski-Krastanov method, to minimise strain. GaAs/AlGaAs QDs serve as the base system, to which small amounts of Al or In are added to provide a detailed understanding of the strain effects. The strain of QDs has been investigated using a combination of InvNMR and the integral saturation NMR technique. The breadth and magnitude of the quadrupolar splittings, to the first order, are analysed. The work then expands upon this by using a Monte-Carlo simulation to identify the strain distribution present within the QD.

We derive the mean major strain within $Al_xGa_{1-x}As$ QDs to be 0.023%, 0.031%, and 0.039% for $x = 0\%$, 5%, and 10%, respectively. The incorporation of Al into the QDs results in inhomogeneous quadrupolar broadening of the NMR spectra. For $Al_{0.1}Ga_{0.9}As$ QDs, the broadening is approximately 0.3 MHz, while for $In_{0.1}Ga_{0.9}As$ QDs, the broadening is more pronounced due to the larger lattice constant mismatch, increasing to 2 MHz.

The work presented in this chapter has been written as a draft manuscript. In this work the NMR experiments were conducted by Peter Millington-Hotze and Evgeny Chekhovich. The simulations were conducted by Peter Millington-Hotze, with advice from Evgeny Chekhovich. The samples were grown by Santanu Manna, Saimon F. Covre da Silva and Armando Rastelli.

Strain and disorder effects in AlGaAs

Peter Millington-Hotze,[1] Santanu Manna,[2,3] Saimon F. Covre da Silva,[2] Armando Rastelli,[2] and Evgeny A. Chekhovich[1,4,*]

[1] *School of Mathematical and Physical Sciences, University of Sheffield, Sheffield S3 7RH, United Kingdom*
[2] *Institute of Semiconductor and Solid State Physics, Johannes Kepler University Linz, Altenberger Str. 69, 4040 Linz, Austria*
[3] *Present address: Department of Electrical Engineering, Indian Institute of Technology Delhi, New Delhi, 110016, India*
[4] *Department of Physics and Astronomy, University of Sussex, Brighton, BN1 9QH*

(Dated: December 12, 2024)

We use optically detected nuclear magnetic resonance (NMR) to non-invasively probe the strain within pure GaAs, $Al_xGa_{1-x}As$, and $In_yGa_{1-y}As$ quantum dots (QDs) embedded in $Al_zGa_{1-z}As$ barriers with $z = 0.3$ and $z = 0.33$ Increasing Al content x (from 0 to 10 %) or In content y (from 0 to 10 %) results in elastic strains, which manifest through inhomogeneous quadrupolar broadening of the single-QD NMR spectra. Since both the Al and In isovalent dopants replace atoms only in the Ga sublattice, the quadrupolar shifts are more pronounced for the ^{75}As nuclei. The maximum strain induced by an isolated Al dopant in a pure GaAs matrix is found to be ≈ 0.3 MHz. This value, found in a high-quality crystal lattice of an epitaxially-grown QD, is a significant revision of the previous estimates tens of MHz derived from NMR on powderized AlGaAs samples. We further examine internal strains in QDs embedded in optical microcavities formed by $Al_{0.95}Ga_{0.05}As/Al_{0.2}Ga_{0.8}As$ Bragg reflectors, finding a reduced mean strain but a similar inhomogeneous strain broadening. Our studies establish the properties of unit-cell-scale strains in the alloys formed by ubiquitous group III-V semiconductors, including GaAs, InAs, and AlAs. Understanding of the alloying effect parameters is crucial for future developments of QD-based devices where internal strains have recently been shown to limit the purity of the quantum light sources and coherence of the spin qubits.

I. INTRODUCTION

Strained semiconductor nanostructures have the possibility for quantum logic devices [1, 2]. However, a comprehensive understanding of the strain distribution within quantum dots (QDs) is essential for their effective application in quantum logic gate operations. This is particularly crucial as the strain distribution significantly influences the coherence time of electron spin qubits [3–11]. Moreover, the nanoscale variation of strain has been found to reduce the efficacy of dynamical decoupling methods [5, 7, 12]. Thus, a thorough investigation into the spatial distribution and magnitude of strain in semiconductor nanostructures is imperative for advancing the development and functionality of quantum logic devices.

Tunneling electron microscopy and atomic force microscopy techniques have previously been employed to measure the strain of QDs by assessing lattice mismatches between the QD and its surrounding barrier [13, 14]. However, determining the distribution of strain within the QD presents a more formidable challenge. Nuclear magnetic resonance (NMR), a well-established method for non-invasive QD probing [6, 15–19], could potentially address this challenge. Previous NMR studies have focused on AlGaAs samples, although in powdered form and with an emphasis on local ordering rather than strain characterization [20–22]. However, this method introduces additional strain, further complicating the understanding of strain distribution.

Here we investigate a variety of QD samples, without pulverizing them, including: $GaAs/Al_{0.3}Ga_{0.7}As$, $Al_xGa_{1-x}As/Al_{0.33}Ga_{0.67}As$ QDs with $x = 5\%$ and 10%, GaAs/AlAs, $In_{0.1}Ga_{0.9}As/Al_{0.33}Ga_{0.67}As$, $Al_{0.05}Ga_{0.95}As/Al_{0.329}Ga_{0.667}In_{0.004}As$, as well as a $GaAs/Al_{0.33}Ga_{0.67}As$ microcavity sample using optically detected NMR techniques. The array of samples included in this study offers a comprehensive overview on the impact of additional isotopes in QDs. Due to this diversity, this paper will be arranged to focus on each sample in turn.

II. SAMPLES AND EXPERIMENTAL TECHNIQUES

All of the QDs studied in this paper were grown via molecular beam epitaxy, using nanohole infilling to create the QDs. The typical QD dimensions are ~ 40 nm in diameter and ~ 7 nm in depth. More information regarding the growth is given in Supplementary Information Section 1. Faraday geometry, where the direction of the static external magnetic field is parallel to the optical axis, is used for all of the experiments in this paper. The samples are kept at 4.2 K within a liquid helium bath cryostat. A small copper coil is mounted close to the sample, which is used to produce a radiofrequency (RF) oscillating magnetic field perpendicular to the static magnetic

* E.Chekhovich@sussex.ac.uk

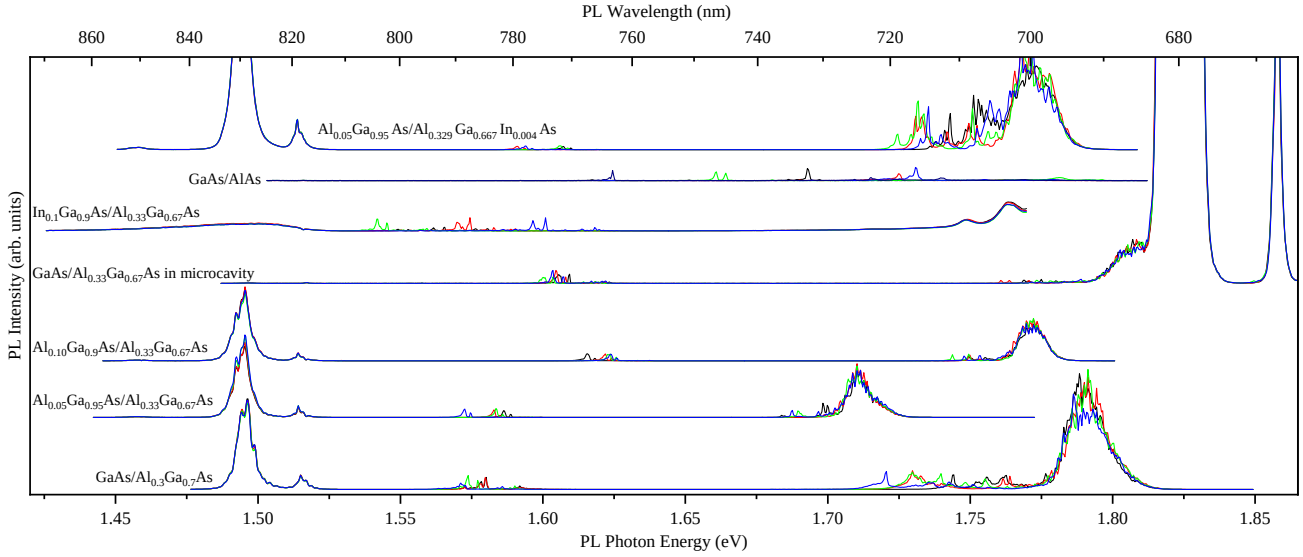

FIG. 1. PL spectra of randomly selected QDs from all samples used in this paper. All spectra were taken using a single-stage grating spectrometer, while the sample was at 4.2 K and with no external magnetic field applied.

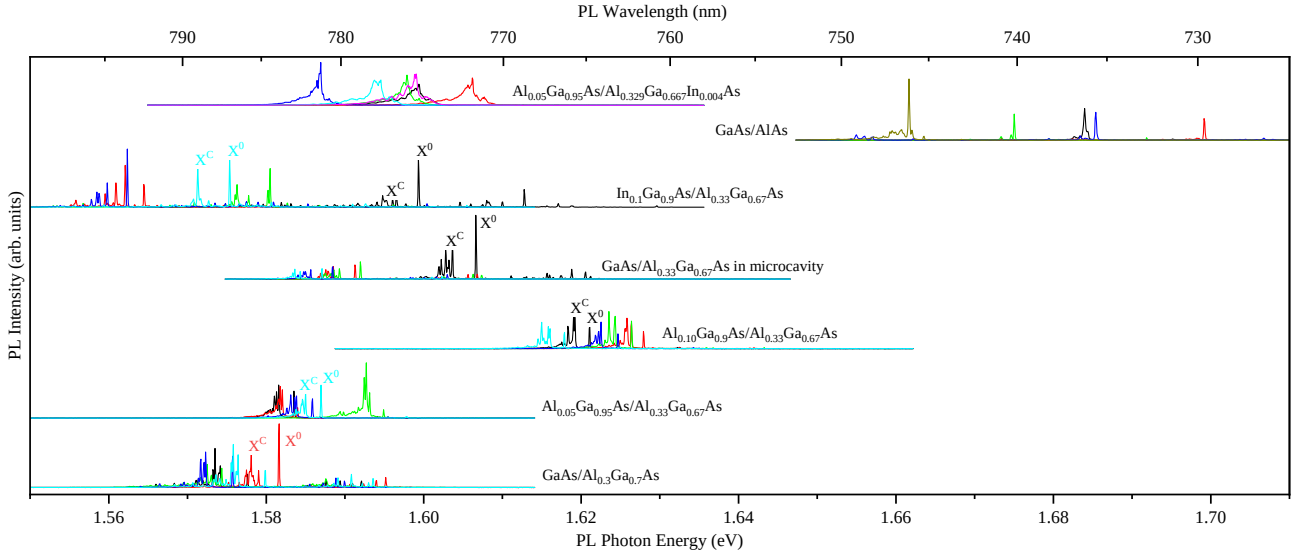

FIG. 2. PL spectra of randomly selected QDs from all samples used in this paper. All spectra were taken using a single-stage grating spectrometer, while the sample was at 4.2 K and with no external magnetic field applied. This figure has reduced the spectral range to focus on the QD region of Fig. 1, while using a higher resolution spectrometer grating. The neutral exciton, X^0, and multi-charged states, X^C, are labeled on representative spectra per sample where identifiable.

field. A confocal microscopy configuration is used, where a QD is optically excited and its photoluminescence (PL) collected through an aspheric lens with a focal distance of 1.45 mm and numerical aperture of 0.58. The collected PL is dispersed in a two-stage grating spectrometer and recorded with a charge-coupled device (CCD) camera.

PL spectra of randomly selected QDs from the samples are shown in Figs. 1 and 2. Fig. 1 shows the signatures of the bulk GaAs, quantum wells (QWs), and QDs. The bulk GaAs emission can clearly be seen at $\sim$ 830 nm. The efficacy of the microcavity which contains $GaAs/Al_{0.33}Ga_{0.67}As$ QDs is shown by the enhanced emission of the QDs and QWs. The emission wavelength of all the QDs from the samples, with the exception of the GaAs/AlAs sample, is between 760-800 nm. Within the higher spectral resolution shown of the QDs in Fig. 2, one can see a $\sim \pm 3$ nm spectral range that QDs were visible at for the majority of the samples. A trend is seen

where the addition of ^{27}Al dopants into the QD causes the spectra to blueshift, consistent with previous findings [23]. These spectral shifts confirm the incorporation of dopants into the QDs.

To perform optically detected NMR, one must first polarize the initially unpolarized nuclear ensemble, to create spectral contrast. This polarization process involves using a circularly polarized pump laser to generate spin polarized electrons within the QD. In III-V semiconductors the polarization of the electron's spin is dictated by the helicity of the polarized pump light, due to strict optical selection rules [4]. Subsequently, the electron's spin interacts with a nuclear spin via the hyperfine interaction. These electron-nuclear flip-flops generate dynamic nuclear polarization (DNP) [18]. The build-up of nuclear spin polarization generates an additional magnetic field, from the static external field, which alters the spectral splitting, ΔE_{PL}, of a negatively charged trion (X^-). This trion is optically probed to measure the average nuclear polarization of the $\sim 10^5$ QD nuclei. The pump laser wavelength and power, as well as the probe time, are calibrated to maximize the DNP measured from the QD, as explained in Ref. [19].

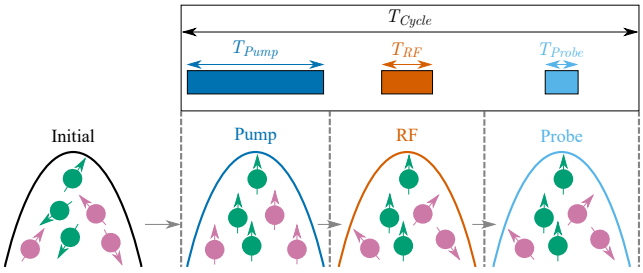

FIG. 3. The pump-RF-probe cycle used for NMR experiments. The nuclear spin ensemble is initially depolarized. A circularly polarized pump laser is employed, for a time T_{Pump}, to generate spin polarized electrons which produce nuclear spin polarization. RF is then applied to selectively depolarize nuclei. The time of this RF burst is chosen to effectively depolarize all the nuclei transitions, within the frequency bandwidth, without applying excess heat to the sample. Finally, a probe laser is used to measure the spectral splitting of the X^- trion. The probe time selected is a compromise between PL intensity and the parasitic depolarization caused by the laser.

The nuclear isotopes in this work are quadrupolar (nuclear spin $> 1/2$), so they are sensitive to variations in the electric field gradient (EFG), e.g. due to strain. In this work we use both integral saturation NMR and the 'inverse' NMR signal amplification technique [15], whose waveforms are shown in Fig. 4, to observe these strain effects. The integral saturation measurement works similarly to optically detected NMR techniques. However, rather than using a fixed excitation bandwidth that is scanned across a span of frequencies, a variable size bandwidth, $\mathrm{w_{exc}}$, is used. $\mathrm{w_{exc}}$ is centered on the $-1/2 \leftrightarrow +1/2$ central transition (CT) of an isotope and its width is varied symmetrically. As the

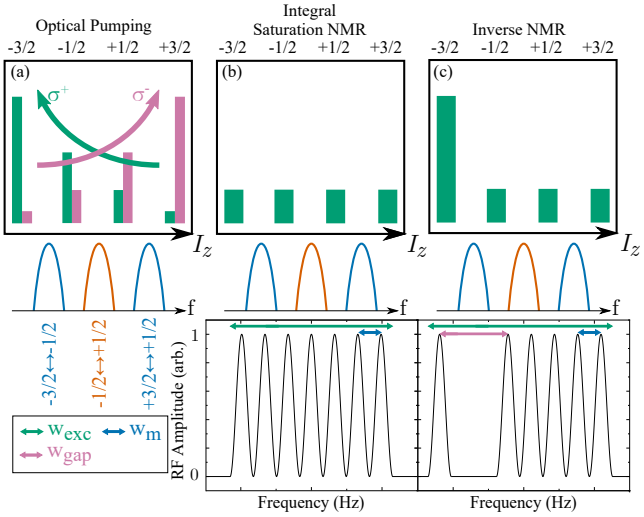

FIG. 4. (a) Polarization of nuclear spins due to optical pumping on nuclei with 3/2 spin. After this polarization has occurred a RF waveform is applied. The nuclear spin polarization states and the RF spectral shape, with individual comb modes visible, is shown for (b) Integral saturation NMR, (c) Inverse NMR.

breadth increases more nuclei (transition states) become saturated, increasing the contrast in hyperfine shift to that of a polarized nuclear spin ensemble. However, with the inverse NMR measurement the excitation bandwidth remains constant, and has enough breadth to fully depolarize all nuclear transitions of a selected isotope. A frequency gap, $\mathrm{w_{gap}}$, is present within this waveform, and its position is adjusted so that specific nuclear transitions remain polarized. Further details of this inverse technique can be found in Ref. [15]. The integral saturation technique allows for the broad spectral components to be determined, however it is not effective at detecting sharp spectral features or the quadrupolar splitting, which the inverse technique can resolve. By using the complementary NMR procedures more information can be extracted about the strain present in the QDs.

III. NMR EXPERIMENTS ON QUANTUM DOTS

A. GaAs/$\mathrm{Al_{0.3}Ga_{0.7}As}$ QDs

GaAs is a widely used III-V semiconductor material for QDs. This is attributed to its exceptional optical properties and capability to generate low intrinsic strain QDs, facilitated by its lattice matching with $\mathrm{Al}_z\mathrm{Ga}_{1-z}\mathrm{As}$ barriers [8, 24, 25]. These GaAs QDs will be the basis of comparison for the rest of the samples in this paper, as one can picture the other samples as having additions made to this base configuration. The inverse NMR spectra of ^{75}As and ^{69}Ga in Figs. 5(a) and 5(b) show well defined satellite transitions (STs) with a quadrupo-

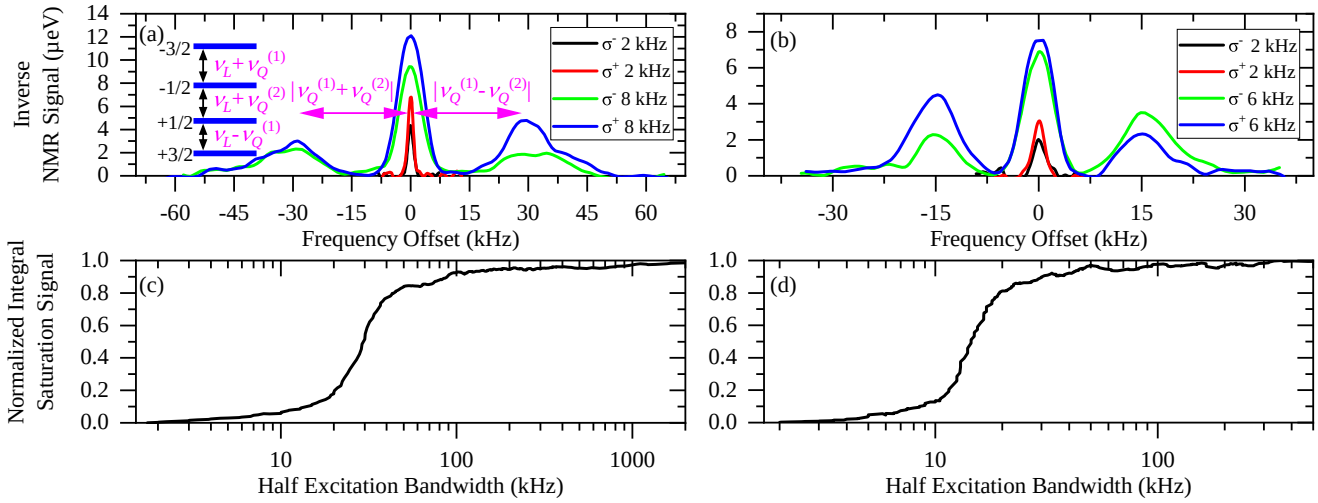

FIG. 5. Inverse NMR conducted at 2.87 T on a GaAs QD for (a) ^{75}As (b) ^{69}Ga isotopes. The central transition (CT) NMR spectra had a w_{gap} of 2 kHz, the broad spectra used 8 kHz and 6 kHz for ^{75}As and ^{69}Ga respectively. In (a) the first and second order quadrupolar shifts are denoted by $\nu_Q^{(1)}$ and $\nu_Q^{(2)}$ respectively. The first-order quadrupolar contribution exhibits at least an order of magnitude larger shift than the second-order contribution. For this reason the approximation $\nu_Q \approx \nu_Q^{(1)} \pm \nu_Q^{(2)}$ is often used. Next to this spectra is a sketch showing the nuclear spin states with their labeled transitions, with the Larmor frequency denoted as ν_L. (c) Integral saturation NMR conducted at 2.87 T using a σ^+ polarized pump on (c) ^{75}As (d) ^{69}Ga.

lar splitting magnitude, $|\nu_Q|$, of ~ 30 kHz and ~ 15 kHz respectively, matching similar QD samples [16]. This splitting indicates the presence of uniaxial strain in the sample, where greater separations reflect larger magnitudes of strain [26]. A large quadrupolar splitting can be useful in nuclear spin quantum registers for quantum computing, such as in [24], however the stress is usually applied externally. The integral saturation NMR spectra, shown in Figs. 5(c) and 5(d), show that the nuclear transition states are 90% saturated with $\frac{w_{exc}}{2} \approx 90$ kHz and 30 kHz for ^{75}As and ^{69}Ga respectively. There is broadening spanning up to 1 MHz for ^{75}As, similar to the presence of a broader pedestals seen previously [11]. This signal, if real, is incredibly weak, only comprising < 3 μeV, close to the noise of the measurement technique.

B. $Al_xGa_{1-x}As/Al_{0.33}Ga_{0.67}As$ QDs

Now that we have introduced our base configuration of GaAs QDs, we can investigate the effect of adding other elements. The first we shall try is the addition of ^{27}Al, which will ensure that the QDs are still lattice matched with AlGaAs barriers. The literature on $Al_xGa_{1-x}As$ has mainly focused on the ordering parameter and stringing, where 'strings' of atoms line up along low-indexed crystallographic directions, of ^{27}Al atoms with varying concentrations [20–22, 27–29]. Among the studies that employed some form of NMR [20–22], the samples were AlGaAs thin films. These films were fabricated using metalorganic vapour-phase epitaxy (MOVPE) and often powdered. There are a couple of issues of determining the strain in these systems. As MOVPE is inherently conducted in a non-vacuum environment, an increased risk of impurities exists during the growth procedure. This may lead to dislocations or point defects in the sample [30], which would also contribute to strain. The samples in this study are grown via molecular beam epitaxy (MBE) with nanohole filling, to avoid this complication. The act of powderization, as performed in previous work [20–22], adds mechanical defects into the lattice, which are indistinguishable from any inherent strain caused by the addition of ^{27}Al, hence the samples used here do not undergo this procedure. Previous works have seen broad spectral NMR components, that span into the MHz range [21, 22]; detecting these using inverse NMR would be challenging due to their weak signal, therefore we compliment the inverse technique with integral saturation NMR.

Fig. 6 shows NMR spectra comparison between varying levels of ^{27}Al concentration in Al_xGa_{1-x} QDs. In Figs. 6(a) and 6(b), it is clear that the addition of ^{27}Al into the QDs increases the total breadth of the spectra. For ^{75}As (^{69}Ga) this increase is from 55 kHz (30 kHz) to 300 kHz (70 kHz). The extent of the broadening can be seen in Figs. 6(c) and 6(d); to obtain half the total saturated signal $\frac{w_{exc}}{2}$ increased from 30 kHz to 44 kHz and then to 65 kHz for the 0%, 5%, and 10% concentrations respectively.

As nearest neighbour interactions are the dominant influence for nuclei, one would expect ^{75}As to have an increased sensitivity to strain, compared to ^{69}Ga, to the ^{27}Al concentration. This is because ^{27}Al atoms replace the $^{69/71}$Ga atoms in the lattice. The $^{69/71}$Ga atoms will be surrounded by four nearest neighbors of ^{75}As, while

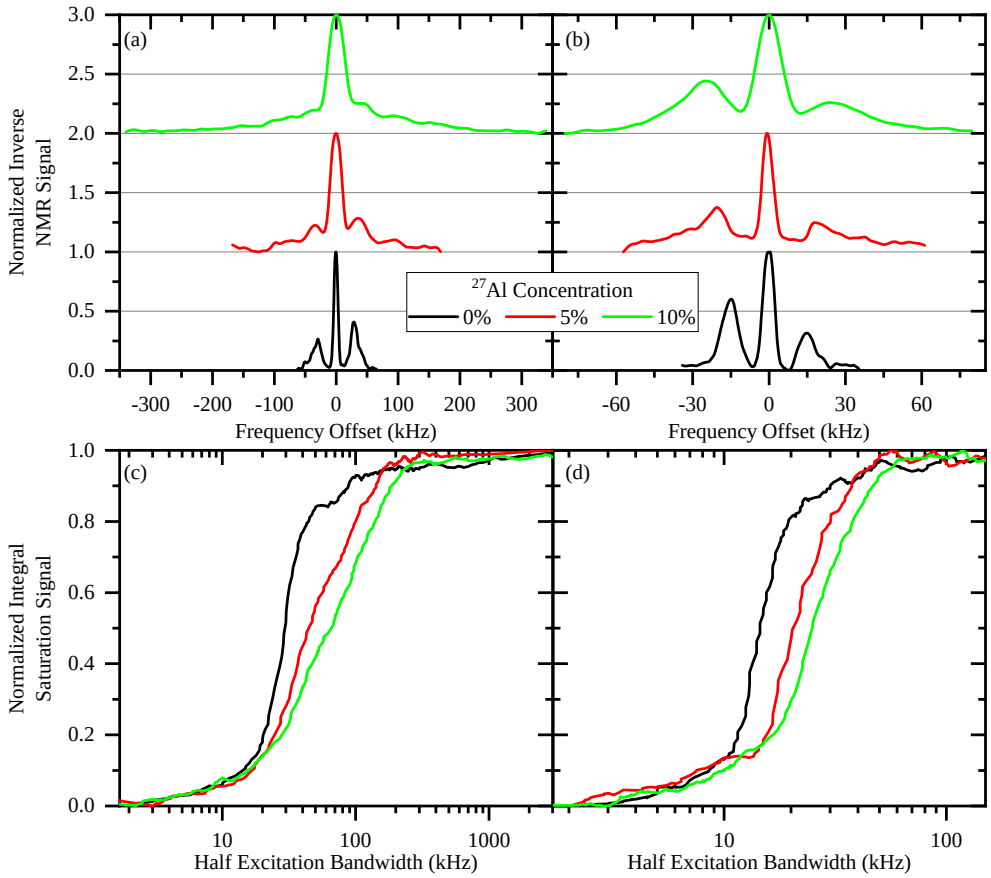

FIG. 6. Inverse NMR conducted at 2.87 T on differing concentrations of ^{27}Al in Al_xGa_{1-x} QDs on (a) ^{75}As (b) ^{69}Ga. w_{gap} was set to be 8 kHz, 20 kHz and 30 kHz in (a) and 6 kHz, 6 kHz and 12 kHz in (b) for the 0%, 5% and 10% concentrations respectively. All optical pumping was σ^+. Integral saturation NMR conducted at 2.87 T using a σ^+ polarized pump on differing concentrations of ^{27}Al in Al_xGa_{1-x} QDs on (c) ^{75}As (d) ^{69}Ga.

^{75}As will be surrounded by either $^{69/71}$Ga atoms or ^{27}Al if Ga has been replaced. This increased sensitivity to strain is confirmed by the more pronounced broadening observed in the NMR spectra for ^{75}As compared to ^{69}Ga in Fig. 6. If we examine the concentrations of ^{27}Al, x, within these QDs, we can derive the likelihood of each nucleus having n ^{27}Al nearest neighbors:

$$P_{\text{Occurrence}} = \frac{4!}{n!(4-n)!}x^n(1-x)^{4-n}. \quad (1)$$

Eq. 1 assumes that each occupational site is equally likely to be filled, i.e. that no stringing/ordering occurs, which may not be the case as mentioned previously. However, even with this limitation, it gives an approximation of the probability that n nearest neighbors are replaced with ^{27}Al. The results from this approximation are shown in Tab. I. Since NMR samples nuclei within the QD (weighted by the electron density), these probabilities will reflect the actual proportion of ^{27}Al nearest neighbors for the nuclei in the spectra. Due to the low probability of two or more neighboring atoms, it must be the case that the majority of the nuclei have zero or one nearest neighbor; this means that the resultant of any strain mechanics occurs on an atomic scale. A simulation of the $Al_xGa_{1-x}As$ QDs was developed to investigate the distribution of strain in the QD, which is discussed in Section IV A.

Concentration of ^{27}Al (%)	Probability of n ^{27}Al Nearest Neighbors (%)				
	$n=0$	$n=1$	$n=2$	$n=3$	$n=4$
5	81.450625	17.1475	1.35375	0.0475	0.000625
10	65.61	29.16	4.86	0.36	0.01

TABLE I. Probability of n ^{27}Al nearest neighbors where the ^{27}Al concentration in the QDs is 5% and 10%, as calculated from Eq. 1.

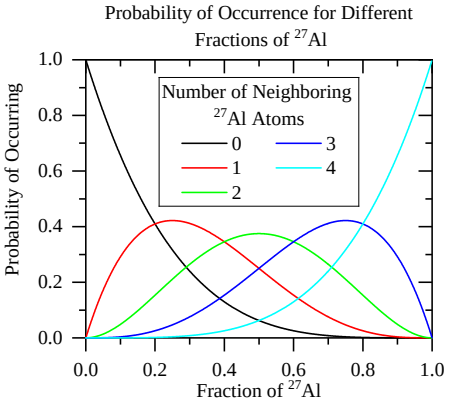

FIG. 7. Probability of occurrence for zero to four nearest neighbors in a zinc-blende structure. The QDs used in this paper are in the 0 to 0.1 concentration range for the fraction of ^{27}Al. This results in the majority of configurations having zero neighbors with a non-negligible contribution from a single nearest neighbor.

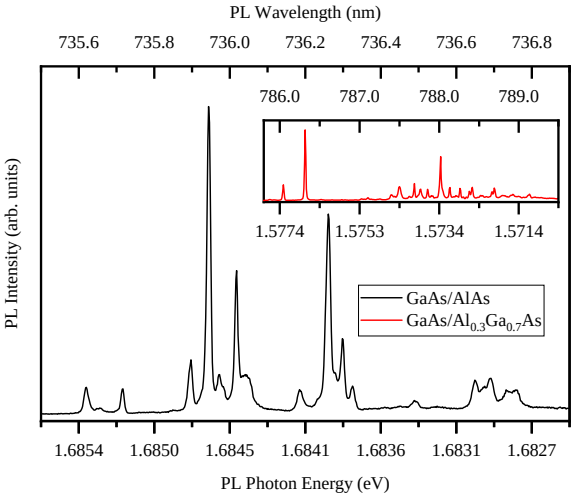

FIG. 8. PL spectra of a GaAs/AlAs QD at 4.2 K with an external magnetic field of 8 T using a 690 nm probe laser. The inset figure shows a GaAs/$Al_{0.3}Ga_{0.7}$As QD spectra also at 4.2 K and with an 8 T field, but using a 645 nm probe. The difference in probe laser is to maximise the PL signal from the dot.

C. GaAs/AlAs QDs

To investigate the effect of diffusion between the QD and the barrier, a GaAs/AlAs sample was produced. As there is no Ga in the barrier, there is a greater lattice mismatch between the QD and the surrounding barriers, given that the lattice constants follow the sequence GaAs < AlGaAs < AlAs. Upon initial probing of the QDs on this sample, the disparity observed in PL spectra, compared to the GaAs QDs with AlGaAs barriers or AlGaAs QDs, was striking. This is shown in Fig. 8. In the GaAs QD with $Al_{0.3}Ga_{0.7}As$ barriers there is a clear exciton doublet at $\sim$ 786.2 nm. At longer wavelengths, spectrally separated from the exciton, there are multi-charged states. However, for the AlAs barrier QDs there was no spectral separation between excitons and the charged states. We were also unable to identify the different charge states of the QD, through the usual processes of varying excitation power or applied bias. A wider spectral range, extending from 650 nm to 820 nm, was employed to explore multiple QDs and validate whether this observation was unique, but all QDs seen showed similar PL signatures with emission occurring at $\sim$ 736 nm. Within this charged state amalgam, there are some PL lines that were responsive to nuclear polarization. However, the maximum hyperfine shift obtained was $\sim$ 40 μeV, which is approximately half of that obtained with the other samples used in this paper. Similar to the PL spectra, multiple QDs were measured and they all displayed consistently low levels of hyperfine shifts. It is impossible to determine whether these issues are specific to the individual sample or are inherent to the AlAs barriers, as only one sample was available for analysis.

An example of the inverse NMR spectra for ^{75}As from a GaAs/AlAs QD is shown in Fig. 9. Even though a relatively large gap width of 14 kHz was used to measure the spectra, the CT amplitude is only $\sim$ 5.5 μeV, which is half that in GaAs/$Al_{0.3}Ga_{0.7}As$ QDs studied with a 6 kHz gap size. It is also visible that $|\nu_Q|$ is larger for the AlAs barrier QD as compared to the GaAs/$Al_{0.3}Ga_{0.7}As$, which is indicative of a larger magnitude strain present in the dot. Due to the low signal amplitude, it was not possible to determine whether there are any spectrally broad components, using the inverse NMR technique.

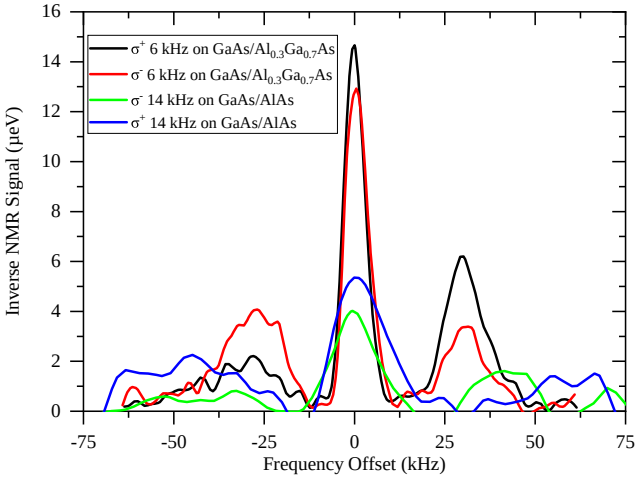

FIG. 9. Inverse NMR spectra of ^{75}As on AlAs and GaAs QDs at 4.2 K with an external magnetic field of 8 T. w_{gap} was set to 14 kHz and 6 kHz for AlAs and GaAs spectra respectively.

D. $In_{0.1}Ga_{0.9}As/Al_{0.33}Ga_{0.67}As$ QDs

Thus far in this paper, the chemical composition of the QDs have been nearly lattice matched with the barriers, to ensure that there is minimal strain within the dot. The lattice constant difference between GaAs and AlAs, at cryogenic temperatures, is only approximately 0.138% [31–34], hence why it is often highlighted as an asset [16, 24, 25, 35–38]. However, InGaAs QDs, which have been used historically due to favorable traits for Stranski–Krastanov growth, have a larger lattice mismatch, 7% in the case of InAs/GaAs [4].

The consequence of this large lattice constant difference is visible in Figs. 10 and 11. These figures also demonstrate the significance of integral saturation NMR in complementing the inverse technique. In the ^{75}As inverse NMR spectra, the spectral broadening spans $\pm$350 kHz before the signal decreases to approximately background noise. However, in the integral saturation technique, the NMR signal increases even with full RF bandwidths above 2 MHz. This is a significant increase, for both ^{75}As and ^{69}Ga, compared to the GaAs or even AlGaAs QDs discussed previously. For the $Al_{0.1}Ga_{0.9}As$ QDs, achieving half the maximum integral saturation NMR signal, i.e. the median quadrupolar shift, required a $\frac{w_{exc}}{2}$ of 65 kHz (25 kHz) for ^{75}As (^{69}Ga), while for these $In_{0.1}Ga_{0.9}As$ QDs it is 217 kHz (122 kHz). This is attributed to the significantly larger contrast in lattice differences. The breadth of the NMR spectra is not as wide as in $In_{0.2}Ga_{0.8}As$ QDs, where a MHz breadth is common [15, 39]. Hence, similar to the effect observed with the inclusion of ^{27}Al, elevated concentrations of adjuncts worsen the broadening of spectra due to the strain they induce.

E. $Al_{0.05}Ga_{0.95}As/Al_{0.329}Ga_{0.667}In_{0.004}As$ QDs

As seen in Section III D, it was shown that the large lattice difference of ^{115}In within the QD causes significant broadening. The question arises, does this broadening occur only if the dopant is within the QD, or does the barrier's composition result in similar spectra. To examine this, we use $Al_{0.05}Ga_{0.95}As/Al_{0.329}Ga_{0.667}In_{0.004}As$ QDs, i.e. dots with a small concentration (0.4%) of ^{115}In within the barrier. If intermixing occurs between ^{115}In in the barrier and the QD, we anticipate results similar to those observed for InGaAs QDs. Conversely, if this alloying is negligible, the NMR lineshapes would resemble those of $Al_{0.05}Ga_{0.95}As/Al_{0.33}Ga_{0.67}As$ QDs. The results from the inverse and integral saturation NMR are shown in Fig. 11. In Fig. 11(a) the inverse spectra are near identical for QDs with and without the ^{115}In present in the barrier; one might argue that the higher-order peaks (absolute frequency offsets from the CT $>$ 50 kHz) exhibit a larger amplitude in the ^{115}In barrier case. However, this variation can be attributed to differences between individual QDs. To complement this reasoning, when analyzing the integral saturation NMR spectra in Fig. 11(b), it can be seen that there are no significant differences between the spectrally broad components. This does not mean that there is no intermixing with ^{115}In in the barrier. However, any intermixing effects are minimal in comparison to the introduction of ^{27}Al in $Al_{0.05}Ga_{0.95}As$ QDs.

F. $GaAs/Al_{0.33}Ga_{0.67}As$ QDs Embedded in Distributed Bragg Reflector Microcavities

One way to aid in the coupling of the QD excitons to the optical modes, as well as increasing the emitted PL, is to use a distributed Bragg reflector (DBR) [40, 41]. The DBR is made by alternating layers of differing refractive index (in this sample $Al_{0.95}Ga_{0.05}As$ and $Al_{0.2}Ga_{0.8}As$), which act as mirrors. These DBRs are grown both below and above the QDs, to construct a microcavity, but the number of layer pairs above the QDs is reduced to allow for the transmission of light out of the sample. Microcavities and DBRs are advantageous for various applications of QDs; however, NMR studies of strain using microcavities have been limited to InGaAs QDs [15, 42, 43]. Given the broad spectral components of InGaAs QDs [15, 39], any strain effects due to the introduction of the microcavity would be obscured. In this paper we use $GaAs/Al_{0.33}Ga_{0.67}As$ nanohole infilled dots to ensure that the strain within the QD is minimal.

Figs. 12(a)-12(c) show a significant deviation in the inverse NMR lineshape compared to the data from Fig. 5, which is shown in Fig. 12 as the purple lines. The expected spectral triplet is replaced by a broad-tailed peak, with the tail appearing on the higher (lower) side of the Larmor frequency for σ^+ and σ^-pumped QDs in ^{75}As ($^{69/71}$Ga). In Fig. 5, where the quadrupolar triplet is fully resolved, the higher and lower frequency STs exhibit differing amplitudes due to the predominance of nuclear spin states with positive or negative I_z, depending on the sign of optical pumping. Therefore, the data in Figs. 12(a)-12(c) is particularly interesting because, unlike in Fig. 5, where these amplitude differences were polarization-dependent, the tails in these figures appear on the same side for both optical pumping signs across all isotopes. Furthermore, the inverse NMR spectra in Fig. 12 show that the signal reaches background noise levels at approximately 30 kHz for ^{75}As and 10 kHz for $^{69/71}$ Ga. This means that the magnitude of biaxial strain in the microcavity sample is smaller than in the $GaAs/Al_{0.3}Ga_{0.7}As$ QDs. Consequently, the lattice constant of the GaAs layer comprising the QDs is closer to that of bulk GaAs with the microcavity structure than without it.

One may consider that this lineshape is a result of the magnetic field direction. If the external magnetic field were aligned, relative to the growth direction, at the 'magic' NMR angle of approximately 54.7°, the STs would merge with the CT [26, 39]. However, the sam-

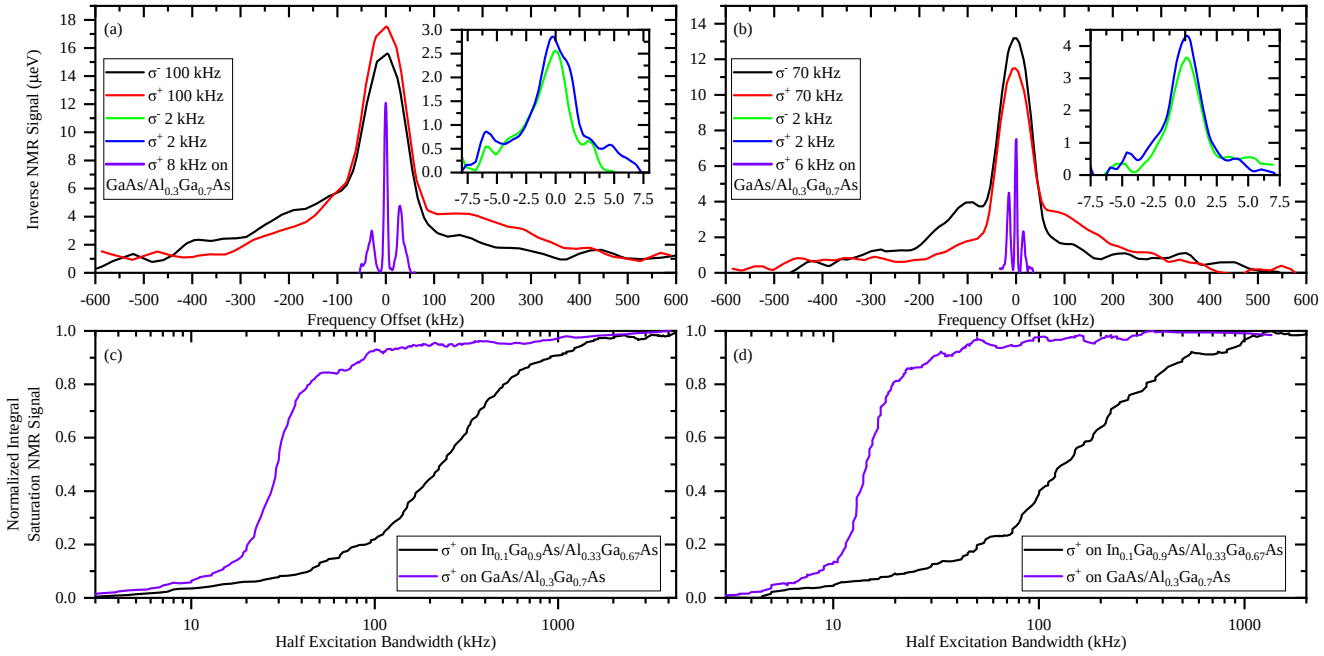

FIG. 10. NMR spectra on $In_{0.1}Ga_{0.9}As$ QDs at 4.2 K with an external magnetic field of 2.87 T. (a) Inverse NMR spectra on ^{75}As. The CT spectra were taken with $w_{gap} = 2$ kHz while the broad spectra used 100 kHz. (b) same as (a) but with ^{69}Ga and the broad spectra used $w_{gap} = 70$ kHz. (c) Integral saturation NMR on ^{75}As. (d) Same as (c) but for ^{69}Ga. In (a)-(d) the NMR measurements from the $GaAs/Al_{0.3}Ga_{0.7}As$ sample, with an external field of 2.87 T, have also been plotted in purple, to serve as a comparison.

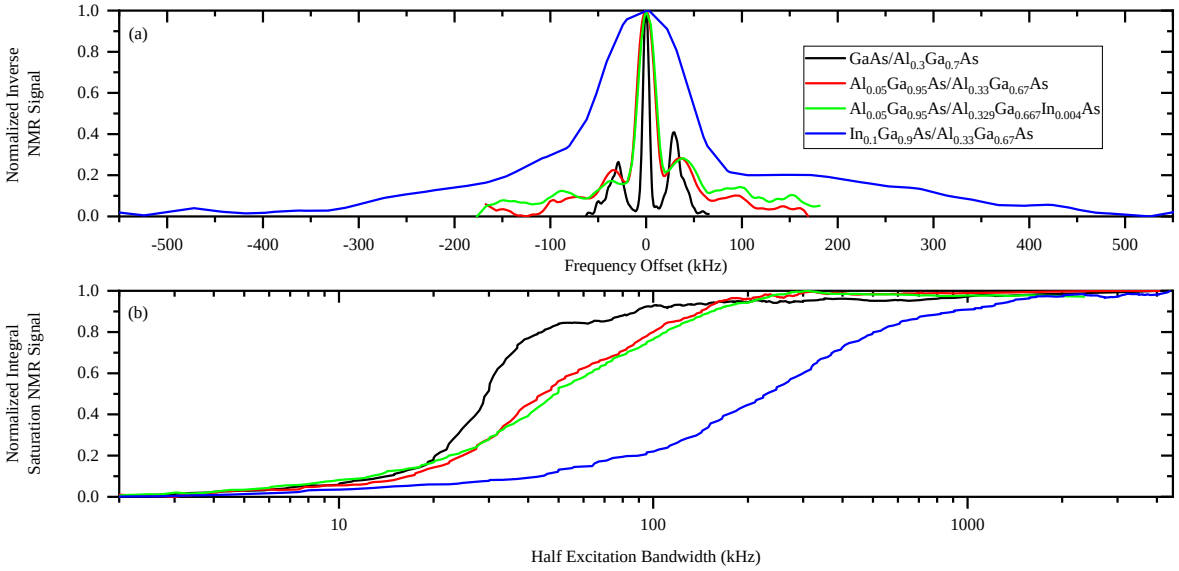

FIG. 11. Comparison of NMR spectra for: GaAs, $Al_{0.05}Ga_{0.95}As$ with and without ^{115}In in the barrier, and $In_{0.1}Ga_{0.9}As$ QDs, at 4.2 K with an external magnetic field of 2.87 T. (a) Inverse NMR spectra on ^{75}As. (b) Integral saturation NMR on the same QDs, also on ^{75}As.

ple is in the Faraday geometry, so this angle is approximately 0°. The magic angle hypothesis can also be dismissed as the one-sided broad-tailed lineshape means that the STs cannot just simply collapse into the CT, but must be spectrally on the same side of the CT. Moreover, in Fig. 12(d), the total excitation bandwidth necessary to completely saturate all nuclear transitions of ^{75}As amounts to hundreds of kHz. This span exceeds the linewidth of the CT observed in the pure $GaAs/Al_{0.3}Ga_{0.7}As$ QDs by two orders of magnitude,

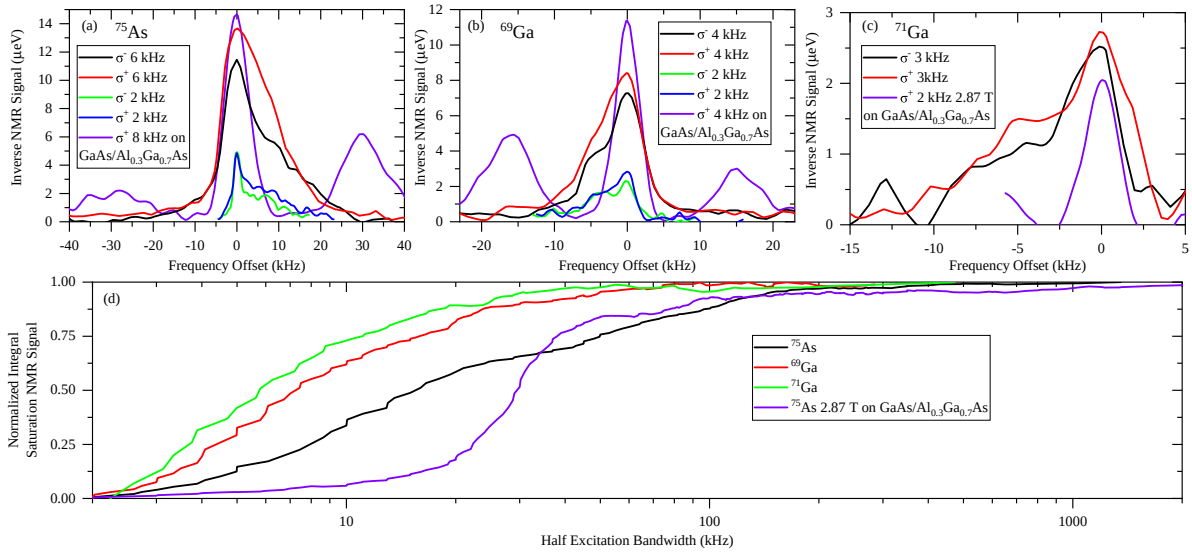

FIG. 12. NMR spectra of a GaAs QD within a microcavity at 4.2 K with an external magnetic field of 8 T. Inverse NMR spectra on (a) ^{75}As (6 kHz/2 kHz for the broad/CT spectra), (b) ^{69}Ga (4 kHz for the broad/CT spectra), (c) ^{71}Ga (3 kHz). (d) Integral saturation NMR on the three isotopes within the same QD as (a)-(c). In (a)-(d) the NMR measurements from the GaAs/Al$_{0.4}$Ga$_{0.6}$As sample, with an external field of 2.87 T, have also been plotted in purple, to serve as a comparison.

further suggesting that the STs have not merged with the CT. This broadening is usually a signature of inhomogeneous strain. However, strain inhomogeneity alone cannot simultaneously explain both the inverse and integral saturation NMR spectra.

One may consider that the DBR itself could be the source of strain for the QDs. According to Saint-Venant's principle, the effect of localized stress diminishes as one moves farther from the source of the stress, with the strain becoming negligible at distances significantly larger than the size of the stressed region. In this case, the separation between the QD layer and the nearest Al$_{0.95}$Ga$_{0.05}$As layer is approximately 120 nm. For the In$_{0.1}$Ga$_{0.9}$As/Al$_{0.33}$Ga$_{0.67}$As QDs, where spectrally separated transitions were observed in their inverse NMR spectra, the distance from QDs to the AlAs layer is approximately 200 nm. Since the QD size is around 40 nm, the distance to the Al$_{0.95}$Ga$_{0.05}$As (AlAs) layer is three (five) times the QD size for the microcavity (In$_{0.1}$Ga$_{0.9}$As/Al$_{0.33}$Ga$_{0.67}$As) sample. In both cases, the distance to the strain source is not comparable to, but significantly greater than, the size of the QDs. Therefore, the differences observed in the inverse NMR spectra cannot be categorically explained by the DBR alone. To further test this hypothesis, samples with larger or smaller cavity widths would be required. However, modifying this layer would also alter the stopband wavelength, necessitating further optimization.

IV. SIMULATION OF STRAIN IN AlGaAs QDs

From experimental results for QDs with differing ^{27}Al concentrations an estimation of the magnitude of strain that occurs in a QD can be deduced, as done in Ref. [15]. Taking the average ν_q values obtained in this study and applying the same methodology as in Ref. [15] with ^{69}Ga, we estimate the magnitude of average biaxial strains to be approximately 0.033%, 0.038%, and 0.052% for the Al$_x$Ga$_{1-x}$As samples with $x = 0$, 0.05, and 0.1, respectively. We can equally approximate the maximum magnitude of strain from the largest observed quadrupolar shift, which for ^{69}Ga was ≈ 85 kHz for the Al$_{0.1}$Ga$_{0.9}$As sample, to be 0.19%. However, to obtain a more precise strain distribution, a more sophisticated approach is necessary. Empirical modeling is employed to determine the statistical distribution of strain magnitudes within the QD volume that could account for the observed NMR spectra.

A. Simulation Setup

To reproduce the NMR spectra the Hamiltonian of the system must be defined. We define the external magnetic field, B, to be tilted away from the crystalline axis O_Z ([001]) by an angle θ. The in-plane component is along the line making the angle ϕ with the O_x ([100]) axis. The Zeeman Hamiltonian is then described by:

$$\mathcal{H}_Z = -\frac{1}{2\pi\hbar}\hbar\gamma \sum_{i=x,y,z} J_i B_i, \tag{2}$$

where J refers to the momentum operators of a spin-3/2 nuclei, and the $1/(2\pi\hbar)$ factor converts the Hamiltonian from energy into frequency units. The external magnetic field is also converted into NMR frequencies, ν_z. The gradient-elastic tensor, S_{ijkl}, is defined explicitly as:

$$S_{ijkl} = \left[\begin{bmatrix} S_{xxxx} & 0 & 0 \\ 0 & S_{xxyy} & 0 \\ 0 & 0 & S_{xxyy} \end{bmatrix} \begin{bmatrix} 0 & S_{yzyz} & 0 \\ S_{yzyz} & 0 & 0 \\ 0 & 0 & 0 \end{bmatrix} \begin{bmatrix} 0 & 0 & S_{yzyz} \\ 0 & 0 & 0 \\ S_{yzyz} & 0 & 0 \end{bmatrix} \right.$$
$$\left[\begin{bmatrix} 0 & S_{yzyz} & 0 \\ S_{yzyz} & 0 & 0 \\ 0 & 0 & 0 \end{bmatrix} \begin{bmatrix} S_{xxyy} & 0 & 0 \\ 0 & S_{xxxx} & 0 \\ 0 & 0 & S_{xxyy} \end{bmatrix} \begin{bmatrix} 0 & 0 & 0 \\ 0 & 0 & S_{yzyz} \\ 0 & S_{yzyz} & 0 \end{bmatrix} \right.$$
$$\left. \left. \begin{bmatrix} 0 & 0 & S_{yzyz} \\ 0 & 0 & 0 \\ S_{yzyz} & 0 & 0 \end{bmatrix} \begin{bmatrix} 0 & 0 & 0 \\ 0 & 0 & S_{yzyz} \\ 0 & S_{yzyz} & 0 \end{bmatrix} \begin{bmatrix} S_{xxyy} & 0 & 0 \\ 0 & S_{xxyy} & 0 \\ 0 & 0 & S_{xxxx} \end{bmatrix} \right] \quad (3)$$

where the high crystal symmetry of the system has been imposed, resulting in only three non-zero parameters (S_{xxxx}, S_{yzyz} and S_{xxyy}) [26]. The convolution of the gradient-elastic tensor and strain tensor, ϵ_{ij}, is then summed, as in Eq. 4 to get the EFG, $V_{i,j}$.

$$V_{i,j} = \sum_{k,l} S_{ijkl}\epsilon_{kl}, \quad (4)$$

where we are using Voigt notation for the indices, where:

$$S_{11} = S_{xxxx} = S_{yyyy} = S_{zzzz} \quad (5)$$

$$S_{12} = S_{xxyy} = S_{yyzz} = S_{zzxx} = S_{yyxx} = S_{zzyy} = S_{xxzz} \quad (6)$$

$$S_{44} = S_{yzyz} = S_{zxzx} = S_{xyxy} \quad (7)$$

Eq. 4 is then simplified by taking into account cubic symmetry, $S_{12} = -S_{11}/2$ [44]. We use $QS_{11} = 0.758 \times 10^{-6}$ V ($QS_{11} = -0.377 \times 10^{-6}$ V) and $QS_{44} = 1.51 \times 10^{-6}$ V ($QS_{44} = 0.151 \times 10^{-6}$ V) for ^{75}As (^{69}Ga) nuclei, as found in Ref. [26], where Q is a nuclear quadrupole moment [4]. The quadrupolar Hamiltonian is then:

$$\mathcal{H}_Q = \frac{1}{2\pi\hbar}\frac{eQ}{6I_z\,(2I_z-1)}\sum_{a,b=x,y,z} V_{a,b}\left(\frac{3}{2}\left(J_aJ_b + J_bJ_a\right) - \delta_{a,b}J^2\right), \quad (8)$$

where,

$$J^2 = J_x \cdot J_x + J_y \cdot J_y + J_z \cdot J_z, \quad (9)$$

e is the elementary charge of an electron, $\delta_{a,b}$ is a Kronecker delta, and I_z is the nuclear spin. The complete Hamiltonian, $\mathcal{H}_{zQ}$ under a generic strain tensor ϵ is the sum of Eq. 2 and 8. The major strain value, ϵ_m, corresponding to the largest absolute eigenvalue of the strain tensor, is used to form a principal axis system (PAS) as shown in Fig. 13. N spin-3/2 nuclei are then assigned their own strain tensor, for which $\mathcal{H}_{zQ}$ is diagonalized and solved using numerical parameters. This generates a list of eigensystems with transition frequencies

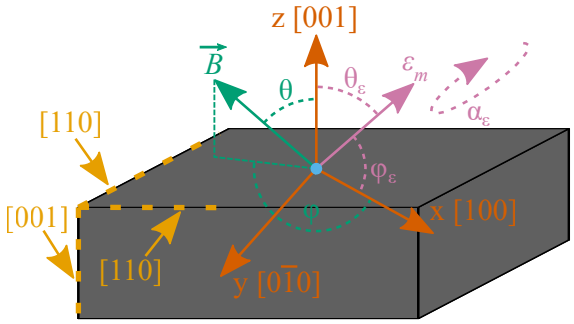

FIG. 13. Geometry used for experimentation and simulation. All angles are not sketched to scale, especially that of the external magnetic field with respect to the growth axis of the sample (θ). The blue circle at the origin of the (x, y, z) axes is the location of a QD.

$(\pm\frac{3}{2} \leftrightarrow \pm\frac{1}{2}$ and $\frac{1}{2} \leftrightarrow -\frac{1}{2})$. In this way one can emulate inhomogeneous broadening of strain within a real QD. In this work only the transitions between adjacent eigenenergies (±1 difference in spin) are used, while strictly speaking more transitions are allowed, they have a small magnetic dipole moment, so only transitions with frequencies similar to the CT are efficiently driven.

These nuclear transition frequencies are then used to calculate the total inverse/integral saturation NMR signal. This is accomplished by comparing the RF spectral shape to the nuclear transition frequencies, to determine which nuclei transitions are saturated by the RF. The spectral shape is varied, as it would be in the experiments, e.g. for inverse NMR the frequency that the gap occurs at is altered. The sum of all these saturated nuclei transitions is given in terms of the change in nuclear polarization degree, ΔP_n. This is then multiplied by the product of the hyperfine constant and nuclear spin to get the NMR signal. In the simulation, the spectral position of the excitation gap and the width of the depolarization band for inverse and integral saturation NMR, respectively, are defined to match those selected experimentally. This allows for a direct Chi-squared (χ^2) comparison between the simulated and experimental spectra by directly calculating the difference between them, without requiring interpolation.

A differential evolution algorithm is employed (following Ref. [45]) to determine the global minimum for the χ^2 of the simulation. Using *Wolfram Mathematica 12.0*, a Monte-Carlo simulation was created where each of the parameters (defined in Supplementary Tabs. 2-5) for the diagonalized Hamiltonian are assumed to vary independently from one another. For these parameters, initial starting conditions were given based on the experimental data to help speed up the optimization.

The strain distribution within the QD is modeled by two distinct strain distributions: one for homogeneous strain and another for inhomogeneous strain, with the major strain direction differing between the two distributions. For most of the parameters required to solve the

Hamiltonian, we randomly sample N points from normal distributions. However, for the inhomogeneous major strain, the angles at which ϵ_m is directed at, θ_ϵ and ϕ_ϵ, are assigned random values within a spherical geometry. For ease of explanation, the homogeneous and inhomogeneous distribution of strains shall be called 'pure GaAs nuclei' and 'alloyed nuclei' strain respectively. The alloyed nuclei strain distribution is also allowed to have a differing magnitude of strain, $\epsilon_{m,\text{alloy}}$, to that of the pure GaAs nuclei strain distribution. In the alloyed nuclei strain distribution, the magnitude of $\epsilon_{m,\text{alloy}}$ can vary for different isotopes of nuclei. This variation is permitted because nuclei in different locations within the zinc-blende lattice will experience varying strains from their nearest neighboring nuclei. The weighting between whether nuclei followed the pure GaAs or alloyed distribution was itself an optimization parameter. To be clear, the distinction between the pure GaAs and alloyed distribution is empirically based and artificial in nature.

The accuracy of the integral saturation technique decreases with narrower excitation bandwidths, mainly due to difficulties in precisely fitting the center of the Larmor frequency distribution. However, by measuring a high-resolution inverse NMR CT spectrum, the Larmor frequency can be determined with a high degree of precision, thereby improving the accuracy of the integral saturation. Equally, if the bandwidth of the integral saturation measurement is too large it may start to depolarize unwanted isotopes. For example at 2.87 T the CT frequencies, in MHz, for ^{75}As : ^{115}In : ^{69}Ga : ^{27}Al : ^{71}Ga are 20.97 : 26.86 : 29.40 : 31.85 : 37.36. When studying ^{69}Ga, if bandwidths more than ≈ 5 MHz are used, a decrease in the hyperfine shift can occur due to depolarization of ^{115}In and ^{27}Al nuclei. To avoid these inaccuracies in experimental data, the simulation can selectively target a safe bandwidth range, excluding the data points that may lead to erroneous results.

A key consideration in simulating the strain distribution within a QD is the number of Monte-Carlo samples. Simulating for a large number of samples is possible; however, as illustrated in Fig. 14, the benefits diminish with increasing numbers. When simulating with a sample size over 1000, the standard deviation of the χ^2 value is $\approx \pm 10^{-4}$, which is 0.15% the value of the mean. While running the differential evolution minimization algorithm there will be some error incorporated from this. The simple solution is to increase the number of samples simulated, the complication with this being running a simulation with more samples requires more time. Ultimately, it is a trade-off as to how many samples to use, but we decided that 1000 was a reasonable amount.

After conducting simulations, it became apparent that the integral saturation and inverse NMR measurements were not entirely consistent with the simulated spectra. Specifically, the amplitude of the computed inverse NMR spectra was disproportionately large compared to the integral saturation spectra. As a result, simultaneous fitting of the two NMR forms was not feasible. To address this discrepancy, an empirical scaling factor was introduced to artificially reduce the overall signal of the inverse NMR spectra, enabling an accurate fit for both NMR forms with the experimental data. A phenomenological distribution was also introduced to allow variation of the Larmor frequency around a central peak, representing dipolar broadening. The full width at half maximum (FWHM) of this broadening was constrained to remain comparable to the known scale of dipolar broadening (~ 1 kHz [6]) during the minimization process.

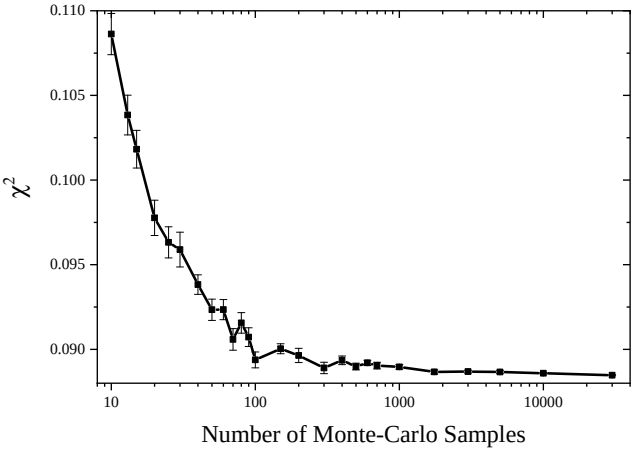

FIG. 14. χ^2 values for simultaneously reproduced inverse and integral saturation NMR spectra at 2.87 T. 20 iterations were run for each value of the Monte Carlo sample size to determine the standard deviation (error bars) around the mean value. Each simulation used the same input parameters.

B. Simulation Results

The simulated spectra accurately reproduce the spectral features seen in the experimental data, as presented in Fig. 15. In Figs. 15(a) and 15(b) the quadrupolar splitting of the STs, which are representative of the magnitude of unimodal strain within the QD, corresponds well to the measured STs.

The mean major strain derived from simulations for the pure GaAs strain distribution was 0.023%, 0.031%, and 0.039% for the $x = 0\%$, 5%, and 10% $Al_xGa_{1-x}As$ QDs, respectively, with FWHM values of 0.006%, 0.01%, and 0.009%. These strain values are smaller than the estimated values but are similar to previously measured GaAs/AlGaAs QDs [16]. In the simulated $Al_{0.1}Ga_{0.9}As$ QD, where more ^{75}As nuclei have ^{27}Al as nearest neighbors and inhomogeneous strain is more pronounced, the alloyed nuclei mean major strain for ^{75}As nuclei was derived to be approximately 0.14% with a FWHM of 0.007%. This matches the AlAs/GaAs lattice constant difference of 0.138% [31–34]. The percentage of Monte-Carlo samples following the alloyed strain distribution for ^{75}As (^{69}Ga) nuclei increased with the concentration

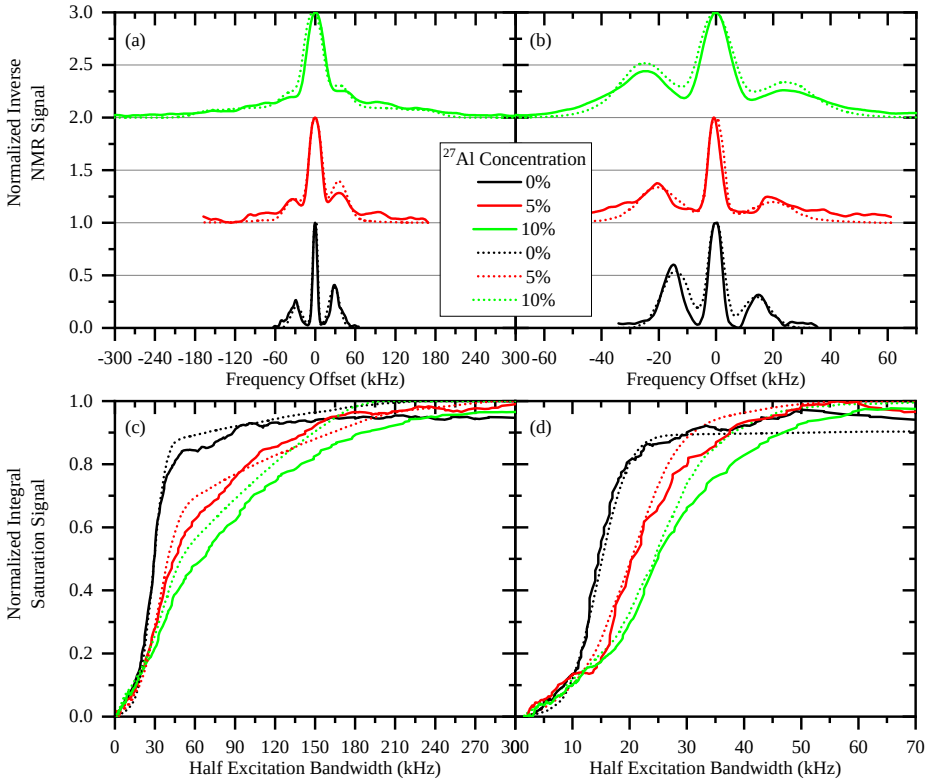

FIG. 15. (a) Inverse NMR conducted on ^{75}As for QDs, at 2.87 T and 4.2 K, with a varying ^{27}Al concentrations. All optical pumping has σ^+ polarization. (b) Same as (a) but for ^{69}Ga. (c) Same as (a) but with the integral saturation NMR technique. The polarization chosen for optical pumping, σ^+/σ^-, was based on which produced the largest hyperfine shift. (d) Same as (c) but for ^{69}Ga. Dotted lines show the simulated results, which have also been normalized.

of ^{27}Al, derived as 21%, 42%, and 80% (8%, 21%, and 48%) for the x = 0%, 5%, and 10% $Al_xGa_{1-x}As$ QDs respectively. The non-zero percentage in the base GaAs configuration could result from the electron wavefunction penetrating into the barrier or diffusion of ^{27}Al nuclei into the QD from the barrier. The impact of the increased contribution from the alloyed strain distribution is shown in Fig. 16, where the strain distribution now accounts for a significant proportion of the total integral saturation NMR spectra. Beyond a half RF bandwidth of 68 kHz, all of the increase in the total NMR signal originates from the alloyed nuclei distribution. This confirms that the broad spectral features in the NMR spectra are predominantly due to the alloyed strain distribution.

In the experimental ^{75}As inverse NMR spectra, Fig. 15(a), reasonably pronounced second-peak structures are observed between 60-100 kHz for the x = 5% and 10% $Al_xGa_{1-x}As$ QDs. However, these peaks could not be replicated in the Monte-Carlo simulation. One potential reason for this is the absence of structural information in the Monte-Carlo sample points. In $Al_xGa_{1-x}As$ QDs, a zinc-blende crystal structure defines the arrangement of nuclei and their nearest/next nearest neighbors. In contrast, the simulation lacks such structural constraints, each Monte-Carlo sample point is independent.

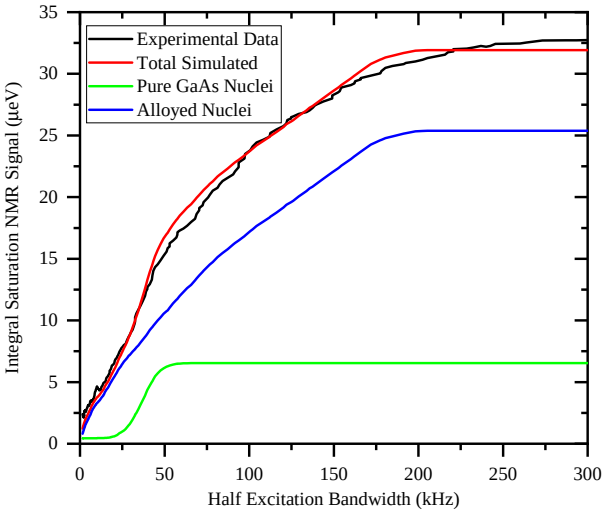

FIG. 16. Comparison between the integral saturation NMR for simulated spectra, using optimized parameters, and experimental data. Data is for the ^{75}As isotope in an $Al_{0.1}Ga_{0.9}As$ QD at 2.87 T and 4.2 K. The weighted strain distributions, which sum to form the total distribution, are presented for comparison.

This absence of structure will contribute to the discrepancy between experimental and reproduced NMR spectra. A different modeling approach, such as tight binding would provide a more comprehensive interpretation of strain [46, 47].

CONCLUSION

A combination of inverse and integral saturation NMR techniques have been used to study the effect of disorder in a variety of QD samples. From Monte-Carlo simulations we have derived the major strain within $Al_xGa_{1-x}As$ QDs to be 0.023%, 0.031%, and 0.039% for the $x = 0\%$, 5%, and 10% dots respectively. We have also determined that, in addition to this major strain, there exists an inhomogeneous strain within the dot, approximately equal to the lattice mismatch of GaAs/AlAs. The presence of this inhomogeneous strain leads to broadened nuclear spin transitions, thereby adversely affecting electron spin decoherence, which is undesirable for quantum information processing using electron spin qubits [4, 6, 11]. The research was further extended to examine the effect of adding ^{115}In to the sample. When present in the QD, it was shown to increase the spectral broadening by up to 2 MHz. However, the presence of 0.4% ^{115}In in the barrier did not produce the same effect, possibly due to the low concentration of ^{115}In in the sample. An optical microcavity constructed from DBRs was found to exhibit lower biaxial strain compared to the same QDs without the structure. However, a one-sided broad-tailed triangular lineshape was observed, with its origin remaining unclear. Given the widespread use of these structures, further investigation is warranted to understand and address this phenomenon.

ACKNOWLEDGMENTS

P.M-H. and E.A.C. were supported by EPSRC through a doctoral training grant and EP/ 048333/1, respectively. E.A.C. was also supported by a Royal Society University Research Fellowship. Author contributions: S.M., S.F.C.S and A.R. developed, grew and processed the quantum dot samples. P.M-H. and E.A.C. conducted the experiments. P.M-H. conducted the simulations with advice from E.A.C. P.M-H drafted the manuscript with input from all authors. E.A.C. coordinated the project.

[1] X. Xu, W. Yao, B. Sun, D. G. Steel, A. S. Bracker, D. Gammon, and L. J. Sham, Optically controlled locking of the nuclear field via coherent dark-state spectroscopy, Nature **459**, 1105 (2009).

[2] D. Brunner, B. D. Gerardot, P. A. Dalgarno, G. Wüst, K. Karrai, N. G. Stoltz, P. M. Petroff, and R. J. Warburton, A coherent single-hole spin in a semiconductor, Science **325**, 70 (2009).

[3] A. V. Khaetskii, D. Loss, and L. Glazman, Electron spin decoherence in quantum dots due to interaction with nuclei, Physical Review Letters **88**, 10.1103/physrevlett.88.186802 (2002).

[4] B. Urbaszek, X. Marie, T. Amand, O. Krebs, P. Voisin, P. Maletinsky, A. Högele, and A. Imamoglu, Nuclear spin physics in quantum dots: An optical investigation, Reviews of Modern Physics **85**, 79–133 (2013).

[5] A. Bechtold, D. Rauch, F. Li, T. Simmet, P.-L. Ardelt, A. Regler, K. Müller, N. A. Sinitsyn, and J. J. Finley, Three-stage decoherence dynamics of an electron spin qubit in an optically active quantum dot, Nature Physics **11**, 1005–1008 (2015).

[6] E. Chekhovich, M. Hopkinson, M. Skolnick, and A. Tartakovskii, Suppression of nuclear spin bath fluctuations in self-assembled quantum dots induced by inhomogeneous strain, Nature Communications **6**, 10.1038/ncomms7348 (2015).

[7] R. Stockill, C. Le Gall, C. Matthiesen, L. Huthmacher, E. Clarke, M. Hugues, and M. Atatüre, Quantum dot spin coherence governed by a strained nuclear environment, Nature Communications **7**, 10.1038/ncomms12745 (2016).

[8] E. A. Chekhovich, Decoherence and fluctuation dynamics of the quantum dot nuclear spin bath probed by nuclear magnetic resonance, Journal of Physics: Conference Series **864**, 012080 (2017).

[9] A. M. Waeber, G. Gillard, G. Ragunathan, M. Hopkinson, P. Spencer, D. A. Ritchie, M. S. Skolnick, and E. A. Chekhovich, Pulse control protocols for preserving coherence in dipolar-coupled nuclear spin baths, Nature Communications **10**, 10.1038/s41467-019-11160-6 (2019).

[10] T. Lettner, S. Gyger, K. D. Zeuner, L. Schweickert, S. Steinhauer, C. Reuterskiöld Hedlund, S. Stroj, A. Rastelli, M. Hammar, R. Trotta, and et al., Strain-controlled quantum dot fine structure for entangled photon generation at 1550 nm, Nano Letters **21**, 10501–10506 (2021).

[11] L. Zaporski, N. Shofer, J. H. Bodey, S. Manna, G. Gillard, M. H. Appel, C. Schimpf, S. F. Covre da Silva, J. Jarman, G. Delamare, G. Park, U. Haeusler, E. A. Chekhovich, A. Rastelli, D. A. Gangloff, M. Atatüre, and C. Le Gall, Ideal refocusing of an optically active spin qubit under strong hyperfine interactions, Nature Nanotechnology **18**, 257–263 (2023).

[12] G. Gillard, *Lifetime and Coherence of the Coupled Electron and Nuclear Spin Systems in Semiconductor Quantum Dots*, Ph.D. thesis, University of Sheffield (2022).

[13] P. E. Vullum, M. Nord, M. Vatanparast, S. F. Thomassen, C. Boothroyd, R. Holmestad, B.-O. Fimland, and T. W. Reenaas, Quantitative strain analysis of InAs/GaAs quantum dot materials, Scientific Reports **7**, 10.1038/srep45376 (2017).

[14] C. Heyn, A. Stemmann, T. Köppen, C. Strelow, T. Kipp, M. Grave, S. Mendach, and W. Hansen, Highly uniform and strain-free GaAs quantum dots fabricated by filling of self-assembled nanoholes, Applied Physics Letters **94**, 183113 (2009).

[15] E. A. Chekhovich, K. V. Kavokin, J. Puebla, A. B. Krysa, M. Hopkinson, A. D. Andreev, A. M. Sanchez, R. Beanland, M. S. Skolnick, A. I. Tartakovskii, and et al., Structural analysis of strained quantum dots using nuclear magnetic resonance, Nature Nanotechnology **7**, 646–650 (2012).

[16] A. Ulhaq, Q. Duan, E. Zallo, F. Ding, O. G. Schmidt, A. I. Tartakovskii, M. S. Skolnick, and E. A. Chekhovich, Vanishing electron g factor and long-lived nuclear spin polarization in weakly strained nanohole-filled GaAs/AlGaAs quantum dots, Physical Review B **93**, 10.1103/physrevb.93.165306 (2016).

[17] E. A. Chekhovich, I. M. Griffiths, M. S. Skolnick, H. Huang, S. F. C. da Silva, X. Yuan, and A. Rastelli, Cross calibration of deformation potentials and gradient-elastic tensors of GaAs using photoluminescence and nuclear magnetic resonance spectroscopy in GaAs/AlGaAs quantum dot structures, Phys. Rev. B **97**, 235311 (2018).

[18] P. Millington-Hotze, S. Manna, S. F. Covre da Silva, A. Rastelli, and E. A. Chekhovich, Nuclear spin diffusion in the central spin system of a GaAs/AlGaAs quantum dot, Nature Communications **14**, 10.1038/s41467-023-38349-0 (2023).

[19] P. Millington-Hotze, H. E. Dyte, S. Manna, S. F. Covre da Silva, A. Rastelli, and E. A. Chekhovich, Approaching a fully-polarized state of nuclear spins in a solid, Nature Communications **15**, 10.1038/s41467-024-45364-2 (2024).

[20] C. Degen, M. Tomaselli, B. H. Meier, M. M. Voncken, and A. P. Kentgens, NMR investigation of atomic ordering in $Al_xGa_{1-x}As$ thin films, Physical Review B **69**, 10.1103/physrevb.69.193303 (2004).

[21] P. J. Knijn, P. J. van Bentum, E. R. van Eck, C. Fang, D. L. Grimminck, R. A. de Groot, R. W. Havenith, M. Marsman, W. L. Meerts, G. A. de Wijs, and A. P. M. Kentegens, A solid-state NMR and DFT study of compositional modulations in $Al_xGa_{1-x}As$, Physical Chemistry Chemical Physics **12**, 11517 (2010).

[22] M. Goswami, P. J. Knijn, G. J. Bauhuis, J. W. Janssen, P. J. van Bentum, G. A. de Wijs, and A. P. Kentgens, Stripline ^{75}As NMR study of epitaxial III-V semiconductor $Al_{0.5}Ga_{0.5}As$, The Journal of Physical Chemistry C **118**, 13394–13405 (2014).

[23] E. Duijs, F. Findeis, A. Zrenner, M. Bichler, and G. Abstreiter, Photoluminescence and AFM studies on blue shifted $InAs/Al_yGa_{1-y}As$ quantum dots, physica status solidi (b) **224**, 47 (2001).

[24] E. A. Chekhovich, S. F. da Silva, and A. Rastelli, Nuclear spin quantum register in an optically active semiconductor quantum dot, Nature Nanotechnology **15**, 999–1004 (2020).

[25] X. Yuan, S. F. Covre da Silva, D. Csontosová, H. Huang, C. Schimpf, M. Reindl, J. Lu, Z. Ni, A. Rastelli, and P. Klenovský, GaAs quantum dots under quasiuniaxial stress: Experiment and theory, Phys. Rev. B **107**, 235412 (2023).

[26] I. M. Griffiths, H. Huang, A. Rastelli, M. S. Skolnick, and E. A. Chekhovich, Complete characterization of GaAs gradient-elastic tensors and reconstruction of internal strain in GaAs/AlGaAs quantum dots using nuclear magnetic resonance, Phys. Rev. B **99**, 125304 (2019).

[27] Z. Li-Ping, Z. Zhen, L. Jia-Chang, L. Xiao-Yun, Z. Chao, L. Huan-Li, and L. Ye, Relations between compositional modulation and atomic ordering degree in thin films of ternary III-V semiconductor alloys, Chinese Physics B **17**, 4619–4621 (2008).

[28] C. Krahmer, M. Philippens, M. Schubert, and K. Streubel, MOVPE growth investigations of doping and ordering in AlGaAs and GaInP with reflectance anisotropy spectroscopy, Journal of Crystal Growth **298**, 18–22 (2007).

[29] A. J. Heinrich, M. Wenderoth, K. J. Engel, T. C. Reusch, K. Sauthoff, R. G. Ulbrich, E. R. Weber, and K. Uchida, Short-range ordering in $Al_xGa_{1-x}As$ grown with metal-organic vapor-phase epitaxy, Physical Review B **59**, 10296–10301 (1999).

[30] D. Koleske, A. Wickenden, R. Henry, and M. Twigg, Influence of MOVPE growth conditions on carbon and silicon concentrations in GaN, Journal of Crystal Growth **242**, 55–69 (2002).

[31] R. Wyckoff, Crystal structures, seconded (1986).

[32] C. Filippi, D. J. Singh, and C. J. Umrigar, All-electron local-density and generalized-gradient calculations of the structural properties of semiconductors, Phys. Rev. B **50**, 14947 (1994).

[33] S. Adachi, *Properties of group-IV, III-V and II-VI semiconductors* (Wiley, 2005).

[34] R. Ahmed, S. Javad Hashemifar, H. Akbarzadeh, M. Ahmed, and F. e Aleem, Ab initio study of structural and electronic properties of III-arsenide binary compounds, Computational Materials Science **39**, 580–586 (2007).

[35] M. Gurioli, Z. Wang, A. Rastelli, T. Kuroda, and S. Sanguinetti, Droplet epitaxy of semiconductor nanostructures for quantum photonic devices, Nature Materials **18**, 799–810 (2019).

[36] N. Ha, T. Mano, Y.-L. Chou, Y.-N. Wu, S.-J. Cheng, J. Bocquel, P. M. Koenraad, A. Ohtake, Y. Sakuma, K. Sakoda, and et al., Size-dependent line broadening in the emission spectra of single GaAs quantum dots: Impact of surface charge on spectral diffusion, Physical Review B **92**, 10.1103/physrevb.92.075306 (2015).

[37] J. D. Plumhof, V. Křápek, L. Wang, A. Schliwa, D. Bimberg, A. Rastelli, and O. G. Schmidt, Experimental investigation and modeling of the fine structure splitting of neutral excitons in strain-free $GaAs/Al_xG_{1-x}As$ quantum dots, Physical Review B **81**, 10.1103/physrevb.81.121309 (2010).

[38] L. Zhai, M. C. Löbl, G. N. Nguyen, J. Ritzmann, A. Javadi, C. Spinnler, A. D. Wieck, A. Ludwig, and R. J. Warburton, Low-noise GaAs quantum dots for quantum photonics, Nature Communications **11**, 10.1038/s41467-020-18625-z (2020).

[39] C. Bulutay, E. A. Chekhovich, and A. I. Tartakovskii, Nuclear magnetic resonance inverse spectra of InGaAs quantum dots: Atomistic level structural information, Physical Review B **90**, 10.1103/physrevb.90.205425 (2014).

[40] K. J. Vahala, Optical microcavities, Nature **424**, 839–846 (2003).

[41] J. P. Reithmaier, G. Sęk, A. Löffler, C. Hofmann, S. Kuhn, S. Reitzenstein, L. V. Keldysh, V. D. Kulakovskii, T. L. Reinecke, and A. Forchel, Strong coupling in a single quantum dot–semiconductor microcavity system, Nature **432**, 197–200 (2004).

[42] A. M. Waeber, *Probing nuclear spin bath dynamics in a self-assembled quantum dot with optically detected NMR*, Ph.D. thesis, University of Sheffield (2016).

[43] G. Ragunathan, *Nuclear spin phenomena in III-V and II-VI Semiconductor Quantum Dots*, Ph.D. thesis, University of Sheffield (2019).

[44] R. J. Harrison and P. L. Sagalyn, Trace relations for tensors relating electric fields and elastic strains to nuclear quadrupole effects, Phys. Rev. **128**, 1630 (1962).

[45] K. Price, R. M. Storn, and J. A. Lampinen, *Differential evolution a practical approach to global optimization* (Springer Berlin, 2014).

[46] M. Roy and P. A. Maksym, Efficient method for calculating electronic states in self-assembled quantum dots, Phys. Rev. B **68**, 235308 (2003).

[47] C. Dion, P. Desjardins, N. Shtinkov, M. D. Robertson, F. Schiettekatte, P. J. Poole, and S. Raymond, Intermixing during growth of InAs self-assembled quantum dots in InP: A photoluminescence and tight-binding investigation, Phys. Rev. B **77**, 075338 (2008).

Supplemental Material: Strain and disorder effects in AlGaAs

Supplementary Section 1. SAMPLE STRUCTURE

There are many quantum dot (QD) samples used within this paper, the schematics of which are all shown within Supplementary Fig. 1. These samples are all grown using molecular beam epitaxy (MBE) on a semi-insulating GaAs (001) substrate. The details of each structure are detailed in the sections below.

A. GaAs/$Al_{0.3}Ga_{0.7}As$ QDs

The GaAs QD sample structure is shown in Supplementary Fig. 1(a). On top of the GaAs substrate a 100 nm layer of $Al_{0.3}Ga_{0.7}As$ is grown. Aluminium droplets are then grown on the surface of this layer, which are used to etch nanoholes [1, 2]. These nanoholes are then infilled by growing a 2 nm layer of GaAs on top of the $Al_{0.3}Ga_{0.7}As$. A 100 nm layer of $Al_{0.3}Ga_{0.7}As$ is then grown on top of the GaAs, which confines the QDs and quantum well (QW) layer.

B. $Al_xGa_{1-x}As/Al_{0.33}Ga_{0.67}As$ QDs

The structures of both the $Al_{0.05}Ga_{0.95}As$ and $Al_{0.1}Ga_{0.9}As$ QD samples are depicted in Supplementary Fig. 1(b) and differ only in the infilling layer. On a GaAs substrate, a 120 nm layer of $Al_{0.33}Ga_{0.67}As$ is initially grown. Subsequently, aluminium droplets are grown on the surface of this layer to facilitate nanohole etching [1, 2]. These nanoholes are then filled by depositing a 4 nm layer of either $Al_{0.05}Ga_{0.95}As$ or $Al_{0.1}Ga_{0.9}As$ atop the $Al_{0.33}Ga_{0.67}As$. Finally, a 120 nm layer of $Al_{0.33}Ga_{0.67}As$ is grown atop the GaAs to confine the QDs and the QW layer.

C. GaAs/AlAs QDs

The GaAs/AlAs QD sample structure is shown in Supplementary Fig. 1(c). On top of the GaAs substrate a 100 nm AlAs layer is grown. Aluminium droplets are used to etch into the AlAs to create nanoholes [1, 2]. 2 nm of GaAs is then grown on top of this AlAs layer, which fills in the nanoholes and forms a QW layer. A 100 nm AlAs layer is then grown on top of this to form the other barrier to the QDs. The sample is then capped with a 4 nm layer of GaAs.

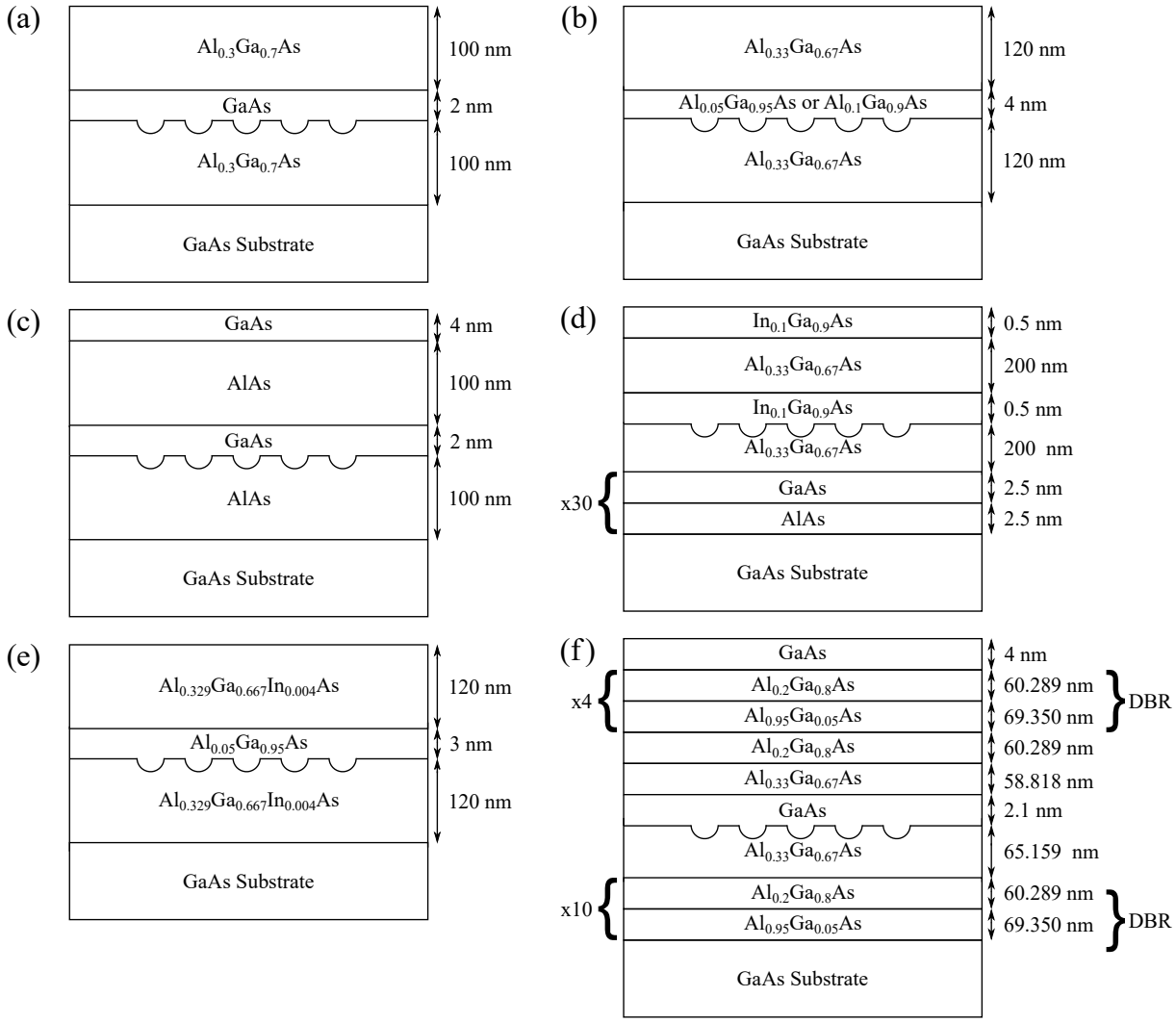

Supplementary Figure 1. Schematic of the QD sample structures. (a) The GaAs QDs that are used for the basis of comparison for this paper. (b) The 5% and 10% $Al_xGa_{1-x}As$ QD samples; these are identical apart from the infilling layer. (c) GaAs QDs with an AlAs barrier. (d) $In_{0.1}Ga_{0.9}As$ QDs with a superlattice of GaAs/AlAs. (e) $Al_{0.05}Ga_{0.95}As$ QDs with 0.4% ^{115}In added to the barrier. (f) GaAs QDs grown inside a microcavity.

D. $In_{0.1}Ga_{0.9}As/Al_{0.33}Ga_{0.67}As$ QDs

The $In_{0.1}Ga_{0.9}As$ QD sample structure is shown in Supplementary Fig. 1(d). After the GaAs substrate, a GaAs/AlAs superlattice is grown, where each of the 60 layers is 2.5 nm. A 200 nm layer of $Al_{0.33}Ga_{0.67}As$ is then grown on top of the superlattice, followed by aluminium droplets which etch nanoholes [1, 2]. A 0.5 nm layer of $In_{0.1}Ga_{0.9}As$ is grown on top of these nanoholes followed by a 200 nm layer of $Al_{0.33}Ga_{0.67}As$. Finally the sample is capped with a 0.5 nm layer of

$In_{0.1}Ga_{0.9}As$.

E. $Al_{0.05}Ga_{0.95}As/Al_{0.329}Ga_{0.667}In_{0.004}As$ QDs

The $Al_{0.05}Ga_{0.95}As/Al_{0.329}Ga_{0.667}In_{0.004}As$ QD sample structure is shown in Supplementary Fig. 1(e). On top of the GaAs substrate a 120 nm $Al_{0.329}Ga_{0.667}In_{0.004}As$ layer is grown to form one side of the barrier. Nanoholes are etched into this layer using aluminium droplets [1, 2]. A 3 nm layer of $Al_{0.05}Ga_{0.95}As$ is then grown on top of these etched nanoholes, followed by a 120 nm layer of $Al_{0.329}Ga_{0.667}In_{0.004}As$ to form the other barrier to the QDs.

F. $GaAs/Al_{0.33}Ga_{0.67}As$ QDs Embedded in Distributed Bragg Reflector Microcavities

The microcavity is the most complex sample discussed in this paper, with its schematic shown in Supplementary Fig. 1(f). After the GaAs substrate, the first Bragg reflector is grown, which consists of ten pairs of $Al_{0.95}Ga_{0.05}As$ and $Al_{0.2}Ga_{0.8}As$ layers. Each $Al_{0.95}Ga_{0.05}As$ layer is 69.35 nm thick, whereas each $Al_{0.95}Ga_{0.05}As$ layer is 60.289 nm thick. This Bragg reflector then has 65.159 nm of $Al_{0.33}Ga_{0.67}As$ grown on top of it. Aluminium droplets are used to etch nanoholes into this layer [1, 2], which are subsequently filled with a 2.1 nm layer of GaAs. This GaAs then has 58.818 nm of $Al_{0.33}Ga_{0.67}As$ grown on top of it, followed by a 60.289 nm layer of $Al_{0.2}Ga_{0.8}As$. The second Bragg reflector is then grown, which consists of four pairs of $Al_{0.95}Ga_{0.05}As$ and $Al_{0.2}Ga_{0.8}As$ layers. The individual layer thicknesses in this Bragg reflector are identical to those in the first Bragg reflector. Using fewer layers in this Bragg reflector reduces its reflectance, thereby enabling the transmission of QD photoluminescence (PL) through the top of the structure. A GaAs cap with a thickness of 4 nm is then grown on top of this second Bragg reflector.

Supplementary Section 2. EXPERIMENTAL DETAILS

All of the experiments within this paper are performed within a liquid helium bath cryostat, which provides a base temperature of 4.2 K. The sample is located within an insert tube, filled with a low-pressure heat-exchange gas, which itself is inserted into the bore of a superconducting magnet. This magnet can generate a maximal static field of 10 T. The optical excitation and magnetic field are applied along the direction of the sample's growth, z, (Faraday geometry). We use a confocal microscopy configuration. An aspheric lens, with focal length 1.45 mm and NA= 0.58, is used as an objective for optical excitation and PL collection of the QDs. The optical excitation laser is

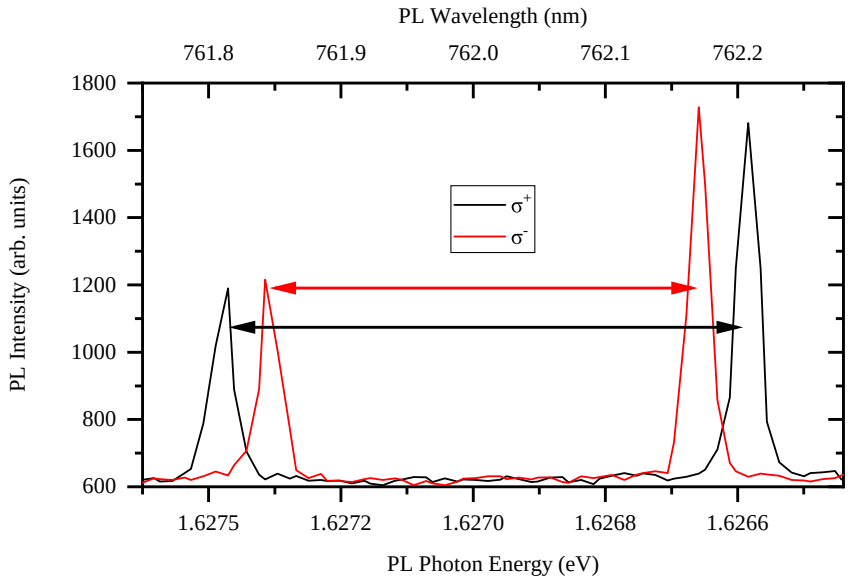

Supplementary Figure 2. PL of an $Al_{0.1}Ga_{0.9}As$ QD at 8 T using a 730 nm probe laser. The spectral splitting of the exciton doublet depends on the helicity of the optical pumping due to the buildup of nuclear spin polarization. The black/red arrow shows the spectral splitting due to σ^+/σ^- polarized light.

focused into a spot of ≈ 1 μm diameter on the sample. The PL emission from a QD is dispersed into a two-stage grating spectrometer and then recorded using a charge-coupled device (CCD) camera. The spectral splitting of an exciton, as shown in Supplementary Fig. 2, is used to measure the hyperfine shift, which is proportional to the nuclear spin polarization degree.

A. Optical Pumping

We utilize optical pumping to create the dynamic nuclear polarization (DNP) for QDs. This method has been proven to be effective in a wide variety of QDs [3–7]. The optical pumping process consists of three stages, all of which occur in T_{Cycle} in Fig. 3 of the main text. The initial stage involves optically generating spin-polarized electron-hole pairs using circularly polarized light. This is possible due to the selection rules in III-V semiconductors. The electron then exchanges its spin to one of the nuclei in the ensemble, enabled because of the spin flip-flop term in the electron-nuclear hyperfine Hamiltonian. The final step is the optical recombination of the electron-hole pair, which removes the spin-flipped electron. This last stage is important, as it allows the QD to accept a new spin-polarized electron. During this pumping process, the polarization degree of the $\approx 10^5$ nuclear spins will increase. In charge-tunable structures, nuclear polarizations of $\geq 95\%$ can be achieved [8], but since none of the samples in our study are charge-tunable, the maximum

achievable polarization degree is $\approx 80\%$ [9].

B. Radiofrequency Depolarization

To conduct the measurements in the main text, it must be possible to effectively depolarize nuclear spin polarizations. This is achieved through saturating the nuclear magnetic resonance (NMR) of the isotopes within the sample. An oscillating magnetic field is produced, $B_x \perp z$, by a coil located ≈ 0.5 mm away from the sample. This coil is made from 10 turns of 0.1 mm diameter enameled copper wire wound on a 0.4 mm spool in 5 layers, with 2 turns in each layer. When the oscillating B_x is resonant with the Larmor frequency of an isotope, nuclear spins undergo Rabi rotation, where the spins will periodically transition from being parallel to antiparallel with the external magnetic field [10]. Each nuclear spin in the ensemble is subject to a local field, due to the nuclear-nuclear dipole interactions. The randomness of these local fields perturbs the Rabi precession frequencies, resulting in ensemble dephasing. After a long resonant radiofrequency (RF) saturation pulse, the nuclear spins become randomly oriented (depolarized). The coil that provides this RF pulse is driven by a class-A RF amplifier, rated up to 20 W.

C. Optical Probing

A variety of probe wavelengths were used for the measurements in the main text, shown in Supplementary Tab. 1. For each of these probe lasers the probe power is chosen to maximize (saturate) the PL intensity of an exciton. Following either σ^+ or σ^- optical excitation from the pump laser and any RF, the spectral splitting of the exciton is measured by applying the probe laser for a time T_{Probe}, as shown in Supplementary Fig. 2. Supplementary Fig. 3 shows how T_{Probe} is calibrated. A longer probe duration allows for the collection of more PL; however, the probe laser induces a parasitic depolarization of nuclear spin. A compromise is reached between the PL intensity and this DNP distortion. In the case of the $In_{0.1}Ga_{0.9}As$ QD described in the main text, $T_{Probe} = 10$ ms, as shown in Supplementary Fig. 3. To increase low PL intensities from the QD, especially if the probe duration is short, multiple pump-RF-probe cycles are taken with a continuous CCD exposure.

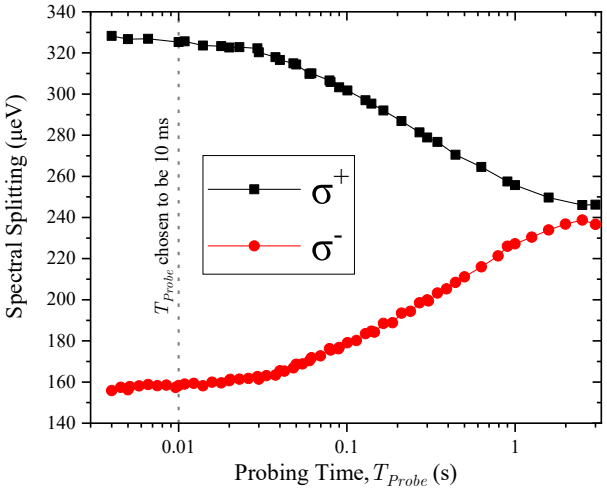

Supplementary Figure 3. Calibration for the optical probing of an $In_{0.1}Ga_{0.9}As$ QD at 2.87 T. The spectral splitting is measured as a function of the probe time, following either σ^+ or σ^- optical pumping. The gray dashed line represents the value of T_{Probe} chosen for the inverse and integral saturation NMR.

Sample	Probe Wavelength (nm)
$GaAs/Al_{0.3}Ga_{0.7}As$	645
$Al_{0.05}Ga_{0.95}As/Al_{0.33}Ga_{0.67}As$	730
$Al_{0.1}Ga_{0.95}As/Al_{0.33}Ga_{0.67}As$	730
GaAs/AlAs	690
$In_{0.1}Ga_{0.9}As/Al_{0.33}Ga_{0.67}As$	532
$Al_{0.05}Ga_{0.95}As/Al_{0.329}Ga_{0.667}In_{0.004}As$	532
$GaAs/Al_{0.33}Ga_{0.67}As$ QDs embedded in distributed Bragg reflector microcavities	645

Supplementary Table 1. Probe laser wavelengths used for the NMR measurements in the main text.

Supplementary Section 3. SIMULATION DETAILS

A. Description of Parameters

Supplementary Tabs. 2-5 describe the parameters which the Monte-Carlo simulation adjusts in order to minimize the difference between the measured and computed NMR spectra.

Variable	**Description**	**Variable**	**Description**
LarmorFreq[“As”, “2.87T”, “σ+”]	The mean Larmor frequency of ^{75}As nuclei, for a generalized normal distribution, using σ^+ optical pumping at a field of 2.87 T	LarmorFreq[“As”, “2.87T”, “σ-”]	The mean Larmor frequency of ^{75}As nuclei, for a generalized normal distribution, using σ^- optical pumping at a field of 2.87 T
LarmorFreq[“Ga”, “2.87T”, “σ+”]	The mean Larmor frequency of ^{69}Ga nuclei, for a generalized normal distribution, using σ^+ optical pumping at a field of 2.87 T	LarmorFreq[“Ga”, “2.87T”, “σ-”]	The mean Larmor frequency of ^{69}Ga nuclei, for a generalized normal distribution, using σ^- optical pumping at a field of 2.87 T
CTFWHMAs	The full width at half maximum of the generalized normal distribution for ^{75}As nuclei at the Larmor frequency, for the homogeneous strain distribution	CTFWHMGa	The full width at half maximum of the generalized normal distribution for ^{69}Ga nuclei at the Larmor frequency, for the homogeneous strain distribution
CTFWHMAsBarr	The full width at half maximum of the generalized normal distribution for ^{75}As nuclei at the Larmor frequency, for the inhomogeneous strain distribution	CTFWHMGaBarr	The full width at half maximum of the generalized normal distribution for ^{69}Ga nuclei at the Larmor frequency, for the inhomogeneous strain distribution
ExponentAs	The exponential factor for the Larmor frequency distribution of ^{75}As nuclei, for the homogeneous strain distribution	ExponentGa	The exponential factor for the Larmor frequency distribution of ^{69}Ga nuclei, for the homogeneous strain distribution
BarrierExponentAs	The exponential factor for the Larmor frequency distribution of ^{75}As nuclei, for the inhomogeneous strain distribution	BarrierExponentGa	The exponential factor for the Larmor frequency distribution of ^{69}Ga nuclei, for the inhomogeneous strain distribution

Supplementary Table 2. Description of variables used in the simulation relating to the Larmor frequencies.

Variable	**Description**	**Variable**	**Description**
$\theta\epsilon$MeanValueAs	The mean θ_ϵ value in a normal distribution, for ^{75}As nuclei	$\theta\epsilon$STDValueAs	The normal distribution's standard deviation for θ_ϵ, for ^{75}As nuclei
$\theta\epsilon$MeanValueGa	The mean θ_ϵ value in a normal distribution, for ^{69}Ga nuclei	$\theta\epsilon$STDValueGa	The normal distribution's standard deviation for θ_ϵ, for ^{69}Ga nuclei
$\phi\epsilon$MeanValue	The mean ϕ_ϵ value in a normal distribution	$\phi\epsilon$STDValue	The normal distribution's standard deviation for ϕ_ϵ
$\alpha\epsilon$MeanValue	The mean α_ϵ value in a normal distribution for the homogeneous strain distribution	$\alpha\epsilon$STDValue	The normal distribution's standard deviation for α_ϵ for the homogeneous strain distribution
$\alpha\epsilon$MeanValueBarrierAs	The mean α_ϵ value in the normal distribution for the inhomogeneous strain distribution of ^{75}As nuclei	$\alpha\epsilon$STDValueBarrierAs	The standard deviation of the normal distribution for α_ϵ in the inhomogeneous strain distribution for ^{75}As nuclei
$\alpha\epsilon$MeanValueBarrierGa	The mean α_ϵ value in the normal distribution for the inhomogeneous strain distribution of ^{69}Ga nuclei	$\alpha\epsilon$STDValueBarrierGa	The standard deviation of the normal distribution for α_ϵ in the inhomogeneous strain distribution for ^{69}Ga nuclei

Supplementary Table 3. Description of variables used in the simulation relating to the major strain angles.

Variable	Description	Variable	Description
ϵmMeanValue	The mean major strain value, corresponding to the largest absolute eigenvalue of strain, in a normal distribution of homogeneous strain	ϵmSTDValue	The standard deviation of the normal distribution for the major strain in the homogeneous strain distribution
$\epsilon r\eta$MeanValue	The strain asymmetry in a normal distribution (truncated to be between 0 and 1) for the homogeneous strain distribution	$\epsilon r\eta$STDValue	The standard deviation of the normal distribution for the strain asymmetry in the homogeneous strain distribution
ϵinhomoAs	The mean major strain value, corresponding to the largest absolute eigenvalue of strain, in a normal distribution of inhomogeneous strain, for ^{75}As nuclei	ϵinhomoSTDAs	The standard deviation of the normal distribution for the major strain in the inhomogeneous strain distribution, for ^{75}As nuclei
ϵinhomoGa	The mean major strain value, corresponding to the largest absolute eigenvalue of strain, in a normal distribution of inhomogeneous strain, for ^{69}Ga nuclei	ϵinhomoSTDGa	The standard deviation of the normal distribution for the major strain in the inhomogeneous strain distribution, for ^{69}Ga nuclei
$\epsilon r\eta$MeanValueBarrierAs	The strain asymmetry in a normal distribution (truncated to be between 0 and 1) for ^{75}As nuclei, for the inhomogeneous strain distribution	$\epsilon r\eta$STDValueBarrierAs	The standard deviation of the normal distribution for the major strain in the inhomogeneous strain distribution of ^{75}As nuclei
$\epsilon r\eta$MeanValueBarrierGa	The strain asymmetry in a normal distribution (truncated to be between 0 and 1) for ^{69}Ga nuclei, for the inhomogeneous strain distribution	$\epsilon r\eta$STDValueBarrierGa	The standard deviation of the normal distribution for the major strain in the inhomogeneous strain distribution of ^{69}Ga nuclei

Supplementary Table 4. Description of variables used in the simulation relating to the major strain magnitudes and asymmetry.

Variable	Description	Variable	Description
Pn[“2.87T”, “σ+”]	Nuclear spin polarization degree induced through σ^+ optical pumping, with an external magnetic field of 2.87 T	Pn[“2.87T”, “σ-”]	Nuclear spin polarization degree induced through σ^- optical pumping, with an external magnetic field of 2.87 T
AHyperfine[“As”]	Hyperfine constant of ^{75}As	AHyperfine[“Ga”]	Hyperfine constant of ^{69}Ga
AsInBarrier	Fraction of ^{75}As nuclei that follow the inhomogeneous, rather than homogeneous, strain distribution	GaInBarrier	Fraction of ^{69}Ga nuclei that follow the inhomogeneous, rather than homogeneous, strain distribution
PhenScalFactorAs	Empirical factor which reduces the simulated inverse NMR signal for ^{75}As nuclei	PhenScalFactorGa	Empirical factor which reduces the simulated inverse NMR signal for ^{69}Ga nuclei

Supplementary Table 5. Description of variables used in the analysis relating to the degree of nuclear spin polarization, hyperfine interactions strength, strain distribution fractions, and empirical scaling factors.

[1] C. Heyn, A. Stemmann, T. Köppen, C. Strelow, T. Kipp, M. Grave, S. Mendach, and W. Hansen, Highly uniform and strain-free GaAs quantum dots fabricated by filling of self-assembled nanoholes, Applied Physics Letters **94**, 183113 (2009).

[2] P. Atkinson, E. Zallo, and O. G. Schmidt, Independent wavelength and density control of uniform GaAs/AlGaAs Quantum Dots Grown by infilling self-assembled nanoholes, Journal of Applied Physics **112**, 10.1063/1.4748183 (2012).

[3] D. Gammon, A. L. Efros, T. A. Kennedy, M. Rosen, D. S. Katzer, D. Park, S. W. Brown, V. L. Korenev, and I. A. Merkulov, Electron and nuclear spin interactions in the optical spectra of single GaAs quantum dots, Phys. Rev. Lett. **86**, 5176 (2001).

[4] B. Eble, O. Krebs, A. Lemaître, K. Kowalik, A. Kudelski, P. Voisin, B. Urbaszek, X. Marie, and T. Amand, Dynamic nuclear polarization of a single charge-tunable InAs/GaAs quantum dot, Phys. Rev. B **74**, 081306 (2006).

[5] J. Skiba-Szymanska, E. A. Chekhovich, A. E. Nikolaenko, A. I. Tartakovskii, M. N. Makhonin, I. Drouzas, M. S. Skolnick, and A. B. Krysa, Overhauser effect in individual InP/$Ga_xIn_{1-x}P$ dots, Phys. Rev. B **77**, 165338 (2008).

[6] A. Ulhaq, Q. Duan, E. Zallo, F. Ding, O. G. Schmidt, A. I. Tartakovskii, M. S. Skolnick, and E. A. Chekhovich, Vanishing electron g factor and long-lived nuclear spin polarization in weakly strained nanohole-filled GaAs/AlGaAs quantum dots, Phys. Rev. B **93**, 165306 (2016).

[7] G. Ragunathan, J. Kobak, G. Gillard, W. Pacuski, K. Sobczak, J. Borysiuk, M. S. Skolnick, and E. A. Chekhovich, Direct measurement of hyperfine shifts and radio frequency manipulation of nuclear spins in individual CdTe/ZnTe quantum dots, Phys. Rev. Lett. **122**, 096801 (2019).

[8] P. Millington-Hotze, H. E. Dyte, S. Manna, S. F. Covre da Silva, A. Rastelli, and E. A. Chekhovich, Approaching a fully-polarized state of nuclear spins in a solid, Nature Communications **15**, 10.1038/s41467-024-45364-2 (2024).

[9] E. A. Chekhovich, A. Ulhaq, E. Zallo, F. Ding, O. G. Schmidt, and M. S. Skolnick, Measurement of the spin temperature of optically cooled nuclei and GaAs hyperfine constants in GaAs/AlGaAs quantum dots, Nature Materials **16**, 982–986 (2017).

[10] F. Bloch, Nuclear induction, Phys. Rev. **70**, 460 (1946).

Chapter 5

Nuclear Spin Diffusion

Now that the strain within QDs has be investigated using NMR techniques, we can investigate the nuclear spin physics of the QD system. The pump-probe technique discussed in Section 2.5 is used to polarise nuclear spins; if III-V semiconductor QDs are to be used as electron spin qubits for quantum computing then it is essential that the spin dynamics of the system are understood, after optical pumping has occurred. If a QD were to exist that was both addressable via optical means and ideally responsive to RF pulses (nuclear spin state population transfer), but the nuclear states lasted for such a short duration that the system could not be read, then the QD would not be a useful spin qubit.

It has been hypothesised that the central spin of a localised electron within a QD could suppress NSD. This is because the hyperfine interaction of the central spin generates inhomogeneous Knight shifts in the nuclear spin energy levels, a phenomenon known as the Knight-field-gradient diffusion barrier. This would, naturally, be beneficial to the application of electron spin qubits; however, thus far the consensus in the literature is mixed as to whether this is a genuine effect ([144, 184, 185] argue for acceleration of NSD while [144, 160, 186–189] favour suppression). The argument for accelerated NSD is that the central spin allows for electron mediated spin flip-flops which would enhance the diffusion of spin away from the QD. In this chapter we focus on which of these two sources dominate the system, using an optical pump-probe cycle on a charge tunable GaAs/AlGaAs sample. The critical factor of this methodology is that, the QD can be determinately charged with/without an electron without altering the initial spin dynamics of the system, thereby directly investigating the effect of the electron on the nuclear spin system. Our measurements reveal that nuclear spin relaxation is accelerated by the presence of the electron, indicating that the Knight-field-gradient diffusion barrier does not apply to GaAs epitaxial QDs.

The work presented is in the form of a paper, which I am first author on, and has been published in a peer-reviewed journal on 9th May 2023, reproduced with permission from Springer Nature. The citation is:

P. Millington-Hotze, S. Manna, S. F. Covre da Silva, A. Rastelli, E. A. Chekhovich. “Nuclear

spin diffusion in the central spin system of a GaAs/AlGaAs quantum dot". *Nat Commun* **14**, 2677 (2023). doi: 10.1038/s41467-023-38349-0.

In this work the NMR experiments and analysis were conducted by Peter Millington-Hotze and Evgeny Chekhovich. The numerical modelling was conducted by Evgeny Chekhovich. The samples were grown by Santanu Manna, Saimon Covre da Silva and Armando Rastelli.

nature communications

Article

https://doi.org/10.1038/s41467-023-38349-0

Nuclear spin diffusion in the central spin system of a GaAs/AlGaAs quantum dot

Received: 5 August 2022

Accepted: 24 April 2023

Published online: 09 May 2023

Check for updates

Peter Millington-Hotze[1], Santanu Manna[2,3], Saimon F. Covre da Silva[2], Armando Rastelli[2] & Evgeny A. Chekhovich[1]

The spin diffusion concept provides a classical description of a purely quantum-mechanical evolution in inhomogeneously polarized many-body systems such as nuclear spin lattices. The central spin of a localized electron alters nuclear spin diffusion in a way that is still poorly understood. Here, spin diffusion in a single GaAs/AlGaAs quantum dot is witnessed in the most direct manner from oscillatory spin relaxation dynamics. Electron spin is found to accelerate nuclear spin relaxation, from which we conclude that the long-discussed concept of a Knight-field-gradient diffusion barrier does not apply to GaAs epitaxial quantum dots. Our experiments distinguish between non-diffusion relaxation and spin diffusion, allowing us to conclude that diffusion is accelerated by the central electron spin. Such acceleration is observed up to unexpectedly high magnetic fields – we propose electron spin-flip fluctuations as an explanation. Diffusion-limited nuclear spin lifetimes range between 1 and 10 s, which is sufficiently long for quantum information storage and processing.

Interacting many-body spin ensembles exhibit a variety of phenomena such as phase transitions[1,2] spin waves[3,4] and emergent thermodynamics[5,6]. Spin diffusion[7,8] is one of the earliest studied phenomena, where unitary quantum-mechanical evolution results in an irreversible dissipation of a localized spin polarization—a process that is well described by the classical diffusion model. Pure spin diffusion in homogeneous solids has been observed in a few notable examples[9,10]. However, most systems of interest are inhomogeneous by nature. In particular, magnetic (hyperfine) interaction with the central spin of a localized electron [Fig. 1a] causes shifts (known as the Knight shifts[11,12]) in the nuclear spin energy levels [Fig. 1b]. The resulting nuclear spin dynamics are complicated, as observed in a wide range of solid-state impurities[13–19] and semiconductor nanostructures[17,20–25]. Due to this complexity, it is still an open question whether the inhomogeneous Knight shifts accelerate[23,26,27] or suppress[16,25,27–30] spin diffusion between the nuclei. Resolving this dilemma is both of fundamental interest and practical importance for the recent proposals to use nuclear spins as quantum memories and registers[31–33], since spin diffusion would set an ultimate limit to the longevity of any useful quantum state. Beyond semiconductor nanostructures, understanding of spin diffusion plays an important role in NMR signal enhancement and structural analysis of polymers[34,35], biomolecules[36–38], proteins[39], and pharmaceutical formulations[40].

Figure 1 sketches the central spin model where an electron can be trapped in a GaAs layer surrounded by the AlGaAs barriers, and for simplicity, spin-1/2 particles are used to describe the energy levels of the nuclei subject to the strong external magnetic field B_z. Any two nuclear spins i and j are coupled by the dipole-dipole interaction $\propto 2\hat{I}_{z,i}\hat{I}_{z,j} - (\hat{I}_{x,i}\hat{I}_{x,j} + \hat{I}_{y,i}\hat{I}_{y,j})$, where $\hat{I}_{x,i}$,$\hat{I}_{y,i}$ and $\hat{I}_{z,i}$ are the Cartesian components of the spin operator $\mathbf{I}_i$ of the ith nucleus. The $\propto (\hat{I}_{x,i}\hat{I}_{x,j} + \hat{I}_{y,i}\hat{I}_{y,j})$ term describes a flip-flop spin exchange process (curved arrows at $z = -1$ and 0 in Fig. 1b), responsible for the transfer of spin polarization in space, known as spin diffusion. The electric quadrupolar moments of the spin-3/2 nuclei make them sensitive to electric field gradients (EFGs), which can be induced by the GaAs/AlGaAs interface roughness ($z = 4.5$) or atomic-scale strains arising

[1]Department of Physics and Astronomy, University of Sheffield, Sheffield S3 7RH, United Kingdom. [2]Institute of Semiconductor and Solid State Physics, Johannes Kepler University Linz, Altenberger Str. 69, Linz 4040, Austria. [3]Present address: Department of Electrical Engineering, Indian Institute of Technology Delhi, New Delhi 110016, India. e-mail: e.chekhovich@sheffield.ac.uk

https://doi.org/10.1038/s41467-023-38349-0

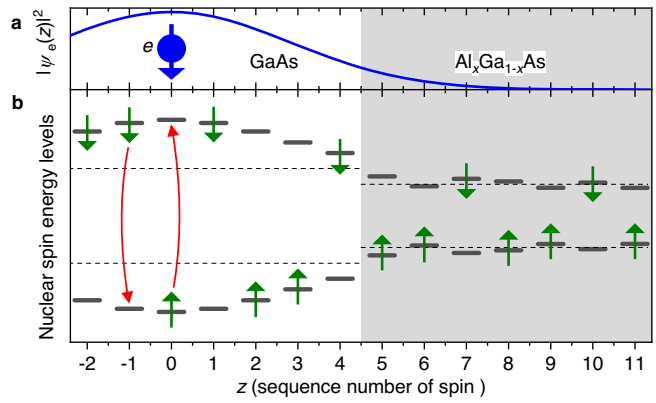

Fig. 1 | Schematic of a central spin model. The sketch is for the one-dimensional case, along the growth axis z of a GaAs/AlGaAs structure. **a** Wavefunction density $|\psi_e|^2$ of an electron (e, ball with arrow) localized in GaAs. **b** Energy levels of the nuclei, that are depicted for simplicity as spins 1/2, and can occupy states with +1/2 and −1/2 spin projections (up and down arrows). Dashed lines show the bulk nuclear spin energies dominated by the external magnetic field B_z. These bulk energies are generally different in GaAs ($z \le 4$) and AlGaAs ($z \ge 5$) due to the difference in chemical shifts and homogeneous strain. The energies of the individual nuclei are further shifted by the electron Knight field (mainly in GaAs) and by the atomic-scale strain disorder in the AlGaAs alloy. Magnetic-dipole interaction between the nuclei can result in spin exchange via a flip-flop process, sketched by the curved arrows for nuclei at $z = -1$ and $z = 0$ as an example. If energy mismatch is larger than the nuclear spin level homogenous broadening, for example for nuclei at $z = 4$ and $z = 5$, the spin exchange becomes prohibited, suppressing nuclear spin diffusion.

from random positioning of the aluminium atoms[41,42] in AlGaAs ($z \ge 5$). These quadrupolar effects lead to mismatches in the energy splittings of adjacent nuclei, which in turn impede the nuclear spin diffusion.

When an electron is added, its spin **s** couples to the nuclear spin ensemble via hyperfine interaction:

$$\hat{H}_{\rm hf} = \sum_j A_j(\hat{s}_x\hat{I}_{x,j} + \hat{s}_y\hat{I}_{y,j} + \hat{s}_z\hat{I}_{z,j}), \quad (1)$$

where the summation goes over all nuclei j, and the coupling energies A_j are proportional to the electron density $|\psi_e(\mathbf{r}_j)|^2$ at the nuclear sites $\mathbf{r}_j$. There are two competing effects of the hyperfine interaction. On the one hand, through the term $\hat{s}_z\hat{I}_z$, the electron spin can produce a further diffusion barrier[16,25,27–30], at the points of strong Knight shift gradient ($z = 3$ in Fig. 1a). On the other hand, the electron spin can mediate spin flip-flops between two distant nuclei with similar energy splitting (e.g., $z = -2$ and $z = 2$), potentially opening a new channel for spin diffusion, especially at low magnetic fields[23,26,27]. Both of these effects have been known for decades, and both were claimed to be dominant in different previous studies, often without giving consideration to the other alternative. The main purpose of this study is to settle this dilemma through systematic experimental work.

Here, we examine electron-controlled nuclear spin diffusion in high-quality epitaxial GaAs/AlGaAs quantum dots (QDs), which emerged recently as an excellent platform for quantum light emitters[43–45] as well as spin qubits[33,46] and quantum memories[32]. Crucially, we design experiments where nuclear spin dynamics are examined either in the absence or in the presence of the electron central spin, but under an otherwise identical initial nuclear spin state. In this way, we distinguish with high accuracy the effects specific to the electron spin. This allows us to demonstrate that no observable Knight-field-gradient diffusion barrier is formed. Instead, the nuclear–nuclear interactions, mediated by the electron spin, accelerate nuclear spin diffusion up to unexpectedly high magnetic fields—we attribute this to the impact of the electron spin flips. Our results answer a long-standing question in spin physics, and provide practical guidelines for the design and optimization of quantum dot electron-nuclear spin qubits and quantum memories.

Results

Sample and experimental techniques

The studied heterostructure is grown by in situ etching of nanoholes[47,48] in the AlGaAs surface [Fig. 2a, b], which are then infilled with GaAs to form the QDs. The structure is processed into a $p-i-n$ diode [Fig. 2c] where an external bias $V_{\rm Gate}$ is applied to charge QDs deterministically with individual electrons (See details in Supplementary Note 1). In this way, it is possible to study nuclear spin dynamics in an empty ($0e$) or single electron ($1e$) state. A static magnetic field B_z is applied along the growth axis z (Faraday geometry) and the sample is kept at a liquid helium temperature of 4.3 K. We use a confocal microscopy configuration where QD photoluminescence (PL) is excited and collected through an aspheric lens with a focal distance of 1.45 mm and numerical aperture of 0.58. The collected PL is dispersed in a two-stage grating spectrometer, and recorded with a charge-coupled device (CCD) camera.

The change in the PL spectral splitting $\Delta E_{\rm PL}$ of a negatively charged trion X^- [see Fig. 2d] is the hyperfine shift $E_{\rm hf}$, which gives a measure of an average spin polarization degree of the $\approx 10^5$ QD nuclei[12]. The hyperfine shifts (also known as Overhauser shifts) arise from the $\hat{s}_z\hat{I}_z$ term of the hyperfine interaction Hamiltonian [Eq. (1)]. Large nonequilibrium nuclear spin polarization is generated on demand by exciting the QD with a circularly polarized pump laser[12], which repeatedly injects spin-polarized electrons into a QD, and causes nuclear spin polarization build up via electron-nuclear spin flip-flops described by the $\hat{s}_x\hat{I}_x + \hat{s}_y\hat{I}_y$ part of Eq. (1). A small copper wire coil is placed near the sample to produce radiofrequency (RF) oscillating magnetic field perpendicular to the static magnetic field. Application of the RF field allows for the energy spectrum of the nuclear spins to be probed via nuclear magnetic resonance (NMR). Moreover, the RF field can be used to depolarize the nuclear spins on demand. Further details can be found in Supplementary Note 2, including sample growth details, PL spectra, characterization of QD charge state control, and additional results at an elevated temperature of 15.2 K.

Nuclear spin system of a GaAs quantum dot

Figure 2e shows NMR spectra of ^{75}As in a single GaAs QD, measured using the "inverse NMR" technique with an optical Pump-RF-Probe cycle shown in the top inset. For an empty QD (open symbols), an NMR triplet is observed[49], corresponding to the three magnetic-dipole transitions between the four Zeeman-split states $I_z = \{-3/2, -1/2, +1/2, +3/2\}$ of a spin-3/2 nucleus (left inset). The central resolution-limited peak originates from the $-1/2 \leftrightarrow +1/2$ NMR transition that is weakly affected by strain. The two satellite transition peaks $\pm 1/2 \leftrightarrow \pm 3/2$ are split from the central transition peak by the strain-induced EFGs. The average splitting $\nu_Q \approx 24$ kHz between the triplet components corresponds to an average elastic strain of $\approx 2.6 \times 10^{-4}$ (refs. 50,51). The satellite transitions are inhomogeneously broadened, with non-zero NMR amplitudes detected approximately in a range of $\nu_Q \in [10, 50]$ kHz, indicating that elastic strain varies within the nanoscale volume of the QD. The ^{69}Ga and ^{71}Ga nuclear spins are also affected by the strain, but the quadrupolar shifts ν_Q are smaller by a factor of ≈2 and ≈3, respectively[50–52].

When a single electron occupies the QD, it induces inhomogeneous Knight shifts that exceed the quadrupolar shifts, leading to a broadened NMR peak [solid symbols in Fig. 2e]. From the NMR peak width, the Knight frequency shifts, characterizing the typical coupling strength between the electron spin and an individual nuclear spin, are estimated to be $A_j/(2h) \approx 50$ kHz, where h is Planck's constant.

These NMR characterization results indicate a complex interplay of dipolar, quadrupolar, and hyperfine interactions governing the nuclear spin dynamics, which we now investigate experimentally.

https://doi.org/10.1038/s41467-023-38349-0

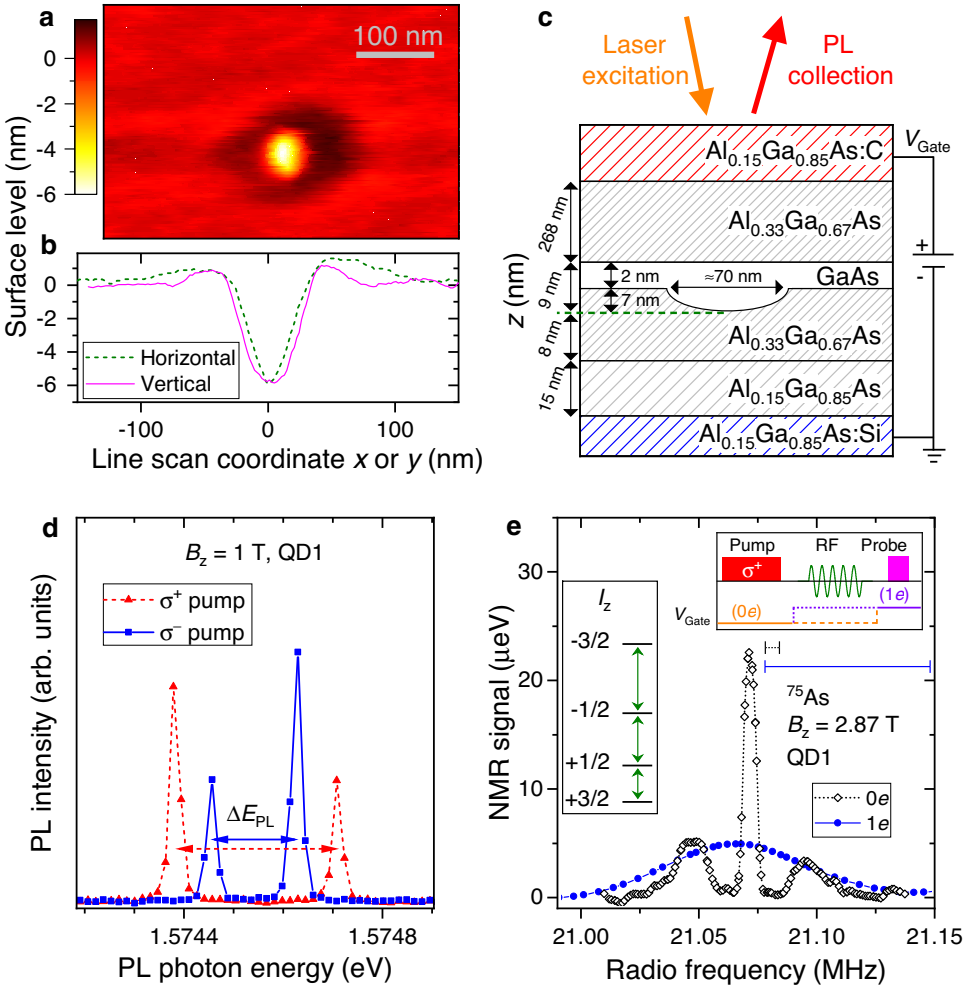

Fig. 2 | Optically active epitaxial GaAs/AlGaAs quantum dots. a Atomic force microscopy (AFM) profile of the AlGaAs surface after nanohole etching. **b** Surface level profiles taken along the horizontal and vertical lines through the center of the nanohole in (**a**). **c** Schematic (not to scale) of the sample structure. GaAs QDs are formed by infilling of the in situ etched nanoholes in the bottom $Al_{0.33}Ga_{0.67}As$ barrier. The bottom (top) $Al_{0.15}Ga_{0.85}As$ layer is n (p) type doped to form a $p-i-n$ diode structure. External gate bias V_{Gate} is applied for deterministic QD charging with electrons. **d** Photoluminescence (PL) spectra of a negatively charged trion X^-, following either σ^+ (triangles) or σ^- (squares) optical pumping, which induces nuclear spin polarization. This polarization manifests in hyperfine shifts E_{hf} of the Zeeman doublet spectral splitting ΔE_{PL}. **e** Optically detected NMR of the ^{75}As spin-3/2 nuclei measured in a single QD. Strain-induced quadrupolar shifts of the nuclear spin-3/2 levels (left inset) give rise to an NMR triplet with splitting $\nu_Q \approx 24$ kHz, observed in an empty QD (0e, diamonds). Charging the QD with a single electron (1e, circles) induces inhomogeneous Knight shifts observed as NMR spectral broadening. The measurement is conducted using the "inverse NMR" signal amplification technique[68], with spectral resolution shown by the horizontal bars (smaller for 0e and larger for 1e). The measurement Pump-RF-Probe cycle is shown in the top inset. The bias V_{Gate} is tuned to 0e charge state for the optical pumping of the nuclear spins and to 1e state for their optical probing. The radio-frequency (RF) pulse is applied in the dark under either 0e or 1e bias.

Observation of nuclear spin diffusion in a GaAs quantum dot

While nuclear spin diffusion is a well-known phenomenon, its direct observation is rarely possible[9,10]. Thus we start with an experiment that reveals spin diffusion in a QD structure in a most convincing manner. The measurement cycle [see timing diagram in Fig. 3a] starts with a long σ^+ polarized optical pump. It creates a negative nuclear polarization degree P_N that diffuses out of the QD into the surrounding material. The resulting spatial profile of $P_N(z)$ is depicted in the left-most sketch in Fig. 3b. Then, a much shorter σ^- pump is applied. This second pump is too short for diffusion to take place, so a positive P_N is localized only in a QD, while the surrounding remains negatively polarized (second sketch in Fig. 3b). This two-stage pumping (similar to "hole burning" implemented previously in shallow donors[15]) is followed by a dark time T_{Dark}. Finally, the remaining polarization within the QD volume (i.e., around $z = 0$) is probed through an optically detected hyperfine shift E_{hf}. The measured dependence $E_{hf}(T_{Dark})$ is plotted in Fig. 3b and shows non-monotonic spin dynamics. A sign-reversal occurs at $T_{Dark} \approx 10$ s when the negative P_N, induced by the first pump and stored in the surrounding barriers, refluxes back into the QD. This diffusion reflux peaks around $T_{Dark} \approx 100$ s where E_{hf} reaches its minimum. At even longer T_{Dark} nuclear spin polarization decays monotonically towards $E_{hf} \approx 0$.

We point out that the thermal-equilibrium hyperfine shifts are very small $|E_{hf}| \lesssim 0.15$ μeV, so that, any non-zero E_{hf} can only arise from dynamical nuclear spin polarization. The non-diffusion nuclear spin relaxation (NSR) mechanisms, such as direct spin-lattice coupling and hyperfine interaction with electrons, can only lead to monotonic decay of E_{hf} towards ≈0. Spatial transfer of polarization is the only mechanism that can produce non-monotonic free evolution and sign-reversal of E_{hf}. Another way to describe the diffusion reflux experiment is to note that switching between σ^+ and σ^- essentially corresponds to time-oscillating nuclear spin pumping, which creates a wave-like initial spatial profile. In the subsequent free evolution, this spatial polarization wave is converted back into temporal oscillations of nuclear polarization at the QD site. To our knowledge, such oscillating spin relaxation

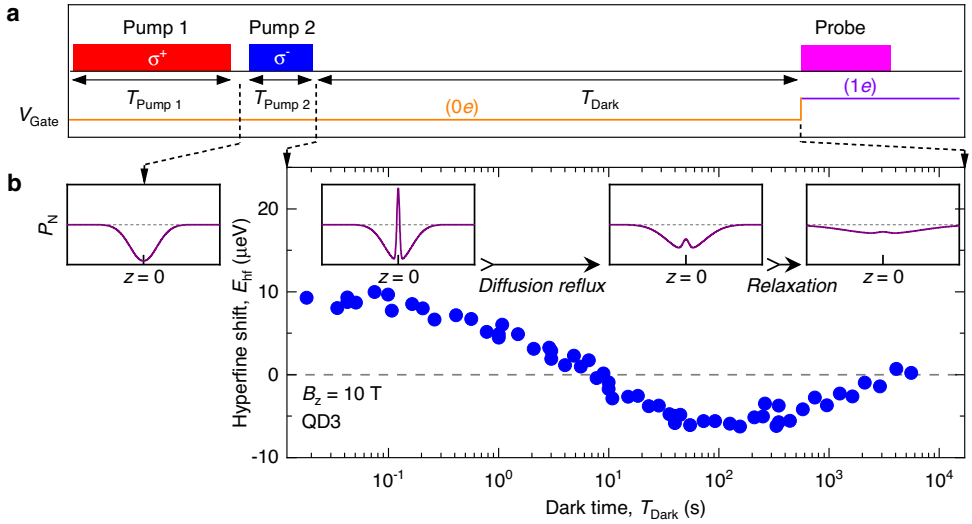

Fig. 3 | Oscillatory nuclear spin relaxation due to spin diffusion reflux. a The measurement cycle starts with a σ^+ polarized laser pump pulse that generates negative nuclear spin polarization with a steady-state hyperfine shift $E_{hf} \approx -36$ μeV. As demonstrated below, this first pump is long enough ($T_{Pump\,1} = 90$ s) for spin polarization induced in the QD to diffuse into the surrounding AlGaAs barriers. This is followed by the second σ^- pump, which is kept short ($T_{Pump\,2} = 0.1$ s) in order to create an inverted positive ($E_{hf} \approx +10$ μeV) nuclear spin polarization localized to the QD volume only. Nuclear spin polarization prepared in this way is then allowed to evolve freely over the variable dark time T_{Dark} while keeping the QD empty of any charges (0*e*) through a large reverse gate bias V_{Gate}. Finally, a short probe laser pulse induces photoluminescence (PL). The hyperfine shifts E_{hf} detected in PL spectra provide a measure of the average polarization of ≈10^5 QD nuclear spins, weighted by the QD electron density $|\psi_e|^2$. **b** Dark time dependence of the hyperfine shift E_{hf} measured in an individual QD3 reveals non-monotonic (oscillating) nuclear spin relaxation. This indicates a diffusion reflux where spin polarization induced by the first pump pulse and stored in the surrounding barriers, diffuses back into the QD. The four insets sketch the spatial profiles $P_N(z)$ of the nuclear spin polarization degree following the two pump pulses and at the different stages of nuclear spin relaxation. The QD is located at $z = 0$.

gives by far the most direct evidence of nuclear spin diffusion between an individual QD and its surrounding.

Nuclear spin relaxation in a GaAs quantum dot

We now proceed to quantitative NSR measurements with a timing diagram shown in Fig. 4a. First, any remnant nuclear spin polarization is erased by saturating the ^{75}As, ^{69}Ga, and ^{71}Ga NMR resonances in the entire heterostructure[53]. This is followed by a single variable-duration (T_{Pump}) optical pumping pulse[15,17,20,22]. In order to localize the nuclear spin polarization to the QD nanoscale volume, we choose the pump photon energy to be below the AlGaAs barrier bandgap. After the pump laser is turned off, the gate bias V_{Gate} is set to a desired level for a dark time T_{Dark}—this way evolution under 0*e* or 1*e* QD charge state is studied for nominally identical initial nuclear spin polarizations. Finally, E_{hf} is measured optically, which provides nuclear spin polarization averaged over all nuclei of the QD. The relative isotope contributions to E_{hf} arising from ^{75}As, ^{69}Ga, and ^{71}Ga are ≈49, 28, and 23%, respectively[54].

Figure 4b shows the average QD nuclear spin polarization as a function of the pump-probe delay T_{Dark} during which the sample is kept in the dark. The decay is non-exponential, thus we characterize the NSR timescale $T_{1,N}$ by the half-life time over which the QD hyperfine shift E_{hf} decays to 1/2 of its initial value. The NSR rate is then defined as $\Gamma_N = 1/T_{1,N}$. When the pumping time T_{Pump} is increased, $T_{1,N}$ notably increases, as can be seen in Fig. 4c, d. Such dependence of $T_{1,N}$ on T_{Pump} is observed both in empty (0*e*) and charged (1*e*) QD states, and in a wide range of magnetic fields.

Relaxation dominated by nuclear spin diffusion

In order to explain the results of Fig. 4, we note that nuclear spin dipole-dipole interactions conserve the nuclear spin polarization for any magnetic field exceeding the dipolar local field, typically ≲1 mT. Therefore, at a high magnetic field the decay of nuclear spin polarization can proceed via two routes: either via spin-conserving diffusion to the surrounding nuclei, or spin transfer to external degrees of freedom, including quadrupolar coupling to lattice vibrations[16,55] or a hyperfine interaction with a charge spin[16,56–58] that is in turn coupled to the lattice or other spins. Spin diffusion can only take place if the spatial profile of the initial nuclear spin polarization is inhomogeneous, as exemplified in the reflux experiment in Fig. 3. By contrast, direct spin-lattice and hyperfine interactions have no explicit dependence on the spin polarization spatial profile. Optical pumping time T_{Pump} that is short compared to spin diffusion timescales creates nuclear spin polarization localized to the QD volume[15,17,20,22]. Therefore, observation of short $T_{1,N}$ at short T_{Pump} is a clear indicator that spin diffusion is the dominant NSR mechanism in the studied QDs. Conversely, if the pumping duration T_{Pump} is long, there is enough time for nuclear polarization to diffuse from the QD into the surrounding AlGaAs barriers, suppressing any subsequent spin diffusion out of the QD and increasing $T_{1,N}$, as observed in Fig. 4c, d.

In order to complement our experimental investigation we model the spatiotemporal evolution of the nuclear spin polarization degree $P_N(t, z)$ by solving numerically the one-dimensional spin diffusion equation

$$\frac{\partial P_N(t,z)}{\partial t} = D(t)\frac{\partial^2 P_N(t,z)}{\partial z^2} + w(t)|\psi_e(z)|^2(P_{N,0} - P_N(t,z)), \qquad (2)$$

where the last term describes optical nuclear spin pumping with a rate proportional to electron density $|\psi_e(z)|^2$ and the time-dependent factor $w(t)$ equal to 0 or w_0 when optical pumping is off or on, respectively. Correspondingly, the spin diffusion coefficient $D(t)$ takes two discrete values D_{Dark} or D_{Pump} when optical pumping is off or on, respectively. $P_{N,0}$ is a steady-state nuclear spin polarization degree that optical pumping would generate in the absence of spin diffusion. Eq. (2) is solved numerically and the parameters such as $D^{(ne)}_{Dark}$, $w_0(B_z)$, $D_{Pump}(B_z)$ are varied to achieve the best fit to the entire experimental datasets of $E_{hf}(T_{Pump}, T_{Dark})$ measured at $B_z = 0.39$ and 9.82 T for empty ($n = 0$) and charged ($n = 1$) QD states. The best fit calculated dynamics are shown by the lines in Fig. 4b and capture well the main features of the

https://doi.org/10.1038/s41467-023-38349-0

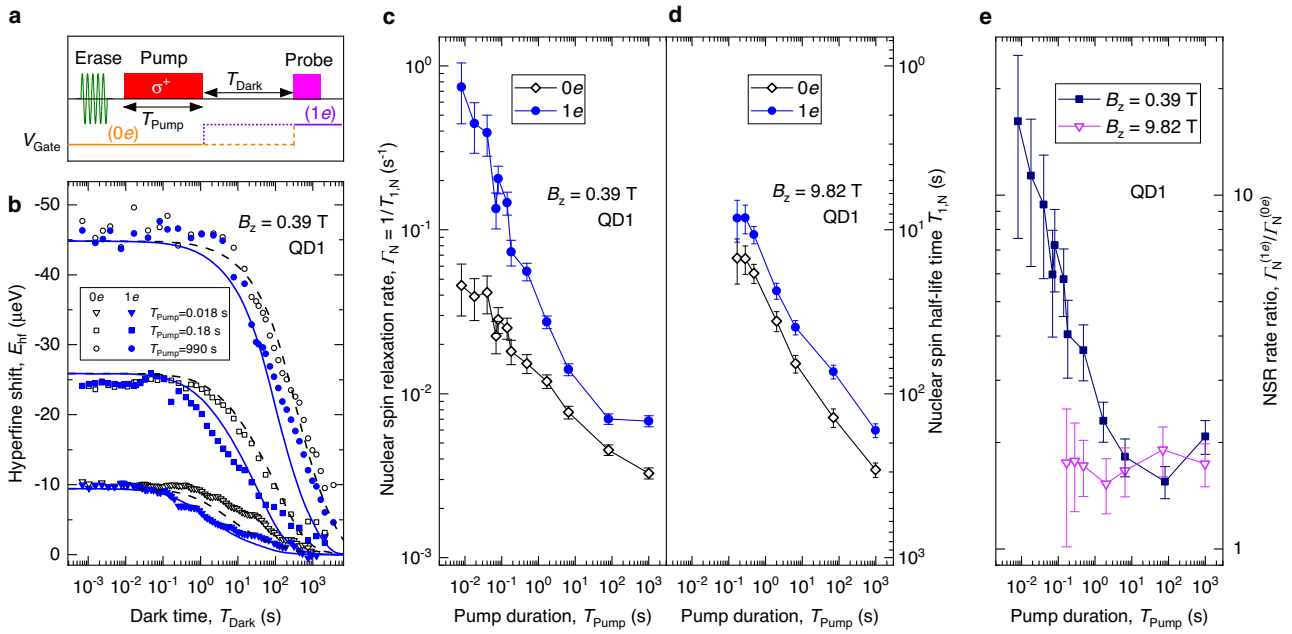

Fig. 4 | Nuclear spin relaxation in a quantum dot. a NSR measurement cycle starting with a radiofrequency erase pulse, followed by circularly polarized (σ^+) optical pumping and then optical probing of the QD nuclear spin polarization after dark evolution delay T_{Dark} (see details in Supplementary Note 2). The sample gate bias V_{Gate} is varied throughout the experiment cycle. During T_{Dark} the bias can be set to achieve either 0*e* (dashed line) or 1*e* (dotted line) QD charge state. **b** Dark time dependence of the hyperfine shift E_{hf}. The nuclear spin decay is measured (symbols) at $B_z = 0.39$ T for different pumping times T_{Pump} while keeping the QD empty (0*e*, open symbols) or charged with one electron (1*e*, solid symbols) during the dark time. Lines show the numerical solution of the spin diffusion equation [Eq. (2)]. **c** Fitted QD nuclear spin half-lifetimes $T_{1,N}$ (right scale) and the corresponding NSR rates $\Gamma_N = 1/T_{1,N}$ (left scale) measured as a function of the pumping time T_{Pump} at magnetic field $B_z = 0.39$ T. **d** same as (**c**) for $B_z = 9.82$ T. **e** Ratio $\Gamma_N^{(1e)}/\Gamma_N^{(0e)}$ of the NSR rates in 1*e* and 0*e* charge states as a function of T_{Pump} measured at $B_z = 0.39$ T (squares) and $B_z = 9.82$ T (triangles). All results are for the same individual dot QD1. Error bars are 95% confidence intervals.

experimentally measured nuclear spin decay, confirming the validity of the spin diffusion picture. The one-dimensional character of diffusion, occurring predominantly along the sample growth *z* direction, is justified by the large ratio of the QD diameter ≈70 nm to QD height < 9 nm, and is further verified by modeling two-dimensional spin diffusion (see Supplementary Note 4).

Effect of central spin on nuclear spin diffusion

Dividing the typical Knight shift of ≈50 kHz by half the QD thickness (4.5 nm) we calculate the gradient and roughly estimate the Knight shift difference of ≈4.4 kHz for the two nearest-neighbor spins of the same isotope separated by $a_0/\sqrt{2}$ (here, $a_0 = 0.565$ nm is the lattice constant). The energy corresponding to such a difference significantly exceeds the energy that can be exchanged with the nuclear dipole-dipole reservoir for a spin flip-flop to happen[25] (the dipole-dipole energy is on the order of $\approx h/T_{2,N}$, where $T_{2,N} \in [1, 5]$ ms is the nuclear spin-echo coherence time[33,59]). The flip-flops would then be limited to the few nuclear spin pairs whose vector differences are nearly orthogonal to the Knight field gradient. Therefore, one may naively expect a Knight-field-gradient barrier to form and suppress spin diffusion in an electron-charged QD. By contrast, Fig. 4c, d show that in an experiment the NSR is faster when the QD is occupied by a single electron (1*e*, solid symbols) for all studied T_{Pump}, demonstrating that no significant Knight-field-gradient barrier is formed. However, in order to quantify the effect of the central spin on nuclear spin diffusion we must distinguish it from other non-diffusion NSR mechanisms introduced by the electron spin. To this end, we examine the magnetic field dependence shown in Fig. 5.

First, we examine a case where long optical pumping is used to suppress spin diffusion, thus highlighting the non-diffusion NSR mechanisms. Figure 5a shows the experimental dependence $\Gamma_N(B_z)$ for long $T_{Pump} = 990$ s. The results indicate that in an empty QD (0*e*) spin diffusion is still the dominant NSR mechanisms at $T_{Pump} = 990$ s. Indeed, the observed rates $\Gamma_N^{(0e)} \in [1\times10^{-3}, 6\times10^{-3}]\ s^{-1}$ are considerably higher than those found in bulk crystal experiments[55], where spin diffusion is negligible, resulting in relaxation rates as low as $\Gamma_N \approx 6\times10^{-5}$ in semi-insulating GaAs[16]. The electron-induced (1*e*) rates under long pumping $\Gamma_N^{(1e)} \in [4\times10^{-3}, 2\times10^{-2}]\ s^{-1}$ are nearly independent of B_z, and exceed the 0*e* rates by no more than a factor of $\Gamma_N^{(1e)}/\Gamma_N^{(0e)} < 4$ [squares in Fig. 5c]. Such a small effect of the electron is explained by the small strain of the GaAs/AlGaAs structures, which reduces the efficiency of the non-diffusion NSR mechanisms related to phonon and electron cotunneling. This is in stark contrast to the large magnetic field-induced variation $\Gamma_N^{(1e)} \in [5\times10^{-4}, 1\times10^{1}]\ s^{-1}$ in Stranski–Krastanov self-assembled InGaAs QDs[58], where phonon and cotunneling non-diffusion mechanisms dominate, both enabled by the noncollinear hyperfine interaction[56,58], arising in turn from the large strain-induced nuclear quadrupolar shifts.

In the case of long optical pumping, the NSR rates are nearly constant, exhibiting only a small irregular dependence on the magnetic field [Fig. 5a]. The long-pumping absolute NSR rates are also consistent across different individual QDs, as demonstrated in Fig. 5b. The main reason for the residual scatter in Fig. 5a, b is the dot-to-dot variation and magnetic field dependence of the QD optical absorption spectrum. As a result, the same optical pump power and wavelength lead to a different nuclear spin pumping rate, which affects the initial spatial profile of the nuclear spin polarization and the subsequent spin diffusion dynamics. Other uncontrollable parameters may include the charge state of the nearby impurities. While the absolute NSR rates $\Gamma_N^{(1e)}$ and $\Gamma_N^{(0e)}$ are subject to uncontrollable effects, their ratio $\Gamma_N^{(1e)}/\Gamma_N^{(0e)}$ is a robust quantity. This is exemplified in Fig. 4e, where at high magnetic field $B_z = 9.82$ T (triangles) the rate ratio is seen to be constant, even though the absolute rates depend strongly on T_{Pump} (Fig. 4d). At low $B_z = 0.39$ T there is a significant dependence of $\Gamma_N^{(1e)}/\Gamma_N^{(0e)}$ on the pumping time T_{Pump} (squares in Fig. 4e). Therefore, we use the

https://doi.org/10.1038/s41467-023-38349-0

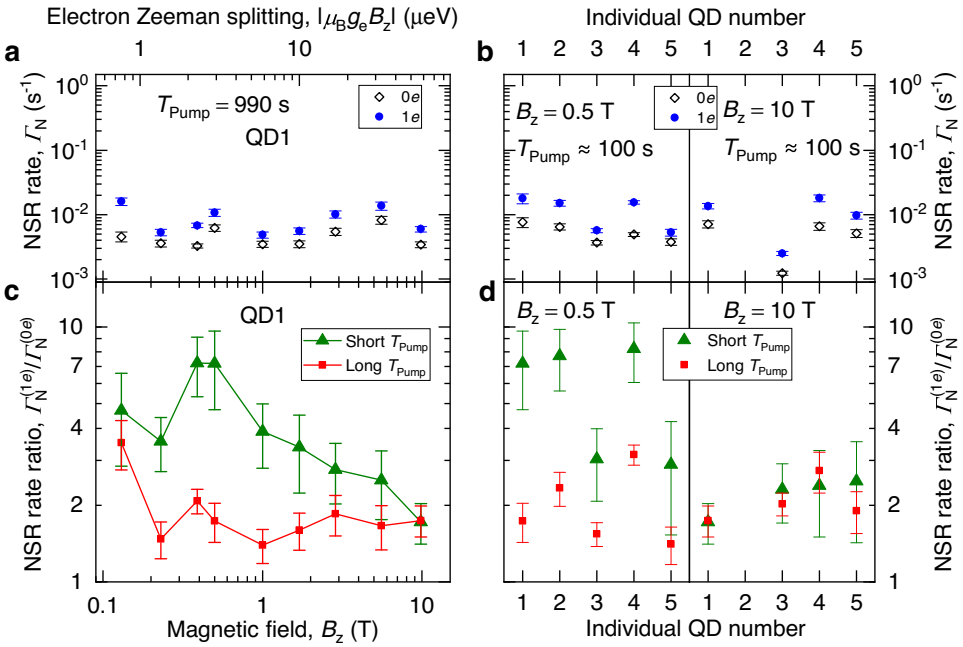

Fig. 5 | Magnetic field dependence of spin diffusion. a Nuclear spin relaxation (NSR) rate Γ_N as a function of B_z measured in 0*e* (open symbols) and 1*e* (solid symbols) QD charge states upon long pumping T_{Pump} = 990 s. The top horizontal axis shows the electron Zeeman splitting at zero nuclear spin polarization. **b** Γ_N for different individual dots QD1-QD5 at B_z = 0.5 T (left) and B_z = 10 T (right) measured with a long pumping time T_{Pump} = 70–100 s. **c** Ratio $\Gamma_N^{(1e)}/\Gamma_N^{(0e)}$ of the NSR rates in 0*e* and 1*e* charge states as a function of B_z measured under long pumping T_{Pump} = 990 s (squares) and short pumping $T_{Pump} \in [0.08, 0.6]$ s (triangles). **d** Ratio $\Gamma_N^{(1e)}/\Gamma_N^{(0e)}$ for QD1-QD5 at B_z = 0.5 T (left) and B_z = 10 T (right). Short pumping is $T_{Pump} \in [0.08, 0.6]$ s, whereas long-pumping time is T_{Pump} = 990 s for QD1-QD2 and T_{Pump} = 100 s for the remaining QDs. Error bars are 95% confidence intervals.

$\Gamma_N^{(1e)}/\Gamma_N^{(0e)}$ ratio to gauge the electron spin's effect on NSR, including its impact on spin diffusion.

In order to discriminate the diffusion-related effect of the QD electron spin, in addition to the long-pumping measurements discussed above [squares in Fig. 5c], we choose for each magnetic field a short pumping time, typically $T_{Pump} \in [0.08, 0.6]$ s, that yields initial QD nuclear spin polarization at ≈1/2 of the steady-state long-pumping polarization. The resulting short-pumping ratio $\Gamma_N^{(1e)}/\Gamma_N^{(0e)}$ is shown by the triangles in Fig. 5c. The ratio $\Gamma_N^{(1e)}/\Gamma_N^{(0e)}$ combines all the electron-induced effects. However, the significant excess of the short-pumping ratio $\Gamma_N^{(1e)}/\Gamma_N^{(0e)}$ [triangles in Fig. 5c] over the long-pumping ratio $\Gamma_N^{(1e)}/\Gamma_N^{(0e)}$ [squares in Fig. 5c] is ascribed to spin diffusion alone, discriminating it from any non-diffusion mechanisms introduced by the electron spin. The electron spin-induced acceleration of the nuclear spin diffusion is seen to be particularly pronounced at low magnetic fields $B_z \lesssim 0.5$ T, consistent with the influence of the electron-mediated nuclear–nuclear spin interaction[23,26,27]. Such pairwise indirect interaction of nuclei *j* and *k* is derived from the second-order perturbation expansion of Eq. (1):

$$\mathcal{H}_{hf,j,k}^{ind} \propto \frac{A_j A_k}{\Delta E_e} \hat{s}_z \hat{I}_j^{(+)} \hat{I}_k^{(-)}, \quad (3)$$

where $\hat{I}_j^{(\pm)} = \hat{I}_{x,j} \pm i\hat{I}_{y,j}$ and $\Delta E_e = \mu_B g_e B_z + E_{hf}$ is the electron spin splitting due to both the Zeeman effect and the nuclear spin-induced hyperfine shift E_{hf}. In our experiments, both contributions are negative, so that any nuclear spin pumping increases $|\Delta E_e|$. The rate of the indirect nuclear–nuclear spin flip-flops scales as $\propto \Delta E_e^{-2}$. Consequently, the resulting acceleration of nuclear spin diffusion in gate-defined GaAs QDs was previously found to be limited to the low fields $B < 0.02$–0.75 T (refs. 23,27,60). By contrast, Fig. 5c shows that such acceleration persists at unexpectedly high magnetic fields, well above $B_z \gtrsim 2$ T. The short- and long-pumping $\Gamma_N^{(1e)}/\Gamma_N^{(0e)}$ ratios converge only at the maximum field B_z = 9.82 T.

Figure 5d shows $\Gamma_N^{(1e)}/\Gamma_N^{(0e)}$ for five different QDs in the same sample. Since it is too time-consuming to measure full dependence, a fixed T_{Pump} was chosen for each QD, which inevitably leads to variation in the actual $\Gamma_N^{(1e)}/\Gamma_N^{(0e)}$ ratios. However, for all QDs, we observe an excess of the short-pumping ratios over the long-pumping ratios at B_z = 0.5 T, which becomes negligible at B_z = 10 T. This confirms that electron-induced acceleration of nuclear spin diffusion is a systematic effect.

Acceleration of spin diffusion at high magnetic fields

We now examine why the electron-induced acceleration of nuclear spin diffusion is observed at high magnetic fields. The electron *g*-factor in the studied epitaxial QDs is $g_e \approx -0.1$ (see Supplementary Note 2), much smaller than $g_e \approx -0.4$ in the gate-defined QDs. Moreover, the number of nuclei is an order of magnitude smaller in our epitaxial QDs. These factors result in a smaller $|\Delta E_e|$ and larger A_j, respectively, which should lead to a stronger hyperfine-mediated coupling in the studied QDs (Eq. (3)). However, this difference does not explain the magnetic field dependence. At high field B_z = 9.82 T the electron spin Zeeman splitting is $|\Delta E_e| \approx 58$ μeV. At low field B_z = 0.39 T we take into account both the Zeeman splitting ≈ −2.3 μeV and the time-averaged hyperfine shift $E_{hf} \approx -2.5$ μeV (half of the initial $E_{hf} \approx -5$ μeV under the shortest used $T_{Pump} \approx 8$ ms) to estimate $|\Delta E_e| \approx 4.8$ μeV. This suggests a factor of $(58/4.8)^2 \approx 150$ reductions in the hyperfine-mediated rates. However, the measured short-pumping NSR rate for QD1 reduces only by a factor of ≈ 6 from $\Gamma_N^{(1e)} \approx 0.74\ s^{-1}$ at low field [Fig. 4c] to $\Gamma_N^{(1e)} \approx 0.12\ s^{-1}$ at high field [Fig. 4d]. Prompted by these observations, we point out that Eq. (3) treats the central electron spin as isolated, while in a real system, the electron is coupled to external environments such as phonons and other charges.

A fluctuating electron spin can accelerate nuclear spin diffusion, provided there is a frequency component in the time-dependent Knight field that equals the energy mismatch of a pair of nuclei[61,62]. This contribution has been considered for deep impurities[14], and, as we now

discuss, should also be taken into account in the context of III-V semiconductor nanostructures. Electron spin flips are always present due to phonons and cotunneling coupling to the electron Fermi reservoir of the *n*-doped layer[58,63,64]. It is worth noting that the acceleration of spin diffusion discussed in this paragraph is distinct from the non-diffusion NSR mechanisms, where the phonon bath and Fermi reservoir act as a sink for the nuclear spin momentum, carried through the electron spin. Preliminary studies of the relaxation dynamics are conducted using single-shot readout of the electron spin via nuclei[65] (see Supplementary Note 5, details to be reported elsewhere). Electron spin lifetimes are found to be $T_{1,e} \approx 7$ ms at $B_z = 2$ T, reducing to $T_{1,e} \approx 0.5$ ms at $B_z = 7$ T. The electron flips are dominated by phonons and occur as abrupt jumps (telegraph process). Hence the Knight field should have a significant spectral density around the [1, 10] kHz range, matching the typical differences in the nuclear spin energies found from NMR spectra of Fig. 2e. Thus we speculate that the electron spin flips contribute to the acceleration of nuclear spin diffusion in the studied GaAs QDs, especially at high magnetic fields. In other words, the widely used model of hyperfine-mediate nuclear–nuclear interactions [Eq. (3)] considers only the zero-frequency component, whereas our data suggest that the entire electron spin fluctuation spectrum must be included. Our explanation is supported by numerical modeling (Supplementary Note 4), which yields a significant increase in the nuclear spin diffusion coefficients under optical pumping $D_{\mathrm{Pump}} \gg D_{\mathrm{Dark}}$ where electron spin flips are accelerated[66]. Future work may address this phenomenon through the measurement of nuclear spin diffusion under simultaneous flipping of the central electron spin with microwave pulses.

Comparison with previous results on nuclear spin diffusion

In order to understand what controls the rate of spin diffusion we first make a comparison with Stranski–Krastanov InGaAs/GaAs and InP/GaInP self-assembled QDs, where quadrupolar shifts are so large (MHz range[67,68]) that all nuclear spins are essentially isolated from each other, eliminating spin diffusion and resulting in very long nuclear spin lifetimes $T_{1,\mathrm{N}}^{(0e)} > 10^4$ s in empty (0*e*) QDs[26,29,56,56,58,69,70]. Even in the presence of the electron spin (1*e*) the nuclear spin diffusion takes place only inside the QD[26,56], without diffusion into the surrounding material.

In the lattice-matched GaAs QDs, the strain-induced effects are smaller but not negligible, characterized by quadrupolar shifts ν_{Q} ranging approximately between 10 and 50 kHz within the QD, as revealed by NMR spectra in Fig. 2e. Nuclei in $I_z = \pm 1/2$ and $|I_z| > 1/2$ states must be considered separately. The central transition between the $I_z = -1/2$ and $+1/2$ spin states is affected only by the second-order quadrupolar shifts, which scale as $\propto \nu_{\mathrm{Q}}^2/\nu_{\mathrm{L}}$ and are within a few kHz for the studied range of nuclear spin Larmor frequencies $\nu_{\mathrm{L}} \in [1, 130]$ MHz. These second-order quadrupolar shifts are comparable to the homogeneous nuclear spin linewidth $\propto 1/T_{2,\mathrm{N}}$, and therefore spin diffusion in GaAs/AlGaAs QDs is expected to be nearly unimpeded for the nuclei in the $I_z = \pm 1/2$ states. By contrast, the $I_z = \pm 3/2$ spin states experience first-order quadrupolar shifts ν_{Q}, which are tens of kHz, significantly exceeding the homogeneous NMR linewidths in the studied GaAs QDs. The resulting dynamics of the $I_z = \pm 3/2$ nuclei are therefore sensitive to nanoscale inhomogeneity of the strain-induced ν_{Q}. Such inhomogeneity is expected to be most pronounced for ^{75}As in the AlGaAs barriers, where random positioning of Ga and Al atoms produces unit-cell-scale strains[41,68]. From the NSR experiments [Fig. 4b], we observe that nuclear spin polarization relaxes to zero, even in an empty QD (0*e*). This can only happen if spin diffusion is unimpeded not only for the $I_z = \pm 1/2$ states, but also for the $I_z = \pm 3/2$ states that are subject to the larger first-order quadrupolar shifts. Our interpretation is that strain in the studied GaAs/AlGaAs QDs is a smooth function of spatial coordinates: for nearly each QD nucleus it is possible to find some neighboring nuclei with a strain variation small enough to form a chain that conducts spin diffusion out of the GaAs QD into the AlGaAs barriers.

Similarly fast NSR was observed previously in neutral QDs formed by monolayer fluctuations in GaAs/AlGaAs quantum wells[22]. However, the opposite scenario was realized in QDs with nanoholes etched in pure GaAs[49] where nuclear spin polarization in an empty QD (0*e*) was preserved for over $T_{1,\mathrm{N}} > 5000$ s, suggesting that some of the nuclei were frozen in the $I_z = \pm 3/2$ states, akin to quadrupolar blockade of spin diffusion in Stranski–Krastanov self-assembled QDs. This contrast is rather remarkable since the average strain, characterized by the average $\nu_{\mathrm{Q}} \approx 20$–$30$ kHz, is very similar for QDs grown in nanoholes etched in AlGaAs (studied here) and in GaAs (ref. 49). This comparison suggests that bare nuclear spin dynamics (without the electron) are sensitive to QD morphology down to the atomic scale, and could be affected by factors such as QD shape, as well as GaAs/AlGaAs interface roughness and intermixing[71–73]. One possible contributing factor is the QD growth temperature, which was 610° C in the structures used here, considerably higher than 520° C in the structures studied previously[48,49]. Further work would be required to elucidate the role of all the underlying growth parameters. Conversely, NSR can be a sensitive probe of the QD internal structure.

We now quantify the spin diffusion process and compare our results to the earlier studies in GaAs-based structures. The best fit of the experimental NSR dynamics [lines in Fig. 4b] yields $D_{\mathrm{Dark}}^{(0e)} = 2.2^{+0.7}_{-0.5}$ nm^2 s^{-1} (95% confidence interval) for the diffusion coefficient in an empty QD and in the absence of optical excitation, in reasonable agreement with $D = 1.0 \pm 0.15$ nm^2 s^{-1} measured previously for spin diffusion between two GaAs quantum wells across an $Al_{0.35}Ga_{0.65}As$ barrier[41]. This is approximately an order of magnitude smaller than the first-principle estimate[74–76] of $D_{\mathrm{Dark}}^{(0e)} \approx 19$ nm^2 s^{-1} for bulk GaAs (see Supplementary Note 3) and the $D = 15.0 \pm 7$ nm^2 s^{-1} value measured in pure AlAs[77]. The reduced diffusion in the AlGaAs alloy can be explained by the quadrupolar disorder, arising from the random positioning of the aluminium atoms[41]. Charging of the QD with a single electron accelerates spin diffusion: we find $D_{\mathrm{Dark}}^{(1e)}(9.82\,\mathrm{T}) = 4.7^{+1.2}_{-1.0}$ nm^2 s^{-1}, which increases to $D_{\mathrm{Dark}}^{(1e)}(0.39\,\mathrm{T}) = 7.7 \pm 1.9$ nm^2 s^{-1} at low magnetic fields where hyperfine-mediated nuclear–nuclear spin exchange is enhanced in accordance with Eq. (3). While the spin diffusion Eq. (2) gives an overall good description of the experimental data in Fig. 4b, some residual deviation is also apparent. The imperfect fit could be linked to a range of simplifications, such as ignoring the spatial variations of the nuclear–nuclear couplings and the dependence of the electron spin splitting ΔE_{e} on the instantaneous nuclear spin polarization. Our model also neglects any spin diffusion orthogonal to the sample growth *z* direction. Furthermore, the nuclei of ^{75}As, ^{69}Ga, and ^{71}Ga are not resolved in the present diffusion experiments. Therefore, these isotopes are treated as identical in the model since their dipole and quadrupolar moments differ only by a factor of ≈2 (see Supplementary Note 3). On the other hand, all these assumptions are justified since the very concept of classical spin diffusion is an inherently simplified description of the underlying quantum dynamics. As such, the diffusion coefficients *D* should be treated as a coarse-grained description, aggregating the numerous lattice constant-scale parameters of the many-body spin ensemble evolution.

Discussion

The GaAs/AlGaAs QDs grown by nanohole infilling combine excellent optical properties with low intrinsic strain, allowing for nuclear spin qubit and quantum memory designs[32,33,46]. The key performance characteristic is the nuclear spin coherence time, which can be extended up to $T_{2,\mathrm{N}} \approx 10$ ms (ref. 33), but is ultimately limited by the longitudinal relaxation time $T_{1,\mathrm{N}}$. Moreover, it is the state longevity of the nuclei interfaced with the QD electron spin that is relevant. Thus, one should consider the NSR time in the regime of short pumping, found here to range from $T_{1,\mathrm{N}}^{(1e)} \approx 1$ s at low magnetic fields to $T_{1,\mathrm{N}}^{(1e)} \approx 10$ s at high fields. For nuclear spin quantum computing with the typical 10

μs coherent control gates[33], a large number of operations $\gtrsim 10^5$ would be possible without the disruptive effect of spin diffusion. Spatially inhomogeneous nuclear spin polarization, such as generated in the two-pump diffusion reflux experiment, may itself be of use for all-electrical control of the electron spin[78].

In conclusion, we have addressed the long-standing dilemma of whether the central spin of an electron accelerates or suppresses diffusion in a nuclear spin-lattice. We have used variable-duration optical pumping[15,17,20,22] to identify nuclear spin diffusion as the dominant NSR mechanism. In contrast to previous studies of nuclear spin diffusion[15,16,20,21,24,25], we use a charge tunable structure and probe nuclear spin dynamics with and without the electron under otherwise identical conditions – importantly, our QD charge control is achieved without reverting to optical pumping[24,25], thus eliminating the unwanted charge fluctuations. Combining these two aspects, we conclude that in a technologically important class of lattice-matched GaAs/AlGaAs nanostructures, the electron spin accelerates the nuclear spin diffusion, with no sign of a Knight-field-gradient barrier. We expect these findings to be relevant for a range of lattice-matched QDs[22,23,27,60] and shallow impurities[16], whereas an efficient spin diffusion barrier can arise from an electron with deep (sub-nanometer) localization[14]. Future work can examine the reduction of spin diffusion in low-strain nanostructures. The proximity of the *n*-doped layer, acting as a sink for nuclear polarization, as well as QD morphology, can be optimized. Alternatively, pure AlAs barriers can be used to grow GaAs QDs with well-isolated Ga nuclei, potentially offering long-lived spin memories and qubits.

Data availability

The key data generated in this study are provided in the Source Data file SourceData.zip. The rest of the data that support the findings of this study are available from the corresponding author upon reasonable request. Source data are provided with this paper.

References

1. Oja, A. S. & Lounasmaa, O. V. Nuclear magnetic ordering in simple metals at positive and negative nanokelvin temperatures. *Rev. Mod. Phys.* **69**, 1–136 (1997).
2. Kessler, E. M. et al. Dissipative phase transition in a central spin system. *Phys. Rev. A* **86**, 012116 (2012).
3. de Gennes, P. G., Pincus, P. A., Hartmann-Boutron, F. & Winter, J. M. Nuclear magnetic resonance modes in magnetic material. I. theory. *Phys. Rev.* **129**, 1105–1115 (1963).
4. Shiomi, Y. et al. Spin pumping from nuclear spin waves. *Nat. Phys.* **15**, 22–26 (2019).
5. Dorner, R., Goold, J., Cormick, C., Paternostro, M. & Vedral, V. Emergent thermodynamics in a quenched quantum many-body system. *Phys. Rev. Lett.* **109**, 160601 (2012).
6. Bardarson, J. H., Pollmann, F. & Moore, J. E. Unbounded growth of entanglement in models of many-body localization. *Phys. Rev. Lett.* **109**, 017202 (2012).
7. Bloembergen, N. On the interaction of nuclear spins in a crystalline lattice. *Physica* **15**, 386–426 (1949).
8. Blumberg, W. E. Nuclear spin-lattice relaxation caused by paramagnetic impurities. *Phys. Rev.* **119**, 79–84 (1960).
9. Zhang, W. & Cory, D. G. First direct measurement of the spin diffusion rate in a homogenous solid. *Phys. Rev. Lett.* **80**, 1324–1327 (1998).
10. Eberhardt, K. W., Mouaziz, S., Boero, G., Brugger, J. & Meier, B. H. Direct observation of nuclear spin diffusion in real space. *Phys. Rev. Lett.* **99**, 227603 (2007).
11. Knight, W. D. Nuclear magnetic resonance shift in metals. *Phys. Rev.* **76**, 1259–1260 (1949).
12. Urbaszek, B. et al. Nuclear spin physics in quantum dots: an optical investigation. *Rev. Mod. Phys.* **85**, 79–133 (2013).
13. Leppelmeier, G. W. & Jeener, J. Measurement of the nuclear spin diffusion coefficient in CaF_2. *Phys. Rev.* **175**, 498–502 (1968).
14. Wolfe, J. P. Direct observation of a nuclear spin diffusion barrier. *Phys. Rev. Lett.* **31**, 907–910 (1973).
15. Paget, D. Optical detection of NMR in high-purity GaAs: direct study of the relaxation of nuclei close to shallow donors. *Phys. Rev. B* **25**, 4444–4451 (1982).
16. Lu, J. et al. Nuclear spin-lattice relaxation in *n*-type insulating and metallic GaAs single crystals. *Phys. Rev. B* **74**, 125208 (2006).
17. Hayashi, H., Itoh, K. M. & Vlasenko, L. S. Nuclear magnetic resonance linewidth and spin diffusion in ^{29}Si isotopically controlled silicon. *Phys. Rev. B* **78**, 153201 (2008).
18. Wittmann, J. J., Eckardt, M., Harneit, W. & Corzilius, B. Electron-driven spin diffusion supports crossing the diffusion barrier in MAS DNP. *Phys. Chem. Chem. Phys.* **20**, 11418–11429 (2018).
19. Ajoy, A. et al. Orientation-independent room temperature optical ^{13}C hyperpolarization in powdered diamond. *Sci. Adv.* **4**, eaar5492 (2018).
20. Tycko, R., Barrett, S., Dabbagh, G., Pfeiffer, L. & West, K. Electronic states in gallium arsenide quantum wells probed by optically pumped NMR. *Science* **268**, 1460–1463 (1995).
21. Bayot, V., Grivei, E., Beuken, J.-M., Melinte, S. & Shayegan, M. Critical behavior of nuclear-spin diffusion in GaAs/AlGaAs heterostructures near Landau level filling $\nu = 1$. *Phys. Rev. Lett.* **79**, 1718–1721 (1997).
22. Nikolaenko, A. E. et al. Suppression of nuclear spin diffusion at a GaAs/$Al_xGa_{1-x}As$ interface measured with a single quantum-dot nanoprobe. *Phys. Rev. B* **79**, 081303 (2009).
23. Reilly, D. J. et al. Exchange control of nuclear spin diffusion in a double quantum dot. *Phys. Rev. Lett.* **104**, 236802 (2010).
24. Makhonin, M. N. et al. Optically tunable nuclear magnetic resonance in a single quantum dot. *Phys. Rev. B* **82**, 161309 (2010).
25. Sallen, G. et al. Nuclear magnetization in gallium arsenide quantum dots at zero magnetic field. *Nat. Commun.* **5**, 3268 (2014).
26. Klauser, D., Coish, W. A. & Loss, D. Nuclear spin dynamics and Zeno effect in quantum dots and defect centers. *Phys. Rev. B* **78**, 205301 (2008).
27. Gong, Z.-X., qi Yin, Z. & Duan, L.-M. Dynamics of the Overhauser field under nuclear spin diffusion in a quantum dot. *N. J. Phys.* **13**, 033036 (2011).
28. Deng, C. & Hu, X. Nuclear spin diffusion in quantum dots: effects of inhomogeneous hyperfine interaction. *Phys. Rev. B* **72**, 165333 (2005).
29. Lai, C. W., Maletinsky, P., Badolato, A. & Imamoglu, A. Knight-field-enabled nuclear spin polarization in single quantum dots. *Phys. Rev. Lett.* **96**, 167403 (2006).
30. Ramanathan, C. Dynamic nuclear polarization and spin diffusion in nonconducting solids. *Appl. Magn. Reson.* **34**, 409 (2008).
31. Heshami, K. et al. Quantum memories: emerging applications and recent advances. *J. Mod. Opt.* **63**, 2005–2028 (2016).
32. Denning, E. V., Gangloff, D. A., Atatüre, M., Mørk, J. & Le Gall, C. Collective quantum memory activated by a driven central spin. *Phys. Rev. Lett.* **123**, 140502 (2019).
33. Chekhovich, E. A., da Silva, S. F. C. & Rastelli, A. Nuclear spin quantum register in an optically active semiconductor quantum dot. *Nat. Nanotechnol.* **15**, 999–1004 (2020).
34. Schmidt-Rohr, K., Clauss, J. & Spiess, H. Correlation of structure, mobility, and morphological information in heterogeneous polymer materials by two-dimensional wideline-separation NMR spectroscopy. *Macromolecules* **25**, 3273–3277 (1992).
35. Demco, D. E., Johansson, A. & Tegenfeldt, J. Proton spin diffusion for spatial heterogeneity and morphology investigations of polymers. *Solid State Nucl. Magn. Reson.* **4**, 13–38 (1995).

36. Hall, D. A. et al. Polarization-enhanced NMR spectroscopy of biomolecules in frozen solution. *Science* **276**, 930–932 (1997).
37. van der Wel, P. C. A., Hu, K.-N., Lewandowski, J. & Griffin, R. G. Dynamic nuclear polarization of amyloidogenic peptide nanocrystals: GNNQQNY, a core segment of the yeast prion protein Sup35p. *J. Am. Chem. Soc.* **128**, 10840–10846 (2006).
38. Viger-Gravel, J. et al. Structure of lipid nanoparticles containing siRNA or mRNA by dynamic nuclear polarization-enhanced NMR spectroscopy. *J. Phys. Chem. B* **122**, 2073–2081 (2018).
39. Manolikas, T., Herrmann, T. & Meier, B. H. Protein structure determination from 13C spin-diffusion solid-state NMR spectroscopy. *J. Am. Chem. Soc.* **130**, 3959–3966 (2008).
40. Rossini, A. J. et al. Dynamic nuclear polarization enhanced NMR spectroscopy for pharmaceutical formulations. *J. Am. Chem. Soc.* **136**, 2324–2334 (2014).
41. Malinowski, A., Brand, M. & Harley, R. Nuclear effects in ultrafast quantum-well spin-dynamics. *Phys. E: Low. Dimens. Syst. Nanostruct.* **10**, 13–16 (2001).
42. Knijn, P. J. et al. A solid-state NMR and DFT study of compositional modulations in $Al_xGa_{1-x}As$. *Phys. Chem. Chem. Phys.* **12**, 11517–11535 (2010).
43. Liu, J. et al. A solid-state source of strongly entangled photon pairs with high brightness and indistinguishability. *Nat. Nanotech.* **14**, 586–593 (2019).
44. Zhai, L. et al. Low-noise GaAs quantum dots for quantum photonics. *Nat. Commun.* **11**, 4745 (2020).
45. Tomm, N. et al. A bright and fast source of coherent single photons. *Nat. Nanotechnol.* **16**, 399–403 (2021).
46. Zaporski, L. et al. Ideal refocusing of an optically active spin qubit under strong hyperfine interactions. *Nat. Nanotechnol.* **18**, 257–263 (2023).
47. Heyn, C. et al. Highly uniform and strain-free GaAs quantum dots fabricated by filling of self-assembled nanoholes. *Appl. Phys. Lett.* **94**, 183113 (2009).
48. Atkinson, P., Zallo, E. & Schmidt, O. G. Independent wavelength and density control of uniform GaAs/AlGaAs quantum dots grown by infilling self-assembled nanoholes. *J. Appl. Phys.* **112**, 054303 (2012).
49. Ulhaq, A. et al. Vanishing electron *g* factor and long-lived nuclear spin polarization in weakly strained nanohole-filled GaAs/AlGaAs quantum dots. *Phys. Rev. B* **93**, 165306 (2016).
50. Chekhovich, E. A. et al. Cross calibration of deformation potentials and gradient-elastic tensors of GaAs using photoluminescence and nuclear magnetic resonance spectroscopy in GaAs/AlGaAs quantum dot structures. *Phys. Rev. B* **97**, 235311 (2018).
51. Griffiths, I. M., Huang, H., Rastelli, A., Skolnick, M. S. & Chekhovich, E. A. Complete characterization of GaAs gradient-elastic tensors and reconstruction of internal strain in GaAs/AlGaAs quantum dots using nuclear magnetic resonance. *Phys. Rev. B* **99**, 125304 (2019).
52. Harris, R. K., Becker, E. D., Cabral de Menezes, S. M., Goodfellow, R. & Granger, P. NMR nomenclature: Nuclear spin properties and conventions for chemical shifts: IUPAC recommendations 2001. *Solid State Nucl. Magn. Reson.* **22**, 458–483 (2002).
53. Barrett, S. E., Dabbagh, G., Pfeiffer, L. N., West, K. W. & Tycko, R. Optically pumped NMR evidence for finite-size skyrmions in GaAs quantum wells near Landau level filling $\nu = 1$. *Phys. Rev. Lett.* **74**, 5112–5115 (1995).
54. Chekhovich, E. A. et al. Measurement of the spin temperature of optically cooled nuclei and GaAs hyperfine constants in GaAs/AlGaAs quantum dots. *Nat. Mater.* **16**, 982 (2017).
55. McNeil, J. A. & Clark, W. G. Nuclear quadrupolar spin-lattice relaxation in some III-V compounds. *Phys. Rev. B* **13**, 4705–4713 (1976).
56. Latta, C., Srivastava, A. & Imamoğlu, A. Hyperfine interaction-dominated dynamics of nuclear spins in self-sssembled InGaAs quantum dots. *Phys. Rev. Lett.* **107**, 167401 (2011).
57. Vladimirova, M. et al. Nuclear spin relaxation in *n*-GaAs: from insulating to metallic regime. *Phys. Rev. B* **95**, 125312 (2017).
58. Gillard, G. et al. Fundamental limits of electron and nuclear spin qubit lifetimes in an isolated self-assembled quantum dot. *npj Quantum Inf.* **7**, 43 (2021).
59. Chekhovich, E. A., Hopkinson, M., Skolnick, M. S. & Tartakovskii, A. I. Suppression of nuclear spin bath fluctuations in self-assembled quantum dots induced by inhomogeneous strain. *Nat. Commun.* **6**, 6348 (2015).
60. Malinowski, F. K. et al. Spectrum of the nuclear environment for GaAs spin qubits. *Phys. Rev. Lett.* **118**, 177702 (2017).
61. Khutsishvili, G. R. Spin diffusion. *Sov. Phys. Uspekhi* **8**, 743–769 (1966).
62. Horvitz, E. P. Nuclear spin diffusion induced by paramagnetic impurities in nonconducting solids. *Phys. Rev. B* **3**, 2868–2872 (1971).
63. Kroutvar, M. et al. Optically programmable electron spin memory using semiconductor quantum dots. *Nature* **432**, 81–84 (2004).
64. Lu, C.-Y. et al. Direct measurement of spin dynamics in InAs/GaAs quantum dots using time-resolved resonance fluorescence. *Phys. Rev. B* **81**, 035332 (2010).
65. Gillard, G., Clarke, E. & Chekhovich, E. A. Harnessing many-body spin environment for long coherence storage and high-fidelity single-shot qubit readout. *Nat. Commun.* **13**, 4048 (2022).
66. Issler, M. et al. Nuclear spin cooling using Overhauser-field selective coherent population trapping. *Phys. Rev. Lett.* **105**, 267202 (2010).
67. Bulutay, C. Quadrupolar spectra of nuclear spins in strained $In_xGa_{1-x}As$ quantum dots. *Phys. Rev. B* **85**, 115313 (2012).
68. Chekhovich, E. A. et al. Structural analysis of strained quantum dots using nuclear magnetic resonance. *Nat. Nanotechnol.* **7**, 646 (2012).
69. Greilich, A. et al. Nuclei-induced frequency focusing of electron spin coherence. *Science* **317**, 1896–1899 (2007).
70. Chekhovich, E. A. et al. Dynamics of optically induced nuclear spin polarization in individual $InP/Ga_xIn_{1-x}P$ quantum dots. *Phys. Rev. B* **81**, 245308 (2010).
71. Jusserand, B. & Mollot, F. Long range gallium segregation in the AlAs layers of GaAs/AlAs superlattices. *Appl. Phys. Lett.* **61**, 423–425 (1992).
72. Saher Helmy, A., Aitchison, J. S. & Marsh, J. H. The kinetics of intermixing of GaAs/AlGaAs quantum confined heterostructures. *Appl. Phys. Lett.* **71**, 2998–3000 (1997).
73. Braun, W., Trampert, A., Däweritz, L. & Ploog, K. H. Nonuniform segregation of Ga at AlAs/GaAs heterointerfaces. *Phys. Rev. B* **55**, 1689–1695 (1997).
74. Lowe, I. J. & Gade, S. Density-matrix derivation of the spin-diffusion equation. *Phys. Rev.* **156**, 817–825 (1967).
75. Redfield, A. G. & Yu, W. N. Moment-method calculation of magnetization and interspin-energy diffusion. *Phys. Rev.* **177**, 1018–1018 (1969).
76. Butkevich, E. R. & Sabirov, R. K. On anisotropy of nuclear spin-diffusion coefficient. *Phys. Status Solidi (b)* **146**, 683–689 (1988).
77. Nguyen, M.-H. et al. Interlayer diffusion of nuclear spin polarization in $\nu = \frac{2}{3}$ quantum Hall states. *Phys. Rev. B* **89**, 041403 (2014).
78. Tokura, Y., van der Wiel, W. G., Obata, T. & Tarucha, S. Coherent single electron spin control in a slanting Zeeman field. *Phys. Rev. Lett.* **96**, 047202 (2006).

Acknowledgements

P.M-H. and E.A.C. were supported by EPSRC through a doctoral training grant and award EP/V048333/1, respectively. E.A.C. was supported by a Royal Society University Research Fellowship. A.R.

acknowledges support of the Austrian Science Fund (FWF) via the Research Group FG5, I 4320, I 4380, I 3762, the European Union's Horizon 2020 research and innovation program under Grant Agreements No. 899814 (Qurope) and No. 871130 (Ascent+), the Linz Institute of Technology (LIT), and the LIT Secure and Correct Systems Lab, supported by the State of Upper Austria. E.A.C. is grateful to René Dost for advice on sample processing and would like to thank H.E. Dyte and G. Gillard for preliminary data on electron spin lifetimes.

Author contributions

S.M., S.F.C.d.S., and A.R. developed, grew, and processed the quantum dot samples. P.M-H. and E.A.C. conducted the experiments and analysed the data. E.A.C. drafted the manuscript with input from all authors. E.A.C. performed numerical modeling and coordinated the project.

Competing interests

The authors declare no competing interests.

Additional information

Supplementary information The online version contains supplementary material available at https://doi.org/10.1038/s41467-023-38349-0.

Correspondence and requests for materials should be addressed to Evgeny A. Chekhovich.

Peer review information *Nature Communications* thanks Yuan Zhan and the other, anonymous, reviewers for their contribution to the peer review of this work. A peer review file is available.

Supplementary Information: Nuclear spin diffusion in the central spin system of a GaAs/AlGaAs quantum dot

Peter Millington-Hotze and Evgeny A. Chekhovich*

Department of Physics and Astronomy, University of Sheffield, Sheffield S3 7RH, United Kingdom

Santanu Manna, Saimon F. Covre da Silva, and Armando Rastelli

Institute of Semiconductor and Solid State Physics,

Johannes Kepler University Linz, Altenberger Str. 69, 4040 Linz, Austria

Supplementary Note 1. SAMPLE STRUCTURE

The sample is grown using molecular beam epitaxy (MBE) on a semi-insulating GaAs (001) substrate. The growth starts with a layer of $Al_{0.95}Ga_{0.05}As$ followed by a single pair of $Al_{0.2}Ga_{0.8}As$ and $Al_{0.95}Ga_{0.05}As$ layers acting as a Bragg reflector in optical experiments. Then, a 95 nm thick layer of $Al_{0.15}Ga_{0.85}As$ is grown. The rest of the structure follows the schematic shown in Fig. 2c of the main text beginning with a 95 nm thick layer of $Al_{0.15}Ga_{0.85}As$ doped with Si at a volume concentration of 1.0×10^{18} cm^{-3}. The low Al concentration of 0.15 in the Si doped layer mitigates the issues caused by the deep DX centers [1–3]. Under optical excitation this $Al_{0.15}Ga_{0.85}As$:Si gives rise to broad photoluminescence between 730 nm and 770 nm as observed in Supplementary Fig. 1a. The n-type doped layer is followed by the electron tunnel barrier layers: first a 15 nm thick $Al_{0.15}Ga_{0.85}As$ layer and then a 15 nm thick $Al_{0.33}Ga_{0.67}As$ layer. Aluminium droplets are grown on the surface of the $Al_{0.33}Ga_{0.67}As$ layer and are used to etch the nanoholes [4, 5]. An atomic force microscopy (AFM) image of a similar sample in Fig. 2a of the main text shows a typical nanohole with a depth of ≈ 6.5 nm and ≈ 70 nm in diameter. Next, a 2.1 nm thick layer of GaAs is grown to form QDs by infilling the nanoholes as well as to form the quantum well (QW) layer. Thus, the maximum height of the QDs in the growth z direction is ≈ 9 nm. Low temperature PL of QDs and QW is observed [Supplementary Fig. 1a] at 785 nm and 690 nm, respectively. The GaAs layer is followed by a 268 nm thick $Al_{0.33}Ga_{0.67}As$ barrier layer. Finally, the p-type contact layers doped with C are grown: a 65 nm thick layer of $Al_{0.15}Ga_{0.85}As$ with a 5×10^{18} cm^{-3} doping concentration, followed by a 5 nm thick layer of $Al_{0.15}Ga_{0.85}As$ with a 9×10^{18} cm^{-3} concentration, and a 10 nm thick layer of GaAs with a 9×10^{18} cm^{-3} concentration.

* e.chekhovich@sheffield.ac.uk

The sample is processed into a $p-i-n$ diode structure. Mesa structures with a height of 250 nm are formed by etching away the p-doped layers and depositing Ni(10 nm)/AuGe(150 nm)/Ni(40 nm)/Au(100 nm) on the etched areas. The sample is then annealed to enable diffusion down to the n-doped layer to form the ohmic back contact. The top gate contact is formed by depositing Ti(15 nm)/Au(100 nm) on to the p-type surface of the mesa areas. The sample gate bias V_{Gate} is the bias of the p-type top contact with respect to the grounded n-type back contact. By changing V_{Gate} the equilibrium charge state of the quantum dot is tuned using the Coulomb blockade effect (see Supplementary Note 2 E). Due to the large thickness of the top $Al_{0.33}Ga_{0.67}As$ layer, the tunneling of the holes is effectively blocked, whereas tunnel coupling to the n-type layer enables deterministic charging of the quantum dots with electrons.

Supplementary Note 2. EXPERIMENTAL DETAILS AND ADDITIONAL RESULTS

The sample is placed in a liquid helium bath cryostat. A superconducting coil is used to apply magnetic field up to $B_{\mathrm{z}} = 10$ T. The field is parallel to the sample growth direction and the optical axis z (Faraday geometry). We use confocal microscopy configuration. An aspheric lens with a focal distance of 1.45 mm and NA=0.58 is used as an objective for optical excitation of the QD and for photoluminescence (PL) collection. The excitation laser is focused into a spot with a diameter of ≈ 1 μm. The collected PL is dispersed in a two-stage grating spectrometer, each stage with a 0.85 m focal length, and recorded with a charge-coupled device (CCD) camera. The changes in the spectral splitting of a negatively charged trion X^-, derived from the PL spectra, are used to measure the hyperfine shifts E_{hf} proportional to the nuclear spin polarization degree.

Supplementary Fig. 2 is a detailed version of Fig. 4a of the main text and shows the timing of the NSR measurement. In what follows we describe the individual elements of the timing sequence. While this discussion is specific to the NSR measurement, the same principles apply to other time-resolved measurements. The differences applicable to NMR spectroscopy and diffusion reflux measurements are highlighted below accordingly.

A. Radiofrequency depolarization of nuclear spin polarization

Investigation of spin diffusion relies on the ability to prepare a reproducible spatial distribution of the nuclear spin polarization. This is achieved with a radiofrequency (RF) erase pulse (Supplementary Fig. 2) which effectively resets the nuclear spin polarization to zero in the entire sample.

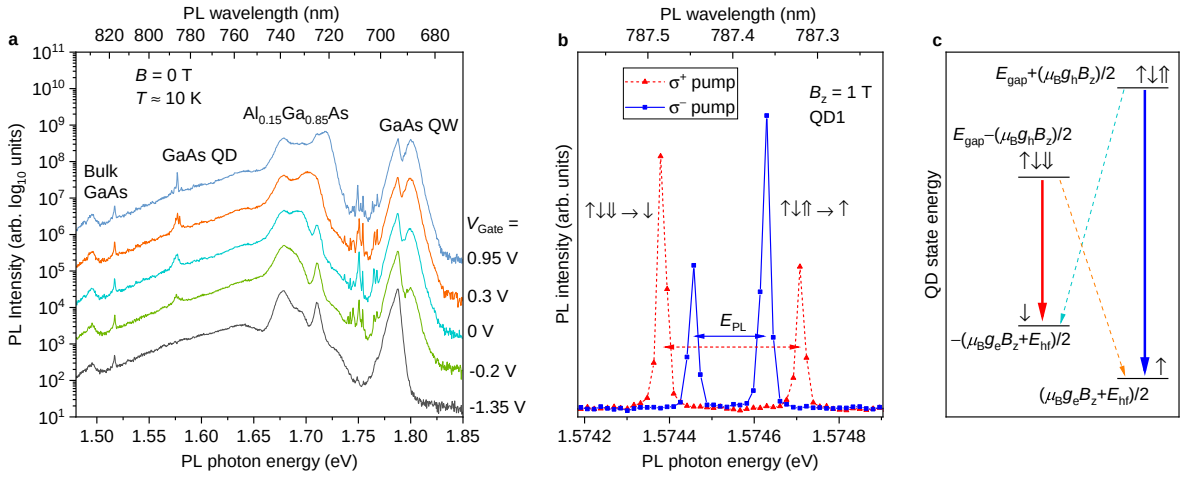

Supplementary Figure 1. **Photoluminescence of GaAs/AlGaAs QD samples. a** Broad range photoluminescence (PL) spectra measured under 532 nm laser excitation at different gate biases V_{Gate}. Spectra are offset in a vertical direction (log scale) by a factor of 10 for clarity. Spectral features arising from the different parts of the sample are labeled accordingly. **b** High resolution PL spectra of a negatively charged X^- trion following σ^+ (triangles) or σ^- (squares) circularly polarized optical pumping, which creates $s_{\mathrm{z}} = -1/2$ ($\downarrow$) and $s_{\mathrm{z}} = +1/2$ ($\uparrow$) spin polarized electrons, respectively. The electrons transfer their spin to the nuclei via magnetic (hyperfine) interaction, resulting in a build up of negative or positive net nuclear spin polarization, respectively. Through the same hyperfine interaction, the average nuclear spin polarization shifts the $s_{\mathrm{z}} = -1/2$ and $s_{\mathrm{z}} = +1/2$ electron spin energy levels in the opposite directions. These Overhauser shifts (E_{hf}) lead to the observed change in the spectral splitting E_{PL} of the trion PL, where the two components of the doublet correspond to an electron-hole recombination in presence of another electron with $s_{\mathrm{z}} = -1/2$ or $s_{\mathrm{z}} = +1/2$ state. **c** Energy level diagram. The electron ground state is split by the Zeeman energy $\mu_{\mathrm{B}} g_{\mathrm{e}} B_{\mathrm{z}}$ and the hyperfine shift E_{hf}. The X^- trion energy includes the QD bandgap energy E_{gap} and the Zeeman splitting of the unpaired hole with a positive ($\Uparrow$) or negative ($\Downarrow$) momentum projection. The valence band hole hyperfine effect can be neglected due to its smaller magnitude [6]. The electron and hole g-factors are g_{e} and g_{h}, respectively, with $|g_{\mathrm{h}}| \gg |g_{\mathrm{e}}|$ in the studied QDs. Solid arrows depict the two optically allowed transitions responsible for the spectral doublet in (b). The dashed lines show the two forbidden "diagonal" transitions.

This is achieved by saturating the nuclear magnetic resonance of the As and Ga isotopes. When subject to an oscillating magnetic field, resonant with the nuclear Larmor frequency, the nuclear spins undergo Rabi rotation, periodically transitioning between the spin states parallel and antiparallel to the external magnetic field [7]. Due to the nuclear-nuclear dipolar interactions each nuclear spin is subject to a local field. The randomness of these local fields perturbs the Rabi precession frequencies, resulting in ensemble dephasing. Consequently, the nuclei become randomly oriented

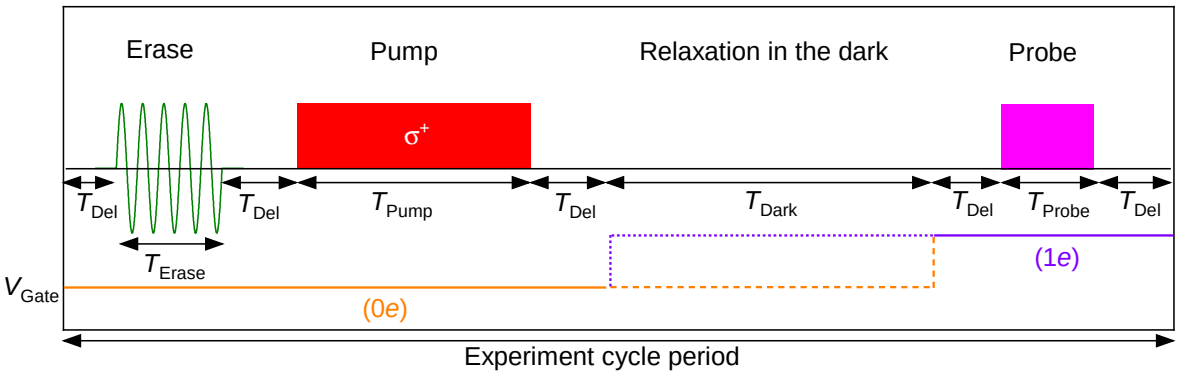

Supplementary Figure 2. **Timing diagram of the nuclear spin relaxation measurement cycle.**

(depolarized) after a long resonant radiofrequency saturation pulse. The required oscillating magnetic field $B_x \perp z$ is produced by a coil placed at a distance of ≈ 0.5 mm from the QD sample. The coil is made of 10 turns of a 0.1 mm diameter enameled copper wire wound on a ≈ 0.4 mm diameter spool in 5 layers, with 2 turns in each layer. The coil is driven by a class-A RF amplifier (rated up to 20 W) which is fed by the output of an arbitrary waveform generator. The spectrum of the RF excitation consists of three bands, each 340 kHz wide and centered on the NMR frequency of the corresponding As or Ga isotope. For each magnetic field the frequencies are adjusted based on NMR spectroscopy. To give a specific example, the central frequencies at 10 T are 73.079, 102.471 and 130.199 MHz for ^{75}As, ^{69}Ga and ^{71}Ga, respectively. Each RF band is generated as a frequency comb [6] with a mode spacing of 120 Hz, much smaller than the homogeneous NMR linewidth. The RF power density in the comb is chosen to be low enough and the RF pulse duration T_{Erase} long enough (ranging between 0.1 and 10 s depending on magnetic field) to achieve noncoherent exponential depolarization of the nuclear spin ensemble.

B. Optical pumping of the quantum dot nuclear spins

Optical pumping of the QD nuclear spin polarization (labelled Pump in Supplementary Fig. 2) is achieved using the emission of a 690 nm circularly polarized diode laser, which is resonant with the GaAs QW states, as seen in Supplementary Fig. 1a. Optical dynamical nuclear spin polarization is a well known process, that has been observed in many types of QDs [8–12], see Ref. [13] for a review. In brief, dynamic nuclear polarization is a three-stage cyclic process. At the first stage a spin polarized electron is created optically. This is made possible by the selection rules, which allow conversion of the circularly polarized photons into spin-polarized electron-hole pairs in group

III-V semiconductors. At the second stage, the electron exchanges its spin with one of the nuclei through the flip-flop term of the electron-nuclear hyperfine Hamiltonian. The third stage is the electron-hole optical recombination, which removes the flipped electron. This final step is required in order to let the QD accept new spin-polarized electrons and continue polarizing the ensemble of $\approx 10^5$ nuclear spins of the QD. Given that optical pumping is resonant with the QW, it is possible that dynamical nuclear polarization takes place not only in the QDs but also in the adjacent parts of the QW. On the other hand, the pump laser photon energy is well below the bandgap of the AlGaAs barriers. For that reason we assume that dynamic nuclear polarization in AlGaAs is induced only through spin diffusion from the GaAs layer of the QW and QDs. During the optical pump the sample gate is set to a large reverse bias, typically $V_{\rm Gate} = -2$ V. The pump power is ≈ 300 μW, which is two orders of magnitude higher than the ground-state PL saturation power. The resulting hyperfine shifts do not exceed $|E_{\rm hf}| < 50$ μeV, corresponding to initial nuclear spin polarization degree within $|P_{\rm N,0}| \lesssim 0.4$. While polarization as high as $P_{\rm N,0} \approx 0.8$ is possible [14], we deliberately use lower values to ensure linear regime of spin diffusion, free from hyperpolarization regime corrections [15]. In the diffusion reflux experiments, presented in Fig. 3 of the main text, the first (long) pump pulse is as described above. The second (shorter) pump is chosen to have a higher power ≈ 3000 μW and a longer wavelength ≈ 793 nm, resonant with the s-shell exciton transition in order to generate inverted nuclear spin polarization localised to the QD volume.

C. Optical probing of the quantum dot nuclear spins

For optical probing of the nuclear spin polarization we use a diode laser emitting at 640 nm. Sample forward bias, typically +0.5 V, and the probe power are chosen to maximize (saturate) PL intensity of the ground state X^- trion. Supplementary Fig. 1b shows X^- PL probe spectra measured at $B_{\rm z} = 1$ T following optical pumping with σ^+ (triangles) or σ^- (squares) circular polarization. The difference in spectral splitting of the X^- trion doublet reveals the hyperfine shifts $E_{\rm hf}$ [see energy level diagram in Supplementary Fig. 1c]. These shifts are used to monitor the average QD nuclear spin polarization in NSR experiments such as shown in Fig. 4b of the main text. Illumination with a probe laser inevitably acts back on the nuclear spin polarization. An example of the probe pulse calibration is shown in Supplementary Fig. 3. In this experiment the QD is first pumped with a σ^+ or σ^- polarized laser in order to create large initial nuclear polarization. Then a probe laser pulse is applied. The hyperfine shift $E_{\rm hf}$ is measured from PL spectroscopy at the end of this probe. Such calibration is carried out for each individual QD at each

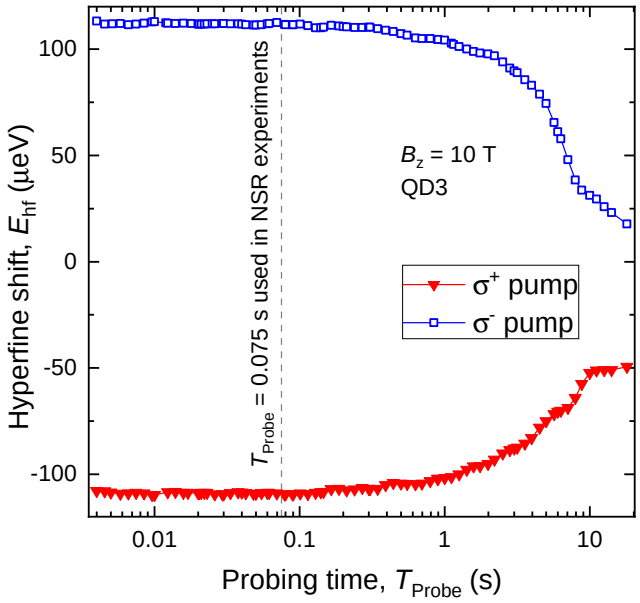

Supplementary Figure 3. **Calibration of the optical probing of the QD nuclear spin polarization.** Hyperfine shift measured as a function of the probing time T_{Probe} following a σ^+ or σ^- pumping of the nuclear spin polarization in a QD. Vertical dashed line shows the T_{Probe} value chosen for the NSR measurements on this individual QD at this particular magnetic field of $B_{\mathrm{z}} = 10$ T.

magnetic field. It can be seen that the probe induces decay of the nuclear spin polarization on a timescale of a few seconds. The probe time T_{Probe} used in the NSR experiments is chosen to ensure minimal distortion of the measured E_{hf}. For example, for the data shown in Supplementary Fig. 3 we choose $T_{\mathrm{Probe}} = 0.075$ s which limits the parasitic depolarization to less than 1% of the true hyperfine shift E_{hf}. Typical T_{Probe} values range between 10 and 80 ms, depending on individual QD and magnetic field.

D. Quantum dot electron g-factors

The energy splitting of the two electron spin states ΔE_{e} is a sum of the Zeeman splitting $\mu_{\mathrm{B}} g_{\mathrm{e}} B_{\mathrm{z}}$ (where μ_{B} is the Bohr magneton) and the hyperfine splitting E_{hf}, arising from the nuclear spin polarization. We quantify the g-factor g_{e} of a resident electron using photoluminescence spectroscopy of a negatively charged trion. In Faraday geometry, two out of four optical transitions are forbidden, so that only the difference $g_{\mathrm{h}} - g_{\mathrm{e}}$ of the heavy hole and electron g-factors can be accessed. In order to derive the individual g-factors, we measure photoluminescence in oblique field configuration, where the sample growth axis is tilted by $\theta \approx 12^\circ$ away from the static magnetic

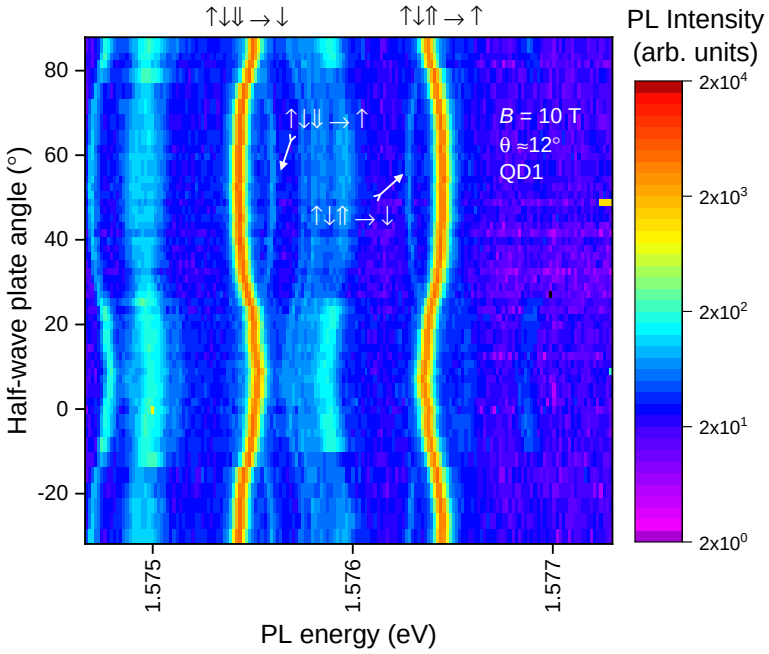

Supplementary Figure 4. **Electron g-factor measurement.** Photoluminescence spectra of a negatively charged trion X^- measured in oblique magnetic field $B = 10$ T tilted by $\theta \approx 12°$ from the Faraday geometry. The measurement uses a pump-probe protocol, where the angle of a half-wave plate on the pump laser is varied, while the probe laser is used to detect the resulting changes in PL spectrum. The two bright lines correspond to the two allowed transitions. When the circularly polarized pump generates a sufficiently large hyperfine shift, the two weakly allowed trion transitions, labeled by the arrows, become resolved. Fitting of the PL energies reveals the electron and hole g-factors. Other (broad) spectral features correspond to PL of excitons charged with more than one electron.

field. In this configuration the "diagonal" transitions, shown by the dashed lines in Supplementary Fig. 1c, become weakly allowed. Owing to the nearly vanishing electron g-factor in this type of GaAs/AlGaAs QDs [11], all four X^- transitions can be resolved in our setup only in high magnetic field $B = 10$ T and in presence of the optically induced hyperfine shifts. The experiment is conducted using an optical pump-probe method. The probe PL spectra are shown in Supplementary Fig. 4 as a function of the half-wave plate angle. The angle is varied to control the degree of circular polarization of the pump laser and the resulting hyperfine shift $E_{\rm hf}$. The two weak transitions (labeled by the arrows) become visible when the splitting of the two bright transitions is maximized by the hyperfine shift. We further measure the spectral splitting of the two bright transitions after RF depolarization of the nuclei, which results in $E_{\rm hf} \approx 0$. It is then possible to perform linear fit of the PL energies of all four X^- transitions and derive the g-factors. For QD1

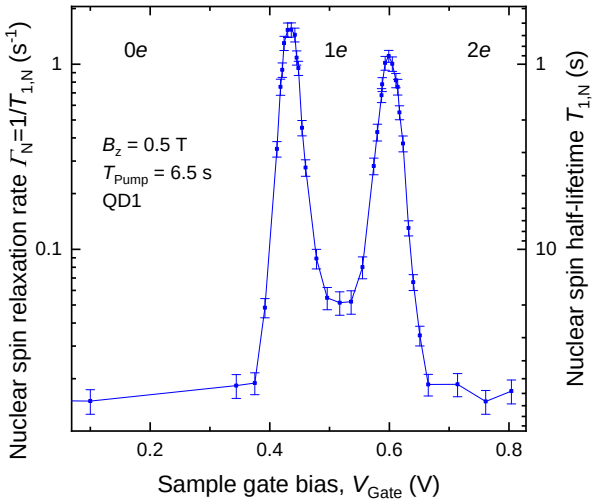

Supplementary Figure 5. **Bias dependence of the nuclear spin relaxation rate Γ_N.** Error bars are 95% confidence intervals.

studied in the main text and examined in Supplementary Fig. 4 we find the 95% confidence estimate $g_e \approx -0.101 \pm 0.007$ for the g-factor of a single resident electron. From the hole spin splitting of X^- at $B = 10$ T we estimate the hole g-factor in presence of two electrons to be $g_h \approx +1.68$. This value should be treated as a rough estimate because of the significant nonlinearity in hole Zeeman splitting for this type of QDs [11]. We also measure the g-factors in a neutral exciton X^0, using PL of the dark states: we find $g_e \approx -0.090 \pm 0.035$ for the electron in presence of one hole. It is notable that the electron g-factor is nearly unaffected by the extra hole [16]. Using PL spectroscopy of the X^- trion state, we have measured g-factors in two more QDs from the same sample to find $g_e \approx -0.077 \pm 0.018$ and $g_e \approx -0.107 \pm 0.002$ for a sole resident electron in QD6 and QD7, respectively. From the X^0 PL of QD6 we find $g_e \approx -0.12 \pm 0.01$ for an electron in presence of a hole, whereas no dark excitons could be observed in QD7. The g-factors found here are in good agreement with the previous studies on the samples where QDs were grown in nanoholes etched in pure GaAs [11].

E. Quantum dot charge state tuning

The sample gate bias V_{Gate} is controlled by the output of an arbitrary waveform generator connected through a 1.9 MHz low pass filter. During the dark evolution time T_{Dark} the bias can be set to an arbitrary value. For an empty dot regime ($0e$) we use large reverse bias $V_{Gate} = -1.3$ V. The bias corresponding to $1e$ Coulomb blockade is found by measuring the bias dependence of

$\Gamma_{\mathrm{N}}(V_{\mathrm{Gate}})$ such as shown in Supplementary Fig. 5. In agreement with the previous studies on InGaAs QDs [17, 18] we observe tunnelling peaks (at ≈ 0.43 V and ≈ 0.6 V), where the electron Fermi reservoir energy matches the QD charging energy. Under these resonant conditions NSR is accelerated by a non-diffusion mechanism, where the nuclear spin momentum is carried into the Fermi reservoir by the rapidly cotunnelling electron. A bias at the middle of the Coulomb valley between the peaks, 0.517 V in this case, is used to charge the QD with one electron ($1e$). Supplementary Fig. 5 shows that when the QD is charged with two electrons ($2e$) forming a spin singlet, the NSR rate is identical to the $0e$ case, confirming that the NSR acceleration produced by the single electron ($1e$) is related to its spin.

F. Pump probe experiment implementation

Optical pump and probe pulses are formed by mechanical shutters with a switching time of a few milliseconds. In order to accommodate these shutter transients, small delays $T_{\mathrm{Del}} = 10$ ms are introduced in the timing sequences as shown in Supplementary Fig. 2. Under certain regimes in B_{z} and V_{Gate} (e.g. resonant cotunnelling with the Fermi reservoir) this T_{Del} is comparable to the nuclear spin relaxation times $T_{1,\mathrm{N}}$. However, the relaxation time in an empty ($0e$) or singly charged ($1e$) QD is always considerably longer. Thus, during the switching delay the QD is kept under either the $0e$ bias (after the pump) or the $1e$ bias (prior to the probe). The dark time T_{Dark} is implemented by pulsing the gate bias to the chosen dark-state value V_{Gate} for a duration T_{Dark}. The QD device responds to the bias on a sub-microsecond scale. This way we ensure that the switching delays T_{Del} have minimal effect on the measured NSR dynamics.

G. Nuclear magnetic resonance of individual quantum dots

Nuclear magnetic resonance (NMR) characterization (Fig. 2e of the main text) is conducted using the inverse NMR method [19] which enhances the signal for $I > 1/2$ spins and improves the signal to noise ratio. In this method the nuclear spins are first polarised with a pump laser ($T_{\mathrm{Pump}} = 6.5$ s) and are then depolarized by a weak RF field, whose spectral profile is a broadband frequency comb with a narrow gap of width w_{gap} in the center. The frequency comb has a total spectral width of 600 kHz and its mode spacing is 125 Hz. The value of w_{gap} controls the balance between the measured NMR signal and the spectral resolution. In an empty QD ($0e$), NMR spectra of As and Ga measured with $w_{\mathrm{gap}} = 6$ kHz consist of well-resolved quadrupolar-split

triplets, consistent with previous observations for similar QD structures [11, 20]. The spin of a single electron ($1e$) leads to inhomogeneous Knight shifts comparable to the quadrupolar splitting. As a result, the NMR triplets are no longer resolved (solid circles in Fig. 2e of the main text). Moreover, the electron spin lifetime, which is on the order of milliseconds in the studied QDs, is much shorter than the radiofrequency burst (typically 0.18 s), and the average electron spin polarization is therefore close to 0. Each nucleus then experiences both positive and negative Knight shifts during the RF burst. These dynamic spectral shifts disrupt the enhancement of the inverse NMR method: for example, if a nuclear spin transition fits into the RF spectral gap $w_{\rm gap}$ under one sign of the Knight shift, it may be moved out of the gap and into resonance with the depolarizing RF field under the opposite Knight shift. As a result, the NMR spectrum amplitude is reduced in the $1e$ measurement. By varying the gap width $w_{\rm gap}$, we find that a spectrum with a reasonable signal to noise ratio is obtained at $w_{\rm gap} = 70$ kHz, as shown by the circles in Fig. 2e of the main text. Although the deterioration of the inverse NMR method precludes an accurate measurement of the NMR lineshape in presence of the electron, the overall width ≈ 50 kHz of the resonance still provides a valid order-of-magnitude estimate of the Knight shifts experienced by the nuclear spins in the QD. More sophisticated measurements, using pulsed NMR (to be reported separately elsewhere) confirm this rough estimate based on inverse NMR measurement.

H. Additional data on nuclear spin relaxation

The QD NSR curves measured at $B_{\rm z} = 0.39$ T and shown in Fig. 4b of the main text are reproduced in Supplementary Fig. 6a, together with the similar measurements carried out at high magnetic field $B_{\rm z} = 9.82$ T and shown in Supplementary Fig. 6b. Similar to the low fields, at $B_{\rm z} = 9.82$ T shorter optical pumping time $T_{\rm Pump}$ results in faster NSR through spin diffusion. However, the acceleration of NSR in presence of a single electron ($1e$) is less pronounced at high magnetic field, owing to the reduction of the hyperfine-mediated nuclear-nuclear spin interaction. It is also worth noting that the optical spin pumping becomes slower at high magnetic field. While $T_{\rm Pump} = 0.018$ s at $B_{\rm z} = 0.39$ T is sufficient to achieve $\approx 1/4$ of the steady state nuclear spin polarization, it takes an order of magnitude longer $T_{\rm Pump} = 0.17$ s to reach the same $\approx 1/4$ level at $B_{\rm z} = 9.82$ T. This difference limits the shortest $T_{\rm Pump}$ for which NSR dynamics can be measured at high magnetic field, as can be seen in Fig. 4d of the main text.

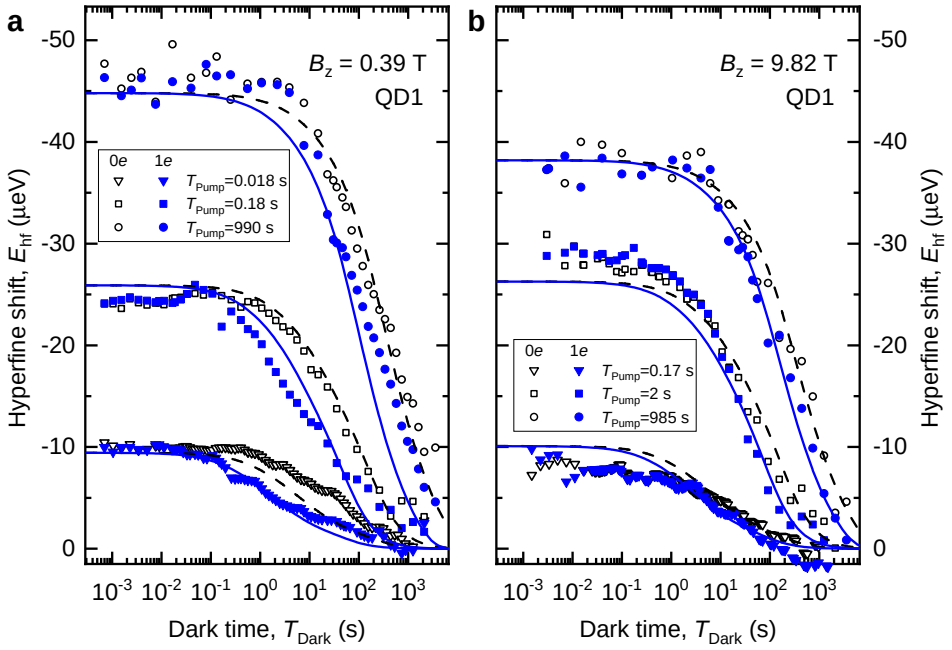

Supplementary Figure 6. **Nuclear spin relaxation in GaAs quantum dots. a** Dark time dependence of the hyperfine shift $E_{\rm hf}$, which probes average nuclear spin polarization weighted by the QD electron density $|\psi_{\rm e}|^2$. Nuclear spin decay is measured (symbols) at $B_{\rm z} = 0.39$ T for different pumping times $T_{\rm Pump}$ while keeping QD empty ($0e$, open symbols) or electron-charged ($1e$, solid symbols) during the dark time. Lines show numerical solution of the spin diffusion equation. **b** Same as (a) but for $B_{\rm z} = 9.82$ T.

I. Nuclear spin relaxation at elevated temperatures

The experiments presented in the main text are conducted at the cryostat base temperature, measured with a resistive sensor to be $T \approx 4.27$ K. Additional measurements, similar to those shown in Fig. 4c,d of the main text, have been conducted on an empty QD ($0e$) at an elevated temperature $T = 15.2$ K and are shown in Supplementary Fig. 7. We find that at high temperature the relaxation rate follows the same trend of reduction at short pumping times $T_{\rm Pump}$, consistent with NSR dominated by spin diffusion. In case of a pure spin diffusion driven by nuclear dipole-dipole interactions, one would expect the rate to be independent of the temperature. From Supplementary Fig. 7 we find that for any given $T_{\rm Pump}$ the relaxation is slightly accelerated at $T = 15.2$ K. One possibility is that temperature dependence of the optical nuclear spin pumping process [21] creates different spatial distributions of the nuclear spin polarization for the same $T_{\rm Pump}$. Contribution of the temperature-dependent non-diffusion mechanisms, such as two-phonon quadrupolar relaxation is also possible, but expected to be small below 20 K (Refs. [22, 23]), in agreement with Fig. 7.

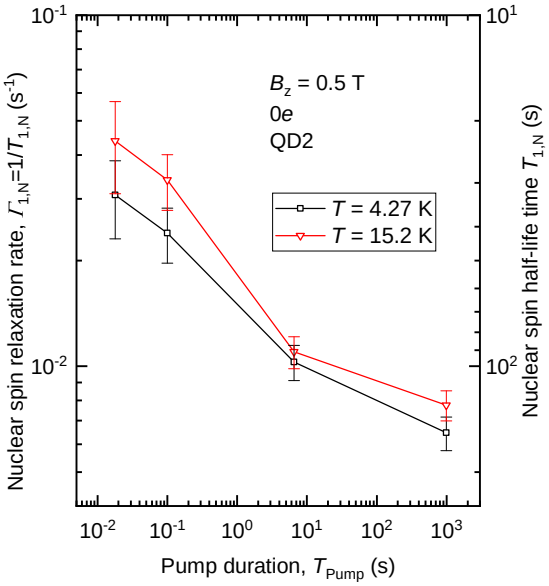

Supplementary Figure 7. **Temperature dependence of the quantum dot nuclear spin relaxation.** Fitted QD nuclear spin half-life times $T_{1,\mathrm{N}}$ (right scale) and the corresponding NSR rates $\Gamma_{\mathrm{N}} = 1/T_{1,\mathrm{N}}$ (left scale) measured for different pumping times T_{Pump} at $B_{\mathrm{z}} = 0.5$ T. Experiments are conducted at base sample temperature ($T = 4.27$ K, squares) and an elevated temperature ($T = 15.2$ K, triangles). Error bars are 95% confidence intervals.

Supplementary Note 3. FIRST PRINCIPLE ESTIMATE OF THE GaAs NUCLEAR SPIN DIFFUSION COEFFICIENT

In the absence of free electrons, nuclear spin diffusion is driven by the dipole-dipole magnetic nuclear spin interaction. The total dipole-dipole Hamiltonian term is a sum of pairwise couplings:

$$\mathcal{H}_{\mathrm{DD}} = \sum_{i<j} b_{i,j} \left(2\hat{I}_{\mathrm{z},i}\hat{I}_{\mathrm{z},j} - \hat{I}_{\mathrm{x},i}\hat{I}_{\mathrm{x},j} - \hat{I}_{\mathrm{y},i}\hat{I}_{\mathrm{y},j} \right),$$
$$b_{i,j} = \frac{\mu_0 \hbar^2}{4\pi} \frac{\gamma_i \gamma_j}{2} \frac{1 - 3\cos^2\theta_{i,j}}{r_{i,j}^3}, \tag{S1}$$

where $\mu_0 = 4\pi \times 10^{-7}$ NA^{-2} is the magnetic constant, $\hbar$ is the reduced Planck's constant and $r_{i,j}$ denotes the length of the vector, which forms an angle θ with the static magnetic field direction (z) and connects the two spins i and j. The typical magnitude of the interaction constants for the nearby nuclei in GaAs is $\max(|b_{j,k}|)/h \approx 100$ Hz. The Hamiltonian of Eq. S1 has been truncated to eliminate all spin non-conserving terms, which is justified for static magnetic fields exceeding $\gtrsim 1$ mT, as used in this work. The evolution of a large nuclear spin ensemble can be described in terms of spin diffusion with coefficient D. In crystalline solids the nuclear spin diffusion

coefficient D, is a rank-2 tensor which can be calculated from the first principles using density matrix approach [24] or the method of moments [25, 26]. The calculation involves a somewhat lengthy evaluation of the various lattice sums. Here we use a more recent version of the method of moments from Ref. [27]. We re-evaluate numerically the sums of Eqns. 8 and 10 from Ref. [27] using an FCC lattice of 6859 spins. Our results are in good agreement with the those derived for 1330 neighboring spins previously [27]. We find the following values for the diagonal components of D: $D_{xx} = D_{yy} \approx 0.2594\frac{\mu_0}{4\pi}\frac{\hbar\gamma^2}{a_0}\rho^{1/3}$ and $D_{zz} \approx 0.3289\frac{\mu_0}{4\pi}\frac{\hbar\gamma^2}{a_0}\rho^{1/3}$, where $a_0 \approx 0.565$ nm is the GaAs lattice constant and γ is the nuclear gyromagnetic ratio. Here we use the coordinate system aligned with the cubic crystal axes $x \parallel [100]$, $y \parallel [010]$, $z \parallel [001]$, and the strong magnetic field is parallel to the z direction. We have also introduced the correction factor $\rho^{1/3}$ to account for the increase of the average internuclear distance for the isotope whose abundance ρ is less then unity.

In case of arsenic, ^{75}As is the only stable isotope, so that $\rho = 1$. For gallium isotopes we have the natural abundances $\rho = 0.601$ and $\rho = 0.399$ for ^{69}Ga and ^{71}Ga, respectively. The gyromagnetic ratios γ are known [28] and, since we approximate the spin diffusion as a one-dimensional process along the sample growth direction z, we are interested in the D_{zz} component of the tensor. Substituting the numerical values we find $D_{zz} \approx 13$, 21, 30 nm^2 s^{-1} for ^{75}As, ^{69}Ga and ^{71}Ga, respectively. The experiments presented in this work do not resolve between spin diffusion of the individual isotopes. As a simple approximation we can treat the observed NSR dynamics as a result of spin diffusion within one type of nuclei but with a weighted average diffusion constant. We use as weights the relative contributions of the isotopes to the optically measured hyperfine shift $E_{\rm hf}$. From the previous studies of the similar QDs [14] these contributions are estimated as 0.49, 0.28 and 0.23 for ^{75}As, ^{69}Ga and ^{71}Ga, respectively, from where the average diffusion coefficient is approximated as $D_{zz} \approx 19$ nm^2.

Supplementary Note 4. NUMERICAL SIMULATION OF NUCLEAR SPIN DIFFUSION

The spatiotemporal evolution of the nuclear spin polarization degree $P_{\rm N}(t,z)$ is modeled by solving the partial differential spin diffusion equation

$$\frac{\partial P_{\rm N}(t,z)}{\partial t} = D(t)\frac{\partial^2 P_{\rm N}(t,z)}{\partial z^2} + w(t)|\psi_{\rm e}(z)|^2(P_{\rm N,0} - P_{\rm N}(t,z)), \tag{S2}$$

where the last term describes optical nuclear spin pumping with a rate proportional to electron density $|\psi_{\rm e}(z)|^2$ and the time-dependent factor $w(t)$ equal to 0 or w_0 when optical pumping is off or on, respectively. The spin diffusion coefficient $D(t)$ also takes two discrete values $D_{\rm Dark}$ or $D_{\rm Pump}$

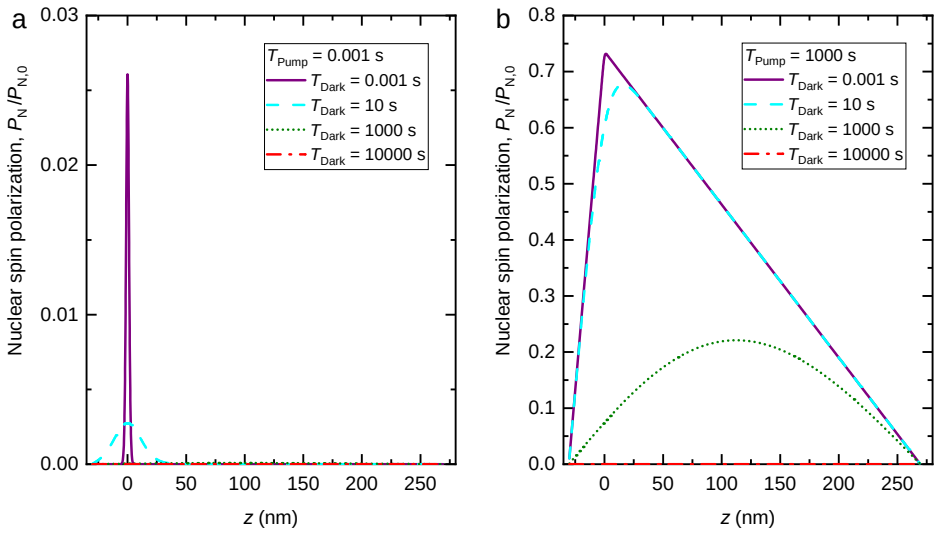

Supplementary Figure 8. **Numerical modeling of the nuclear spin diffusion.** Calculated normalized nuclear spin polarization as a function of the z coordinate at different T_{Dark}. **a** Calculations for $T_{\mathrm{Pump}} = 1$ ms. **b** Same calculations as (a) but for $T_{\mathrm{Pump}} = 1000$ s.

when optical pumping is off or on, respectively. $P_{\mathrm{N},0}$ is a steady state nuclear spin polarization degree that optical pumping would generate in the absence of spin diffusion. At each time point we assume the same diffusion coefficient D across the entire structure. The equation describes a one-dimensional problem where diffusion can take place only along the z coordinate so that the nuclear spin polarization degree P_{N} does not depend on x or y. The GaAs QD layer is modeled by taking a Gaussian profile for the electron density $|\psi_{\mathrm{e}}(z)|^2 \propto 2^{-\left(\frac{z-z_0}{h_{\mathrm{QD}}/2}\right)^2}$, where h_{QD} is the full width at half maximum of the $|\psi_{\mathrm{e}}(z)|^2$ function and the center of the QD is set to be $z_0 = 0$. We use Dirichlet boundary condition $P_{\mathrm{N}} = 0$ to model fast nuclear spin depolarization in presence of the free carriers both in the n- and p-type doped layers. The boundary coordinates, where Dirichlet conditions are enforced, are chosen to match the actual sample structure as described in Supplementary Note 1. We note that the hyperfine interaction of the valence band holes is approximately 10 times weaker than for the conduction band electrons [6]. Moreover, the p-type layer is approximately 10 times further away from the QDs than the n-type layer. As a result the dynamics of the nuclear spin polarization at the QD are dominated by the n-type layer, while the exact boundary condition at the p-type layer is less important, justifying the use of the Dirichlet condition at both doped layers.

Supplementary Eq. S2 is solved numerically using the method of lines implemented in WOLFRAM MATHEMATICA 12.0. The initial condition is taken to be $P_{\mathrm{N}} = 0 \ \forall \ z$, which models the result of

the RF Erase pulse at the start of each measurement cycle. Optical nuclear spin pumping starts at $t = -T_{\mathrm{Pump}}$ and the equation is solved until $t = 0$ with $D = D_{\mathrm{Pump}}$ and $w = w_0$. At $t = 0$ optical pumping is switched off by setting $w = 0$ and the equation is solved until $t = T_{\mathrm{Dark}}$ with $D = D_{\mathrm{Dark}}$. Supplementary Fig. 8 shows the calculated spatial profiles of the final nuclear spin polarization $P_{\mathrm{N}}(T_{\mathrm{Dark}}, z)$ normalized by its steady-state value $P_{\mathrm{N},0}$. The results are shown for several T_{Dark} values in case of a short pumping (a, $T_{\mathrm{Pump}} = 1$ ms) and long pumping (b, $T_{\mathrm{Pump}} = 1000$ s). Short pumping results in a small-magnitude ($P_{\mathrm{N}} \ll P_{\mathrm{N},0}$) spatially-narrow nuclear spin polarization, which quickly dissipates at $t > 0$. By contrast, long pumping leads to a steady-state spatial distribution where polarization peaks at the quantum dot coordinate $z = 0$ and reduces linearly towards the doped layers which act as nuclear spin polarization sinks. Interestingly, this calculation predicts that the maximum polarization $P_{\mathrm{N},0}$ is not achieved because of the diffusion towards the doped layers, especially the closely located n-type layer at $z < 0$.

In order to compare simulations with the experimental results the final spatial distribution $P_{\mathrm{N}}(T_{\mathrm{Dark}}, z)$ is multiplied by $|\psi_{\mathrm{e}}(z)|^2$ and integrated over z. This way we reproduce the optical probing of the nuclear spin polarization, where the measured hyperfine shift E_{hf} is effectively weighted by the electron envelope wavefunction density $|\psi_{\mathrm{e}}(z)|^2$. The simulated hyperfine shift is then derived as $E_{\mathrm{hf}} = AIP_{\mathrm{N}}$, where I is the nuclear spin number and A is the hyperfine constant. We then use a differential evolution algorithm to vary the parameters such as $D^{(ne)}_{\mathrm{Dark}}(B_{\mathrm{z}})$, $w_0(B_{\mathrm{z}})$ and $D_{\mathrm{Pump}}(B_{\mathrm{z}})$ and fit the simulated E_{hf} dynamics to the entire experimental datasets of $E_{\mathrm{hf}}(T_{\mathrm{Pump}}, T_{\mathrm{Dark}})$ measured at $B_{\mathrm{z}} = 0.39$ and 9.82 T for empty ($n = 0$) and charged ($n = 1$) QD states. As discussed in the main text the best-fit diffusion coefficients in the dark are $D^{(1e)}_{\mathrm{Dark}}(9.82\ \mathrm{T}) = 4.7^{+1.2}_{-1.0}$ nm^2 s^{-1}, $D^{(1e)}_{\mathrm{Dark}}(0.39\ \mathrm{T}) = 7.7 \pm 1.9$ nm^2 s^{-1} and $D^{(0e)}_{\mathrm{Dark}} = 2.2^{+0.7}_{-0.5}$ nm^2 s^{-1} independent of magnetic field. For spin diffusion coefficients under optical pumping we find significantly larger values $D^{(1e)}_{\mathrm{Pump}}(9.82\ \mathrm{T}) = 96^{+44}_{-28}$ nm^2 s^{-1} and $D^{(1e)}_{\mathrm{Pump}}(0.39\ \mathrm{T}) = 850^{+240}_{-220}$ nm^2 s^{-1}. Such increase in D can be ascribed to the spectrally broad fluctuations of the optically generated electron spins which facilitate coupling between the distant nuclear spins, thus accelerating the spin diffusion. This is also consistent with the proposed influence of the phonon-induced electron spin flips on nuclear spin diffusion in the dark (see main text). The other best-fit parameters are $w_0(0.39\ \mathrm{T}) = 37^{+7}_{-5}$ s^{-1}, $w_0(9.82\ \mathrm{T}) = 5.7^{+1.1}_{-0.9}$ s^{-1} and $h_{\mathrm{QD}} = 2.1^{+0.3}_{-0.2}$ nm. Previous studies on GaAs/AlGaAs QDs emitting at a similar wavelength estimated that 0.92 of the electron density resides in the GaAs layer [14], whose full width can then be estimated as $h_{\mathrm{QD}} \frac{\mathrm{erf}^{-1}(0.92)}{\sqrt{\ln(2)}} = 3.2^{+0.4}_{-0.3}$ nm. This best-fit value somewhat underestimates the true QD thickness in z direction, but is within the range bounded by the QW thickness (2.1 nm) and the maximum QD thickness ($\approx$ 9 nm)

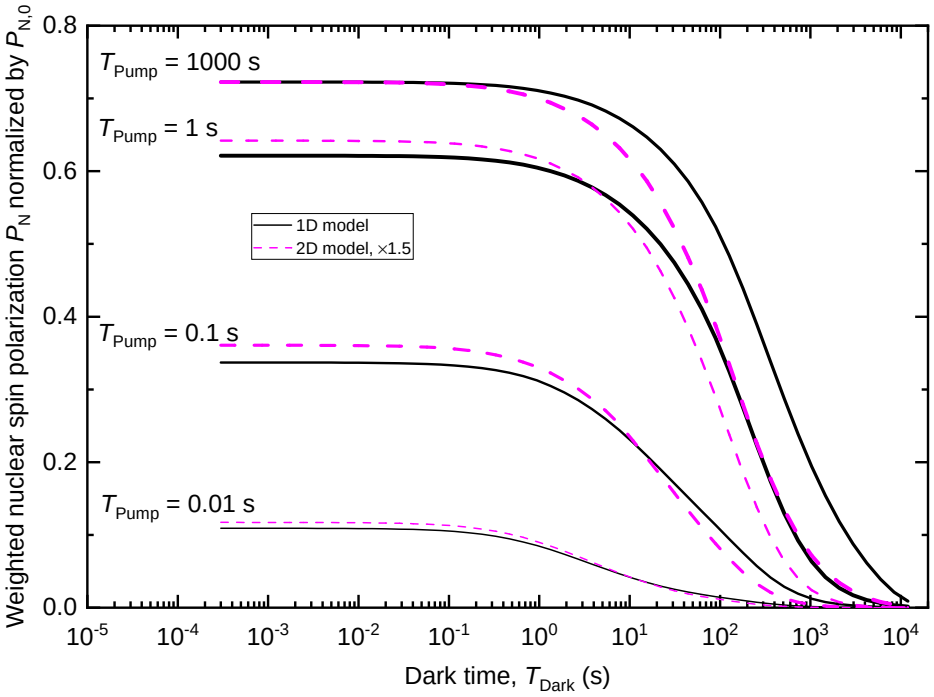

Supplementary Figure 9. **Numerical modeling of 1D and 2D nuclear spin diffusion.** Numerically simulated nuclear spin polarization degree P_{N} weighted by the electron envelope wavefunction density $|\psi_{\mathrm{e}}(z)|^2$ and normalized by the maximum nuclear spin polarization $P_{\mathrm{N},0}$ in the absence of spin diffusion. The weighted polarization is plotted as a function of the dark time T_{Dark} for different T_{Pump}. The results are shown for the case of one dimensional diffusion (1D, solid lines) and two dimensional diffusion (2D, dashed lines, P_{N} values multiplied by 1.5).

estimated from the nanohole depth in AFM. The spatial profiles shown in Supplementary Fig. 8 are calculated with the best-fit parameters for the $1e$ case at $B_{\mathrm{z}} = 0.39$ T.

The use of the one dimensional spin diffusion model is motivated by the large aspect ratio of the QD. Indeed, the diffusion proceeds predominantly along the direction of the strongest gradient in the nuclear spin polarization degree, which is the growth z direction. For numerical simulations, the one dimensional model is also advantageous as it requires significantly less computational resources than a full three dimensional diffusion model. In order to evaluate the limitations of the one dimensional model we run a simulation of a two dimensional diffusion problem, where the equation now reads:

$$\frac{\partial P_{\mathrm{N}}(t,x,z)}{\partial t} = D(t)\left(\frac{\partial^2 P_{\mathrm{N}}(t,x,z)}{\partial x^2} + \frac{\partial^2 P_{\mathrm{N}}(t,x,z)}{\partial z^2}\right) + w(t)|\psi_{\mathrm{e}}(x,z)|^2(P_{\mathrm{N},0} - P_{\mathrm{N}}(t,x,z)) \quad \text{(S3)}$$

The electron density is taken to be $|\psi_{\mathrm{e}}(x,z)|^2 \propto 2^{-\left(\frac{x-x_0}{d_{\mathrm{QD}}/2}+\frac{z-z_0}{h_{\mathrm{QD}}/2}\right)^2}$, where d_{QD} is a full width at

half maximum diameter of the QD, which we set to $d_{\mathrm{QD}} = 47$ nm in order to match the 0.92 electron wavefunction density in a QD with a full diameter of 70 nm. The same $|\psi_{\mathrm{e}}(x,z)|^2$ is used to calculate the weighted nuclear spin polarization degree, emulating the optical probing of the QD hyperfine shift E_{hf}. The computational domain is limited to $|x| < 700$ nm and we implement the additional Dirichlet boundary condition $P_{\mathrm{N}}(x = \pm 700\ \mathrm{nm}) = 0$.

Supplementary Fig. 9 shows the simulated QD NSR dynamics in the one dimensional (1D, solid lines) and two dimensional (2D, dashed lines) cases, following nuclear spin pumping with different durations T_{Pump}. One apparent difference in the resulting dynamics is the lower weighted nuclear spin polarization degree within the QD volume in the 2D case. Consequently, all the 2D-case P_{N} values in Supplementary Fig. 9 have been multiplied by 1.5, to simplify comparison with the 1D case. At short $T_{\mathrm{Pump}} \leq 0.1$ s QD nuclear spin polarization decays on the same timescale both in the 1D and 2D cases. This is expected since the spatial profile of the nuclear spin polarization produced by short pumping is proportional to $\propto |\psi_{\mathrm{e}}(x,z)|^2$ in the 2D case. As a result, the subsequent diffusion in the dark proceeds predominantly along the direction of the highest gradient (the growth z direction), making diffusion essentially one dimensional. By contrast, long pumping $T_{\mathrm{Pump}} \geq 0.1$ s in a 2D model makes the polarization profile more isotropic in the xz plane (for an unbounded problem at $T_{\mathrm{Pump}} \to \infty$ the polarization will tend to a profile with circular contour lines in the xz plane). In other words, after long pumping the system "forgets" the initial profile $\propto |\psi_{\mathrm{e}}(x,z)|^2$ of the QD pumping source. The subsequent diffusion in the absence of pumping (i.e. in the dark) is controlled by the dimensionality of the unpolarized space, and is seen to be faster in the 2D case. From these additional results we conclude that the one dimensional model is sufficient to capture the key aspects of QD NSR dynamics, such as slower relaxation following long optical nuclear spin pumping. However, some deviation of the 1D model from the real dynamics is inevitable, especially at long T_{Pump}, where dimensionality affects the diffusion dynamics. Such discrepancies are likely to introduce systematic errors in the best fit dynamics (Supplementary Fig. 6) and spin diffusion coefficient D values. On the other hand, in a real QD system D is not constant, and the approximate nature of the spin diffusion concept itself entails a range of systematic errors. This justifies the use of a simplified one dimensional model to describe our experimental results.

Supplementary Note 5. ELECTRON SPIN RELAXATION TIME

Here we present electron spin lifetimes $T_{1,\mathrm{e}}$ obtained from preliminary measurements in a sep-

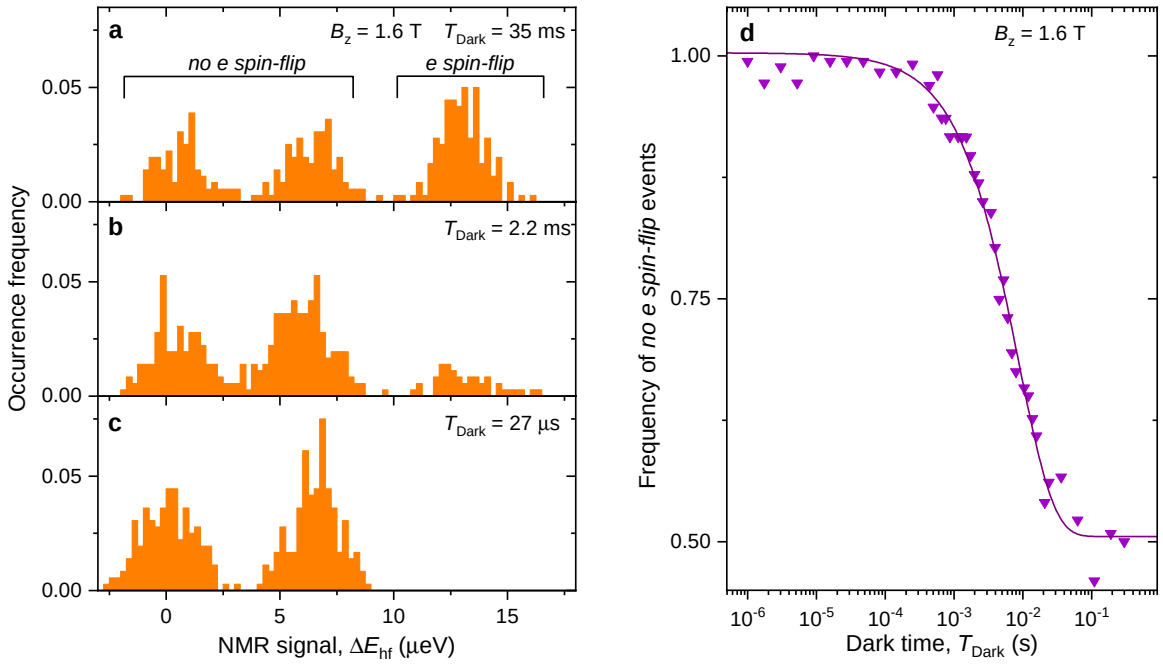

Supplementary Figure 10. **Electron spin lifetime measurements. a-c** Histograms of the single-shot NMR measurements in presence of an electron conducted for different intervals T_{Dark} between the two detuned RF pulses. **d** Frequency of the events where the electron spin does not flip over the T_{Dark} time interval (symbols). Lines shows fitting used to derive the electron spin relaxation time.

arate piece of the same epitaxial GaAs/AlGaAs QD structure. Experimental investigation of the relaxation dynamics requires a tool to measure the state of the resident electron spin trapped in a QD. We use a variation of the method demonstrated recently in Stranski-Krastanov QDs [29]. The technique uses the nuclear spin ensemble of a QD and the Knight shifts, which reduce (increase) the NMR frequency if the electron spin is in the $s_z = -1/2$ ($s_z = +1/2$) state. The state of the electron is encoded into the nuclear spin polarization by applying an RF pulse whose frequency is tuned to be resonant with the nuclei only if the electron is in the $s_z = -1/2$ spin state. The amplitude and the duration of the pulse are calibrated to produce a π rotation (polarization inversion) of the nuclei when $s_z = -1/2$. By contrast, for $s_z = +1/2$, the Knight field detunes the nuclei out of resonance with the RF pulse, meaning that nuclear polarization is not inverted. Following the RF π pulse an optical probe is used to measure the changes in the nuclear spin polarization (the changes in the hyperfine shift E_{hf}). In this way, a single-shot readout of the electron spin is performed with high fidelity, exceeding 99%.

We take this method one step further by applying two RF π pulses separated by a free evolution time T_{Dark}. The first pulse performs heralded initialization of the electron spin state through

measurement, while the second RF pulse probes whether the state of the electron spin has changed during the free evolution time $T_{\rm Dark}$. There are three possible outcomes of such an experiment: (i) The electron is in the $s_{\rm z} = +1/2$ state initially and remains in this state. Both RF pulses are then out of resonance with the nuclei, so that a minimal NMR signal (variation in $E_{\rm hf}$) is expected. (ii) The electron is in the $s_{\rm z} = -1/2$ state initially and remains in this state. Both RF pulses are in resonance, so that the nuclei get rotated twice. While a 2π rotation is supposed to return the nuclei into the original state, the Knight shift inhomogeneity means that the rotations are imperfect. Thus a small but finite variation in $E_{\rm hf}$ is expected. (iii) The electron is in the $s_{\rm z} = \pm 1/2$ state initially, but flips into the opposite state $s_{\rm z} = \mp 1/2$ during the $T_{\rm Dark}$ interval. In this case one of the RF pulses will be in resonance and one out of resonance. The overall rotation will be π, so that a large change in $E_{\rm hf}$ is expected.

The results of the single-shot NMR measurements are shown in Supplementary Figs. 10a-c for different $T_{\rm Dark}$. At short $T_{\rm Dark}$ there is a bimodal distribution of the NMR signals. The two modes correspond to the no-spin-flip cases (i) and (ii), where the electron preserves its spin during $T_{\rm Dark}$. As the free evolution time becomes longer, the third mode emerges, corresponding to the spin-flip case (iii), where the electron has the opposite spin projections at the start and the end of the $T_{\rm Dark}$ interval. From such histograms, we evaluate the frequency of the events where the electron spin is not flipped and plot it as a function of $T_{\rm Dark}$ (symbols in Supplementary Fig. 10d). At short $T_{\rm Dark}$ the frequency is close to unity, while in the limit of long $T_{\rm Dark}$ the frequency tends to 0.5 because the initial and the final electron spin states become completely uncorrelated. The solid line in Supplementary Fig. 10d shows the best stretched-exponential fit, which reveals the electron spin relaxation time $T_{1,\rm e} \approx 8.5$ ms in this particular experiment conducted at $B_{\rm z} = 1.6$ T. Similar measurements at different magnetic fields yield $T_{1,\rm e} \approx 7$ ms at $B_{\rm z} = 2$ T, reducing to $T_{1,\rm e} \approx 0.5$ ms at $B_{\rm z} = 7$ T. Further details and results are to be reported by H. E. Dyte, G. Gillard, *et al.* in a forthcoming publication.

Supplementary Note 6. RAW DATA

The raw data of Fig. 3b from the main text (diffusion reflux measurement) can be found in Supplementary file Fig3b.xls. This experimental dataset is not filtered.

The raw data for nuclear spin relaxation measurements can be found in Supplementary File FigS6.xls. This file contains a full dataset, part of which is shown by the symbols in Supplementary Fig. 6 and Fig. 4b of the main text. The data shown in the figures is mildly filtered (Gaussian

kernel filter with full width at half maximum of 0.2 in $\log_{10}$ units). The filtered data is given in the first four sheets of the file. The same unfiltered data is given in the last four sheets of the file. Each sheet corresponds to a certain QD charge state and magnetic field. In each sheet, the first column is the dark time T_{Dark} (horizontal axis) and the remaining columns are the E_{hf} values (vertical axis) for different pump times T_{Pump}.

---

[1] A. Oshiyama and S. Ohnishi, DX center: Crossover of deep and shallow states in Si-doped $Al_xGa_{1-x}As$, Phys. Rev. B **33**, 4320 (1986).

[2] P. M. Mooney, Deep donor levels (DX centers) in III-V semiconductors, Journal of Applied Physics **67**, R1 (1990).

[3] L. Zhai, M. C. Löbl, G. N. Nguyen, J. Ritzmann, A. Javadi, C. Spinnler, A. D. Wieck, A. Ludwig, and R. J. Warburton, Low-noise GaAs quantum dots for quantum photonics, Nat. Commun. **11**, 4745 (2020).

[4] C. Heyn, A. Stemmann, T. Koppen, C. Strelow, T. Kipp, M. Grave, S. Mendach, and W. Hansen, Highly uniform and strain-free GaAs quantum dots fabricated by filling of self-assembled nanoholes, Appl. Phys. Lett. **94**, 183113 (2009).

[5] P. Atkinson, E. Zallo, and O. G. Schmidt, Independent wavelength and density control of uniform GaAs/AlGaAs quantum dots grown by infilling self-assembled nanoholes, J. Appl. Phys. **112**, 054303 (2012).

[6] E. A. Checkhovich, M. M. Glazov, A. B. Krysa, M. Hopkinson, P. Senellart, A. Lemaître, M. S. Skolnick, and A. I. Tartakovskii, Element-sensitive measurement of the hole-nuclear spin interaction in quantum dots, Nat. Phys. **9**, 74 (2013).

[7] F. Bloch, Nuclear induction, Phys. Rev. **70**, 460 (1946).

[8] D. Gammon, A. L. Efros, T. A. Kennedy, M. Rosen, D. S. Katzer, D. Park, S. W. Brown, V. L. Korenev, and I. A. Merkulov, Electron and nuclear spin interactions in the optical spectra of single GaAs quantum dots, Phys. Rev. Lett. **86**, 5176 (2001).

[9] B. Eble, O. Krebs, A. Lemaître, K. Kowalik, A. Kudelski, P. Voisin, B. Urbaszek, X. Marie, and T. Amand, Dynamic nuclear polarization of a single charge-tunable InAs/GaAs quantum dot, Phys. Rev. B **74**, 081306 (2006).

[10] J. Skiba-Szymanska, E. A. Chekhovich, A. E. Nikolaenko, A. I. Tartakovskii, M. N. Makhonin, I. Drouzas, M. S. Skolnick, and A. B. Krysa, Overhauser effect in individual $InP/Ga_xIn_{1-x}P$ dots, Phys. Rev. B **77**, 165338 (2008).

[11] A. Ulhaq, Q. Duan, E. Zallo, F. Ding, O. G. Schmidt, A. I. Tartakovskii, M. S. Skolnick, and E. A. Chekhovich, Vanishing electron g factor and long-lived nuclear spin polarization in weakly strained nanohole-filled GaAs/AlGaAs quantum dots, Phys. Rev. B **93**, 165306 (2016).

[12] G. Ragunathan, J. Kobak, G. Gillard, W. Pacuski, K. Sobczak, J. Borysiuk, M. S. Skolnick, and E. A. Chekhovich, Direct measurement of hyperfine shifts and radio frequency manipulation of nuclear spins in individual CdTe/ZnTe quantum dots, Phys. Rev. Lett. **122**, 096801 (2019).

[13] B. Urbaszek, X. Marie, T. Amand, O. Krebs, P. Voisin, P. Maletinsky, A. Högele, and A. Imamoglu, Nuclear spin physics in quantum dots: An optical investigation, Rev. Mod. Phys. **85**, 79 (2013).

[14] E. A. Chekhovich, A. Ulhaq, E. Zallo, F. Ding, O. G. Schmidt, and M. S. Skolnick, Measurement of the spin temperature of optically cooled nuclei and GaAs hyperfine constants in GaAs/AlGaAs quantum dots, Nature Mater. **16**, 982 (2017).

[15] Y. Wang and K. Takeda, Speedup of nuclear spin diffusion in hyperpolarized solids, New Journal of Physics **23**, 073015 (2021).

[16] D. Huber, B. U. Lehner, D. Csontosová, M. Reindl, S. Schuler, S. F. Covre da Silva, P. Klenovský, and A. Rastelli, Single-particle-picture breakdown in laterally weakly confining GaAs quantum dots, Phys. Rev. B **100**, 235425 (2019).

[17] C. Latta, A. Srivastava, and A. Imamoğlu, Hyperfine Interaction-Dominated Dynamics of Nuclear Spins in Self-Assembled InGaAs Quantum Dots, Phys. Rev. Lett. **107**, 167401 (2011).

[18] G. Gillard, I. M. Griffiths, G. Ragunathan, A. Ulhaq, C. McEwan, E. Clarke, and E. A. Chekhovich, Fundamental limits of electron and nuclear spin qubit lifetimes in an isolated self-assembled quantum dot, npj Quantum Inf. **7**, 43 (2021).

[19] E. A. Chekhovich, K. V. Kavokin, J. Puebla, A. B. Krysa, M. Hopkinson, A. D. Andreev, A. M. Sanchez, R. Beanland, M. S. Skolnick, and A. I. Tartakovskii, Structural analysis of strained quantum dots using nuclear magnetic resonance, Nature Nanotechnol. **7**, 646 (2012).

[20] E. A. Chekhovich, I. M. Griffiths, M. S. Skolnick, H. Huang, S. F. Covre da Silva, X. Yuan, and A. Rastelli, Cross calibration of deformation potentials and gradient-elastic tensors of GaAs using photoluminescence and nuclear magnetic resonance spectroscopy in GaAs/AlGaAs quantum dot structures, Phys. Rev. B **97**, 235311 (2018).

[21] B. Urbaszek, P.-F. Braun, T. Amand, O. Krebs, T. Belhadj, A. Lemaítre, P. Voisin, and X. Marie, Efficient dynamical nuclear polarization in quantum dots: Temperature dependence, Phys. Rev. B **76**, 201301 (2007).

[22] R. L. Mieher, Quadrupolar nuclear relaxation in the III-V compounds, Phys. Rev. **125**, 1537 (1962).

[23] J. A. McNeil and W. G. Clark, Nuclear quadrupolar spin-lattice relaxation in some III-V compounds, Phys. Rev. B **13**, 4705 (1976).

[24] I. J. Lowe and S. Gade, Density-matrix derivation of the spin-diffusion equation, Phys. Rev. **156**, 817 (1967).

[25] A. G. Redfield and W. N. Yu, Moment-method calculation of magnetization and interspin-energy diffusion, Phys. Rev. **169**, 443 (1968).

[26] A. G. Redfield and W. N. Yu, Moment-method calculation of magnetization and interspin-energy diffusion, Phys. Rev. **177**, 1018 (1969).

[27] E. R. Butkevich and R. K. Sabirov, On anisotropy of nuclear spin-diffusion coefficient, Physica Status Solidi (b) **146**, 683 (1988).

[28] R. K. Harris, E. D. Becker, S. M. Cabral de Menezes, R. Goodfellow, and P. Granger, NMR nomenclature: Nuclear spin properties and conventions for chemical shifts: IUPAC recommendations 2001, Solid State Nuclear Magnetic Resonance **22**, 458 (2002).

[29] G. Gillard, E. Clarke, and E. A. Chekhovich, Harnessing many-body spin environment for long coherence storage and high-fidelity single-shot qubit readout, Nature Communications **13**, 4048 (2022).

Chapter 6

Approaching a Fully-Polarised Nuclear Spin State

Thus far we have discussed the strain present in QDs and the spin dynamics of the nuclei after they have been polarised; however, the polarisation degree, P_N, of the QDs, which is an important metric, is yet to be discussed.

Let us consider an initial eigenstate, $|i\rangle$, of a Hamiltonian independent of hyperfine coupling, which connects a spin up electron with the nuclear spins of a QD. This eigenstate would be a basis vector for an electron spin qubit. Due to hyperfine interactions, the electron spin can flip (i.e. dephase) resulting in the system going into a final state $|f\rangle$. $|f\rangle$ is also an eigenstate of the original Hamiltonian, but the electron is now spin down. For this spin flip to have occurred, the total spin of the system needs to be conserved, so a single nucleus' spin must also have increased by $2s = 1$ [190]. As $|P_N|$ approaches unity the rate at which this electron spin qubit dephasing occurs decreases; this response rate is not linear, rather it scales as $\sqrt{1 - P_N^2}$ [191]. Apart from the rate of electron spin qubit dephasing, another figure of merit is the entropy of the system. This characterises the disorder within the nuclear ensemble; optically cooling the QD nuclear spins (by increasing P_N) reduces this disorder. Similar to the rate of electron spin qubit dephasing, the difference in entropy from $|P_N| = 80\%$ to $P_N = 0$ is minimal (approximately a factor of two smaller). However, when $|P_N|$ exceeds 95% for every additional '9' in the place value after the decimal point the entropy decreases by approximately an order of magnitude. This allows for a new, more interesting, regime to be achieved in which there is a highly-correlated many-body nuclear state.

In the theoretical literature there is some debate about whether it is even possible to reach near unity polarisations. References [192, 193] state that the maximum possible nuclear polarisation is $\approx 75\%$. They state this limitation is due the formation of dark states, which prevent any further polarisation build up [192–195]. Experimental work that occurred at a similar time to these papers was consistent with this high polarisation limit, only ever reaching $P_N \approx 65\%$. However, later work by that same group reached polarisations degrees of $\lesssim 80\%$ [131]. In the

early 2000s there was a paper that reached $P_N = 95\%$ (and $P_N = -55\%$), however this was for a different electronic system compared with QDs. A rhodium (spin-$\frac{1}{2}$) crystal at ~ 10 mK was used, and the time take to reach these polarisations was on the order of hours [196]. For practical quantum computing applications this duration is fairly limiting, as spin states would need to be repeatedly initialised; therefore, a process which requires such lengthy times would not be viable. It is also desirable to attain high polarisations at elevated temperatures, provided that the system maintains stability, thus the sub-Kelvin temperatures used here are not preferred.

In this chapter we will discuss our success in obtaining a higher degree of polarisation than has been demonstrated in the past, in GaAs/AlGaAs QDs at 4.2 K. This achievement paves the way for leveraging these QDs as quantum memories, providing a practical approach for addressing challenges in advanced tasks such as quantum error correction or quantum repeaters [197–199]. The work presented is in the form of a paper, which I am first author on, and has been published in a peer-reviewed journal on 2^{nd} February 2024, reproduced with permission from Springer Nature. The citation is:

P. Millington-Hotze, H. E. Dyte, S. Manna, S. F. Covre da Silva, A. Rastelli, E. A. Chekhovich. "Approaching a fully-polarized state of nuclear spins in a solid". *Nat Commun* **15**, 985 (2024). doi: 10.1038/s41467-024-45364-2.

In this work the optical spin pumping and NMR experiments along with their analysis were conducted by Peter Millington-Hotze and Evgeny Chekhovich. Additional NMR measurements on externally strained QDs was conducted by Harry Dyte and Evgeny Chekhovich. The samples were grown by Santanu Manna, Saimon Covre da Silva and Armando Rastelli.

nature communications

Article

https://doi.org/10.1038/s41467-024-45364-2

Approaching a fully-polarized state of nuclear spins in a solid

Received: 14 October 2023

Accepted: 18 January 2024

Published online: 02 February 2024

Check for updates

Peter Millington-Hotze[1], Harry E. Dyte[1], Santanu Manna[2,3], Saimon F. Covre da Silva[2], Armando Rastelli[2] & Evgeny A. Chekhovich[1]

Magnetic noise of atomic nuclear spins is a major source of decoherence in solid-state spin qubits. In theory, near-unity nuclear spin polarization can eliminate decoherence of the electron spin qubit, while turning the nuclei into a useful quantum information resource. However, achieving sufficiently high nuclear polarizations has remained an evasive goal. Here we implement a nuclear spin polarization protocol which combines strong optical pumping and fast electron tunneling. Nuclear polarizations well above 95% are generated in GaAs semiconductor quantum dots on a timescale of 1 minute. The technique is compatible with standard quantum dot device designs, where highly-polarized nuclear spins can simplify implementations of qubits and quantum memories, as well as offer a testbed for studies of many-body quantum dynamics and magnetism.

The capability of initializing a quantum system into a well-defined eigenstate is one of the fundamental requirements in quantum science and technology. This has been demonstrated for individual and dilute nuclear spins in the solid state[1,2], but remains a long-standing challenge for dense three-dimensional lattices of nuclear spins. For the quantum ground state of a spin ensemble the polarization degree is $P_N = \pm 100\%$, which is equivalent to absolute zero spin temperature. Very high polarizations, $P_N \approx 95$–99%, can be reached through brute-force cooling in certain bulk materials, but the cooling cycle may take hours or even days[3,4]. More scalable approaches seek to use individual or dilute electron spins to polarize the dense nuclear ensembles. Microwave pumping of paramagnetic impurities in bulk solids[5,6] provides polarizations up to $P_N \approx 80$–90%. In semiconductor nanostructures, $P_N \approx 50$–80% is achieved either through electronic transport[7] or optical excitation[8]. However, polarizations much closer to unity are needed to suppress the electron spin qubit dephasing, whose rate scales as $\sqrt{1-P_N^2}$[9], or reduce the nuclear ensemble entropy, which scales as $\frac{1-P_N}{2}(1-\ln(\frac{1-P_N}{2}))$[10]. Therefore, different techniques are needed to approach a fully-polarized nuclear state.

Extensive theoretical studies have been conducted to understand what limits nuclear spin pumping in a central-spin scenario, where the electron can be polarized on demand, while the ensemble of N nuclei can only be accessed through hyperfine (magnetic) coupling with that central electron (Fig. 1a). The formation of coherent "dark" states[11] has been shown to suppress the transfer of polarization from the electron to nuclei[12]. Thus an open question remains – is it possible, even in principle, to reach a fully-polarized nuclear state in a real central-spin system?

We work with GaAs/AlGaAs quantum dots (QDs) and use optical excitation to polarize nuclear spins. While the optical method is well known[13], achieving near-unity polarizations and understanding the underlying physics proved challenging. Here, we show that the solution is to combine strong optical excitation with fast carrier tunneling, which resolves the main bottleneck of slow optical recombination. Moreover, no "dark"-state limitation occurs, which we also attribute to the extremely short lifetime of the electron spin. As a result, we achieve nuclear polarization degrees well above $P_N > 95\%$. The maximum polarizations vary between individual QDs, which we ascribe to slight fluctuations in QD shapes and partial relaxation of the optical selection rules. For the best dots we derive $P_N \gtrsim 99\%$, limited only by the accuracy of the existing measurement techniques. These high polarizations surpass the predicted $P_N \gtrsim 90\%$ threshold for achieving extended electron spin qubit coherence[14,15], quantum memory operation[15,16],

[1]Department of Physics and Astronomy, University of Sheffield, Sheffield S3 7RH, United Kingdom. [2]Institute of Semiconductor and Solid State Physics, Johannes Kepler University Linz, Altenberger Str. 69, Linz 4040, Austria. [3]Present address: Department of Electrical Engineering, Indian Institute of Technology Delhi, New Delhi 110016, India. e-mail: e.chekhovich@sheffield.ac.uk

https://doi.org/10.1038/s41467-024-45364-2

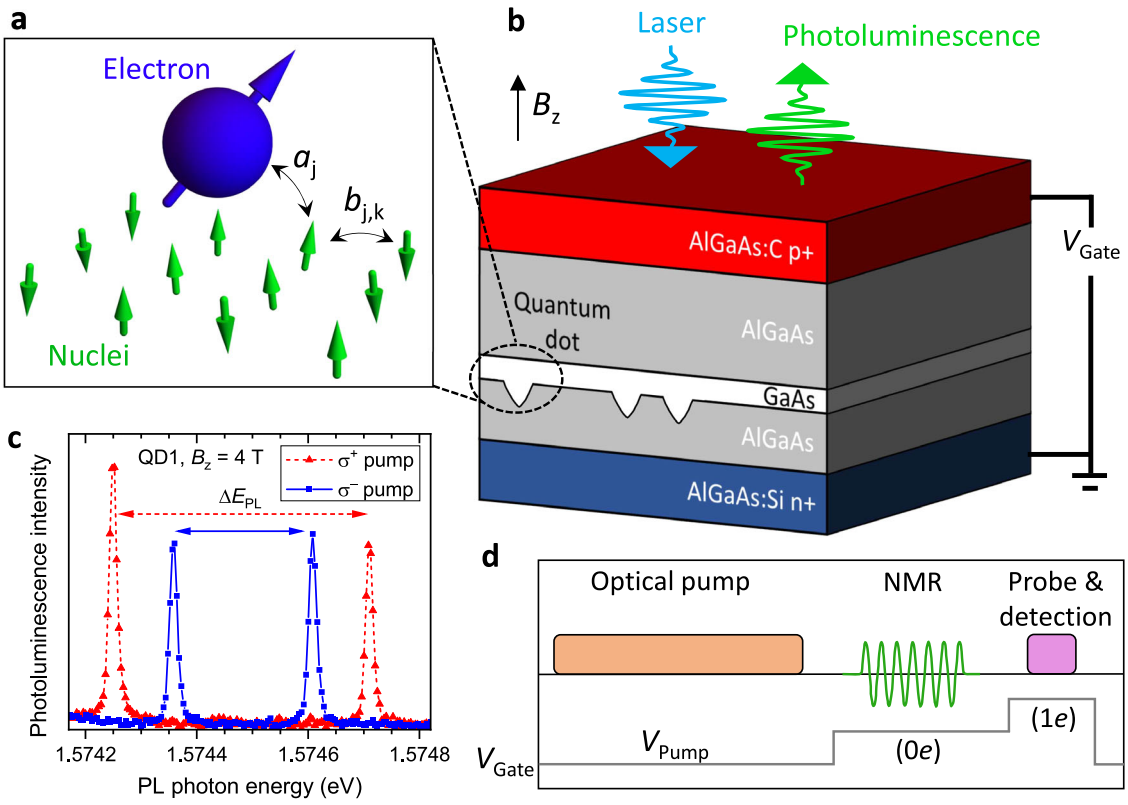

Fig. 1 | Optical control of quantum dot nuclear spins. a Schematic of a central electron spin and an ensemble of nuclear spins coupled through hyperfine interaction with constants a_j. The nuclei are coupled through dipolar interactions with pairwise constants $b_{j,k}$ (see Supplementary Note 2). **b** Schematic cross-section of a $p-i-n$ diode with embedded epitaxial GaAs quantum dots. Laser excitation, photoluminescence collection and the external magnetic field are directed along the sample growth axis z. Doped semiconductor layers are used to apply the gate bias V_{Gate}, resulting in a tunable electric field along z. **c** Typical photoluminescence spectra of a negatively charged trion X^- in an individual QD. The spectral splitting ΔE_{PL} depends both on magnetic field B_z and the helicity (σ^+ or σ^-) of the optical pumping due to the buildup of the nuclear spin polarization. **d** Experimental cycle consisting of nuclear spin optical pumping, nuclear magnetic resonance (NMR) excitation, and optical probing of the photoluminescence spectrum. V_{Gate} is switched between an arbitrary level V_{Pump} and the levels that tune the QD into the electron-charged (1e) and neutral (0e) states.

superradiant electron-nuclear spin dynamics[17,18], as well as magnetic-ordering phase transition[19,20].

Results

The semiconductor device, sketched in Fig. 1b, is a $p-i-n$ diode with epitaxial GaAs QDs embedded into the AlGaAs barrier layers (see Supplementary Note 1). By changing the gate bias V_{Gate} it is possible to charge the QD with individual resident electrons[21,22] and apply a tunable electric field. Each individual QD contains $N \approx 10^5$ nuclei, with the three abundant isotopes ^{75}As, ^{69}Ga and ^{71}Ga, all possessing spin momentum $I = 3/2$. The sample is cooled to ≈4.25 K and placed in a magnetic field B_z parallel to the electric field and sample growth direction (see Supplementary Note 3). Thanks to the selection rules[13], optical excitation creates spin-polarized electron-hole pairs; $\sigma^{\pm}$ polarized photons with ±1 angular momentum (in units of $\hbar$) generate electrons with spin projection $s_z = \mp 1/2$. Owing to the electron-nuclear hyperfine interaction (Fig. 1a), a polarized electron can transfer its spin to one of the nuclei and, through repeated optical pumping, induce a substantial polarization $|P_N|$. Conversely, the energy of the photon emitted from electron-hole recombination depends on the mutual alignment of the electron spin and the total magnetic field, which is a sum of B_z and the effective field of the polarized nuclei. The resulting optical spectrum is a doublet (Fig. 1c), whose splitting ΔE_{PL} is used as a sensitive probe of the nuclear spin polarization state. We define the exciton hyperfine shift $E_{hf} = -(\Delta E_{PL} - \Delta E_{PL,0})$, where $\Delta E_{PL,0}$ is the splitting measured for depolarized nuclei ($P_N \approx 0$).

The high resolution optical spectra (Fig. 1c), required to measure E_{hf}, can only be observed for a narrow range of gate biases and optical excitation powers. Therefore, we use a pump-probe technique (Fig. 1d), where the nuclear spins are polarized by an optical pump with an arbitrary set of parameters, while the optical probe parameters are fixed and optimized for the readout of E_{hf}. Conducting experiments at high magnetic field $B_z = 10$ T, we maximize the hyperfine shift $|E_{hf}|$ by optimizing the following parameters: the elliptical polarization of the optical pump, its power P_{Pump}, photon energy E_{Pump} and the bias V_{Pump} during pumping. The results are interpreted with reference to photoluminescence data. Figure 2a shows low power luminescence spectra, which reveal a well-known bias-controlled charging of the ground state (s-shell) exciton in a QD[22]. High optical power (Fig. 2b) broadens the spectra, also populating the higher shells p, d, etc.[23,24]. (See additional data in Supplementary Note 4).

The dependence of nuclear-induced shift E_{hf} on E_{Pump} and V_{Pump}, shown in Fig. 2c, reveals spectral bands that match the excitonic shells in Fig. 2b, demonstrating that nuclear spin pumping proceeds through resonant optical driving of the QD exciton transitions. The largest $|E_{hf}|$ is observed when the pump is resonant with the s shell ($E_{Pump} \approx 1.565$ eV), and at a large reverse bias $V_{Pump} = -2.3$ V, where photoluminescence is completely quenched. Moreover, the optimal pump laser power $P_{Pump} = 1.5$ mW is five orders of magnitude higher than the saturation power of the s-shell luminescence. Based on these observations, the nuclear spin pumping effect can be understood as a cyclic process sketched in Fig. 2d. First, circularly-polarized resonant

https://doi.org/10.1038/s41467-024-45364-2

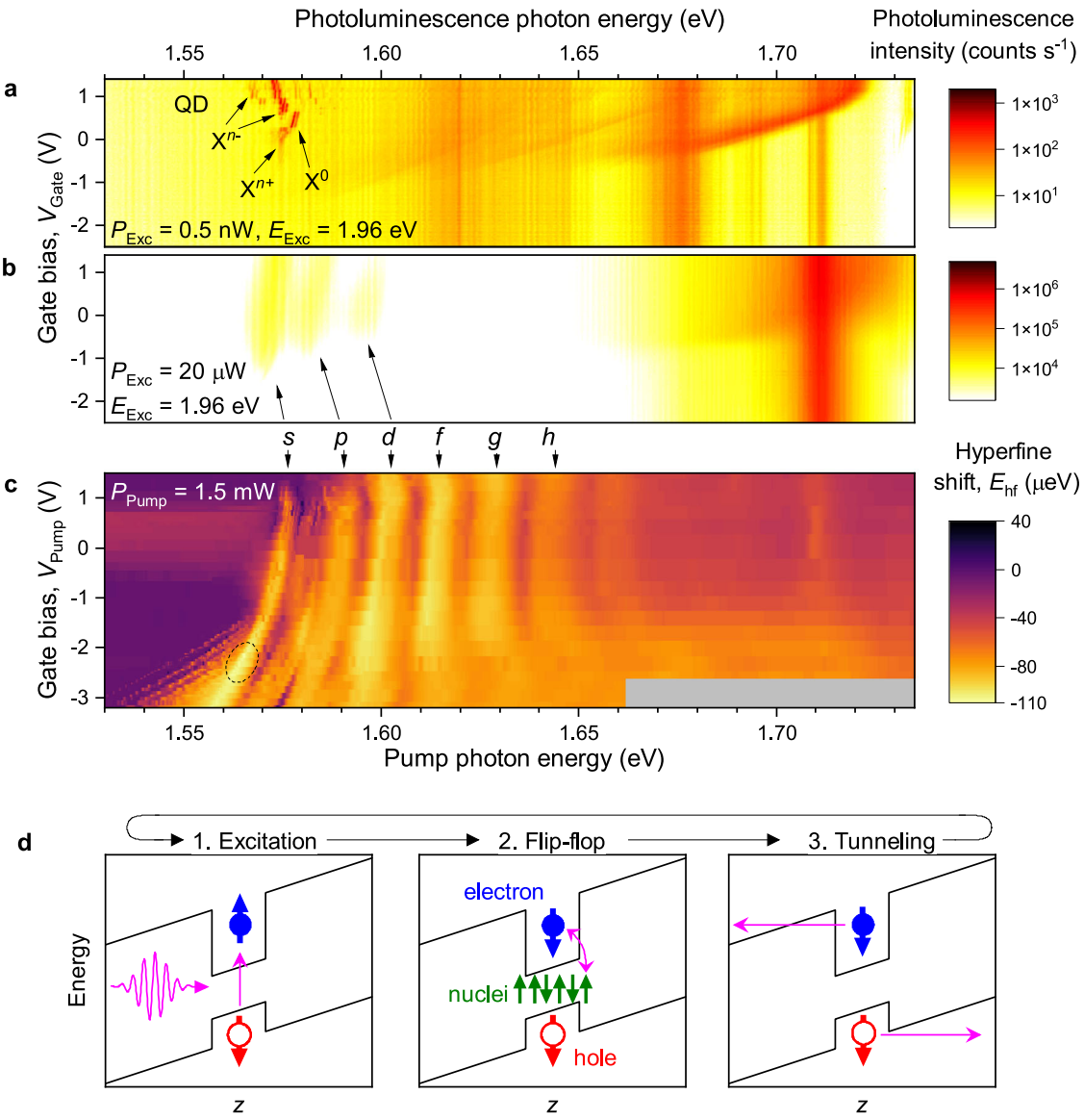

Fig. 2 | Tunneling-assisted optical nuclear spin pumping. a Bias-dependent photoluminescence spectra of an individual dot QD1 measured at $B_z = 10$ T at low excitation power $P_{Exc} = 0.5$ nW and excitation photon energy $E_{Exc} = 1.96$ eV. Labels show neutral (X^0), positively (X^{n+}) and negatively (X^{n-}) multi-charged QD excitons. Broad spectral features at higher energies arise from the AlGaAs layers. **b** Photoluminescence spectra at an increased power $P_{Exc} = 20\,\mu$W reveal saturated emission from higher QD exciton shells, labeled *s*, *p*, *d*. **c** Hyperfine shift measured in a pump-probe experiment (Fig. 1d) on QD1 as a function of gate bias V_{Pump} and the photon energy E_{Pump} of the σ^+ polarized optical pump with power $P_{Pump} = 1.5$ mW. Parameter regions where no data has been measured are shown in gray. Excitonic spectral features are labeled up to the *h* shell. The dashed ellipse highlights the parameters that result in the most efficient nuclear spin polarization. **d** Schematic of the conduction and valence band edges along the *z* direction, as well as confined electron (full circles) and hole (open circles) states. The three stages of the cyclic nuclear spin pumping process are shown schematically. Source data for **a**–**c** are provided as a Source Data file.

optical excitation creates a spin-polarized electron-hole pair in the quantum dot. Then, the electron has a small but finite probability to undergo a flip-flop with one of the nuclei, increasing the ensemble polarization $|P_N|$. Finally, in order to proceed to the next cycle, the electron is removed through tunneling. The tunneling time, estimated from bias-dependent photoluminescence in Supplementary Note 4, is $\lesssim 0.1$ ps, much shorter than the ≈ 300 ps radiative recombination time[25]. The combination of high-power optical pumping and fast tunneling escape results in rapid cycling. This in turn leads to a high rate of nuclear spin pumping, which helps to outpace the inevitable nuclear spin relaxation. The cycling time is also much shorter than the period of coherent electron precession $\gtrsim 20$ ps, ensuring the spin-flipped electrons are removed before they can undergo a reverse flip-flop[26]. The ultimate result is a large steady-state nuclear hyperfine shift $|E_{hf}| > 110\,\mu$eV, exceeding $|E_{hf}|$ observed previously[8,27].

Although E_{hf} scales linearly with nuclear polarization degree P_N, its absolute value depends on the QD structure. The electron wavefunction leaks into the barriers where the fraction of Ga atoms replaced with Al atoms is not known precisely. A more reliable measurement of the P_N is achieved through nuclear magnetic resonance (NMR) spin thermometry (see Supplementary Note 5 for details). The method assumes Boltzmann probability distribution $p_m \propto e^{m\beta}$ for each nucleus to occupy a state with spin projections m, where β is the dimensionless inverse spin temperature. For spin $I = 1/2$, where $m = \pm 1/2$, any statistical distribution has the Boltzmann form. By contrast, for $I > 1/2$, the Boltzmann distribution expresses the non-trivial nuclear spin temperature hypothesis[28], verified for epitaxial GaAs quantum dots previously[8].

In order to perform spin thermometry, we first measure the single-QD NMR spectra[29], as exemplified in Fig. 3a for ^{69}Ga spins. The

https://doi.org/10.1038/s41467-024-45364-2

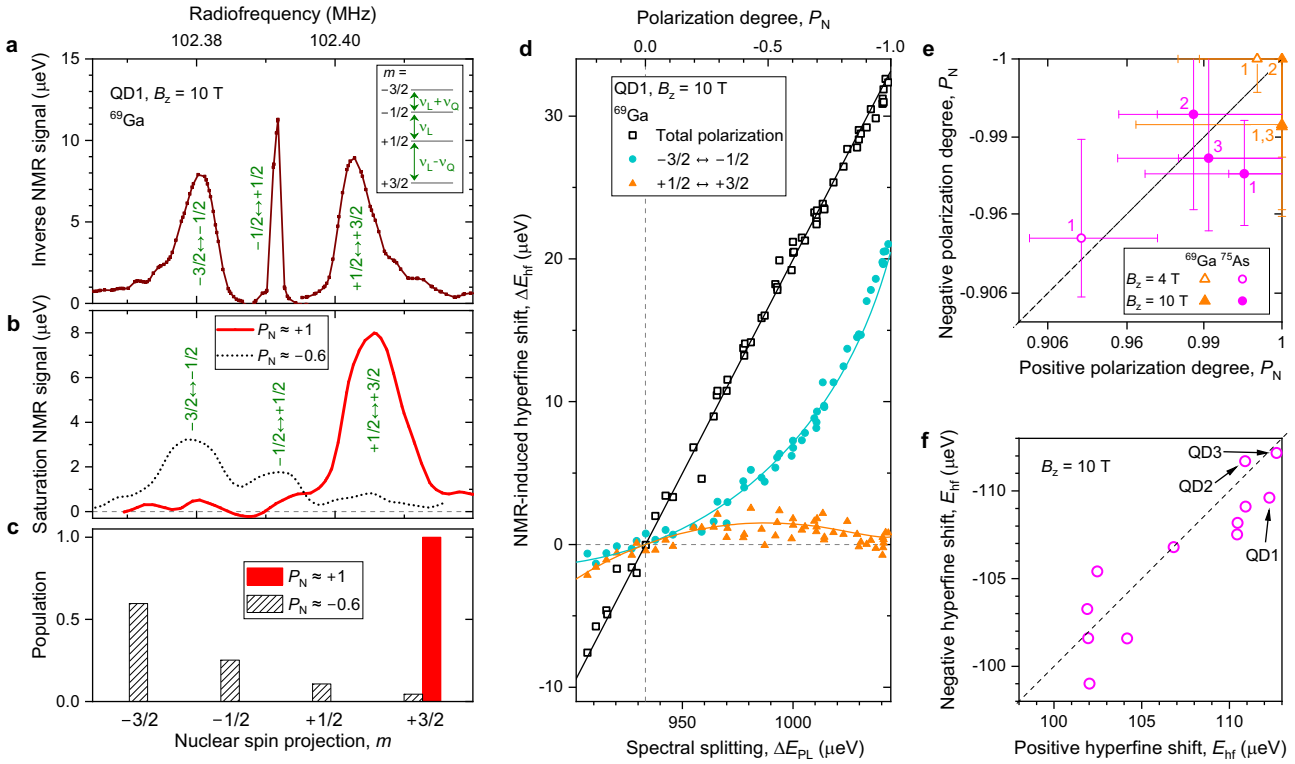

Fig. 3 | Nuclear magnetic resonance spin thermometry. a High-resolution spectrum of ^{69}Ga measured in QD1 at $B_z = 10$ T using "inverse NMR" signal enhancement technique[29]. Inset shows the nuclear energy levels with spin projections $m = \pm 1/2, \pm 3/2$. The resonance between $m = \pm 1/2$ is at a pure Larmor frequency ν_L, whereas the satellite transitions involving $m = \pm 3/2$ are split off by the quadrupolar shifts $\mp \nu_Q$ (for Ga nuclei the shifts are predominantly negative $\nu_Q < 0$). **b** Low-resolution spectrum of the same QD1, but measured using the saturation technique in order to reveal the population probabilities of the nuclear spin levels. **c** Population probabilities of spin levels with different m, sketched for the same two nuclear polarization degrees as in **b**. **d** Hyperfine shift variation arising from selective NMR manipulation of the ^{69}Ga nuclear spins plotted against the initial photoluminescence spectral splitting ΔE_{PL}, varied by changing the optical pump wavelength and polarization. Squares show the total ^{69}Ga hyperfine shift measured by broadband saturation of the entire NMR triplet, which equalizes populations p_m for all m. Circles and triangles show the selective signals of the $\pm 1/2 \leftrightarrow \pm 3/2$ resonances measured via frequency-swept adiabatic inversion. Lines show fitting, from which nuclear spin polarization degree is derived and plotted in the top horizontal scale (see Supplementary Note 5). **e** Maximum positive and minimum negative nuclear spin polarization degrees P_N derived for ^{69}Ga (triangles) and ^{75}As (circles) in individual dots QD1 - QD3 (indexed by numbers adjacent to the symbols) at $B_z = 10$ T (solid symbols) and $B_z = 4$ T (open symbols). Error bars are 95% confidence intervals. **f** Maximum positive and minimum negative hyperfine shifts measured on individual dots QD1–QD12 at $B_z = 10$ T. Source data for **d** and **f** are provided as a Source Data file. Source data for **e** can be found in Supplementary Information.

three magnetic-dipole transitions of the 3/2 spins are well resolved thanks to the quadrupolar shifts ν_Q, which originate from the lattice mismatch of GaAs and AlGaAs. Compared to the Larmor frequency $\nu_L \approx 100$ MHz, these strain-induced quadrupolar effects $|\nu_Q| \lesssim 100$ kHz are still too small to impede nuclear spin pumping. This is a significant advantage over the highly-strained Stranski–Krastanov QDs[29], where $|\nu_Q| \approx 1$–10 MHz so that large $|P_N|$ is prohibited simply because nuclear eigenstates are not aligned along the magnetic field[30] (the misalignment is characterized by the ratio $\propto (\nu_Q/\nu_L)^2$). The resolved NMR triplet is essential, as it allows β to be derived from the Boltzmann exponent, which then relates to P_N through the standard Brillouin function. Qualitatively this is demonstrated in Fig. 3b with simple saturation NMR spectroscopy[31]. At moderate polarization $P_N \approx -0.6$ (dashed line) all three magnetic-dipole transitions $m \leftrightarrow m+1$ are observed, and their amplitudes are proportional to the differences $|p_{m+1} - p_m|$ (Fig. 3c). At the maximum positive polarization (solid line) a single NMR peak $+1/2 \leftrightarrow +3/2$ is observed, indicating that nearly all spins have been cooled to the $m = +3/2$ state.

For quantitative spin thermometry we measure the peak areas of the $-3/2 \leftrightarrow -1/2$ and $+1/2 \leftrightarrow +3/2$ NMR transitions at different nuclear polarizations. The results are shown in Fig. 3d (circles and triangles), together with the total signal obtained by saturating all three NMR transitions (squares). We take into account the small overlaps of the NMR triplet components (see Supplementary Note 5) and use Boltzmann model fitting (lines) to derive the polarization degree P_N (top axis). The model reproduces well both the linear dependence of the total NMR signal and the non-linear dependencies of the selective $\pm 1/2 \leftrightarrow \pm 3/2$ signals, revealing a close approach to $P_N \approx -1$. Qualitatively, at $P_N = -1$ the $m = +1/2, +3/2$ states must be depopulated, resulting in a vanishing $+1/2 \leftrightarrow +3/2$ signal, as indeed observed experimentally. Moreover, at $P_N = -1$ the $-3/2 \leftrightarrow -1/2$ signal must be 2/3 of the total NMR signal, also in good agreement with experiment. By switching from σ^+ to σ^- optical pumping we also approach $P_N \approx +1$. The largest positive and negative P_N are shown in Fig. 3e for individual dots QD1–QD3, chosen for their highest $|E_{hf}|$. At the highest static field $B_z = 10$ T the best-fit estimates for ^{69}Ga are around $|P_N| \approx 0.99$, with somewhat lower $|P_N| \approx 0.98$ for ^{75}As. With 95% confidence, $|P_N|$ exceeds 0.95, but the data is also compatible with $|P_N| = 1$. It is thus possible that the actual polarization is much closer to unity – at present, the measurement accuracy is the main limitation. Spin thermometry on one of the QDs at $B_z = 4$ T yields similarly high polarizations $|P_N| \gtrsim 0.93$, although the measurement accuracy is reduced due to the less efficient optical probing.

A simpler measurement of the largest positive and negative hyperfine shift E_{hf} is shown in Fig. 3f for 12 randomly chosen dots. For some QDs, nuclear polarization does not exceed $|P_N| \approx 0.9$. We also observe that for all studied QDs the optimal optical polarization of the pump is not circular, but is rather elliptical[32], with a randomly-oriented linearly-polarized contribution ranging between 0 and 0.4 (see Supplementary Note 3). This points to heavy-light hole mixing, which is

https://doi.org/10.1038/s41467-024-45364-2

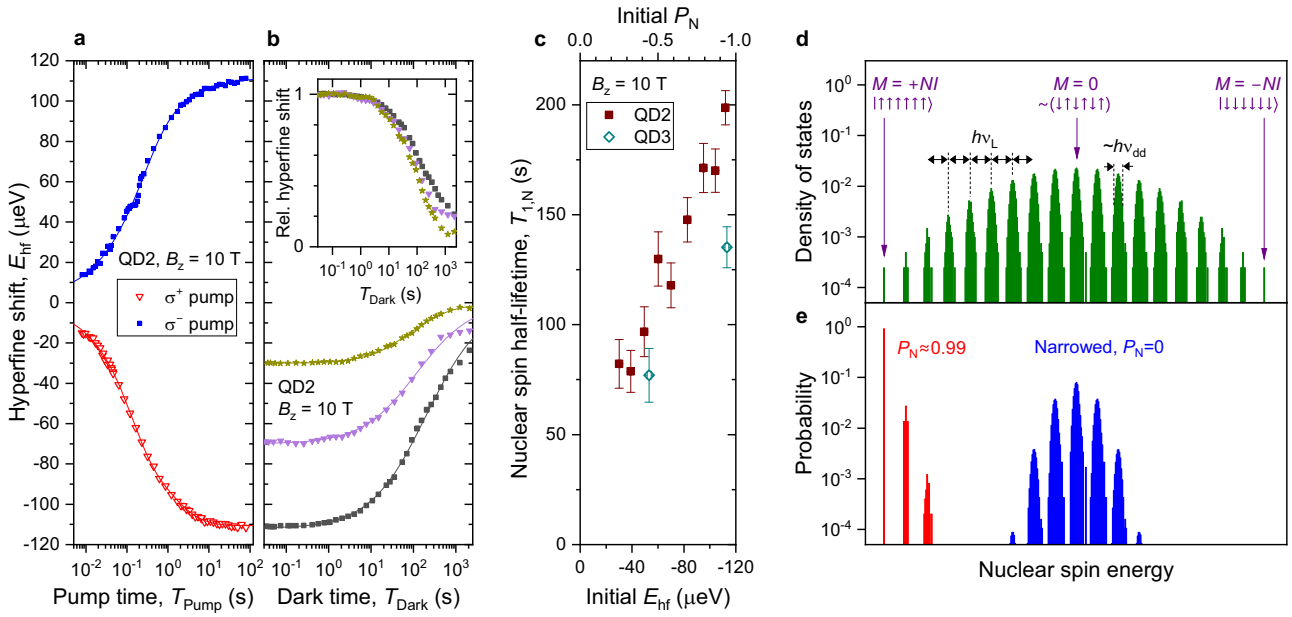

Fig. 4 | Nuclear spin dynamics. a Nuclear spin buildup dynamics measured (symbols) in an individual dot QD2 at $B_z = 10$ T under σ^+ (triangles) and σ^- (squares) optical pumping. Lines show biexponential fitting. **b** Nuclear spin relaxation dynamics in the dark measured in a neutral QD state following σ^+ optical pumping (squares). The same relaxation dynamics are also measured with partial NMR saturation after the optical pump, which reduces the initial P_N (triangles and stars). Lines show fitting used to derive the nuclear spin half-lifetimes $T_{1,N}$. Inset shows the same data, but normalized by the initial hyperfine shift at short dark times T_{Dark}. **c** Nuclear spin relaxation times $T_{1,N}$ as a function of the initial hyperfine shift E_{hf}. The corresponding approximate initial P_N is shown on the top axis. Error bars are 95% confidence intervals. **d** Density of states calculated for $N = 6$ dipolar-coupled $I = 3/2$ nuclei (without the electron). Each band, broadened by dipolar couplings $hν_{dd} \propto \max|b_{j,k}|$, corresponds to a well-defined total spin projection M. The adjacent bands are split by the Zeeman energy $hν_L$. **e** Population probability of the eigenstates, calculated for the spectrum in **d** and for two types of mixed states: Boltzmann distribution of Zeeman energies with high polarization $P_N \approx 0.99$ (red) and a narrowed Gaussian distribution with $P_N = 0$ (blue). Source data for **a**–**c** are provided as a Source Data file.

always present in QDs[33] and is more pronounced under low-symmetry confinement[34,35]. In additional measurements, where the symmetry is reduced on purpose through uniaxial stress or tilting the magnetic field by ≈ 12°, we indeed find a significant reduction in maximum $|E_{hf}|$. Therefore, the dot-to-dot variation of P_N is attributed to the randomness of the QD morphology.

The buildup dynamics, measured under optimal nuclear spin pumping, are shown in Fig. 4a. The approach to the steady state is non-exponential since the nuclei that are further away from the center of the QD are less coupled to the electron and take longer to polarize. It takes on the order of ≈ 60 s to reach the steady-state P_N within the measurement accuracy. Once optical pumping is switched off, nuclear spins depolarize in the dark (squares in Fig. 4b) on a timescale of minutes, mainly through spin diffusion[36]. Such long lifetimes mean that a highly-polarized nuclear spin state can be prepared and used to extend electron spin qubit coherence over a large number of short (few nanoseconds) qubit operations. We further examine the effect of the initial P_N on the relaxation dynamics by augmenting the optically-pumped nuclear state with a short partially-depolarizing NMR pulse (triangles and stars in Fig. 4b). When normalized by the initial polarization, the plot reveals accelerated nuclear spin relaxation under reduced initial polarization (inset in Fig. 4b). This is quantified in Fig. 4c, where at high polarization the nuclear spin relaxation half-lifetime $T_{1,N}$ is seen to be a factor of ≈ 2–3 longer than in case of low initial polarization (the lowest studied initial polarization is limited by the accuracy of the $T_{1,N}$ measurement). This is a non-trivial result: scaling of the initial P_N should not change $T_{1,N}$ within the linear spin diffusion model.

In order to explain the non-linear diffusion, we consider the eigenspectrum of a nuclear spin ensemble, with an example shown in Fig. 4d for $N = 6$ spins $I = 3/2$. The adjacent bands are separated by the large Zeeman energy $hν_L$ (typical $ν_L \approx 100$ MHz at $B_z = 10$ T), which corresponds to a flip of a single nucleus, accompanied by a ±1 change in the total ensemble spin projection M. Each band consists of all possible superpositions with a given M, with degeneracy lifted by the small ($ν_{dd} \approx 1$ kHz) nuclear-nuclear dipolar magnetic interaction. For $M \approx 0$ (i.e. $P_N \approx 0$) the broadening of each band is maximal, characterized by the dipole-dipole energy $hν_{dd}$. With $|P_N|$ approaching unity, the distribution of the available dipolar energies narrows, eventually vanishing for the two fully-polarized states with $M = \pm NI$ (i.e. $P_N = \pm 1$). The dipolar reservoir can act as a source or sink of energy for a flip-flop spin exchange between two nuclei whose energy gaps are slightly different (for example due to the inhomogeneity of the quadrupolar shifts $ν_Q$). Nuclear spin diffusion proceeds through such flip-flops. Therefore, the slow-down of diffusion at high initial $|P_N|$ is well explained by the narrowing of the dipolar reservoir.

The narrowing of the nuclear dipolar reservoir is conceptually similar to the state-narrowing technique, which aims to reduce the statistical dispersion of the nuclear Zeeman energies $\propto M$ in order to enhance the coherence of the electron spin qubit. An example of a narrowed mixed state is sketched in Fig. 4e for $P_N \approx 0$, but with uncertainty in M reduced down to a few units, as demonstrated experimentally previously[37,38]. The fundamental advantage of a polarized state (also sketched in Fig. 4e), is that it not only narrows the uncertainty in M by a factor $\propto \sqrt{1-P_N^2}$ (see derivation in Supplementary Note 4D and Supplementary Data 1 and 2), but also reduces the dipolar broadening. In other words, our scheme represents true cooling with $|P_N| \to 1$, whereas the narrowing schemes can be seen as partial cooling of certain degrees of freedom of the nuclear ensemble. The ultimate limit of $P_N = \pm 1$ corresponds to the only two non-degenerate nuclear states, for which the electron spin qubit coherence is predicted to be essentially non-decaying[14,15]. By contrast, even if the dispersion of M is reduced to zero, the dipolar energy uncertainty of a depolarized ensemble may still cause dynamics on the timescales of $1/ν_{dd} \approx 1$ ms, leading in turn to electron spin qubit decoherence.

Investigation of electron spin coherence in a highly-polarized nuclear spin environment is an interesting subject for future work and may also provide a more sensitive tool for nuclear spin thermometry near $|P_N| \approx 1$. Alternatively, more accurate measurement of P_N can be sought through "trigger" detection method[28], relying on nuclear-nuclear interactions.

Discussion

Large nuclear polarizations are achieved here on a standard $p-i-n$ diode device, fully compatible with high-quality electron spin qubit operation, as demonstrated recently in the same semiconductor structure[39]. The technique is simple to implement and robust – once optical pumping parameters are optimized for a certain QD, they do not require any correction over months of experiments. Even larger nuclear polarizations can be sought by combining QDs of high in-plane symmetry with biaxial strain in order to reduce the heavy-light hole mixing. Our nuclear spin cooling method uses the purity of the optical pump polarization as the final heat sink, ultimately limiting the achievable P_N. This is different from the resonant "dragging" schemes[40–42] where the ultimate heat sink is the photon number in the optical mode, offering in principle a much closer approach to $|P_N| \approx 1$, provided the dark-state bottleneck could be avoided. Combining the advantages of the two approaches in a two-stage cooling cycle can be a route towards the ultimate goal of initializing a nuclear spin ensemble into its fully-polarized quantum ground state. This would be a pre-requisite for turning the enormously large Hilbert space of the $N \approx 10^5$ QD nuclei into a high-capacity quantum information resource.

Data availability

The key data generated in this study are provided in the Source Data file SourceData.zip. The rest of the data that support the findings of this study are available from the corresponding author upon request. Source data are provided with this paper.

References

1. Jacques, V. et al. Dynamic polarization of single nuclear spins by optical pumping of nitrogen-vacancy color centers in diamond at room temperature. *Phys. Rev. Lett.* **102**, 057403 (2009).
2. Falk, A. L. et al. Optical polarization of nuclear spins in silicon carbide. *Phys. Rev. Lett.* **114**, 247603 (2015).
3. Reichertz, L. et al. Polarization reversal of proton spins in a solid-state target by superradiance. *Nucl. Instrum. Methods Phys. Res. Sect. A* **340**, 278–282 (1994).
4. Knuuttila, T. A. et al. Polarized nuclei in normal and superconducting rhodium. *J. Low. Temp. Phys.* **123**, 65–102 (2001).
5. Jacquinot, J. F., Wenckebach, W. T., Goldman, M. & Abragam, A. Polarization and NMR Observation of ^{43}Ca Nuclei in CaF_2. *Phys. Rev. Lett.* **32**, 1096–1097 (1974).
6. Goldman, M. & Jacquinot, J. F. Measurement of ^{43}Ca-^{19}F Dipolar Energy in Antiferromagnetic CaF_2. *Phys. Rev. Lett.* **36**, 330–333 (1976).
7. Petersen, G. et al. Large nuclear spin polarization in gate-defined quantum dots using a single-domain nanomagnet. *Phys. Rev. Lett.* **110**, 177602 (2013).
8. Chekhovich, E. A. et al. Measurement of the spin temperature of optically cooled nuclei and GaAs hyperfine constants in GaAs/AlGaAs quantum dots. *Nat. Mater.* **16**, 982 (2017).
9. Kloeffel, C. & Loss, D. Prospects for spin-based quantum computing in quantum dots. *Annu. Rev. Cond. Matt. Phys.* **4**, 51–81 (2013).
10. Wenckebach, W. T. The solid effect. *Appl. Magn. Reson.* **34**, 227 (2008).
11. Imamoglu, A., Knill, E., Tian, L. & Zoller, P. Optical pumping of quantum-dot nuclear spins. *Phys. Rev. Lett.* **91**, 017402 (2003).
12. Christ, H., Cirac, J. I. & Giedke, G. Quantum description of nuclear spin cooling in a quantum dot. *Phys. Rev. B* **75**, 155324 (2007).
13. Urbaszek, B. et al. Nuclear spin physics in quantum dots: An optical investigation. *Rev. Mod. Phys.* **85**, 79–133 (2013).
14. Khaetskii, A. V., Loss, D. & Glazman, L. Electron Spin Decoherence in Quantum Dots due to Interaction with Nuclei. *Phys. Rev. Lett.* **88**, 186802 (2002).
15. Deng, C. & Hu, X. Electron-spin dephasing via hyperfine interaction in a quantum dot: An equation-of-motion calculation of electron-spin correlation functions. *Phys. Rev. B* **78**, 245301 (2008).
16. Giedke, G., Taylor, J. M., D'Alessandro, D., Lukin, M. D. & Imamoğlu, A. Quantum measurement of a mesoscopic spin ensemble. *Phys. Rev. A* **74**, 032316 (2006).
17. Kessler, E. M., Yelin, S., Lukin, M. D., Cirac, J. I. & Giedke, G. Optical superradiance from nuclear spin environment of single-photon emitters. *Phys. Rev. Lett.* **104**, 143601 (2010).
18. Schuetz, M. J. A., Kessler, E. M., Cirac, J. I. & Giedke, G. Superradiance-like electron transport through a quantum dot. *Phys. Rev. B* **86**, 085322 (2012).
19. Oja, A. S. & Lounasmaa, O. V. Nuclear magnetic ordering in simple metals at positive and negative nanokelvin temperatures. *Rev. Mod. Phys.* **69**, 1–136 (1997).
20. Kotur, M. et al. Ultra-deep optical cooling of coupled nuclear spin-spin and quadrupole reservoirs in a GaAs/(Al,Ga)As quantum well. *Commun. Phys.* **4**, 193 (2021).
21. Miller, B. T. et al. Few-electron ground states of charge-tunable self-assembled quantum dots. *Phys. Rev. B* **56**, 6764–6769 (1997).
22. Warburton, R. J. et al. Optical emission from a charge-tunable quantum ring. *Nature* **405**, 926–929 (2000).
23. Raymond, S. et al. Excitonic Energy Shell Structure of Self-Assembled InGaAs/GaAs Quantum Dots. *Phys. Rev. Lett.* **92**, 187402 (2004).
24. Babinski, A., Potemski, M., Raymond, S., Lapointe, J. & Wasilewski, Z. R. Emission from a highly excited single InAs – GaAs quantum dot in magnetic fields: An excitonic Fock-Darwin diagram. *Phys. Rev. B* **74**, 155301 (2006).
25. Schimpf, C. et al. Resolving the temporal evolution of line broadening in single quantum emitters. *Opt. Express* **27**, 35290–35307 (2019).
26. Taylor, J. M., Marcus, C. M. & Lukin, M. D. Long-lived memory for mesoscopic quantum bits. *Phys. Rev. Lett.* **90**, 206803 (2003).
27. Gammon, D. et al. Electron and nuclear spin interactions in the optical spectra of single GaAs quantum dots. *Phys. Rev. Lett.* **86**, 5176–5179 (2001).
28. Goldman, M. *Spin temperature and nuclear magnetic resonance in solids* (Oxford University Press, Oxford, 1970).
29. Chekhovich, E. A. et al. Structural analysis of strained quantum dots using nuclear magnetic resonance. *Nat. Nanotechnol.* **7**, 646 (2012).
30. Bulutay, C., Chekhovich, E. A. & Tartakovskii, A. I. Nuclear magnetic resonance inverse spectra of InGaAs quantum dots: Atomistic level structural information. *Phys. Rev. B* **90**, 205425 (2014).
31. Bloch, F. Nuclear induction. *Phys. Rev.* **70**, 460–474 (1946).
32. Koudinov, A. V., Akimov, I. A., Kusrayev, Y. G. & Henneberger, F. Optical and magnetic anisotropies of the hole states in Stranski-Krastanov quantum dots. *Phys. Rev. B* **70**, 241305 (2004).
33. Luo, J.-W., Bester, G. & Zunger, A. Supercoupling between heavy-hole and light-hole states in nanostructures. *Phys. Rev. B* **92**, 165301 (2015).
34. Huo, Y. H. et al. A light-hole exciton in a quantum dot. *Nat. Phys.* **10**, 46–51 (2014).
35. Yuan, X. et al. Uniaxial stress flips the natural quantization axis of a quantum dot for integrated quantum photonics. *Nat. Commun.* **9**, 3058 (2018).
36. Millington-Hotze, P., Manna, S., Covre da Silva, S. F., Rastelli, A. & Chekhovich, E. A. Nuclear spin diffusion in the central spin system of a GaAs/AlGaAs quantum dot. *Nat. Commun.* **14**, 2677 (2023).

37. Xu, X. et al. Optically controlled locking of the nuclear field via coherent dark-state spectroscopy. *Nature* **459**, 1105–1109 (2009).
38. Jackson, D. M. et al. Optimal purification of a spin ensemble by quantum-algorithmic feedback. *Phys. Rev. X* **12**, 031014 (2022).
39. Zaporski, L. et al. Ideal refocusing of an optically active spin qubit under strong hyperfine interactions. *Nat. Nanotechnol.* **18**, 257–263 (2023).
40. Latta, C. et al. Confluence of resonant laser excitation and bidirectional quantum-dot nuclear-spin polarization. *Nat. Phys.* **5**, 758–763 (2009).
41. Högele, A. et al. Dynamic nuclear spin polarization in the resonant laser excitation of an InGaAs quantum dot. *Phys. Rev. Lett.* **108**, 197403 (2012).
42. Gangloff, D. A. et al. Witnessing quantum correlations in a nuclear ensemble via an electron spin qubit. *Nat. Phys.* **17**, 1247–1253 (2021).

Acknowledgements

P.M-H. and H.E.D. were supported by EPSRC doctoral training grants. E.A.C. was supported by a Royal Society University Research Fellowship and EPSRC award EP/V048333/1. A.R. acknowledges support of the Austrian Science Fund (FWF) via the Research Group FG5, I 4320, I 4380, I 3762, the Linz Institute of Technology (LIT), and the LIT Secure and Correct Systems Lab, supported by the State of Upper Austria, the European Union's Horizon 2020 research and innovation program under Grant Agreements No. 899814 (Qurope), No. 871130 (Ascent+), the QuantERA II project QD-E-QKD and the FFG (grant No. 891366).

Author contributions

S.M., S.F.C.S. and A.R. developed, grew, and processed the quantum dot samples. P.M-H. and E.A.C. conducted nuclear spin pumping experiments. H.E.D. and E.A.C. conducted supporting experiments on a stressed semiconductor sample. E.A.C. and P.M-H. analyzed the data. E.A.C. drafted the manuscript with input from all authors. E.A.C. coordinated the project.

Competing interests

The authors declare no competing interests.

Additional information

Supplementary information The online version contains supplementary material available at https://doi.org/10.1038/s41467-024-45364-2.

Correspondence and requests for materials should be addressed to Evgeny A. Chekhovich.

Peer review information *Nature Communications* thanks Neelesh Kumar Vij, Edo Waks and the other, anonymous, reviewers for their contribution to the peer review of this work. A peer review file is available.

Supplemental Information: Approaching a fully-polarized state of nuclear spins in a solid

Peter Millington-Hotze, Harry E. Dyte, Santanu Manna, Saimon F. Covre da Silva, Armando Rastelli, and Evgeny A. Chekhovich

CONTENTS

Supplementary Note 1. SAMPLE STRUCTURE

The sample is grown using molecular beam epitaxy (MBE) on a semi-insulating GaAs (001) substrate. The layer sequence of the semiconductor structure is shown in Supplementary Fig. 1. The growth starts with a layer of $Al_{0.95}Ga_{0.05}As$ followed by a single pair of $Al_{0.2}Ga_{0.8}As$ and $Al_{0.95}Ga_{0.05}As$ layers acting as a Bragg reflector in optical experiments. Then, a 95 nm thick layer of $Al_{0.15}Ga_{0.85}As$ is grown, followed by a 95 nm thick layer of $Al_{0.15}Ga_{0.85}As$ doped with Si at a volume concentration of 1.0×10^{18} cm^{-3}. The low Al concentration of 0.15 in the Si doped layer mitigates the issues caused by the deep DX centers [1–3]. The n-type doped layer is followed by the electron tunnel barrier layers: first a 5 nm thick $Al_{0.15}Ga_{0.85}As$ layer is grown at a reduced temperature of 560 °C to suppress Si segregation, followed by a 10 nm thick $Al_{0.15}Ga_{0.85}As$ and then a 15 nm thick $Al_{0.33}Ga_{0.67}As$ layer grown at 600 °C. Aluminium droplets are grown on the surface of the $Al_{0.33}Ga_{0.67}As$ layer and are used to etch the nanoholes [4, 5]. Atomic force microscopy shows that typical nanoholes have a depth of ≈ 6.5 nm and are ≈ 70 nm in diameter. Next, a 2.1 nm thick layer of GaAs is grown to form QDs by infilling the nanoholes as well as to form the quantum well (QW) layer. Thus, the maximum height of the QDs in the growth z direction is ≈ 9 nm. The GaAs layer is followed by a 268 nm thick $Al_{0.33}Ga_{0.67}As$ barrier layer. Finally, the p-type contact layers doped with C are grown: a 65 nm thick layer of $Al_{0.15}Ga_{0.85}As$ with a 5×10^{18} cm^{-3} doping concentration, followed by a 5 nm thick layer of $Al_{0.15}Ga_{0.85}As$ with a 9×10^{18} cm^{-3} concentration, and a 10 nm thick layer of GaAs with a 9×10^{18} cm^{-3} concentration.

The sample is processed into a $p-i-n$ diode structure. Mesa structures with a height of 250 nm are formed by etching away the p-doped layers and depositing Ni(10 nm)/AuGe(150 nm)/Ni(40 nm)/Au(100 nm) on the etched areas. The sample is then annealed to enable diffusion down to the n-doped layer to form the ohmic back contact. The top gate contact is formed by depositing Ti(15 nm)/Au(100 nm) on to the p-type surface of the mesa areas. Quantum dot photoluminescence (PL) is excited and collected through the top of the sample. The sample gate bias V_{Gate} is the bias of the p-type top contact with respect to the grounded n-type back contact. Due to the large thickness of the top $Al_{0.33}Ga_{0.67}As$ layer, the tunneling of the holes is suppressed, whereas tunnel coupling to the n-type layer enables deterministic charging of the quantum dots with electrons by changing V_{Gate}.

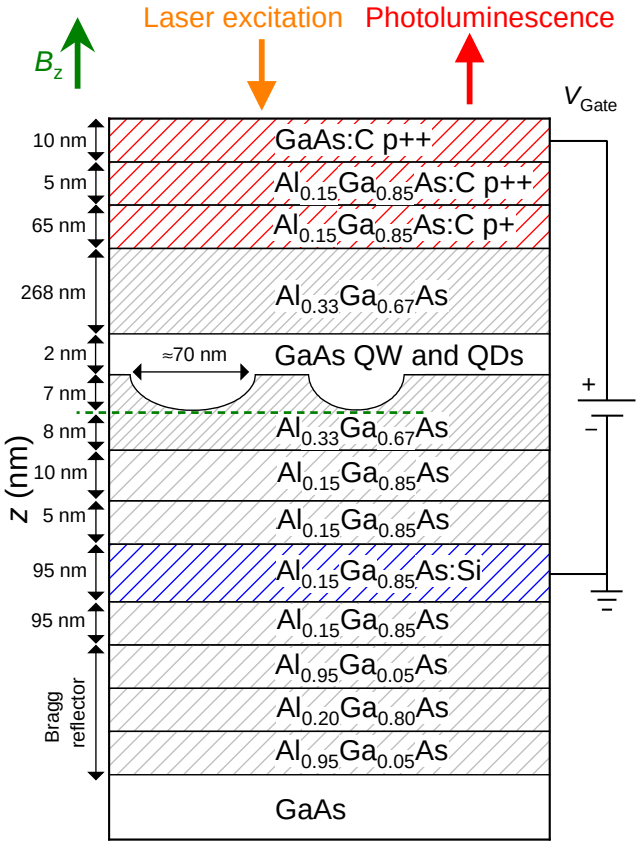

Supplementary Figure 1. **Quantum dot sample structure used in this work.**

Supplementary Note 2. ELECTRON-NUCLEAR SPIN SYSTEM OF A QUANTUM DOT

The band structure of the electrons and holes in a GaAs QD is sketched in Supplementary Fig. 2 (see for example Ref. [6] for a review). The electron conduction band in GaAs has spin $s = 1/2$, with two possible spin projections $s_z = \pm 1/2$ along the quantizing magnetic field. The valence band is four-fold degenerate at the center of the Brillouin zone in bulk GaAs. The confinement along the z growth axis is sufficient to split the valence band into the heavy hole and light hole subbands with total momentum projections $j_z = \pm 3/2$ and $j_z = \pm 1/2$, respectively. The typical heavy-light hole splitting is $\Delta E_{\mathrm{hh-lh}} \approx 10 - 15$ meV in GaAs/AlGaAs quantum wells, depending on their thickness [7, 8]. The selection rules for the ground state heavy-hole excitons are such that σ^+ (σ^-) circularly polarized light couples only to the $s_z = -1/2$ ($s_z = +1/2$) electron state in the conduction band. For the light hole excitons the selection rules are inverted. This means that high-fidelity initialization of the electron spin via circularly-polarized optical pumping is only

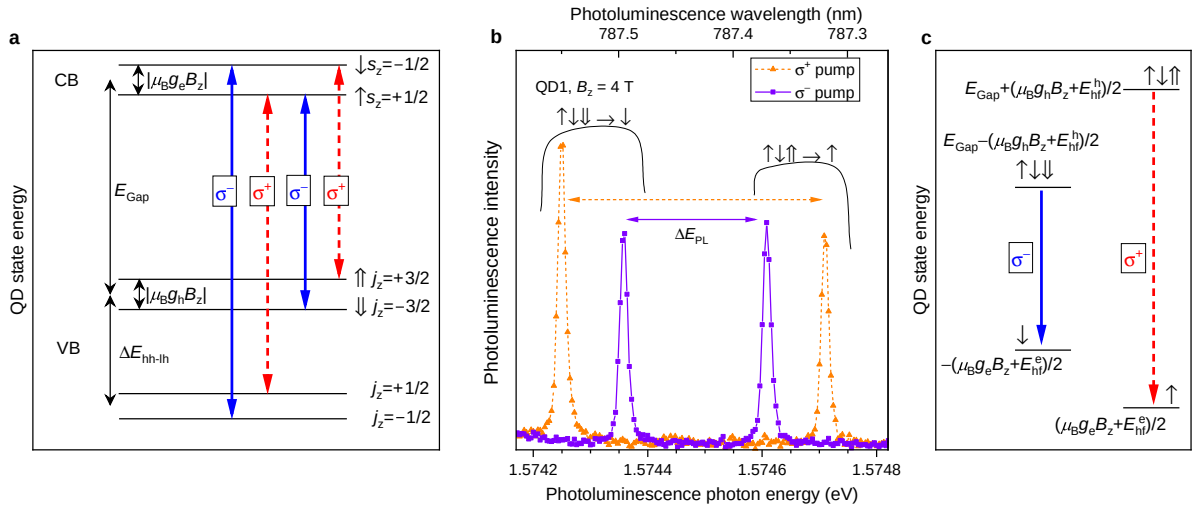

Supplementary Figure 2. **Optical transitions in a GaAs quantum dot. a,** Electron energy levels in the conduction band (CB) and hole energy levels in the valence band (VB). Electron states with spin up (↑) and down (↓) have spin projections $s_z = +1/2$ and $s_z = -1/2$, respectively. The heavy hole states with pseudospin up (⇑) and down (⇓) have momentum projections $j_z = +3/2$ and $j_z = -3/2$, respectively. The light hole states have momentum projections $j_z = \pm 1/2$. Dashed (solid) arrows show σ^+ (σ^-) polarized optical transitions. **b,** Typical photoluminescence spectra of an individual QD. The spectral splitting $\Delta E_{\rm PL}$ depends on the helicity of the optical pumping ($\sigma^\pm$) due to the buildup of the nuclear spin polarization. **c,** Energy level diagram of a negatively charged trion in a GaAs QD. The electron ground state is split by the Zeeman energy $\mu_{\rm B} g_{\rm e} B_{\rm z}$ and the hyperfine shift $E_{\rm hf}^{\rm e}$. The X^- trion energy includes the QD bandgap energy $E_{\rm Gap}$, the Zeeman splitting and a small [9] hyperfine shift $E_{\rm hf}^{\rm h}$. The electron and hole g-factors are $g_{\rm e}$ and $g_{\rm h}$, respectively, with $|g_{\rm h}| \gg |g_{\rm e}|$ in the studied QDs. Arrows depict the two optically allowed transitions responsible for the spectral doublet in (b). Note that the g-factors shown in (a) do not necessarily coincide with those shown in (c), since the states used for excitation and detection are in general different.

possible for a sufficiently large spectral separation $\Delta E_{\rm hh-lh}$ of the heavy and light hole exciton transitions.

Apart from the quantum-well type of confinement along the z axis, carriers in a QD are also confined in the orthogonal xy plane. In a real semiconductor structure there is always some breaking of the symmetry in the xy plane. Such in-plane anisotropy can mix the heavy and light holes, so that the eigenstates are no longer described by pure $j_{\rm z} = \pm 3/2$ or $j_{\rm z} = \pm 1/2$ projections. As a result of such mixing the selection rules change, and the optical transitions in general become elliptically polarized.

In the pump-probe experiments we use photoluminescence of a negatively charged trion X^-, where the electron-hole recombination occurs in presence of another resident electron. The X^-

spectra, such as shown in Supplementary Fig. 2b, tend to have the narrowest linewidths and their Zeeman splittings are free from the non-linearity which is presented for neutral excitons X^0 due to the fine structure splitting. The energies of the states involved in X^- photoluminescence are shown in Supplementary Fig. 2c. The energy of the ground state resident electron is $(\mu_\mathrm{B} g_\mathrm{e} B_\mathrm{z} + E^\mathrm{e}_\mathrm{hf}) s_\mathrm{z}$, while the energy of the optically excited trion is $E_\mathrm{Gap} + (\mu_\mathrm{B} g_\mathrm{h} B_\mathrm{z} + E^\mathrm{h}_\mathrm{hf}) j_\mathrm{z}/3$, where E_Gap is the X^- transition energy in the absence of Zeeman and hyperfine shifts. Taking the differences and substituting the momentum projections allowed by the selection rules $s_\mathrm{z} + j_\mathrm{z} = \pm 1$, we find the photon energies of the two optically-allowed transitions $E_\mathrm{Gap} \pm \left(\mu_\mathrm{B}(g_\mathrm{h} - g_\mathrm{e})B_\mathrm{z} + (E^\mathrm{h}_\mathrm{hf} - E^\mathrm{e}_\mathrm{hf})\right)/2$, where g_e (g_h) is the electron (heavy hole) g-factor, E^e_hf (E^h_hf) is the electron (heavy hole) hyperfine shift. The splitting of the spectral doublet is then

$$\Delta E_\mathrm{PL} = \mu_\mathrm{B}(g_\mathrm{h} - g_\mathrm{e})B_\mathrm{z} + (E^\mathrm{h}_\mathrm{hf} - E^\mathrm{e}_\mathrm{hf}). \tag{S1}$$

Next we eliminate the Zeeman contribution and define the excitonic hyperfine shift:

$$E_\mathrm{hf} = -(\Delta E_\mathrm{PL} - \Delta E_\mathrm{PL,0}) = E^\mathrm{e}_\mathrm{hf} - E^\mathrm{h}_\mathrm{hf}, \tag{S2}$$

where $\Delta E_\mathrm{PL,0}$ is the photoluminescence doublet splitting at zero nuclear spin polarization. The valence band hole hyperfine interaction is of the order of 10% of the electron hyperfine interaction [9]. Consequently, the excitonic hyperfine shift E_hf is dominated by the electronic contribution E^e_hf.

The Hamiltonian describing the nuclear spin system alone includes the Zeeman, the quadrupolar and the dipole-dipole terms. The Zeeman term accounts for the coupling of the QD nuclear spins $\mathbf{I}_j$ to the static magnetic field B_z directed along the z axis:

$$\mathcal{H}_\mathrm{Z,N} = -\sum_{j=1}^{N} \hbar \gamma_j B_\mathrm{z} \hat{I}_{\mathrm{z},j}, \tag{S3}$$

where the summation goes over all individual nuclei $1 \leq j \leq N$, $\hbar = h/(2\pi)$ is the reduced Planck's constant, γ_j is the gyromagnetic ratio of the j-th nuclear spin and $\hat{\mathbf{I}}_j$ is a vector of spin operators with Cartesian components $(\hat{I}_{\mathrm{x},j}, \hat{I}_{\mathrm{y},j}, \hat{I}_{\mathrm{z},j})$. The result of the Zeeman term alone is a spectrum of equidistant single-spin eigenenergies $m\hbar\gamma_j B_\mathrm{z}$, corresponding to $2I+1$ eigenstates with $\hat{I}_\mathrm{z}$ projections m satisfying $-I \leq m \leq +I$.

The interaction of the nuclear electric quadrupolar moment with the electric field gradients is described by the term (Ch. 10 in Ref. [10]):

$$\mathcal{H}_\mathrm{Q,N} = \sum_{j=1}^{N} \frac{q_j}{6} [3\hat{I}^2_{\mathrm{z}',j} - I^2_j + \eta_j (\hat{I}^2_{\mathrm{x}',j} - \hat{I}^2_{\mathrm{y}',j})], \tag{S4}$$

where q_j and η_j describe the magnitude and asymmetry of the electric field gradient tensor, whose principal axes are $x'y'z'$. The strain is inhomogeneous within the QD volume, so that q_j and η_j vary between the individual nuclei. The axes $x'y'z'$ are different for each nucleus and generally do not coincide with crystallographic axes or magnetic field direction. In lattice-matched GaAs/AlGaAs QDs the electric field gradients at the nuclear sites do not exceed $q_j/h \approx 200$ kHz, as witnessed via NMR spectroscopy. At sufficiently strong magnetic fields $|\hbar\gamma_j B_z| \gg |q_j|$, quadrupolar effects can be treated perturbatively – the main effect is the anharmonicity of the nuclear spin energies and the resulting quadrupolar NMR multiplet of $2I$ magnetic-dipole transitions, split by $\nu_Q \approx q_j/h$. The $m = \pm 1/2$ states of a half-integer nuclear spin are influenced by quadrupolar effects only in the second order, resulting in a smaller inhomogeneous broadening, which scales as $\propto \nu_Q^2/\nu_L$ with nuclear spin Larmor frequency $\nu_L = \gamma B_z/(2\pi)$.

Quadrupolar effects have a direct impact on nuclear spin cooling, which we now discuss briefly. According to the Hamiltonians of Supplementary Equations S3 and S4, the nuclear eigenstates have well-defined spin projections along the external magnetic field only under special conditions. For example, if the quadrupolar shifts are absent ($\nu_Q = 0$), or if the quadrupolar tensor has high symmetry ($\eta_j = 0$) with the major axis parallel to magnetic field ($z' \parallel z$), then the energy eigenstates are also the eigenstates of the nuclear spin z-projection operator $\hat{I}_{z,j}$, with eigenvalues $m = \pm 1/2, 3/2$ in case of spin-3/2 nuclei. But this is not the case for an arbitrary quadrupolar tensor. Thus, if a nuclear spin is initialized into a state with a definite m (for example through interaction with optically pumped electron spins), it will be a superposition state, which will evolve in time, decaying probabilistically (through decohering) into one of the energy eigenstates. In simple words, the nuclear spin eigenstates are generally not aligned with the external magnetic field. As a result, achieving complete nuclear spin polarization is strictly speaking impossible in the presence of low-symmetry quadrupolar interactions, as has been pointed out previously [11]. The scale of the effect can be characterized by considering the expectation value of the spin projection operator $\hat{I}_{z,j}$ for the true energy eigenstates. First-order expansion of the exact solution of the Hamiltonians of Supplementary Equations S3 and S4 shows that the deviation of the $\hat{I}_{z,j}$ expectation values from the ideal half-integer values scales as $\propto (\nu_Q/\nu_L)^2$. For GaAs QDs ($|\nu_Q| \lesssim 200$ kHz) in high magnetic field ($\nu_L \approx 100$ MHz) the deviation parameter is very small $(\nu_Q/\nu_L)^2 \approx 4 \times 10^{-6}$. The picture is very different with Stranski-Krastanov InGaAs QDs, where quadrupolar effects are large (up to $|\nu_Q| \lesssim 10$ MHz) and the distribution of the major quadrupolar axes is inhomogeneous [11, 12]. As a result, for a realistic range of magnetic fields, near-unity polarization of nuclear spins is fundamentally unachievable with InGaAs QDs [11].

Direct interaction between the nuclei is described by the dipole-dipole Hamiltonian:

$$\mathcal{H}_{\rm DD} = \sum_{1\le j<k\le N} b_{j,k}\left(3\hat{I}_{{\rm z},j}\hat{I}_{{\rm z},k} - \hat{\mathbf{I}}_j\cdot\hat{\mathbf{I}}_k\right),$$
$$b_{j,k} = \frac{\mu_0\hbar^2}{4\pi}\frac{\gamma_j\gamma_k}{2}\frac{1-3\cos^2\theta_{j,k}}{r_{j,k}^3} \tag{S5}$$

Here, $\mu_0 = 4\pi\times10^{-7}$ NA^{-2} is the magnetic constant and $r_{j,k}$ denotes the length of the vector, which forms an angle θ with the z axis and connects the two spins j and k. The typical magnitude of the interaction constants for the nearby nuclei in GaAs is $\max(|b_{j,k}|)/h \approx 100$ Hz. The Hamiltonian of Supplementary Eq. (S5) has been truncated to eliminate all spin non-conserving terms – this is justified for static magnetic field exceeding $\gtrsim 1$ mT. While the eigenstates of an isolated nucleus have well-defined spin projections m, the presence of the dipole-dipole interactions means that the true eigenstates of the nuclear spin ensemble in general cannot be written as product states of the single-nucleus states. The only two states where the nuclei are not entangled are the fully-polarized states, where all individual spins occupy the states with the same $m = -I$ or with the same $m = +I$. On the other hand, at high magnetic field the total z-projection operator $\sum_j \hat{I}_{{\rm z},j}$ approximately commutes with the nuclear spin Hamiltonian. Therefore, the nuclear ensemble eigenstates can be described by the well-defined total spin projections M. An example of an eigenenergy spectrum, calculated for $N = 6$ nuclei of ^{75}As, is shown in Fig. 4d of the main text. In this calculation we use $\nu_{\rm L} = 1.8$ kHz, $\nu_{\rm Q} = 0$ and the nuclei are taken from a single cubic cell of the group-III face-centered-cubic sublattice of GaAs. The bands observed in the spectrum correspond to the different values of M, ranging between $-NI$ and $+NI$. The broadening of each band is due to the dipole-dipole interactions, which lifts the degeneracy of the different states with the same M.

The interaction of the conduction band electron spin $\mathbf{s}$ with the ensemble of the QD nuclear spins is dominated by the contact (Fermi) hyperfine interaction, with the following Hamiltonian:

$$\mathcal{H}_{\rm hf}^{\rm e} = \sum_{j=1}^{N} a_j(\hat{s}_{\rm x}\hat{I}_{{\rm x},j} + \hat{s}_{\rm y}\hat{I}_{{\rm y},j} + \hat{s}_{\rm z}\hat{I}_{{\rm z},j}), \tag{S6}$$

where the hyperfine constant of an individual nucleus j is $a_j = A^{(j)}|\psi(\mathbf{r}_j)|^2 v$. Unlike a_j, the $A^{(j)}$ hyperfine constant is a parameter describing only the material and the isotope type to which nucleus j belongs, $|\psi(\mathbf{r}_j)|^2$ is the density of the electron envelope wavefunction at the nuclear site $\mathbf{r}_j$ of the crystal lattice, and v is the crystal volume per one cation or one anion. The definitions of the hyperfine constants differ between different sources. With the definition adopted here, a fully polarized isotope with spin I, hyperfine constant A and a 100% abundance (e.g. ^{75}As), would shift

the energies of the electron spin states $s_z = \pm 1/2$ by $\pm AI/2$, irrespective of the shape of $|\psi(\mathbf{r}_j)|^2$. With such definition, the typical values in GaAs are $A \approx 50$ μeV [13].

For valence band holes the contact (Fermi) contribution vanishes, leaving the weaker dipole-dipole terms to dominate the hyperfine interaction. Compared to the valence band electrons, the coupling has a more complicated non-Ising form [9]. The effect of the net nuclear polarization on the heavy-hole spin splitting can be captured by a simplified expression:

$$\mathcal{H}_{\rm hf}^{\rm h} \approx \sum_{j=1}^{N} \frac{1}{3} C^{(j)} |\psi(\mathbf{r}_j)|^2 v \hat{j}_z \hat{I}_{z,j}, \tag{S7}$$

where $\hat{j}_z$ is the z component of the hole spin momentum operator. The valence band hyperfine material constants $C^{(j)}$ are sensitive to heavy-light hole mixing and both their signs and magnitudes depend on the material [9].

Owing to the flip-flop term $\propto (\hat{s}_x \hat{I}_{x,j} + \hat{s}_y \hat{I}_{y,j})$ of the hyperfine Hamiltonian (Supplementary Eq. S6) the eigenstates of the electron-nuclear central spin system are in general entangled, i.e. they cannot be written as a direct product of the electron spin single-particle state and the nuclear spin ensemble state. Consequently, when such a product state is generated through optical injection of a spin-polarized electron into the quantum dot, the wavefunction of the central spin system starts evolving. We estimate the rate of coherent evolution using the Rabi frequency $\propto \sqrt{\sum_j a_j^2}/h \approx A/(h\sqrt{N})$ derived previously in Ref. [14] for the limit of vanishing electron spin splitting. For a fully polarized nuclear spin ensemble coupled to an electron spin polarized in the opposite direction, this Rabi frequency describes the exact solution of periodic spin exchange between the electron and the collective nuclear spin state. Therefore, in order for dynamic nuclear spin polarization to be efficient, the polarized electron spins need to be removed and injected much faster than the hyperfine-induced Rabi rotations (otherwise the electron spin will periodically polarize and depolarize the nuclei, without any net spin transfer). For a typical GaAs QD with $N \approx 10^5$ nuclear spins we have $h\sqrt{N}/A \approx 25$ ns. When electron spin splitting is not zero, there is an increase in the frequency of coherent oscillations that follow initialization into a product electron-nuclear state. In the limit of large electron spin splitting this is approximately the electron spin resonance frequency. For experimental conditions used in our work the maximum sum of the net hyperfine shift and the electron Zeeman splitting at $B_z = 10$ T does not exceed $\lesssim 180$ μeV, which corresponds to electron Larmor period of $\gtrsim 20$ ps. From these basic derivations, we arrive to a rough estimate that electron spin recycling must occur on a sub-picosecond timescale in order to achieve near-unity nuclear spin polarization.

Supplementary Note 3. EXPERIMENTAL METHODS AND TECHNIQUES

All measurements are performed in a liquid helium bath cryostat. The sample is placed in an insert tube filled with a low-pressure heat-exchange helium gas. The base temperature is ≈ 4.25 K. We use confocal microscopy configuration where QD photoluminescence (PL) is excited by a laser beam focused by a cryo-compatible apochromatic objective with a focal length of 2.89 mm and a numerical aperture of 0.81. The excitation spot diameter is ≈ 1 μm. Both the optical excitation and a static magnetic field B_z up to 10 T are applied along the sample growth axis z (Faraday geometry). Quantum dot photoluminescence is collected and collimated by the same cryo-compatible objective. The PL signal is dispersed in a two-stage grating spectrometer, followed by a pair of achromatic doublets, which transfers the spectral image onto a charge-coupled device (CCD) detector with a magnification of 3.75. The orientation of the semiconductor sample is verified by reflecting a collimated laser off the sample surface – the small unintentional tilt of the sample is found to be $\approx 0.7^\circ$. The laser used for optical pumping of the nuclear spins is a ring-cavity tunable titanium sapphire (Ti:Sa) laser, operating in a single-mode continuous-wave regime. This laser is coupled with a wavelength meter (30 MHz accuracy) for precise tuning and stabilization of the optical pumping wavelength. The sample gate bias is connected by a combination of a twisted pair (inside the cryostat) and a 50 Ω coaxial cable (outside the cryostat) to an arbitrary function generator through a low-pass LC filter with a 1.9 MHz cut-off frequency. Selective manipulation of the nuclear spins is achieved with a resonant radiofrequency oscillating magnetic field, generated by a small copper wire coil. This coil is placed to have its axis within the top surface of the semiconductor sample and perpendicular to the static magnetic field. A 50 Ω cryogenic coaxial cable is used to connect the coil to a radiofrequency amplifier with a maximum rated power of 100 W.

A. Pump probe experiment timing

Supplementary Fig. 3 shows the timing diagrams for the different types of experiments. Supplementary Fig. 3a shows the experimental cycle used in NMR spectroscopy, adiabatic sweep calibration and in nuclear spin polarization measurement (nuclear spin thermometry). The cycle consists of a radiofrequency burst between the pump and the probe optical pulses. During the cycle, the sample gate bias V_{Gate} is switched between the required levels by an arbitrary function generator. Both the pump and the probe optical pulses are implemented with mechanical shutters. A mechanical shutter on the spectrometer is synchronized with the probe laser shutter to prevent

the pump laser reaching the detector. Multiple pump-probe cycles, typically between 5 and 15, are accumulated by the CCD detector in order to improve the signal to noise ratio. For inverse NMR spectroscopy and adiabatic sweep calibration the pump duration is reduced to $T_{\mathrm{Pump}} = 5$ s to speed up the measurements. For saturation NMR spectroscopy and spin thermometry we use T_{Pump} between 25 s and 30 s in order to approach the steady-state of the nuclear spin polarization. The maximum T_{Pump} is limited by the need to collect photoluminescence from a sufficient number of probe pulses and the thermal noise of the CCD detector, which affects long exposures. While radiofrequency pulses can be applied at any bias, in this work we use $V_{\mathrm{Pump}} = -1.3$ V in order to keep the quantum dot free of charges during the radiofrequency manipulation of the nuclei.

Supplementary Fig. 3b shows a cycle used in the measurements of the nuclear spin buildup dynamics. Each cycle starts from a radiofrequency pulse that saturates the resonances of ^{75}As, ^{69}Ga, ^{71}Ga and ^{27}Al in order to depolarize these nuclei in the entire sample. Next, the pump pulse of a variable duration T_{Pump} is applied, and the resulting hyperfine shift is measured with a probe pulse.

Supplementary Fig. 3c shows a cycle used in the nuclear spin relaxation measurements. The cycles start with radiofrequency depolarization that is sufficiently long to eliminate any effect of the nuclear polarization left over from the previous measurement cycle. This is followed by optical pumping for $T_{\mathrm{Pump}} = 60$ s. After the pump, the sample is kept in the dark for a time T_{Dark} under gate bias V_{Dark}. After that, a probe pulse is applied to measure the fraction of the nuclear spin polarization that decayed during T_{Dark}. In this type of experiments the number of the pump-probe cycles used to collect the probe photoluminescence signal varies between 1 and 10 – single-shot probing is required when T_{Dark} exceeds a few hundred seconds. Furthermore, we perform measurements using the cycle of Supplementary Fig. 3c, but with a second radiofrequency (Rf) pulse added after the pump and before the dark interval. The duration of this second Rf pulse $T_{\mathrm{Rf},2}$ is typically varied between 0 and 5 s to control the degree of the initial nuclear spin polarization. In principle, there are multiple ways to control the degree of the initial nuclear spin polarization in the quantum dot, such as the duration T_{Pump} of the pump or its power and wavelength. However, any such changes in the optical pumping also affect the rate of nuclear spin diffusion into the barriers around the quantum dot [15]. The degree of nuclear polarization in the barriers then affects the rate of nuclear spin relaxation in the subsequent dark interval. The advantage of the second radiofrequency pulse is that it depolarizes the nuclei at the same rate in the entire sample. Therefore, the spatial profile of the nuclear spin polarization P_{N} after the second pulse is simply a scaled profile of the P_{N} profile produced by the optical pulse. Spin diffusion

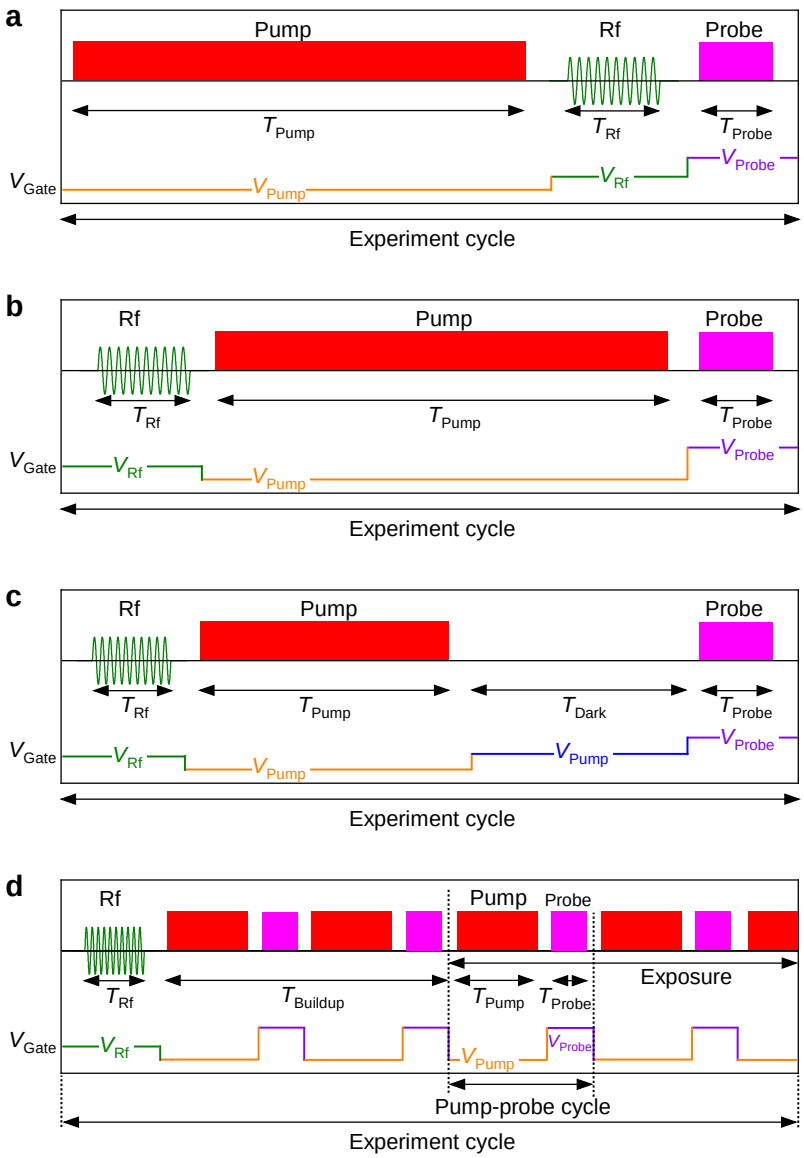

Supplementary Figure 3. **Timing diagrams of different experiments.** **a,** NMR spectroscopy and measurement of nuclear spin polarization. **b,** Nuclear spin buildup dynamics. **c,** Nuclear spin relaxation in the dark. **d,** Optical pump power and wavelength dependence of the steady state nuclear spin polarization.

is described by a linear differential equation, so that proportional reduction of P_N in the entire sample should not affect the timescales of the subsequent nuclear spin diffusion and relaxation in the dark. Consequently, any dependence of the relaxation time on the degree of the initial nuclear spin polarization (left after the second radiofrequency pulse) is ascribed purely to the reduction (narrowing) of the energy that the dipole-dipole reservoir can supply or absorb during the nuclear flip-flop events of the spin diffusion process. We note that the second radiofrequency pulse has

minimal effect on the measurement of the subsequent relaxation dynamics, since its duration is no more than 10% of the shortest measured nuclear spin relaxation time $T_{1,\mathrm{N}}$ (except for one measurement with $T_{\mathrm{Rf},2} = 18$ s).

Supplementary Fig. 3d shows the timing of the experiment used to study the dependence of the steady-state nuclear spin polarization on the optical pumping parameters such as gate bias V_{Pump}, pump power and wavelength. The experiment cycle starts with a single radiofrequency erase that eliminates any leftover nuclear polarization. Then the pump and probe pulses start, but the acquisition (CCD detector exposure) of the probe photoluminescence begins only after a delay $T_{\mathrm{Buildup}} = 50$ s. This delay allows nuclear spin polarization to build up closer towards its steady state so that relatively short pump pulses $T_{\mathrm{Pump}} = 5$ s can be used for faster acquisition of the photoluminescence signal. The probe pulses are kept short, in order to produce minimal nuclear spin depolarization during each pump-probe cycle (see details in Supplementary Note 3 C). The probe pulses are also much shorter than the pump ($T_{\mathrm{Probe}}/T_{\mathrm{Pump}} < 0.003$), to ensure minimal effect on the steady-state nuclear spin polarization.

B. Optical pumping of quantum dot nuclear spins

The steady-state nuclear spin polarization depends on the wavelength of the pump laser. Maximum hyperfine shifts $|E_{\mathrm{hf}}|$ are found to occur when the laser is resonant with a certain optical transition of the quantum dot. Calibration of the optimal pumping parameters starts with a measurement of a broad-range wavelength dependence – an example is shown in Supplementary Fig. 4. Once the individual spectral features, such as s-, p-, d- and f-shell exciton peaks, are identified a more detailed optimization is performed. We focus on the s-shell pumping peak and measure more detailed dependencies on the wavelength (or equivalently the pump photon energy) at different values of pump power P_{Pump} and sample gate bias V_{Pump}. The inset in Supplementary Fig. 4 shows an example of such a detailed dependence at the optimum $P_{\mathrm{Pump}} = 2.7$ mW, $V_{\mathrm{Pump}} = -2.7$ V. It can be seen that the pump laser needs to be tuned to within a narrow margin of ≈ 0.2 meV in order to achieve the highest possible $|E_{\mathrm{hf}}|$.

In the experimental setup the collimated pump laser beam first passes through a linear polarizer and then a $\lambda/2$ waveplate installed in a motorized rotation mount. This way it is possible to create arbitrary orientation of the linearly polarized beam, which is then directed to a cube beamsplitter, followed by a $\lambda/4$ waveplate installed in another motorized rotation mount. By placing the $\lambda/4$ waveplate last, it is possible to compensate for any polarization imperfections of the nominally non-

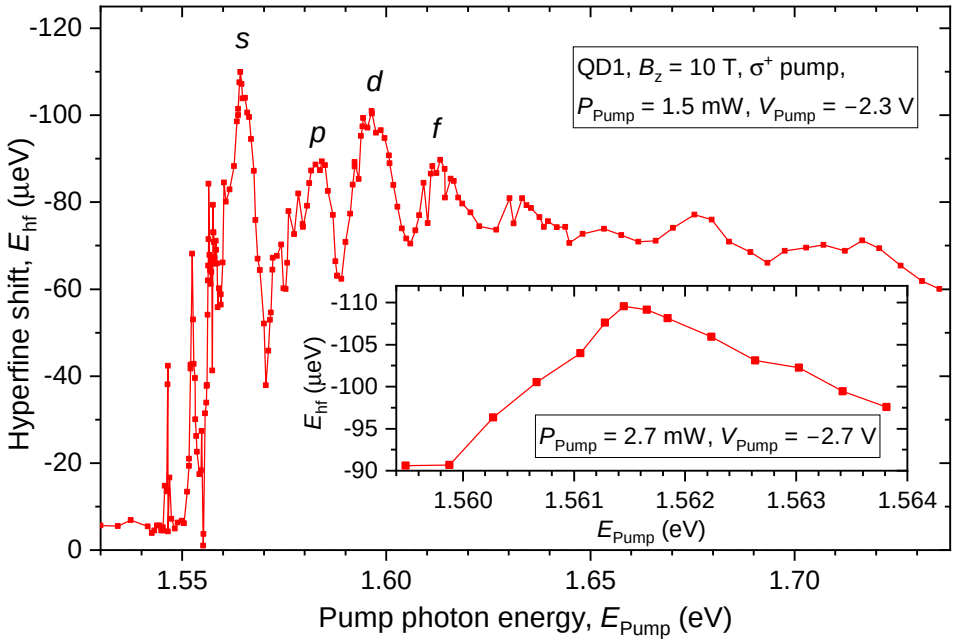

Supplementary Figure 4. **Calibration of the pump laser wavelength.** Hyperfine shift measured as a function of the pump laser wavelength expressed in terms of the photon energies E_{Pump}. Results are shown for QD1 at $B_z = 10$ T under σ^+ pumping. The pump power is $P_{\mathrm{Pump}} = 1.5$ mW and the gate bias is $V_{\mathrm{Pump}} = -2.3$ V. Inset shows a zoomed in dependence for the s-shell peak measured at slightly different optimized parameters $P_{\mathrm{Pump}} = 2.7$ mW, $V_{\mathrm{Pump}} = -2.7$ V.

polarizing beamsplitter and obtain a beam with high degree of circular polarization. This beam is then directed through a quartz window of the cryostat insert and the cryogenic objective, which focuses it on the surface of the QD semiconductor sample. In order to account for any polarization imperfections in the optical path we perform calibration measurements where both the $\lambda/2$ and $\lambda/4$ waveplate orientations are scanned and the resulting hyperfine shifts E_{hf} are measured. The results shown in Supplementary Fig. 5, indicate that the waveplate must be set within $\pm 2^\circ$ in order to attain the highest nuclear spin polarization degree. The optimal orientations of the $\lambda/2$ and $\lambda/4$ waveplates are different for the minimum negative (triangles) and the maximum positive (squares) E_{hf}.

Once the orientations of the $\lambda/2$ and $\lambda/4$ waveplates are optimised, we examine the polarization state of the pump beam directed to the cryostat. To this end, we place a linear polarizer (analyzer) after the $\lambda/4$ waveplate, followed by a power meter. The linear polarizer is rotated to find the minimum (I_{min}) and the maximum (I_{max}) intensities of the transmitted beam. For a perfect circularly polarized beam $I_{\mathrm{min}} = I_{\mathrm{max}}$, whereas for a linearly polarized beam $I_{\mathrm{min}} = 0$. We

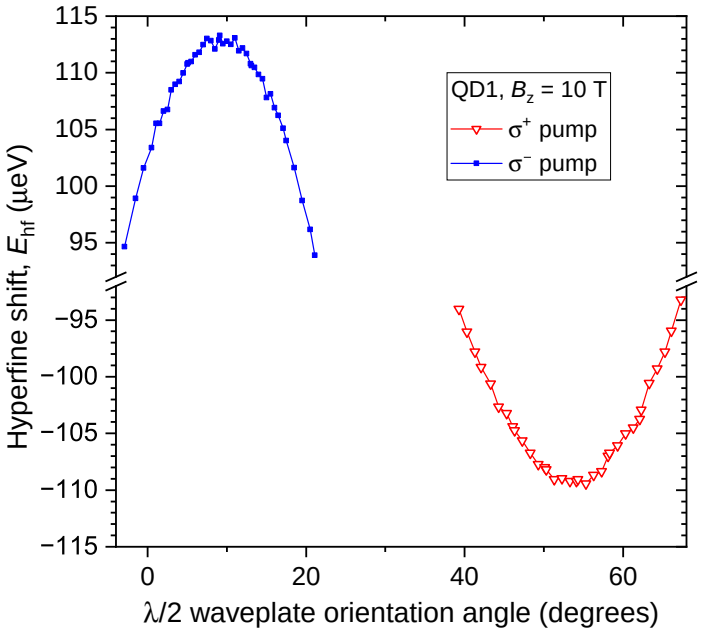

Supplementary Figure 5. **Calibration of the optical polarization of the pump.** Hyperfine shift measured as a function of the orientation angle of a $\lambda/2$ waveplate installed in the pump laser beam. Other parameters, such as $\lambda/4$ waveplate orientation, pump power, wavelength and bias are optimized separately for both σ^+ (triangles) and σ^- (squares) pumping of the QD nuclear spin polarization. Results are shown for QD1 at $B_z = 10$ T.

characterise the optimized beams using the degree of linear polarization $\rho_{\rm lin} = (I_{\rm max} - I_{\rm min})/I_{\rm max}$ and the analyzer orientation angle $\alpha_{\rm max}$ where the maximum intensity is achieved. These results are summarized in the polar plot of Supplementary Fig. 6.

The optimal degree $\rho_{\rm lin}$ and orientation $\alpha_{\rm max}$ of the linearly polarized components vary between individual quantum dots. Moreover, optimal polarization parameters are different for σ^+ and σ^- pumping and even depend on magnetic field for the same QD1. Such variability, as well as the large values of $\rho_{\rm lin} \lesssim 0.4$ suggest that polarization imperfections in the optical elements (e.g. mechanical stress in the cryo-objective) are not the major contribution. The large deviation of the optimal optical pumping from pure circular polarization is therefore attributed to the properties of the individual quantum dots. These may include anisotropy of the QD shape and inhomogeneous microstrains that make semiconductor material around the QD act as an optical waveplate and give rise to heavy-light hole mixing [16] that causes optical selection rules to depart from those of the bulk GaAs. Indeed, previous studies have shown that a sufficiently large uniaxial strain $\gtrsim 0.5$ % can flip the valence band hole quantization axis into the sample growth plane [17]. We note that

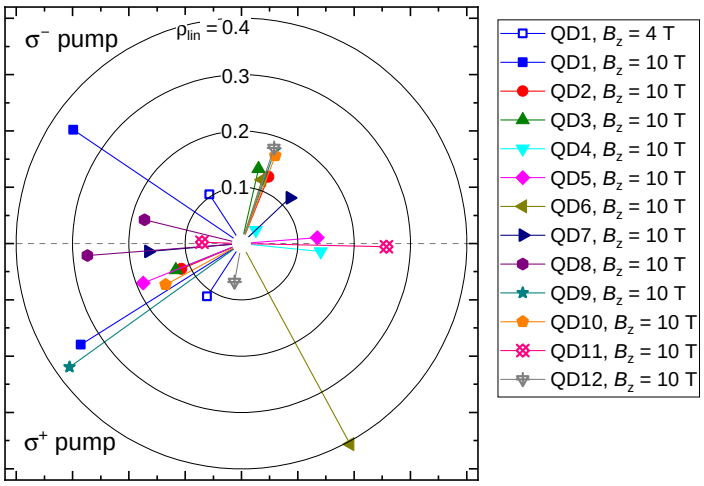

Supplementary Figure 6. **Optical polarization properties of the optimal nuclear spin pumping beams.** Vectors show the orientation of the linear polarization and the magnitude of the linear polarization degree $\rho_{\rm lin}$ of the pump beam that produces maximum nuclear spin polarization in individual dots QD1 - QD12. The bottom part shows the results for minimum negative hyperfine shift (σ^+ character of the circularly polarized component of the pump) while the top part shows results for maximum positive hyperfine shift (σ^- character). The horizontal and vertical axes of the plot correspond approximately to the edges of the semiconductor sample, cleaved along the [110] and [1$\bar{1}$0] crystallographic directions.

the indirect effect of strain on nuclear spin cooling through mixing of the valence band states should be distinguished from the direct effect through modification of the nuclear spin eigenstates discussed in Supplementary Note 2.

Another measure of the QD anisotropy is the fine structure splitting (FSS) of a neutral exciton at zero magnetic field. While we have not conducted systematic correlation studies, selective measurement on QD1, where very large nuclear spin polarization has been achieved, reveals a FSS of ≈ 28 μeV. This is considerably larger than the few-μeV FSS observed in symmetric GaAs QDs [18]. This comparison suggests that QD anisotropy does not preclude large nuclear spin polarization, as long as optical selection rules permit coupling to spin-polarized conduction band electronic states. Depending on the type of anisotropy, the heavy hole state $j_z = +3/2$ is mixed with the $j_z = -1/2$ or the $j_z = +1/2$ light-hole state. In case of $j_z = -1/2$ admixing to $j_z = +3/2$ the resulting exciton state becomes elliptically polarized, whereas the admixture of $j_z = +1/2$ to $j_z = +3/2$ is associated with optical transition dipole element polarized along the sample growth axis z [19, 20]. From that perspective, optimization of the $\lambda/2$ and $\lambda/4$ waveplate angles can be understood as matching of the optical pump polarization to the elliptical polarization of

the QD optical transition, allowing generation of spin-polarized electrons. In case of z-polarized optical transition, such polarization matching is not possible, which may explain why nuclear spin polarization degree is much lower than unity in some of the QDs (Fig. 3f of the main text) even after optimizing the elliptical polarization of the pump laser.

It is also possible that spin-polarized holes contribute to nuclear spin pumping, although the hyperfine flip-flops of the heavy holes are expected to be much smaller than for electrons [9]. Further investigations (both experimental and theoretical) would be needed to elucidate which types of QD anisotropies are compatible with efficient nuclear spin polarization. For brevity, throughout this work we use the term "σ^+ pumping" ("σ^- pumping") to describe the optimized elliptically-polarized optical pumping beam with a σ^+ (σ^-) character of the circularly polarized component.

C. Optical probing of quantum dot nuclear spins

For optical probing of the nuclear spin polarization we use a diode laser emitting at 690 nm. Sample forward bias, typically +0.7 V, and the probe power are chosen to maximize (nearly saturate) PL intensity of the ground state X^- trion. The difference between the spectral splitting ΔE_{PL} of the X^- trion doublet and the same splitting $\Delta E_{\mathrm{PL},0}$ measured for depolarized nuclei reveals the hyperfine shifts $E_{\mathrm{hf}} = -(\Delta E_{\mathrm{PL}} - \Delta E_{\mathrm{PL},0})$. Illumination with a probe laser inevitably acts back on the nuclear spin polarization. In order to quantify such back-action we perform calibration measurements with examples shown in Supplementary Fig. 7. In these experiments the QD is first pumped with a σ^+ or σ^- polarized laser with power and bias set to maximize the steady state nuclear polarization. Then the pump is switched off and the probe laser pulse is applied. The hyperfine shift E_{hf} is measured from PL spectroscopy at the end of this probe. It can be seen that the probe induces decay of the nuclear spin polarization. For QD1 the unwanted probe-induced depolarization is faster at $B_{\mathrm{z}} = 4$ T (solid symbols) compared to $B_{\mathrm{z}} = 10$ T (open symbols), even though the same probe power of $P_{\mathrm{Probe}} = 30$ nW is used at both fields. For selective-NMR measurements of the nuclear spin polarization (spin thermometry) in QD1 we use $T_{\mathrm{Probe}} = 15$ ms at $B_{\mathrm{z}} = 10$ T, so that the resulting depolarization is negligible ($< 1\%$). PL intensity of the same QD1 is weaker at $B_{\mathrm{z}} = 4$ T so we use a longer $T_{\mathrm{Probe}} = 24$ ms in order to obtain a sufficiently strong probe PL signal. However, this leads to a larger depolarization of $\approx 4\%$ under σ^- pumping. Depolarization itself is not an issue, since it would simply rescale all the measured E_{hf}, which would not affect the differential NMR spin thermometry. In practice, the probe-induced depolarization

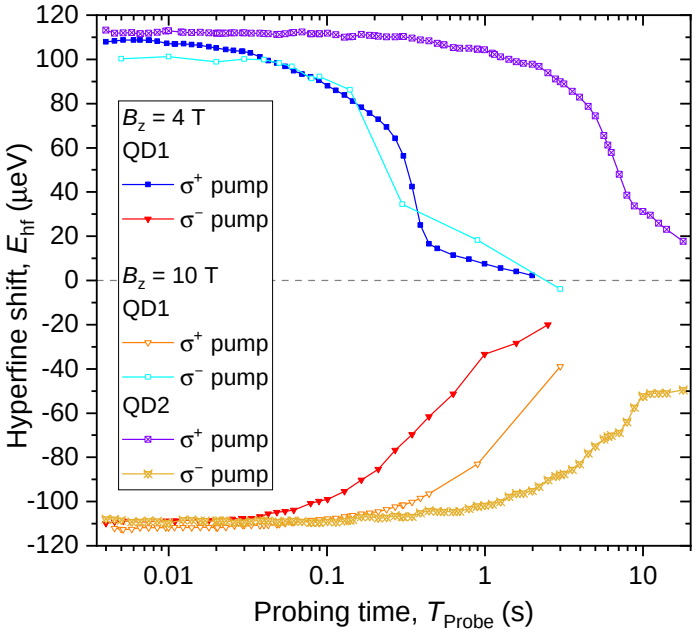

Supplementary Figure 7. **Calibration of the optical probing of the QD nuclear spin polarization.** Hyperfine shift measured as a function of the probing time T_{Probe} following a σ^+ (triangles) or σ^- (squares) pumping of the nuclear spin polarization in a QD. For QD1 results are shown for $B_z = 4$ T (solid symbols) and $B_z = 10$ T (open symbols), measured with a probe power of $P_{\mathrm{Probe}} = 30$ nW. For QD2 results are shown for $B_z = 10$ T (crossed symbols), measured with a probe power of $P_{\mathrm{Probe}} = 7$ nW.

also depends on the instantaneous E_{hf} – such nonlinearity is what causes the distortion, resulting in larger uncertainties of the nuclear spin polarization measured at $B_z = 4$ T. For QD2 we use a lower probe power $P_{\mathrm{Probe}} = 7$ nW (crossed symbols in Supplementary Fig. 7), which leads to an even slower probe-induced depolarization than for QD1. This allows to have a longer probe pulse ($T_{\mathrm{Probe}} = 40$ ms) for QD2, while keeping parasitic depolarization small ($< 1\%$).

D. Radiofrequency control of nuclear spins

The radiofrequency oscillating magnetic field $B_x \perp z$ is produced by a coil placed at a distance of ≈ 0.5 mm from the QD sample. The coil is made of 10 turns of a 0.1 mm diameter enameled copper wire wound on a ≈ 0.4 mm diameter spool in 5 layers, with 2 turns in each layer. Two main types of radiofrequency signals are used in this work. The first type is a frequency-swept monochromatic excitation which is used for adiabatic inversion of the nuclear spin population. The amplitude of the radiofrequency field is constant and the frequency is swept linearly in time. Radiofrequency sweeps are discussed further in Supplementary Note 5 D.

The second type is the broadband radiofrequency excitation which is required to saturate inhomogeneously broadened quadrupolar resonances. The typical width of the resonances that needs to be saturated is tens to hundreds of kHz (further details are given in Supplementary Note 5 B), which is significantly larger than the typical homogeneous NMR linewidth (< 1 kHz). Therefore monochromatic radiofrequency excitation cannot provide a sufficiently uniform saturation of the entire inhomogeneously broadened resonance. This necessitates the use of a broadband radiofrequency excitation. Ideally, one wants a signal with a rectangular spectral profile, which has a constant spectral density in the required frequency interval, and a zero intensity outside that interval. In practice, when implementing the radiofrequency waveforms on a digital generator, it is convenient to approximate the required rectangular spectral band with a frequency comb. In spectral domain, the comb consists of periodically spaced monochromatic modes of constant amplitude, covering the desired interval of frequencies. The mode spacing of 120 Hz is chosen to be smaller than the homogeneous NMR linewidth. Under these conditions, by using a sufficiently small amplitude of each mode we achieve exponential depolarization (i.e. without nuclear spin Rabi oscillations) of the nuclear spin ensemble [21] with a typical time constant of $\tau \approx 30$ ms. The saturation of a chosen NMR resonance is achieved by applying a frequency comb excitation for a period of $\approx 5\tau$. When subject to such excitation, the nuclear spins undergo slow Rabi rotation, transitioning between the spin states parallel and antiparallel to the external magnetic field [22]. Due to the nuclear-nuclear dipole-dipole interactions each nuclear spin is subject to a local field. The randomness of these local fields results in dephasing between Rabi precessions of the individual nuclei. Consequently, the nuclear spin ensemble becomes depolarized (i.e. each nucleus is randomly polarized) after a long saturation pulse.

For the saturation NMR spectra, shown in Fig. 3b of the main text, we use a frequency comb with a total width of 6 kHz. The central frequency of the comb is scanned to obtain the spectra – this frequency is the horizontal axis of the spectral plots. For the high-resolution NMR spectra, shown in Fig. 3a of the main text, we employ the "inverse NMR" technique [23] which enhances the NMR signal and allows the spectra to be measured even on those nuclear spin transitions that are depopulated at high polarization degrees. In this approach the radiofrequency excitation spectrum is a broadband frequency comb with a narrow gap. The central frequency of the gap is scanned and is used for the horizontal axis of the "inverse NMR" spectra. The width of the gap controls the balance between the NMR signal amplitude and the spectral resolution. For the spectra of Fig. 3a of the main text we use a 4 kHz gap to measure the satellite transitions and a 2 kHz gap to measure the narrow central transition NMR peak. The spectra of Fig. 3a are measured with

σ^+ optical pumping. When measured with σ^- pumping, the NMR spectral peaks are shifted to a higher frequency, typically by ≈ 1 kHz. This shift is attributed to dipolar interaction of the measured isotope with the polarized nuclei of the other isotopes.

During the NMR measurements, the superconducting magnet is set into persistent mode, resulting in a predictable nearly-linear decay of the NMR frequencies with time. The typical relative decay rate is $\approx 5 \times 10^{-10}$ s^{-1}. The NMR measurements are programmed to track this decay of the persistent magnetic field. The typical errors in NMR frequencies resulting from uncertainty in the decay rate are within 1 kHz. Some apparent shifts between the same NMR peaks plotted in Fig. 3a and in Fig. 3b of the main text include these contributions of the dipolar interactions and the decaying magnetic fields. In addition, the difference in the spectral resolutions causes some apparent shifts. In particular, in the higher-resolution spectra (4 kHz, Fig. 3a of the main text) the satellite transitions appear as asymmetric peaks. By contrast, in the lower-resolution spectra (6 kHz, Fig. 3b of the main text) the same peaks are smoothed and appear shifted.

Supplementary Note 4. ADDITIONAL EXPERIMENTAL DATA AND DISCUSSION

A. Extended data from nuclear spin pumping measurements

Our approach to maximizing the nuclear spin polarization is through line-search optimization of the optical pumping parameters, such as pump photon energy E_{Pump}, pump power P_{Pump}, optical polarization and the sample bias V_{Pump}. In order to understand the physics of the nuclear spin pumping process we also measure a systematic parametric dependence. Given the typical timescales of the nuclear spin process ($1-100$ s) it is not possible to explore the entire parameter space within a reasonable experimental time. Therefore, we measure various one- and two- dimensional sections in the multidimensional parameter space. An example is shown in Supplementary Fig. 4, where a one-dimensional dependence on E_{Pump} is shown. The spectral dependence of the nuclear spin polarization is interpreted by comparing it with photoluminescence spectroscopy.

Supplementary Fig. 8a is a bias-dependent photoluminescence spectroscopy map measured under non-resonant optical excitation (HeNe laser emitting at 632.8 nm). At low excitation power $P_{\mathrm{Exc}} = 0.5$ nW we observe multiple spectral features, labelled accordingly. The emission of the bulk GaAs free exciton is observed at ≈ 1.518 eV, accompanied by a low energy band at ≈ 1.50 eV arising from doping and impurities. The broad emission between $\approx 1.57 - 1.67$ eV is attributed to both the Si-doped and C-doped AlGaAs layers. The peak at ≈ 1.675 eV is also ascribed to

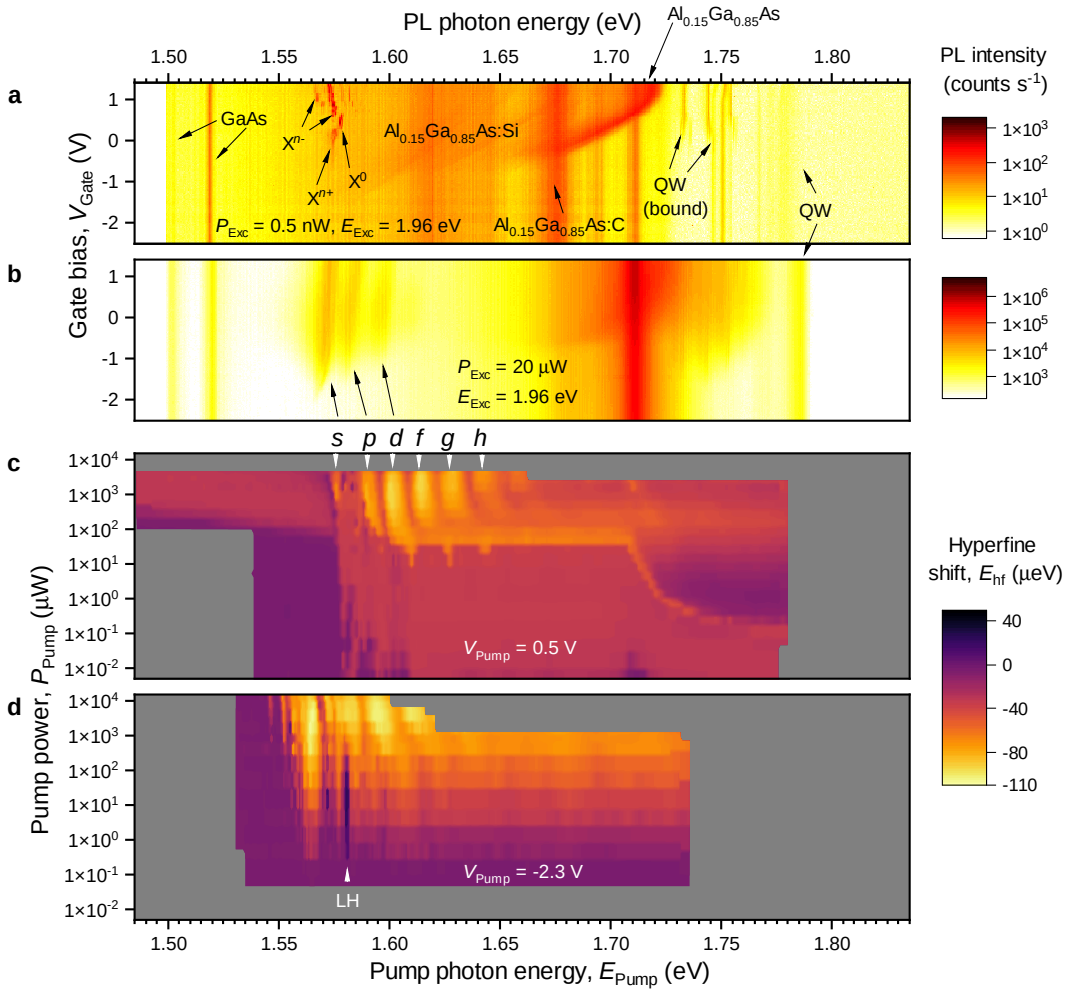

Supplementary Figure 8. **Power dependence of nuclear spin pumping. a,** Bias dependent photoluminescence spectra of QD1 at $B_z = 10$ T measured at a low excitation power $P_{\mathrm{Exc}} = 0.5$ nW. Optical excitation is continuous wave at a wavelength of 632.8 nm. Each spectrum is an average of three 20 s long exposures. **b,** Same photoluminescence spectra but at a high power of $P_{\mathrm{Exc}} = 20$ μW. Each spectrum is an average of three 50 ms long exposures. **c,** Steady-state hyperfine shift measured as a function of the pump power P_{Pump} and the pump photon energy E_{Pump}. Measurement is conducted on QD1 at $B_z = 10$ T using σ^+ pump polarization. The gate bias is kept at $V_{\mathrm{Pump}} = +0.5$ V during pumping. The regions where no data was measured are shown in gray. **d,** Same as (c) but for $V_{\mathrm{Pump}} = -2.3$ V. "LH" labels the feature ascribed to the resonant absorption of a light-hole exciton.

AlGaAs:C. The undoped $Al_{0.15}Ga_{0.85}As$ layers emit at ≈ 1.71 eV under positive bias $V_{\mathrm{Gate}} \approx +1$ V. When the bias is reduced to $V_{\mathrm{Gate}} \approx 0$ V the emission of the $Al_{0.15}Ga_{0.85}As$ electron tunnel barrier Stark-shifts down to ≈ 1.675 eV. By contrast, the luminescence of the $Al_{0.15}Ga_{0.85}As$ layer bellow the n-type barrier is not affected by the applied electric field and remains at ≈ 1.71 eV.

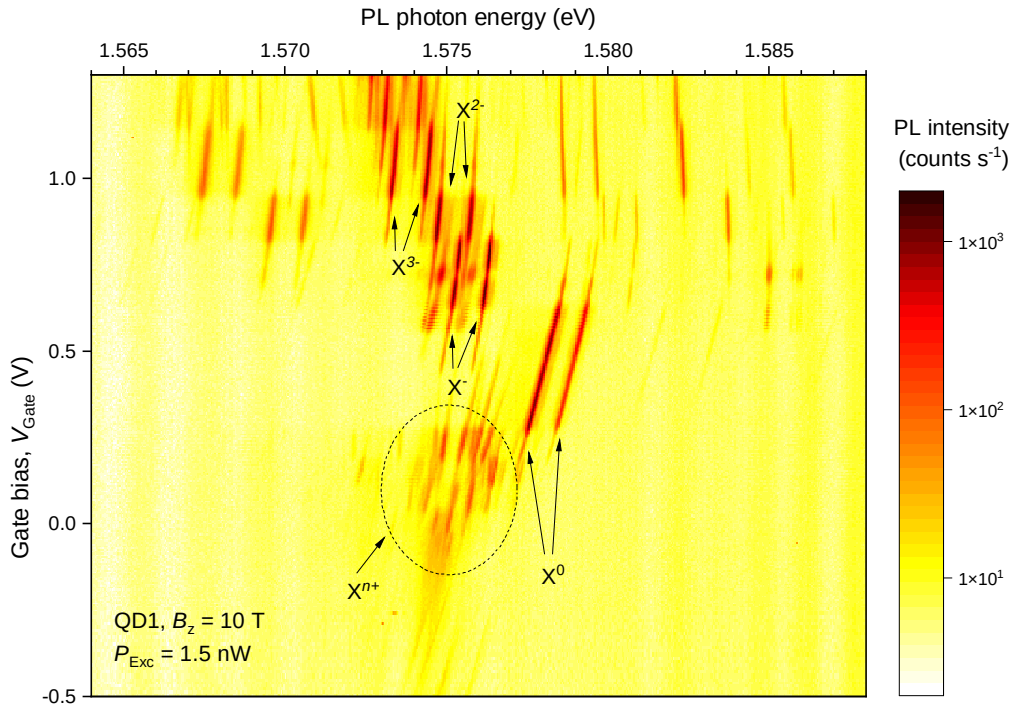

Supplementary Figure 9. **Photoluminescence spectroscopy of QD excitons. a,** Bias dependent photoluminescence spectra of QD1 at $B_z = 10$ T measured at a low excitation power $P_{Exc} = 1.5$ nW and an excitation wavelength of 632.8 nm.

The emission at ≈ 1.785 eV is ascribed to the quantum well (QW) formed when the nanoholes are infilled with GaAs. The narrower lines observed at low excitation power around $\approx 1.73 - 1.75$ eV are attributed to the QW excitons bound by the thickness fluctuations of the QW. Single-QD emission is observed between $\approx 1.56 - 1.59$ eV as a series of Zeeman doublets that switch over as the gate bias V_{Gate} is changed. The higher-resolution spectra of the QD excitons are shown in Supplementary Fig. 9. At $V_{Gate} \approx +0.5$ V photoluminescence is dominated by the neutral exciton X^0, identified from its fine structure splitting at $B_z = 0$ T. At more negative biases the emission of positively charged excitons dominates, since electrons rapidly tunnel out of the dot, leaving excess photogenerated (non-equilibrium) holes. At more positive biases the emission of X^0 is superseded by the negatively charged trion X^-, which becomes dominant when QD confines a resident (equilibrium) electron. At even more positive biases the dot is charged with multiple resident electrons. The spectral features originating from doubly (X^{2-}) and triply (X^{3-}) charged excitons can be distinguished, while the photoluminescence peaks at even higher charge numbers tend to overlap.

When the power is increased ($P_{Exc} = 20$ μW in Supplementary Fig. 8b) the emission peaks of

the s-shell QD excitons with different charging broaden into a single red-shifted band (≈ 1.572 eV). Emission of the higher-shell excitons (p, d and f) also becomes visible. By contrast, photoluminescence intensity of the AlGaAs layer (located below the doped region) increases with power without saturation.

Supplementary Fig. 8c shows the two-dimensional map of the hyperfine shift E_{hf} measured as a function of the pump power P_{Pump} and photon energy E_{Pump} at a fixed $V_{\mathrm{Pump}} = +0.5$ V, which roughly corresponds to a bias where the QD equilibrium state switches from 0 to 1 electron. Nuclear spin pumping evidently takes place at powers as low as $P_{\mathrm{Pump}} \approx 10$ nW (which is close to saturation power of the s-shell QD excitons) as long as the pump laser is tuned above the s-shell exciton transition, so that the QD can absorb the pump photons. However, the resulting nuclear spin polarization degree is low, characterized by $E_{\mathrm{hf}} \approx -30$ μeV. Spin pumping efficiency increases when the pump power is increased to hundreds of μW, which is well above the ground state exciton saturation. The lowest negative $E_{\mathrm{hf}} \approx -90$ μeV is achieved at $P_{\mathrm{Pump}} \approx 1$ mW. At this high power, a series of spectral peaks is observed. Their periodicity matches the periodicity observed in the high-power photoluminescence spectra (Supplementary Fig. 8b), which allows us to identify the peaks as originating from different excitonic shells (up to six visible). The mechanism of nuclear spin pumping can then be understood to arise from resonant absorption of the circularly polarized pump photons, which generate spin-polarized electrons and holes in the excited orbital states. It also follows from Supplementary Fig. 8c that at $V_{\mathrm{Pump}} = +0.5$ V the steady-state $|E_{\mathrm{hf}}|$ produced by pumping via the higher d and f shells is larger than via the p and ground s shells. Excitation via higher shells means that excitons can relax towards the ground state before recombination. Such energy relaxation provides a route for a simultaneous exchange of spin with the nuclei [24], since it helps to absorb or supply a small amount of energy required to compensate the mismatch of the electron and nuclear Zeeman energies. Without the coupling to external energy reservoirs the electron-nuclear spin flip-flop would be energetically forbidden.

At high powers $P_{\mathrm{Pump}} \gtrsim 100$ μW, nuclear spins can be polarized even via optical excitation well below the ground state QD exciton transition, indicating that it's a distinct spin pumping mechanism which we further discuss below.

Supplementary Fig. 8d shows the same dependence of E_{hf} on P_{Pump} and E_{Pump} but with the sample gate voltage changed to a large reverse bias regime $V_{\mathrm{Pump}} = -2.3$ V. At this bias, no QD photoluminescence is observed, even at high optical excitation power, meaning that the excitons become ionized before they can recombine to emit a photon. Nevertheless, nuclear spin pumping is observed and is more efficient than at $V_{\mathrm{Pump}} = +0.5$ V. Under large reverse bias, a higher

threshold power (of a few μW) is needed to induce measurable nuclear spin polarization, which can be explained by the need for the optical excitation to outpace the fast tunneling of the charges from the QD. We again observe spectral peaks that can be matched to the individual excitonic shells (at $V_{\mathrm{Pump}} = -2.3$ V the shells are red-shifted with respect to $V_{\mathrm{Pump}} = +0.5$ V because of the Stark shift). Large $|E_{\mathrm{hf}}|$ are observed for all four lowest exciton peaks, but from experiments on multiple individual QDs we consistently find that pumping through the ground state s-shell exciton under large reverse bias leads to the most efficient spin pumping (characterized by the highest $|E_{\mathrm{hf}}|$).

It is also worth noting that inverted E_{hf} is observed under certain pumping conditions. For example, in Supplementary Fig. 8d we observe $E_{\mathrm{hf}} > 0$ around $P_{\mathrm{Pump}} \approx 10$ μW and $E_{\mathrm{Pump}} \approx 1.580$ eV, which is ≈ 16 meV above the energy of the s-shell nuclear spin pumping peak. This feature at $E_{\mathrm{Pump}} \approx 1.580$ eV, labelled "LH", is ascribed to a light-hole exciton. Optical excitation of a heavy-hole exciton transition with a σ^+ polarized light (with photons carrying a $+1$ momentum in units of $\hbar$) generates a hole with momentum projection $j_{\mathrm{z}} = +3/2$ and an electron with a $s_{\mathrm{z}} = -1/2$ spin projection. The $s_{\mathrm{z}} = -1/2$ electrons then lead to nuclear spin pumping with a negative $E_{\mathrm{hf}} < 0$, as indeed observed in Supplementary Fig. 8d for a wide range of the pump parameters. However, when resonant with a light-hole exciton transition, the same σ^+ photon generates a hole with $j_{\mathrm{z}} = +1/2$ and an electron with $s_{\mathrm{z}} = +1/2$ (see Supplementary Fig. 2a), which then leads to an inverted $E_{\mathrm{hf}} > 0$. The same argument applies to σ^- optical excitation, and manifests in experiments as $E_{\mathrm{hf}} < 0$, observed under resonant excitation of the light-hole exciton transition.

In order to investigate the nuclear spin pumping mechanisms further, we fix the pump power at $P_{\mathrm{Exc}} = 1.5$ mW and measure E_{hf} as a function of E_{Pump} and V_{Pump}. The results are presented in Supplementary Fig. 10c, which shows an extension of the data from Fig. 2c of the main text. The spectral peaks, ascribed to individual excitonic shells, are seen to Stark-shift with the applied bias (Supplementary Fig. 10c). The largest hyperfine shift $|E_{\mathrm{hf}}|$ is again observed for the s-shell exciton at reverse bias, which varies between -2.7 and -2.1 V for different individual QDs. The higher-shell excitons (p, d, etc.) differ from the s shell in that their excitation can be followed by relaxation into a lower energy shell. The slightly lower $|E_{\mathrm{hf}}|$ can then be ascribed to such relaxation between shells, which may involve flipping of the electron without spin transfer to the nuclei. In other words, relaxation between shells may result in a reduced electron spin polarization, which in turn leads to reduction of the maximum achievable $|E_{\mathrm{hf}}|$. Resonant pumping into the s-shell can only generate up to two electrons and two holes in the QD. This leaves only four excitonic complexes that can take part in dynamic nuclear spin polarization: neutral exciton X^0, neutral biexciton

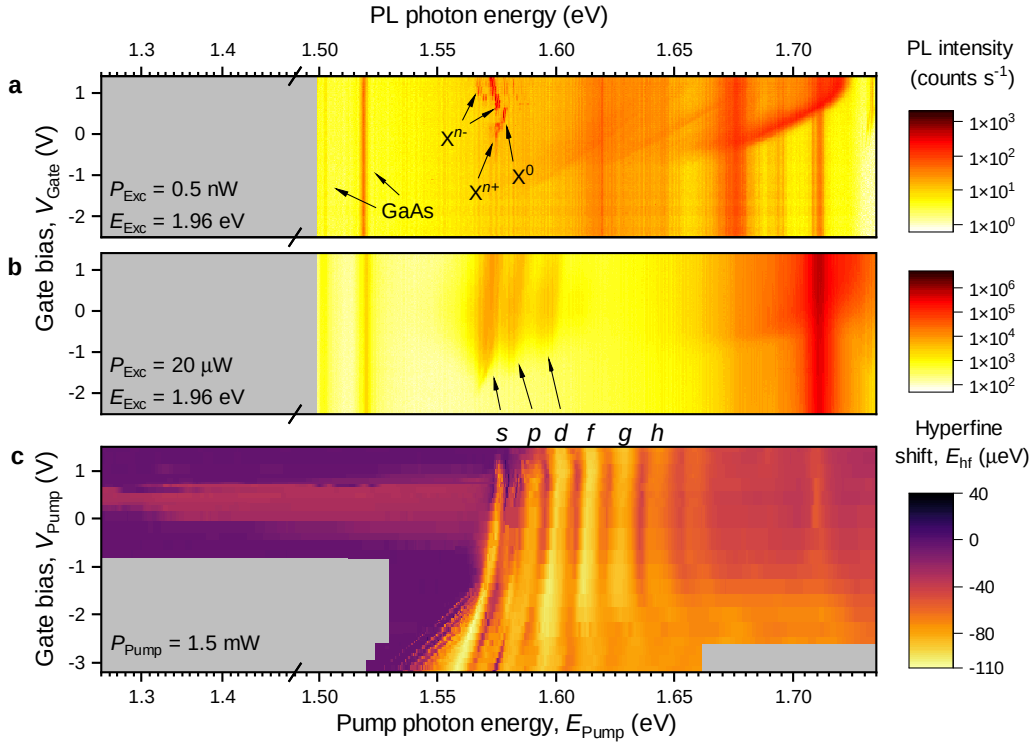

Supplementary Figure 10. **Bias dependence of nuclear spin pumping. a, b,** Same bias-dependent photoluminescence spectra as in Supplementary Figs. 8a,b reproduced for reference. The scale of the horizontal axis is changed at 1.49 eV for better visibility and resolution. **c,** Steady-state hyperfine shift measured as a function of the pump bias V_{Pump} and the pump photon energy E_{Pump}. Measurement is conducted on QD1 at $B_{\mathrm{z}} = 10$ T. Excitation power is $P_{\mathrm{Exc}} = 1.5$ mW with a σ^+ polarization. The regions where no data was measured are shown in gray.

XX^0, negatively charged trion X^- and positively charged trion X^+. We have performed the same measurements as in Supplementary Figs. 4 and 10c but with σ^- pump polarization (producing positive E_{hf}). We find that the spectral positions E_{Pump} of the optimal nuclear spin pumping peaks under σ^+ and σ^- pumping are split by ≈ 900 μeV at $B_{\mathrm{z}} = 10$ T, matching excitonic spectral splitting observed in photoluminescence (Supplementary Fig. 9). However, it is not possible to determine directly which excitonic feature is responsible for nuclear spin pumping with maximum $|E_{\mathrm{hf}}|$. The biexciton XX^0 is unlikely to play a role – it consists of an electron spin singlet (two electrons, one with spin projection $s_{\mathrm{z}} = -1/2$ and one with $s_{\mathrm{z}} = +1/2$) and a hole spin singlet (two holes, one with momentum projection $j_{\mathrm{z}} = -3/2$ and one with $j_{\mathrm{z}} = +3/2$) which do not couple to nuclear spins. The X^- trion is also unlikely to cause efficient nuclear spin pumping, because the two electrons are in a singlet state. Moreover, spin-selective optical excitation of

X^- requires prior injection of another spin-flipped electron, for which there is no sufficiently fast process that could compete with rapid tunneling. The X^+ trion is more likely to contribute to nuclear spin pumping, since it contains only one (spin-polarized) electron. However, to form a hole spin singlet, X^+ excitation would still need to be accompanied by hole spin flipping, which would create a bottleneck and slow down the cyclic nuclear spin pumping process. Therefore, we argue that resonant optical excitation of X^0 is the most likely route for efficient nuclear spin pumping, as it enables fast optical reexcitation upon tunneling of the previously-excited electron-hole pair out of the QD. In addition to the broad resonance that gives the most efficient nuclear spin pumping ($E_{\mathrm{Pump}} \approx 1.564$ eV at $V_{\mathrm{Pump}} = -2.3$ V in Supplementary Fig. 10c), there are narrower and less efficient Stark-shifting resonances observed at lower E_{Pump} (intersecting the same $V_{\mathrm{Pump}} = -2.3$ V around $E_{\mathrm{Pump}} \approx 1.552$ eV and $E_{\mathrm{Pump}} \approx 1.546$ eV). These narrow resonances may correspond to optical excitation of X^+ and X^-. This would be consistent with photoluminescence spectra (Supplementary Fig. 10a), which show that all charged exciton transitions appear on the low-energy side of X^0. Further investigation, both experimental and theoretical, would be needed to establish with certainty which excitonic transition is responsible for high-efficiency nuclear spin pumping in the regime of fast tunneling.

Supplementary Fig. 10c shows that nuclear spins can be polarized at photon energies down to $E_{\mathrm{Pump}} \approx 1.25$ eV, which is well below the ground state QD exciton energy and bulk GaAs bandgap. This mechanism leads to negative hyperfine shifts $E_{\mathrm{hf}} \approx -30$ μeV for both σ^+ and σ^- pumping, suggesting that optical excitation plays a different role, possibly related to activation of charge traps or Auger effect. The trapped-charge hypothesis is further supported by the bias dependence, which shows that the sub-bandgap nuclear spin pumping disappears for $V_{\mathrm{Pump}} < -0.5$ V and $V_{\mathrm{Pump}} > +0.9$ V. The buildup time of the nuclear spin polarization is found to be around ≈ 5 s, which is approximately an order of magnitude slower than nuclear spin pumping via resonant excitation of the QD excitons (see Supplementary Note 4 C). The exact mechanism of sub-bandgap optical nuclear spin pumping is currently unclear and would require a separate systematic investigation.

Focusing on the s-shell pumping, we plot the minimum E_{hf} (i.e. maximum $|E_{\mathrm{hf}}|$) as a function of bias V_{Pump} in Supplementary Fig. 11a. The corresponding photoluminescence intensity of the s-shell exciton under above-gap excitation is shown in Supplementary Fig. 11b. At positive V_{Gate} the electric field in the sample is small and the band structure is close to flat-band (right sketch in Supplementary Fig. 11c). As a result, optical recombination is the only way the photo-generated carriers can leave the QD. The typical radiative lifetimes for the studied type of GaAs QDs are

≈ 300 ps, which creates a bottleneck for how quickly the spin-polarized electrons can be injected into the QD, limiting in turn the rate of the nuclear spin pumping. When the sample gate is tuned towards larger reverse (negative) bias, the maximum hyperfine shift $|E_{\mathrm{hf}}|$ increases. At the same time, photoluminescence intensity gradually decreases when $V_{\mathrm{Gate}} < -1$ V, indicating that electrons and holes tunnel out of the QD (left sketch in Supplementary Fig. 11c) faster than they can recombine optically. We attribute this correlation to the key role that the tunneling plays in dynamic nuclear spin polarization. Fast tunneling overcomes the radiative-recombination bottleneck, so that high-power optical excitation can be used to inject spin polarized electrons at a high rate. The efficiency of nuclear spin pumping reaches its maximum at $V_{\mathrm{Pump}} = -2.3$ V. For even larger reverse bias (i.e. more negative V_{Pump}) the maximum hyperfine shift $|E_{\mathrm{hf}}|$ is seen to reduce slightly. For $V_{\mathrm{Pump}} < -2.3$ V tunneling becomes even faster, which would require an even higher pump power $P_{\mathrm{Pump}} \gtrsim 10$ mW to maintain steady-state occupation of the QD with spin-polarized electrons. However, when focused into a diffraction-limited spot, such high-power optical excitation causes heating of the crystal lattice, which may result in accelerated nuclear spin relaxation, explaining why the highest achievable nuclear spin polarization is reduced at very large reverse biases.

B. Estimate of the electron tunneling rate

In order to quantify the optical nuclear spin pumping process, we estimate the electron tunneling rate using the photoluminescence intensity data. We employ a rate equation approach by considering the probability p_{eh} that the QD s-shell is occupied by an electron-hole pair. Since we are only interested in an order of magnitude estimate, we ignore the contributions of the biexcitons (two electron-hole pairs) and charged excitons (an electron-hole pair with extra one electron or one hole). The steady state is defined by the balance between the rate of the optical excitation (Γ_{Exc}) and the rates of deexcitation through optical recombination (Γ_{R}) and tunneling ionization (Γ_{Tun}):

$$\begin{aligned} &(1-p_{\mathrm{eh}})\Gamma_{\mathrm{exc}} - p_{\mathrm{eh}}(\Gamma_{\mathrm{R}} + \Gamma_{\mathrm{Tun}}) = 0 \Rightarrow \\ &p_{\mathrm{eh}} = \Gamma_{\mathrm{exc}}/(\Gamma_{\mathrm{exc}} + \Gamma_{\mathrm{R}} + \Gamma_{\mathrm{Tun}}) \end{aligned} \tag{S8}$$

The intensity of photoluminescence I_{PL} is proportional to p_{eh}. We further assume that the maximum observed PL intensity $I_{\mathrm{PL,max}}$ corresponds to a regime where the tunneling rate is negligible $\Gamma_{\mathrm{Tun}} \to 0$. With this assumption we eliminate the unknown PL intensity that would be observed

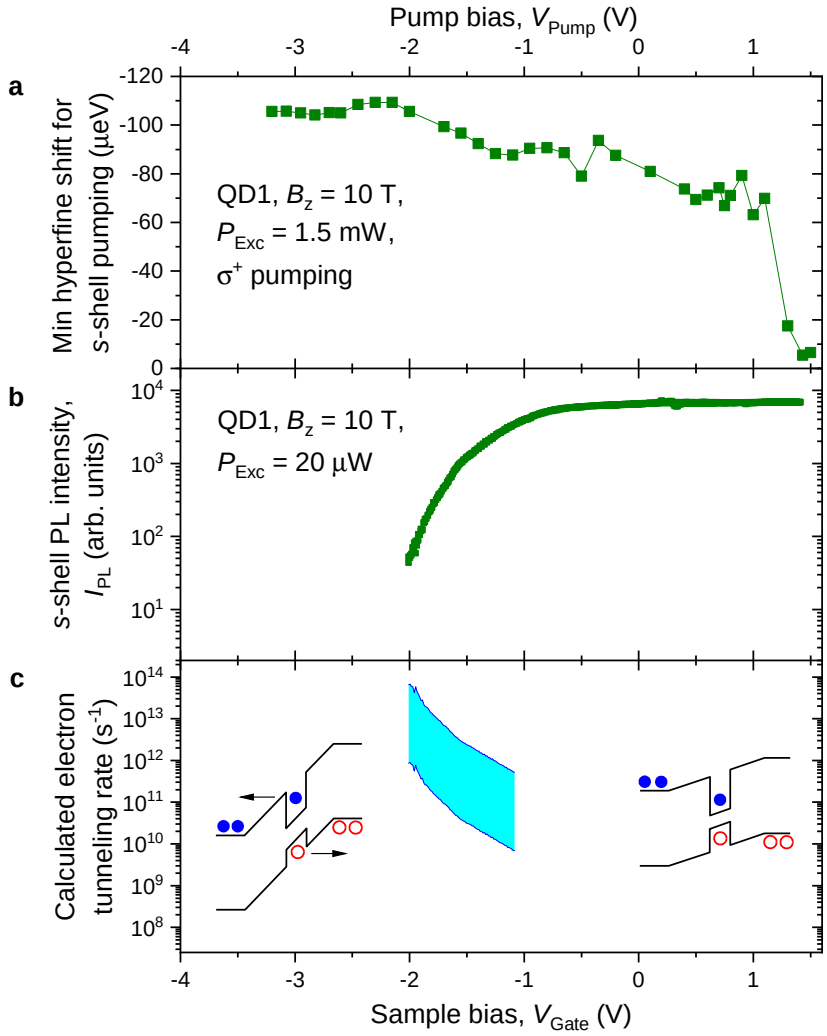

Supplementary Figure 11. **Bias dependence of nuclear spin pumping via *s*-shell excitation. a,** Steady-state hyperfine shift measured as a function of the pump bias V_{Pump} for pump photon energy E_{Pump} tuned into resonance with the *s*-shell exciton at each bias. Measurement is conducted on QD1 at $B_z = 10$ T. **b,** Photoluminescence intensity of the *s*-shell exciton measured as a function of bias V_{Gate} under 632.8 nm high-power saturation. **c,** Calculated rate for the electron to tunnel out of the QD, shown as a shaded area between lower and upper bound estimates. Sketches show conduction and valence band profiles at positive and negative V_{Gate}.

at $p_{\mathrm{eh}} = 1$ and find for the tunneling rate at an arbitrary bias:

$$\Gamma_{\mathrm{Tun}} = (\Gamma_{\mathrm{R}} + \Gamma_{\mathrm{exc}}) \left(\frac{I_{\mathrm{PL,max}}}{I_{\mathrm{PL}}} - 1 \right) \tag{S9}$$

It then follows that the reduction of the photoluminescence intensity I_{PL} under reverse bias signifies that the tunneling rate exceeds the sum $(\Gamma_{\mathrm{R}} + \Gamma_{\mathrm{exc}})$ of the radiative recombination and optical excitation rates. The radiative recombination time is $1/\Gamma_{\mathrm{R}} \approx 300$ ps [25] for the studied type of

QDs ($\Gamma_R \approx 3.3 \times 10^9$ s^{-1}). Since photoluminescence intensity of the s-shell exciton is saturated, we assume that the excitation rate exceeds the recombination rate $\Gamma_{Exc} > \Gamma_R$. This gives the lower bound estimate for the tunneling rate. The photoluminescence measurement shown in Supplementary Fig. 11b was conducted at high excitation power, exceeding the ground state exciton saturation power by a factor of ≈ 150. Thus we write $\Gamma_{Exc} \lesssim 150\Gamma_R$, which gives an upper bound estimate, since some of the photo-excited electron-hole pairs can recombine from higher shells, without reaching the s-shell. Using Supplementary Eq. S9 we calculate Γ_{Tun} taking I_{PL} and the maximum observed intensity $I_{PL,max}$ from Supplementary Fig. 11b. The range between the lower bound ($\Gamma_{Exc} = \Gamma_R$) and the upper bound ($\Gamma_{Exc} = 150\Gamma_R$) estimates is shown by the shaded area in Supplementary Fig. 11c. Such direct evaluation of Γ_{Tun} is possible only when the bias is high enough to detect photoluminescence, but also low enough to have a substantial reduction of I_{PL} compared to $I_{PL,max}$. These estimates show that the tunneling time at $V_{Gate} = -2$ V is on the order of $\approx 0.1 - 1$ ps.

In order to estimate Γ_{Tun} below $V_{Gate} < -2$ V we consider the well-known WKB approximation of the tunneling rate through a triangular barrier (see e.g. Ref. [26]). Up to a constant factor, we have:

$$\Gamma_{Tun} \propto \exp\left(-\frac{4\sqrt{2m_e}}{\hbar e F_z}|\epsilon_e|^{3/2}\right), \tag{S10}$$

where m_e^* is the effective electron mass, ϵ_e is the electron ionization energy and F_z is the electric field in the growth direction. The total thickness of the structure between the doped layers is ≈ 300 nm, so the electric field is estimated as $F_z = -(V_{Gate} - V_{Gate,0})/300$ nm, where $V_{Gate,0} = +1.55$ V is the built-in potential of the structure, deduced as the bias at which the PL Stark shift vanishes. Based on Ref. [27] we estimate the conduction band discontinuity between GaAs and $Al_{0.33}Ga_{0.67}As$ to be $U_e \approx 0.28$ eV and take $m_e^* = 0.067m_e$, where m_e is the free electron mass. The s-shell photoluminescence of the QD is observed at ≈ 0.055 eV above the bulk GaAs. Taking that 0.63 of this offset is in the conduction band [27], we estimate the ionization energy $\epsilon_e = U_e - 0.63 \times (0.055 \text{ eV}) \approx 0.25$ eV. Substituting this, we find the numerical estimate $\Gamma_{Tun} \propto \exp\left(\frac{64.2}{V_{Gate}-1.55}\right)$, where V_{Gate} is in the units of Volts. Firstly, we see that the exponent is far from saturation in the studied range of V_{Gate}, so that further reduction of V_{Gate} (i.e. making the bias more negative) would result in shortened tunneling times. Secondly, going from $V_{Gate} = -2$ V, where photoluminescence is measurable, to $V_{Gate} \in [-2.7, -2.3]$ V, where dynamical nuclear spin polarization is most efficient, results in an order of magnitude higher Γ_{Tun}. Therefore we estimate $\Gamma_{Tun} \approx 10^{13} - 10^{14}$ s^{-1} for optimal nuclear spin pumping (tunneling time $\approx 0.01 - 0.1$ ps).

We can now independently estimate the optical excitation rate that leads to optimal nuclear spin pumping. Resonance fluorescence intensity, measured on InGaAs/GaAs QDs in the same setup and under similar experimental conditions, saturates at $P_{\mathrm{Exc}} \approx 5$ nW. We assume that $\Gamma_{\mathrm{Exc}} \approx \Gamma_{\mathrm{R}}$ at saturation, where the radiative rate is $\Gamma_{\mathrm{R}} \approx 10^9$ s^{-1} for InGaAs QDs. Assuming that the excitation rate scales linearly with optical power, we find that the resonant pumping power of $P_{\mathrm{Pump}} \approx 1.5$ mW, used for optimal nuclear spin pumping, corresponds to $\Gamma_{\mathrm{Exc}} \approx \frac{1.5\ \mathrm{mW}}{5\ \mathrm{nW}} 10^9$ s^{-1} $\approx$ 3×10^{14} s^{-1}. This corresponds to optical reexcitation time of ≈ 0.0033 ps. These estimates yield Γ_{Exc} that are comparable to or somewhat higher than the above-calculated Γ_{Tun}, as would be expected for a steady-state condition. In other words, having $\Gamma_{\mathrm{Exc}} \gtrsim \Gamma_{\mathrm{Tun}}$ ensures that optical excitation generates as many spin-polarized electrons per unit of time as permitted by the rate of the tunnel escape. The typical linewidths of the excitonic shell peaks in the spectra of the steady state E_{hf} at large reverse biases (Supplementary Figs. 4, 10c) are on the order of ≈ 10 meV, which translates to ≈ 0.4 ps, corroborating our order-of-magnitude estimates of Γ_{Tun}.

Apart from the fast cycling of the optically-generated electrons, we expect that fast tunneling also facilitates the nuclear spin pumping by disrupting the formation of coherent nuclear "dark" states, which are otherwise predicted to prevent the approach to a near-unity nuclear spin polarization [28, 29]. Indeed, recent studies have shown that fluctuations of the electron spin reduce the coherence of the nuclear spins in a QD [30]. Moreover, the short (tunneling-limited) lifetime of the electron spin can be interpreted as spectral broadening of the electron spin levels. Such spectral broadening can facilitate nuclear spin pumping by compensating the energy mismatch of the electron and nuclear spin Zeeman energies, which otherwise inhibits the electron-nuclear spin flip-flops. The role played by tunneling is then similar to the effect that elevated lattice temperatures have on nuclear spin polarization, as studied previously in InGaAs QDs [24]. Future theoretical work may explain the details of the nuclear spin pumping process by treating optical excitation, tunneling and electron-nuclear spin interactions in a unified framework.

C. Nuclear spin buildup dynamics

The nuclear spin buildup dynamics under optical pumping are non-exponential (Fig. 4a of the main text). The exact description of nuclear spin buildup dynamics is complicated due to the multitude of the contributing factors, including spin diffusion [15] and the inhomogeneity of the hyperfine coupling between the nuclei and the localized QD electron. Precise description of the buildup dynamics is beyond the scope of this work. Therefore, we limit the analysis to an empirical

fit of the data by a sum of two stretched exponentials:

$$E_{\rm hf} = E_{\rm hf,fast}\left(1-\exp(-(t/\tau_{\rm fast})^{\kappa_{\rm fast}})\right) + E_{\rm hf,slow}\left(1-\exp(-(t/\tau_{\rm slow})^{\kappa_{\rm slow}})\right). \tag{S11}$$

The best fits are shown by the solid lines in Fig. 4a of the main text and are seen to capture well the strongly non-exponential buildup dynamics. The fitting parameters for the optimal steady-state nuclear spin pumping of QD2 at $B_{\rm z} = 10$ T are as follows:

Parameter	σ^+ pumping	σ^- pumping
$\tau_{\rm fast}$	0.1215 s	0.2446 s
$\tau_{\rm slow}$	0.5174 s	1.1903 s
$E_{\rm hf,fast}$	-43.03 μeV	69.46 μeV
$E_{\rm hf,slow}$	-67.51 μeV	41.44 μeV
$\kappa_{\rm fast}$	0.88	0.68
$\kappa_{\rm slow}$	0.44	0.36

(S12)

Due to the empirical nature of the fitting model, its parameters should be treated as estimates. Nevertheless, we can establish that the fast initial buildup occurs on a $0.1-0.3$ s timescale, slowing down to $0.5-1.5$ s when the nuclear spin polarization approaches closer to its steady state. The fast initial buildup is likely dominated by the nuclear spins located at the center of the QD, and therefore characterizes the inherent nuclear spin pumping rate. The slower dynamics at the later stage are likely dominated by the nuclei that are further away from the QD center. This slower component is a result of a complex interplay between several competing processes. On the one hand, these distant nuclei are polarized both directly by the electron and indirectly through spin diffusion from the center of the QD. On the other hand, spin diffusion from these nuclei further into the barriers also causes the depolarization.

Electron-nuclear spin dynamics become nonlinear when electron spin Zeeman splitting is cancelled by the hyperfine shift. This is manifested in a kink in the nuclear spin buildup dynamics, observed at $E_{\rm hf} \approx +50$ μeV in Fig. 4a of the main text. From the zero-splitting condition $E_{\rm hf} \approx -\mu_{\rm B} g_{\rm e,z} B_{\rm z}$ we can estimate the electron g-factor $g_{\rm e,z} \approx -0.09$, in agreement with previous measurements on the same structure [15].

It is also interesting to estimate the rate of the electron-nuclear spin flip-flops. Starting from a depolarized state, it takes IN spin flips to achieve a fully polarized state of $N \approx 10^5$ nuclei with spin I. The hyperfine shift $E_{\rm hf}$ corresponding to a fully polarized state is $IF_{\rm tot} \approx 110-115$ μeV. On the other hand, from the nuclear spin buildup dynamics measurements we find that the highest rate of change in $E_{\rm hf}$ (the derivative at the start of pumping from a depolarized state) is ≈ 600 μeV/s, in

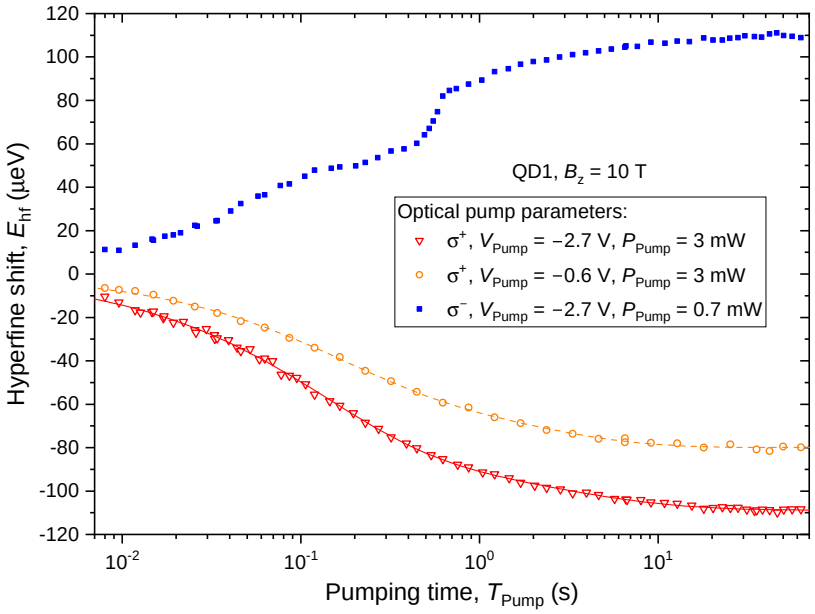

Supplementary Figure 12. **Nuclear spin buildup dynamics.** Symbols show nuclear spin buildup dynamics measured for an individual dot QD1 at $B_z = 10$ T under σ^- (squares) and σ^+ (triangles, circles) optical pumping. Optical pump photon energy is tuned into the s-shell resonance at pump bias $V_{\rm Pump} = -2.7$ V (squares, triangles) or $V_{\rm Pump} = -0.6$ V (circles). Lines show biexponential fitting.

agreement with $\tau_{\rm fast}$ derived above. Combining these parameters we estimate the electron-nuclear flip-flop rate to be $\approx 8 \times 10^5$ s^{-1} (i.e. one nucleus flipped every ≈ 1 μs). Assuming that the cycling of the spin-polarized electrons is limited by the tunneling rate of $\Gamma_{\rm Tun} \approx 10^{13}$ s^{-1}, we estimate that only a small fraction $\approx 10^{-7}$ of the injected electrons transfer their spin to the nuclei, while the rest tunnel out of the QD without polarizing the nuclear spins.

Supplementary Fig. 12 shows the buildup dynamics in another individual quantum dot (QD1). Here, the pump bias is set to either the optimal value of $V_{\rm Pump} = -2.7$ V (squares, triangles) or a suboptimal value of $V_{\rm Pump} = -0.6$ V (circles), and the photon energy of the optical pump is tuned into the s-shell resonance at each pump bias. The best fits for σ^+ pumping are shown by the lines.

The fitting parameters for QD1 at $B_z = 10$ T are as follows:

Parameter	$\sigma^-, V_{\mathrm{Pump}} = -0.6$ V	$\sigma^+, V_{\mathrm{Pump}} = -2.7$ V
τ_{fast}	0.1391 s	0.1228 s
τ_{slow}	1.325 s	1.5697 s
$E_{\mathrm{hf,fast}}$	-44.13 μeV	-71.37 μeV
$E_{\mathrm{hf,slow}}$	-35.80 μeV	-37.39 μeV
κ_{fast}	0.72	0.69
κ_{slow}	0.58	0.50

(S13)

The fitted buildup times for QD1 are similar to those found for QD2 (Supplementary Eq. S12). Moreover, although the steady-state nuclear polarization is lower at the suboptimal bias of $V_{\mathrm{Pump}} = -0.6$ V, the buildup times are nearly the same as at the optimal bias $V_{\mathrm{Pump}} = -2.7$ V where the steady-state nuclear polarization is maximized. This is rather unexpected and is in contrast to the tunneling rate dependence, which is seen to change by orders of magnitudes between $V_{\mathrm{Pump}} = -2.7$ V and -0.6 V (Supplementary Fig. 11c). This indicates that the change in the cycling rate of the spin-polarized electrons is not the only effect of the bias. The alternative effects of a large reverse bias, discussed above, may include the relaxation of the coherent-dark-state bottleneck, and the bridging of the electron-nuclear energy gap by the tunneling-broadened electron spin states. There are further effects of the large reverse bias which may explain why the largest nuclear polarization is observed at $V_{\mathrm{Pump}} = -2.7$ V, even though the tunneling escape rate is already sufficiently fast at $V_{\mathrm{Pump}} = -0.6$ V. For example, the large electric field, produced by the reverse bias, changes the composition of the valence band in terms of the heavy and light hole contributions [31], which in turn may change the purity of the electron spin polarization produced by the elliptically polarized pump light. A large electric field may also increase the spatial spread of the electron envelope wavefunction, helping to polarize the nuclear spins that are further away from the center of the QD. These considerations highlight the considerable complexity of the processes responsible for cooling of a many-body nuclear spin ensemble. Our demonstration of experimental conditions that lead to a large nuclear polarizations is an important starting point for future work which would be needed to unravel this complexity.

D. Relation between nuclear spin cooling and state narrowing

Here we compare nuclear spin polarization, described in this work, to the class of "state narrowing" techniques [32–34], which are sometimes also described as spin cooling. The simplest way

to describe the difference is to note that dynamic nuclear polarization with $|P_{\mathrm{N}}| \to 1$ corresponds to the true cooling of the nuclear spin ensemble, whereas the narrowing schemes can be described as partial cooling of certain degrees of freedom, while leaving the remaining degrees of freedom of the nuclear ensemble in a "hot" state. In order to explain this in more detail, we refer to Figs. 4d,e of the main text. Fig. 4d of the main text sketches the density of states calculated for $N = 6$ dipolar-coupled $I = 3/2$ nuclei (without the electron). At high magnetic fields the density of state spectrum consists of well resolved bands. Each individual band corresponds to a well-defined total spin projection M. The adjacent bands are split by the Zeeman energy $h\nu_{\mathrm{L}}$, where the Larmor frequency is in the $\nu_{\mathrm{L}} \approx 30 - 100$ MHz range in our experiments. The transition between any two adjacent bands can be described as flipping (i.e. a ± 1 change in the z-projection m) of a single spin in the ensemble. Without the nuclear-nuclear interaction, each band would represent a degenerate state. The dipole-dipole interaction between the nuclei lifts the degeneracy, broadening each band. The broadening of each band is governed by the magnitude of the nuclear-nuclear dipolar couplings $h\nu_{\mathrm{dd}} \propto \max|b_{j,k}|$ and is on the order of $\nu_{\mathrm{dd}} \approx 1$ kHz in GaAs based structures. The origin of this broadening can be understood as follows. There are a large number of combinations of the individual nuclear states that result in a given total polarization M. However, each such combination (microstate) has a slightly different energy depending on the mutual orientation of the adjacent nuclei in the ensemble. For $M \approx 0$ (i.e. for small nuclear spin polarization $P_{\mathrm{N}} \approx 0$) the broadening is maximal and the number of microstates is large, meaning that such bands have a quasicontinuous spectrum. With the increasing polarization degree P_{N} the number of possible microscopic configuration reduces and the distribution of the available dipolar energies becomes narrower. There are only two non-degenerate many-body eigenstates, achieved in the ultimate limit of a fully-polarized ensemble (i.e. at $M = \pm NI$, $P_{\mathrm{N}} = \pm 1$). Notably, these fully-polarized states are separated by a large Zeeman energy gap $h\nu_{\mathrm{L}}$ from all the other states many-body states.

The difference between polarization and state narrowing is illustrated in Fig. 4e of the main text. In case of state narrowing, the degree of freedom that is cooled down is the distribution of the total z-projection M of the nuclear spins (blue bars show Gaussian distribution of M with a full width of half maximum of 2). In an ideal case, one aims to narrow the distribution down to just one value of M. However, even for such ultimate narrowing the dipolar energy reservoir remains in a "hot" state, in a sense that a fixed M can be implemented with equal probability by any of the large number of microstates. In case of a polarized state (true cooling), the probability to find the ensemble in a microstate with a total projection M approximately follows the Boltzmann distribution $\propto \exp(\beta M)$, where β is the dimensionless inverse spin temperature. The probabilities

of the microstates are shown by the red bars in Fig. 4e for a polarized ensemble at $P_{\mathrm{N}} = 0.99$. It can be seen that true cooling (polarization) both narrows the distribution M and narrows the dipolar energy distribution. This is a fundamental advantage of true cooling via polarization.

Due to the difference between polarization and state narrowing the figures of merit are also different. One metric is the polarization degree P_{N}. Although state narrowing protocols are primarily designed to reduce the uncertainty in M, they can be tailored to produce a non-zero mean M. However, the resulting polarization degrees are modest, for example $P_{\mathrm{N}} \approx 0.3$ in a recent demonstration [34]. The likely limiting factor is the nuclear spin polarization rate, arising from the need to have a coherent electron spin qubit in the QD. The polarization protocol reported here benefits from operating the QD in a regime of fast tunneling, which allows much high polarizations $|P_{\mathrm{N}}| \geq 0.95$ to be achieved.

Another figure of merit is the uncertainty in M. Recent algorithmic cooling experiments [34] reported an uncertainty of 5.7. In case of polarization, currently there is no measurement of uncertainty in M. Such measurement would require additional experiments, for example a measurement of the electron spin qubit dephasing. However, we can calculate the uncertainty in M from the first principles. To this end we describe the state of the nuclear spin ensemble in terms of probabilities p_m for each nuclear spin to occupy a state with spin z projections m. In case of the spin-3/2 nuclei $m \in \{-3/2, -1/2, +1/2, +1/2\}$. For the state induced by optical dynamical nuclear polarization we model these probabilities using the Boltzmann distribution:

$$p_m = e^{m\beta} / \sum_{m=-I}^{+I} e^{m\beta}, \tag{S14}$$

where $\beta = h\nu_{\mathrm{L}}/k_{\mathrm{b}}T_{\mathrm{N}}$ is the dimensionless inverse temperature, expressed in terms of the nuclear spin Larmor frequency ν_{L} and the spin temperature T_{N} (h is Planck's constant and k_{b} is the Boltzmann constant). We then consider an ensemble of N identical spins, assuming that their states follow the Boltzmann distribution independently. We are interested in the random variable M, which is the total of the spin projections m of the individual spins. We calculate the variance of M. The details of the calculations, carried out using Wolfram Mathematica software, can be found in the Supplementary file `SupplementaryData1.nb` (pdf version of this file can be found in `SupplementaryData2.pdf`). The variance can be written in terms of the hyperbolic cosecant functions:

$$V(M) = \frac{N}{4}\left(\mathrm{csch}^2[\beta/2] - (2I+1)^2\mathrm{csch}^2[(I+1/2)\beta]\right), \tag{S15}$$

We consider a QD with $N \approx 10^5$ nuclei with spin $I = 3/2$. For an unpolarized state ($P_{\mathrm{N}} \approx 0$)

the standard deviation uncertainty is $\sqrt{V(M)} \approx 354$. For a conservative estimate of $P_{\mathrm{N}} \approx 0.95$ ($\beta \approx 2.66$) in the best QDs we find $\sqrt{V(M)} \approx 90$. For $P_{\mathrm{N}} \approx 0.99$ ($\beta \approx 4.2$), the uncertainty in M reduces to $\sqrt{V(M)} \approx 39$. This is still worse than the state-of-the-art performance of the state narrowing techniques. However, our assumption of independent spins could be leading to an overestimate. Usually nuclear spin pumping processes result in some additional narrowing of M, for example through electron-nuclear spin feedback [6]. Investigation of nuclear spin statistics beyond the measurement of P_{N} is a subject for future work.

Overall, the polarization protocol implemented in our work and the state narrowing techniques use rather different approaches, with their advantages and disadvantages. The state narrowing methods offer a reliable reduction of M, which is key to reducing the QD electron spin qubit dephasing time $T_{2,\mathrm{e}}^{*}$. Yet, even in an ideal case, where M is known down to one unit of spin, such a narrowed state still has a large statistical uncertainty associated with different mutual orientations of the nuclear spins. When the electron spin qubit is added into consideration, such uncertainty in the dipolar energy also translates into uncertainty of the effective nuclear field acting on the electron (due to the inhomogeneity of the hyperfine coupling of the localized electron). The quasicontinuous distribution of the dipolar energies for any given M opens the channels for electron-nuclear spin dynamics which can reduce the electron spin coherence time $T_{2,\mathrm{e}}$. Our approach of cooling through polarization requires further investigation and improvement to be comparable with state narrowing. However, true cooling has a unique fundamental advantage of being the only route towards a ground eigenstate of a many-body nuclear spin ensemble. Since such a ground state is non-degenerate and is spectrally isolated by a large energy gap $h\nu_{\mathrm{L}}$ it results in essentially nondecaying electron spin coherence, as shown through exact analytical solution [35]. For practical applications one may envisage combining the true cooling and the state narrowing into a two-stage process with the aim of achieving new levels of control over the nuclear spin ensemble state.

Supplementary Note 5. DERIVATION OF NUCLEAR SPIN POLARIZATION

A. Nuclear magnetic resonance thermometry of spin-3/2 nuclei

We use again the model of Supplementary Eq. S14. We assume $\nu_{\mathrm{L}} > 0$ and $B_{\mathrm{z}} > 0$, so that $m = +I$ is the ground state for nuclei with $\gamma > 0$, in agreement with Supplementary Eq. S3. For spin $I = 1/2$ where $m = \pm 1/2$ any statistical distribution is described by Supplementary Eq. S14 with some T_{N}. By contrast, for $I > 1/2$ Supplementary Eq. S14 states the non-trivial nuclear

spin temperature hypothesis [36] – previous experimental studies on low-strain epitaxial quantum dots [13] have shown its validity for the state induced by optical dynamical nuclear polarization. Nuclear spin polarization degree is defined as

$$P_{\mathrm{N}} = \frac{1}{I}\sum_{m=-I}^{+I} m p_m. \tag{S16}$$

For the Boltzmann distribution of Supplementary Eq. S14 the polarization degree is given by the Brillouin function:

$$P_{\mathrm{N}} = \frac{1}{2I}\left((2I+1)\coth[(I+1/2)\beta] - \coth[\beta/2]\right). \tag{S17}$$

It is worth noting that the polarization degree P_{N} and the dimensionless inverse temperature β provide more relevant description of the nuclear spin state than the temperature T_{N}. Indeed, when the Larmor frequency ν_L is changed (by varying the external magnetic field) P_{N} and β are preserved, whereas T_{N} is not constant, even if it is the same optically-pumped nuclear spin state. The temperature T_{N} only gains physical meaning at low magnetic fields $\lesssim 1$ mT, comparable to the local nuclear dipolar fields. P_{N} and β are also related to entropy [37, 38]. For N spin-1/2 nuclei the entropy reads:

$$\frac{S}{Nk_{\mathrm{B}}} \approx \ln 2 - \frac{1}{2}\left[(1+P_{\mathrm{N}})\ln(1+P_{\mathrm{N}}) + (1-P_{\mathrm{N}})\ln(1-P_{\mathrm{N}})\right]. \tag{S18}$$

For $P_{\mathrm{N}} \to 1$ this can be approximated as

$$\frac{S}{Nk_{\mathrm{B}}} \approx \frac{1-P_{\mathrm{N}}}{2}(1+\ln 2 - \ln(1-P_{\mathrm{N}})) = \frac{1-P_{\mathrm{N}}}{2}\left(1-\ln\left(\frac{1-P_{\mathrm{N}}}{2}\right)\right). \tag{S19}$$

The dependence is plotted by the solid line in Supplementary Fig. 13 and is very nonlinear. A significant reduction in the entropy (i.e. reduction in disorder) requires P_{N} to be close to unity. For example, at $P_{\mathrm{N}} \approx 0.8$ the entropy is reduced only to $\approx 1/2$ of its maximum value at $P_{\mathrm{N}} = 0$, while a factor of 10 reduction requires $P_{\mathrm{N}} \approx 0.974$. The minimum in entropy is achieved only for $P_{\mathrm{N}} = \pm 1$ ($\beta \to \pm\infty$). An alternative way to characterize the polarization degree of a nuclear spin ensemble is through the reduction of the dephasing time of the central (electron) spin qubit coupled to such an ensemble. Under certain approximations, the dephasing rate can be shown to scale as $\sqrt{1-P_{\mathrm{N}}^2}$ with nuclear spin polarization degree [39]. This is shown by the dashed line in Supplementary Fig. 13, once again demonstrating that nuclear polarization must be close to unity in order to make a difference in terms of the central spin coherence.

The hyperfine shift experienced by the quantum dot exciton is linearly proportional to the nuclear spin polarization degree P_{N}:

$$E_{\mathrm{hf}} = \sum_j F^{(j)} I_j P_{\mathrm{N},j}, \tag{S20}$$

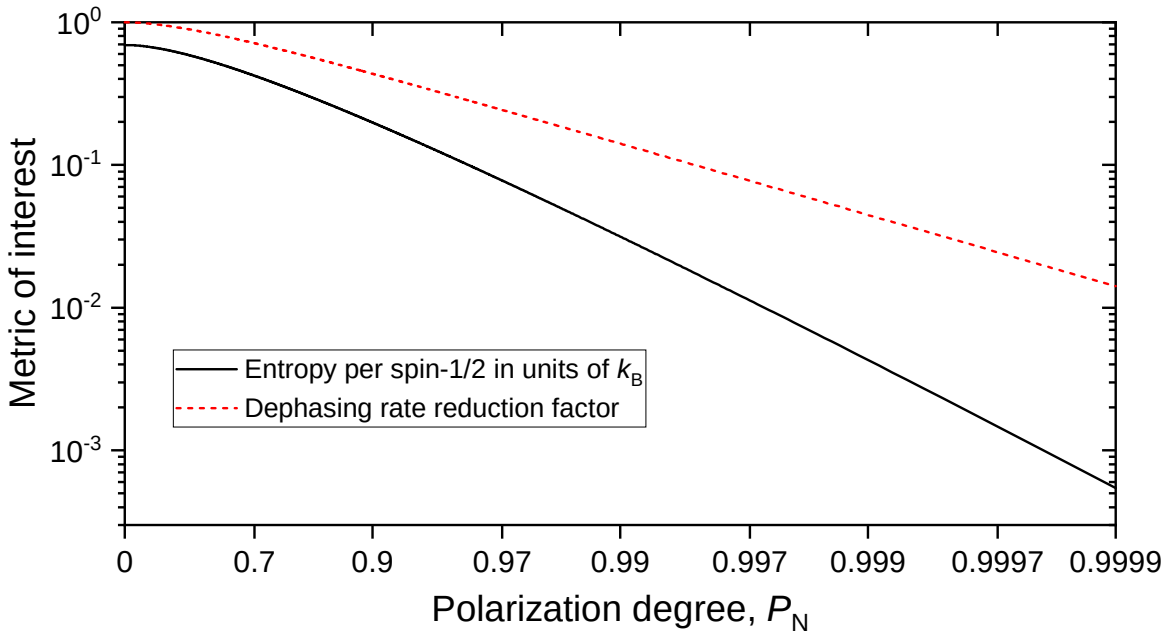

Supplementary Figure 13. **Nuclear spin ensemble properties as a function of nuclear spin polarization degree P_N.** Solid line shows entropy per nucleus of a nuclear spin ensemble. Dashed line shows the factor by which the dephasing time of an electron spin qubit is reduced, when its nuclear spin environment is polarized.

where the sum is over individual isotope species. Although the hyperfine shift E_{hf} can be measured accurately from the photoluminescence spectra, the proportionality factor $F^{(j)}$ depends not only on the material's hyperfine constants $A^{(j)}$, but also on the leakage of the electron wavefunction into the AlGaAs barrier. Since it is difficult to estimate this leakage independently, the measurement of E_{hf} alone is not suitable for accurate derivation of P_N. The unknown proportionality factor between E_{hf} and P_N can be eliminated for $I > 1/2$ nuclei, provided that it is possible to address selectively the magnetic dipole transitions between states with spin projections m and $m+1$. For example, if a long radiofrequency (Rf) pulse is applied to saturate the $m \leftrightarrow m+1$ NMR transition, it equalizes the populations of these states. The resulting final population probabilities p_m, p_{m+1} both equal the average $(p_m + p_{m+1})/2$ of their initial populations. For an ideal selective NMR Rf excitation the population probabilities of all other nuclear spin states remain unchanged.

One can then substitute Supplementary Eq. S16 into Supplementary Eq. S20 to calculate the change in the optically detected hyperfine shift ΔE_{hf} resulting from selective saturation of a single NMR transition $m \leftrightarrow m+1$. For example, for $+1/2 \leftrightarrow +3/2$ of the j-th isotope, we calculate $\Delta E_{hf}^{+1/2 \leftrightarrow +3/2} = F^{(j)}\left[(+\frac{3}{2})\frac{p_{+3/2}+p_{+1/2}}{2} + (+\frac{1}{2})\frac{p_{+3/2}+p_{+1/2}}{2}\right] - F^{(j)}\left[(+\frac{3}{2})p_{+3/2} + (+\frac{1}{2})p_{+1/2}\right] =$

$-F^{(j)}(p_{+3/2}-p_{+1/2})/2$. This result has a simple interpretation that the hyperfine shift variation $\Delta E_{\rm hf}$ depends only on the difference in the initial populations of the states that are selectively saturated with Rf.

In the same manner, simultaneous selective saturation of the NMR transitions $m \leftrightarrow m+1$ and $m+1 \leftrightarrow m+2$ leads to complete averaging of the populations of the three involved spin states. Their final population probabilities become $p_m, p_{m+1}, p_{m+2} \to (p_m + p_{m+1} + p_{m+2})/3$. Saturation of all three NMR transitions of spin $I = 3/2$ nuclei leads to complete depolarization and equal populations of all four spin states $p_{-3/2} = p_{-1/2} = p_{+1/2} = p_{+3/2} = 1/4$. Using Supplementary Eqs. S16 and S20 we evaluate the changes in the hyperfine shift $\Delta E_{{\rm hf},j}$ arising from the j-th isotope, to arrive to the following results, derived previously in Ref. [13]:

$$\begin{aligned}
\Delta E_{{\rm hf},j}^{m\leftrightarrow m+1} &= -F^{(j)}(p_{m+1,j}-p_{m,j})/2 = -F^{(j)}\frac{e^{(m+1)\beta_j}-e^{m\beta_j}}{4\cosh(\beta_j/2)+4\cosh(3\beta_j/2)},\\
\Delta E_{{\rm hf},j}^{m\leftrightarrow m+2} &= -F^{(j)}(p_{m+2,j}-p_{m,j}) = -F^{(j)}e^{(m+1)\beta_j}\sinh(\beta_j/2)/\cosh(\beta_j),\\
\Delta E_{{\rm hf},j}^{-I\leftrightarrow +I} &= -F^{(j)}P_{{\rm N},j}I_j = -F^{(j)}[3/2+1/\cosh(\beta_j)]\tanh(\beta_j/2).
\end{aligned} \tag{S21}$$

The last expression in each of these equations is obtained by substituting the Boltzmann distribution (Supplementary Eq. S14) for spin $I = 3/2$.

B. Corrections for the nuclei with small or inverted quadrupolar shifts

For a fully resolved NMR triplet, Supplementary Eq. S21 is sufficient to extract the inverse temperatures β_j and derive the polarization degree of the spin-3/2 nuclei. In a real semiconductor system the separation of the quadrupolar NMR components is not perfect. Here we examine the role that the nuclei with small or inverted quadrupolar shift $\nu_{\rm Q}$ have on the derivation of nuclear spin polarization from experimental data. The case of an experiment where a radiofrequency comb is used to saturate two out of three NMR transitions is considered in Supplementary Fig. 14. For unstrained GaAs, nuclear quadrupolar effects are absent ($\nu_{\rm Q} = 0$) and all NMR transitions of the spin-3/2 nucleus appear at the same Larmor frequency $\nu_{\rm L}$. Strain induces quadrupolar effects which are characterized to first order by the shift $\nu_{\rm Q}$. In all our experiments $|\nu_{\rm Q}| \ll |\nu_{\rm L}|$, so that first-order approximation is valid. The central transition $-1/2 \leftrightarrow +1/2$ between nuclear states with spin projections $m = \pm 1/2$ is unaffected by quadrupolar shifts in the first order, hence its NMR frequency is $\nu_{\rm L}$ for all nuclei (vertical solid line in Supplementary Fig. 14). The satellite transitions are affected by quadrupolar shifts: the NMR frequency of the $-3/2 \leftrightarrow -1/2$ transition is $\nu_{\rm L} + \nu_{\rm Q}$, whereas the NMR frequency of the $+1/2 \leftrightarrow +3/2$ transition is $\nu_{\rm L} - \nu_{\rm Q}$ (solid lines in

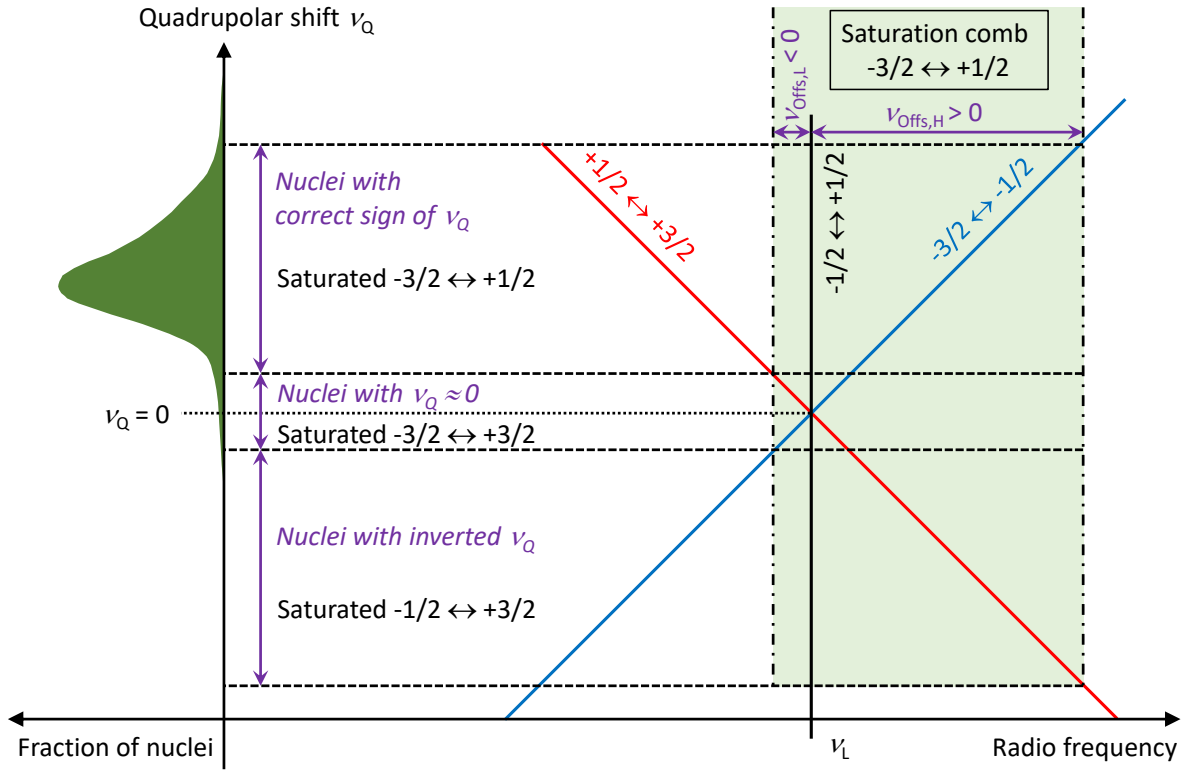

Supplementary Figure 14. **Effect of the nuclei with different quadrupolar shifts in a two-transition comb saturation measurement.**

Supplementary Fig. 14 with slopes +1 and −1, respectively).

The strain varies within the QD volume, so there is a statistical distribution of ν_Q values within the ensemble of the nuclei (sketched in the left part of Supplementary Fig. 14). The majority of the ^{75}As nuclei have a positive quadrupolar shift $\nu_Q > 0$ (for Ga nuclei the shift is predominantly negative $\nu_Q < 0$). Therefore, if we want to saturate simultaneously the two NMR transitions $-3/2 \leftrightarrow -1/2$ and $-1/2 \leftrightarrow +1/2$ (labelled $-3/2 \leftrightarrow +1/2$ for brevity) we choose a radiofrequency comb band sketched by the shaded area in Supplementary Fig. 14. The low-offset edge of the band at frequency $\nu_L + \nu_{Offs,L}$ (with negative $\nu_{Offs,L} < 0$) is tuned just below the Larmor frequency, in order to saturate the narrow $-1/2 \leftrightarrow +1/2$ transition. The high-offset edge of the band $\nu_L + \nu_{Offs,H}$ (with positive $\nu_{Offs,H} > 0$) is chosen to be far enough from the Larmor frequency to cover the $-3/2 \leftrightarrow -1/2$ satellite transition for most nuclei. The typical values in two-transition comb saturation experiments are $\nu_{Offs,L} = -5$ kHz, $\nu_{Offs,H} = +178$ kHz for ^{75}As and $\nu_{Offs,L} = +5$ kHz, $\nu_{Offs,H} = -80$ kHz for ^{69}Ga. For the $-1/2 \leftrightarrow +3/2$ two-transition saturation the values of $\nu_{Offs,L}$ and $\nu_{Offs,H}$ are inverted.

As can be seen in Supplementary Fig. 14 the nominal $-3/2 \leftrightarrow +1/2$ comb saturates the desired

transitions for the majority of nuclei, which have $-\nu_{\mathrm{Offs,L}} < \nu_{\mathrm{Q}} < \nu_{\mathrm{Offs,H}}$ (note that the lower bound $-\nu_{\mathrm{Offs,L}}$ is positive for a negative $\nu_{\mathrm{Offs,L}} < 0$). These nuclei give a correct contribution to the Rf-induced hyperfine shifts. But there are also several cases, where nuclei give contributions that differ from those intended. For a fraction of nuclei with small quadrupolar shifts $\nu_{\mathrm{Offs,L}} < \nu_{\mathrm{Q}} < -\nu_{\mathrm{Offs,L}}$ all three NMR transitions are excited by the comb, resulting in full depolarization of such nuclei. Furthermore, for those ^{75}As nuclei where quadrupolar shift is inverted $-\nu_{\mathrm{Offs,H}} < \nu_{\mathrm{Q}} < \nu_{\mathrm{Offs,L}}$, the $-3/2 \leftrightarrow -1/2$ transition will be out of resonance with the Rf band, while the $+1/2 \leftrightarrow +3/2$ transition will be saturated. Such nuclei will produce hyperfine shifts that would correspond to the $-1/2 \leftrightarrow +3/2$ two-transition saturation, rather than the intended $-3/2 \leftrightarrow +1/2$ saturation. Finally, for a small fraction of nuclei with very large absolute quadrupolar shifts $|\nu_{\mathrm{Q}}| > |\nu_{\mathrm{Offs,H}}|$, only the central $-1/2 \leftrightarrow +1/2$ transition will be saturated. Thus, introducing the empirical coefficients c, the observed hyperfine shift $\Delta E_{\mathrm{hf,Obs}}^{-3/2\leftrightarrow+1/2}$ in the $-3/2 \leftrightarrow +1/2$ two-transition saturation experiment can be written as:

$$\begin{aligned}\Delta E_{\mathrm{hf,Obs}}^{-3/2\leftrightarrow+1/2} &= c_{\mathrm{Sat,Ideal}}\Delta E_{\mathrm{hf}}^{-3/2\leftrightarrow+1/2}+ \\ &+ c_{\mathrm{Sat,Full}}\Delta E_{\mathrm{hf}}^{-3/2\leftrightarrow+3/2} + c_{\mathrm{Sat,Inv}}\Delta E_{\mathrm{hf}}^{-1/2\leftrightarrow+3/2} + c_{\mathrm{Sat,CT}}\Delta E_{\mathrm{hf}}^{-1/2\leftrightarrow+1/2},\end{aligned} \tag{S22}$$

where we have dropped the isotope index. If the quadrupolar NMR triplet is fully resolved, then $c_{\mathrm{Sat,Ideal}} = 1$ with all other c coefficient equal to zero. In a real quantum dot $c_{\mathrm{Sat,Ideal}} < 1$ and the remaining coefficients are non-zero, so that the observed hyperfine shift $\Delta E_{\mathrm{hf,Obs}}^{-3/2\leftrightarrow+1/2}$ deviates from the ideal $\Delta E_{\mathrm{hf}}^{-3/2\leftrightarrow+1/2}$. For example, if all nuclei are in a $m = +3/2$ state (that is $P_{\mathrm{N}} = +1$), the expected ideal is $\Delta E_{\mathrm{hf}}^{-3/2\leftrightarrow+1/2} = 0$. In reality, due to the non-zero contributions of the fully-saturated nuclei ($c_{\mathrm{Sat,Full}} > 0$) and the nuclei with an inverted quadrupolar shift ($c_{\mathrm{Sat,Inv}} > 0$) the observed hyperfine shift $\Delta E_{\mathrm{hf,Obs}}^{-3/2\leftrightarrow+1/2}$ is non-zero even if nuclei are fully polarized.

The expression for the hyperfine shift in the other two-transition experiment $\Delta E_{\mathrm{hf,Obs}}^{-1/2\leftrightarrow+3/2}$ can be obtained from Supplementary Eq. S22 by changing the sings of all the m indices. It is worth noting that in the experiment with intentional saturation of all three-transitions ($-3/2 \leftrightarrow +3/2$) all nuclei get fully depolarized as long as the satellite transitions fit within the Rf band. In the three-transition experiments we use frequency combs with total widths of 347 kHz (^{69}Ga) and 578 kHz (^{75}As), centred at the Larmor frequency ν_{L}. These widths are sufficient for complete depolarization of essentially all the nuclei of the quantum dot and the surrounding barriers. Therefore, the three-transition non-selective saturation measurement is expected to be more robust than the selective two-transition Rf depolarization.

Similar analysis applies to selective Rf excitation of a single NMR transition (Supplementary

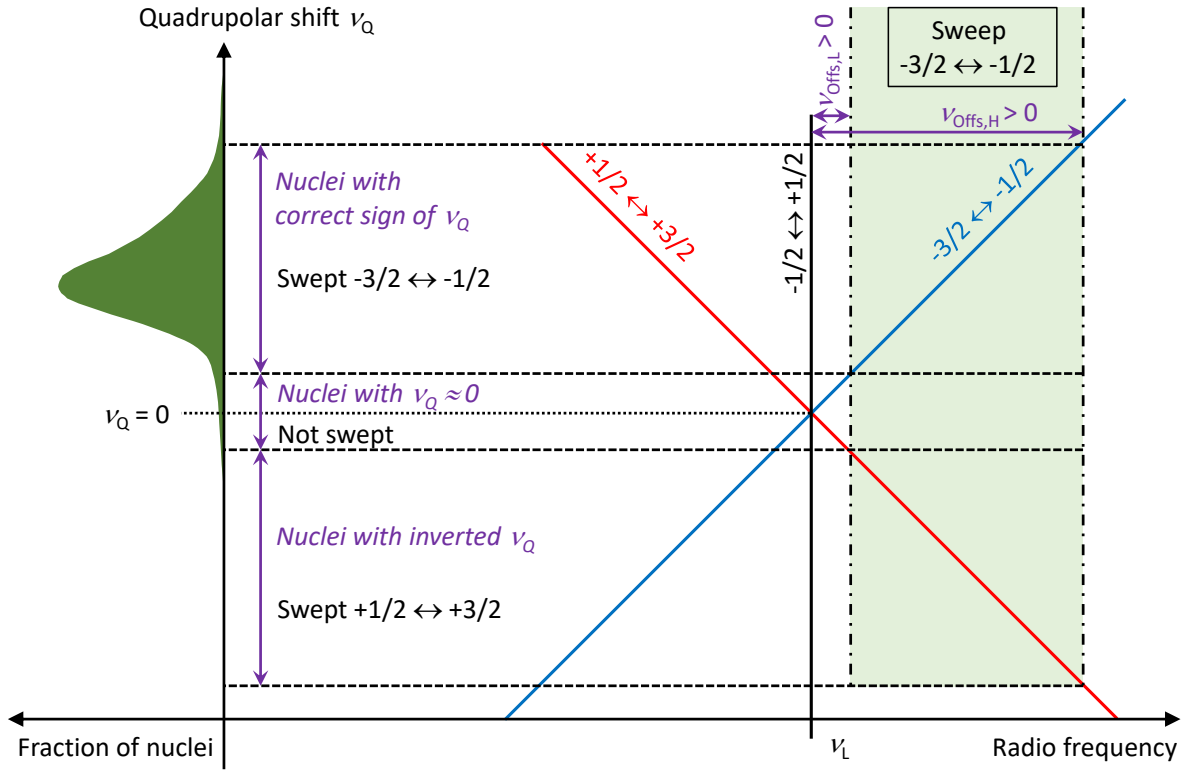

Supplementary Figure 15. **Effect of the nuclei with different quadrupolar shifts in a single-transition adiabatic inversion measurement.**

Fig. 15. Here, rather than saturating the NMR resonance we perform a radiofrequency sweep, which adiabatically inverts the populations of the chosen pair of spin states. Adiabatic sweep has the advantage of doubling the hyperfine shift compared to saturation – this simple relation holds only if a single NMR transition is excited. By contrast, for an adiabatic sweep over multiple quadrupolar NMR transitions the result is more complicated, making comb saturation preferable for two-transition and three-transition NMR excitation. The radiofrequency is always swept in the direction away from the central NMR transition, starting at $\nu_L + \nu_{Offs,L}$ and ending at $\nu_L + \nu_{Offs,H}$. The amplitude and the sweep rate are derived from calibration measurements discussed in Supplementary Note 5 D. For adiabatic sweeping of the $-3/2 \leftrightarrow -1/2$ transition we use $\nu_{Offs,L} = +8$ kHz, $\nu_{Offs,H} = +180$ kHz for ^{75}As and $\nu_{Offs,L} = -5$ kHz, $\nu_{Offs,H} = -50$ kHz for ^{69}Ga. For the sweep over the $+1/2 \leftrightarrow +3/2$ transition the values of $\nu_{Offs,L}$ and $\nu_{Offs,H}$ are inverted. The $-3/2 \leftrightarrow -1/2$ sweep works as designed for the majority of nuclei with $\nu_{Offs,L} < \nu_Q < \nu_{Offs,H}$ (note that both $\nu_{Offs,L}$ and $\nu_{Offs,H}$ are positive in this example). For the small number of nuclei with $-\nu_{Offs,H} < \nu_Q < -\nu_{Offs,L}$ the nominal $-3/2 \leftrightarrow -1/2$ sweep results in an adiabatic inversion of the $+1/2 \leftrightarrow +3/2$ transition instead. The remaining nuclei with $|\nu_Q| < |\nu_{Offs,L}|$ or $|\nu_Q| > |\nu_{Offs,H}|$ are

not affected by the Rf sweep. Thus the observed hyperfine shift $\Delta E_{\mathrm{hf,Obs}}^{-3/2\leftrightarrow-1/2}$ in the $-3/2 \leftrightarrow -1/2$ single-transition sweep experiment can be written as:

$$\Delta E_{\mathrm{hf,Obs}}^{-3/2\leftrightarrow-1/2} = 2\left(c_{\mathrm{Swp,Ideal}}\Delta E_{\mathrm{hf}}^{-3/2\leftrightarrow-1/2} + c_{\mathrm{Swp,Inv}}\Delta E_{\mathrm{hf}}^{+1/2\leftrightarrow+3/2}\right) \tag{S23}$$

An important property of the single-transition selective excitation is that the nuclei with small absolute quadrupolar shifts ν_{Q} are eliminated from the measured hyperfine shifts. This is preferred over the two-transition saturation measurement, where such nuclei are fully depolarized, resulting in a parasitic hyperfine shift characterised by the $c_{\mathrm{Sat,Full}}$ coefficient in Supplementary Eq. S22.

C. NMR spectra of the QD nuclei

Supplementary Figs. 16a,b show typical nuclear magnetic resonance spectra measured on ^{75}As and ^{69}Ga nuclei in QD1. The three magnetic dipole transitions of each of the spin-3/2 isotopes are split due to the natural elastic strain within the quantum dot volume, arising most likely from the lattice mismatch between the GaAs QD and the AlGaAs barriers. Although the NMR triplet is well resolved, there is a few-percent overlap between the spectral components. When quantifying nuclear spin polarization degrees close to unity, such overlap must be taken into consideration. In order to quantify the spectral overlap, we study a piece of the same QD sample but subject to a uniaxial stress along the [110] crystallographic direction (i.e. the strain is applied perpendicular to the sample growth direction). Nuclear quadrupolar shifts induced by the external stress significantly exceed the intrinsic quadrupolar shifts. As a result the NMR triplet is fully resolved, as can be seen in the inverse NMR spectra of Supplementary Figs. 17a,b where we focus on the $-1/2 \leftrightarrow +1/2$ and $-3/2 \leftrightarrow -1/2$ transitions.

The spectral shapes of the $-3/2 \leftrightarrow -1/2$ satellites measured in a stressed QD sample are similar to those in the unstressed sample (Supplementary Fig. 16). The satellite lineshape consists mainly of an asymmetric peak, but also shows evidence of spectral wings that are broad enough to overlap with the $-1/2 \leftrightarrow +1/2$ central transition in an unstressed sample. In principle, the overlap can be derived by integrating the relevant part of the satellite lineshape, measured with inverse NMR and shown in Supplementary Figs. 17a,b. However, this approach is vulnerable to noise – it is more efficient to incorporate integration into the NMR spectroscopy method [40, 41]. Such an integral NMR measurement is performed by selectively saturating all nuclear spin transitions within a certain spectral band. The high-frequency edge of the saturating band (implemented as a frequency comb) is kept fixed. The low-frequency edge is scanned and the resulting change in

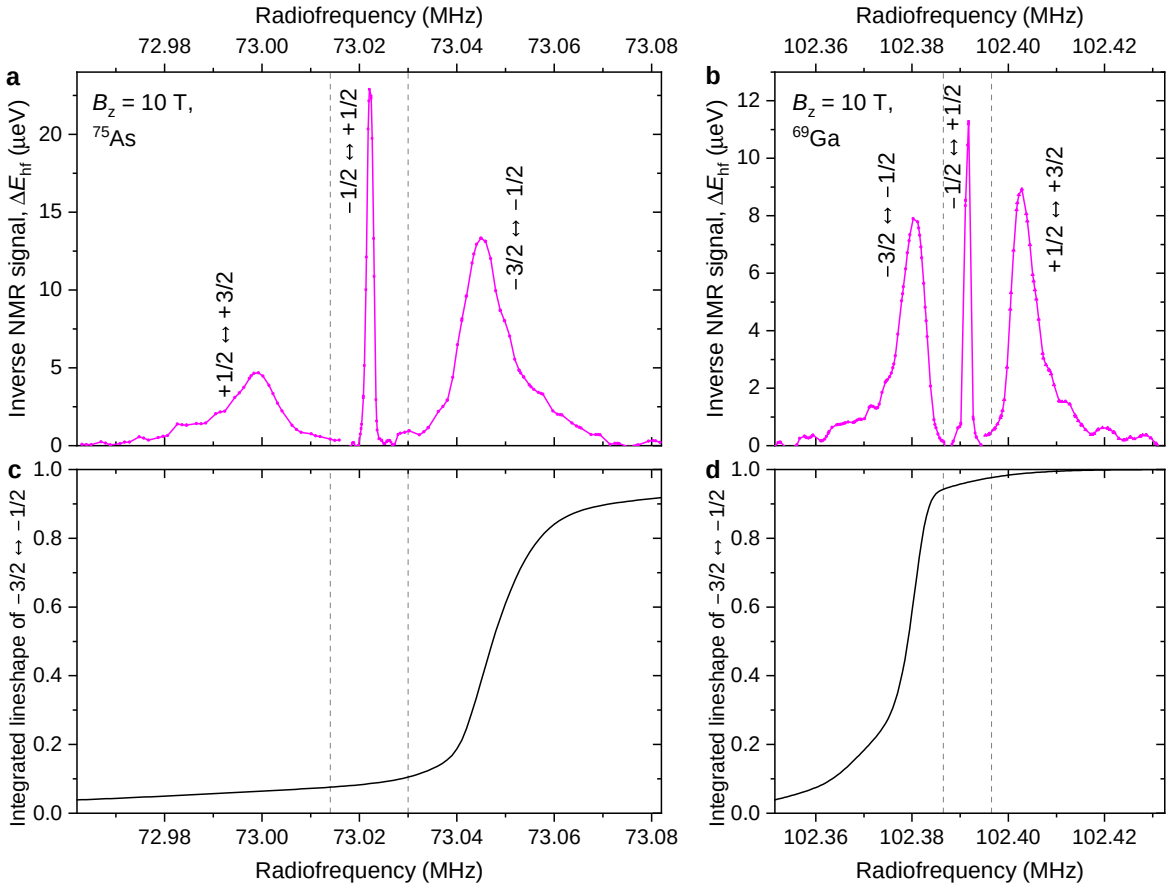

Supplementary Figure 16. **Nuclear magnetic resonance spectra of a single quantum dot. a,** Nuclear magnetic resonance spectra of the ^{75}As nuclei measured in QD1 at $B_z = 10$ T using the "inverse NMR" technique for signal enhancement [23]. The $-1/2 \leftrightarrow +1/2$ central transition is measured with a 2 kHz resolution, while the satellites $-3/2 \leftrightarrow -1/2$ and $+1/2 \leftrightarrow +3/2$ are measured with a 6 kHz resolution. Vertical dashed lines are offset from the central transition by ±8 kHz and indicate the starting points of the frequency sweeps over the satellite peaks. **b,** Same as (a) but for ^{69}Ga nuclei. The $-1/2 \leftrightarrow +1/2$ central transition is measured with a 2 kHz resolution, while the satellites are measured with a 4 kHz resolution. Vertical dashed lines are offset from the central transition by ±5 kHz. **c,** Integrated lineshape of the $-3/2 \leftrightarrow -1/2$ transition of ^{75}As, derived from experiments on a stressed piece of the same semiconductor QD sample. **d,** Same as (c) but for the $-3/2 \leftrightarrow -1/2$ transition of ^{69}Ga.

the hyperfine shift $\Delta E_{\rm hf}$ is measured. This dependence of $\Delta E_{\rm hf}$ reveals the fraction of the nuclei covered by the saturating Rf band, and therefore provides a scaled definite integral of the NMR lineshape. For ^{75}As nuclei the fixed-frequency edge of the Rf band is detuned by +500 kHz from the central transition to ensure that the entire $-3/2 \leftrightarrow -1/2$ transition can be covered. For ^{69}Ga nuclei the fixed-frequency edge of the Rf band is detuned by +230 kHz from the central transition,

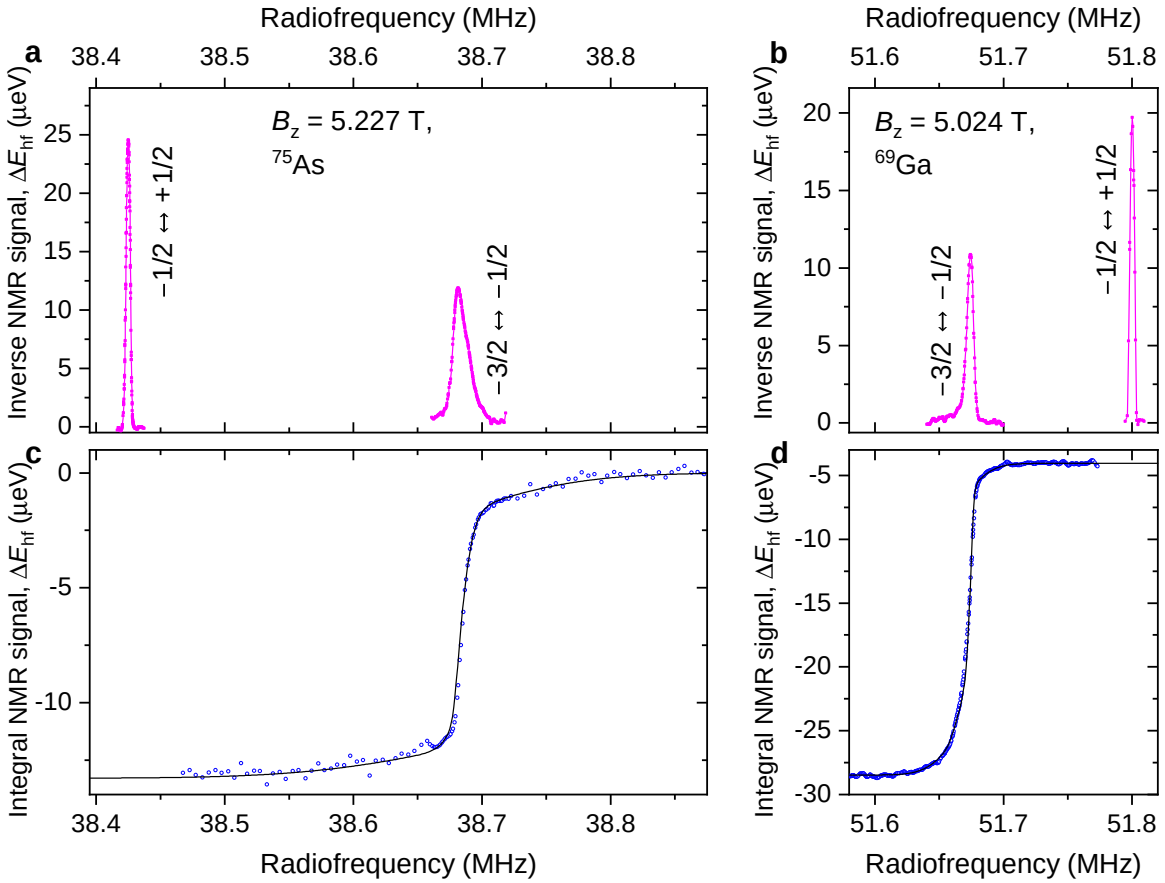

Supplementary Figure 17. **Nuclear magnetic resonance spectra of a quantum dot under external uniaxial stress. a,** Inverse NMR spectrum of ^{75}As at $B_z = 5.227$ T measured with a 4 kHz resolution. **b,** Inverse NMR spectrum of ^{69}Ga at $B_z = 5.024$ T measured with a 4 kHz resolution. **c,** Integral saturation NMR spectrum of ^{75}As measured (symbols) under the same condition as inverse NMR in (a). Line shows a smoothed fitted profile. **d,** Integral saturation NMR spectrum of ^{69}Ga measured under the same condition as inverse NMR in (b).

so that the entire $-1/2 \leftrightarrow +1/2$ and $+1/2 \leftrightarrow +3/2$ transitions are also included in the band, in order to amplify the integral NMR signal of the $-3/2 \leftrightarrow -1/2$ satellite.

Supplementary Fig. 17c shows the integral NMR spectrum of the $-3/2 \leftrightarrow -1/2$ transition of the ^{75}As nuclei in a stressed sample. The steepest rise in the integral signal matches the position of the sharp peak in the inverse NMR spectrum of Supplementary Fig. 17a. However, we also observe the slopes that stretch as far as $\approx \pm 150$ kHz from the satellite peak maximum, indicating the contribution of a broad NMR signal. Broad spectral features are also observed in Supplementary Fig. 17d for ^{69}Ga nuclei, though in a narrower spectral range and with an overall smaller contribution. This broad background can be ascribed to the NMR signal from AlGaAs

barriers or any Al atoms diffusing into the GaAs QD layer [41]. The Al atoms that randomly replace the Ga atoms distort the tetrahedral symmetry of the four nearest neighbours surrounding each As atom. The resulting unit-cell-scale strain results in pronounced quadrupolar shifts. By contrast, all Ga atoms have four identical As atoms as nearest neighbours. Therefore, Ga atoms are affected by Al/Ga random alloying only through next-nearest neighbours, explaining why the broad nuclear quadrupolar wings are smaller than for As nuclei.

Integral NMR spectra are processed in order to derive the correction coefficients. The experimental data is first smoothed (lines in Supplementary Figs. 17c,d) by fitting with a sum of three skew normal distribution peaks. The integral lineshapes are then normalized and shifted along the frequency scale to have the $-3/2 \leftrightarrow -1/2$ satellite NMR peaks in the stressed sample (Supplementary Figs. 17a,b) match the peak positions in the unstressed sample (Supplementary Figs. 16a,b). The resulting integrals of the $-3/2 \leftrightarrow -1/2$ lineshapes are shown by the solid lines in Supplementary Figs. 16c,d and are used to derive the c correction coefficients in Supplementary Eqs. S22, S23. For example, the vertical dashed lines in Supplementary Figs. 16a,b indicate the starting points of the frequency sweeps over the satellite peaks. The integral value at the lower starting point for ^{75}As is ≈ 0.07 and approximately corresponds to the fraction $c_{\mathrm{Swp,Inv}}$ of the nuclei where the $+1/2 \leftrightarrow +3/2$ satellite is swept instead of the intended $-3/2 \leftrightarrow -1/2$. The difference of the integral at the higher and lower sweep starting points gives approximately the fraction of nuclei (≈ 0.03) that are not swept at all. The summary of all the coefficients derived from the integrated lineshapes can be found in the following table:

Coefficient	^{75}As	^{69}Ga
$c_{\mathrm{Sat,Ideal}}$	0.8979	0.9424
$c_{\mathrm{Sat,Full}}$	0.0170	0.0341
$c_{\mathrm{Sat,Inv}}$	0.0750	0.0234
$c_{\mathrm{Sat,CT}}$	0.0100	0.0003
$c_{\mathrm{Swp,Ideal}}$	0.8893	0.9272
$c_{\mathrm{Swp,Inv}}$	0.0721	0.0234

(S24)

It can be seen that the contributions of the ideal signals are higher for the ^{69}Ga nuclei due to their smaller inhomogeneous quadrupolar broadening. As a result, nuclear spin polarization measurements are more accurate for ^{69}Ga than for ^{75}As. It is worth noting that the nuclear spin thermometry data measured on QDs in an unstrained sample is corrected with the c coefficients measured on a different individual QD (in a stressed sample). However, measurements conducted

on several individual QDs from the same sample reveal NMR spectra very similar to those shown Supplementary Fig. 16a,b. Thus, while there is always some uncertainty arising from dot-to-dot variation, its effect is expected to be smaller than the actual correction introduced through the c coefficients.

D. Calibration of the adiabatic radiofrequency sweeps

Supplementary Fig. 18 shows the dependence of the Rf-induced hyperfine shift on the frequency sweep rate. The amplitude of the Rf field is expressed in terms of the corresponding Rabi frequency ν_1. Supplementary Fig. 18a shows the results of an experiment where radiofrequency is swept from -50 kHz to $+50$ kHz around the ^{69}Ga Larmor frequency. This sweep range covers nearly the entire ^{69}Ga quadrupolar triplet. For a sufficiently large Rf amplitude $\nu_1 \gtrsim 1.64$ kHz and a sufficiently low rate the sweep is adiabatic, resulting in population transfer from the optically-populated $m = -3/2$ states into the $m = +3/2$ states. The variation of the hyperfine shift under adiabatic conditions is $\Delta E_{\rm hf} \approx 53$ μeV (dashed horizontal line). As expected [42], the sweep rate that produces adiabatic transfer increases quadratically with the Rf amplitude ν_1. When ν_1 is reduced below ≈ 1 kHz, the magnitude of the hyperfine shift $\Delta E_{\rm hf}$ in the slow-sweep limit decreases, indicating that population transfer becomes non-adiabatic. This non-adiabaticity is a result of demagnetization in the rotating frame, where Zeeman energy is transferred into the nuclear dipole-dipole interaction reservoir [10, 42, 43]. For all ν_1 the sweep also becomes non-adiabatic in the large-rate limit.

Supplementary Fig. 18b shows sweep rate dependence for the range starting from -5 kHz to -50 kHz, which selectively covers the $-3/2 \leftrightarrow -1/2$ satellite NMR transition (the starting points of the sweeps are shown by the dashed lines in Supplementary Fig. 16b). The adiabatic inversion of the subspace spanned by the $m = -1/2$ and $m = -3/2$ states results in a hyperfine shift of $\Delta E_{\rm hf} \approx 20$ μeV. Unlike for $-1/2 \leftrightarrow +1/2$, adiabaticity is achieved at a lower Rf amplitude $\nu_1 \gtrsim 0.27$ kHz. This is explained by the difference in the inhomogeneous broadening of the satellite transitions and the central transition $-1/2 \leftrightarrow +1/2$. In case of the $-1/2 \leftrightarrow +1/2$ transition (that is driven when the frequency is swept over the entire quadrupolar triplet) the inhomogeneous broadening is due to the second order quadrupolar shifts which are small compared to dipolar nuclear-nuclear interactions. By contrast, the first-order inhomogeneous quadrupolar broadening of the $-3/2 \leftrightarrow -1/2$ satellite ($\gtrsim 10$ kHz) is much larger than the dipole-dipole interaction. As a result the Zeeman and the dipolar energy reservoirs remain isolated during the sweep over the satellite, inhibiting the demagnetization. In other words, the Rf field sweeping over the broadened

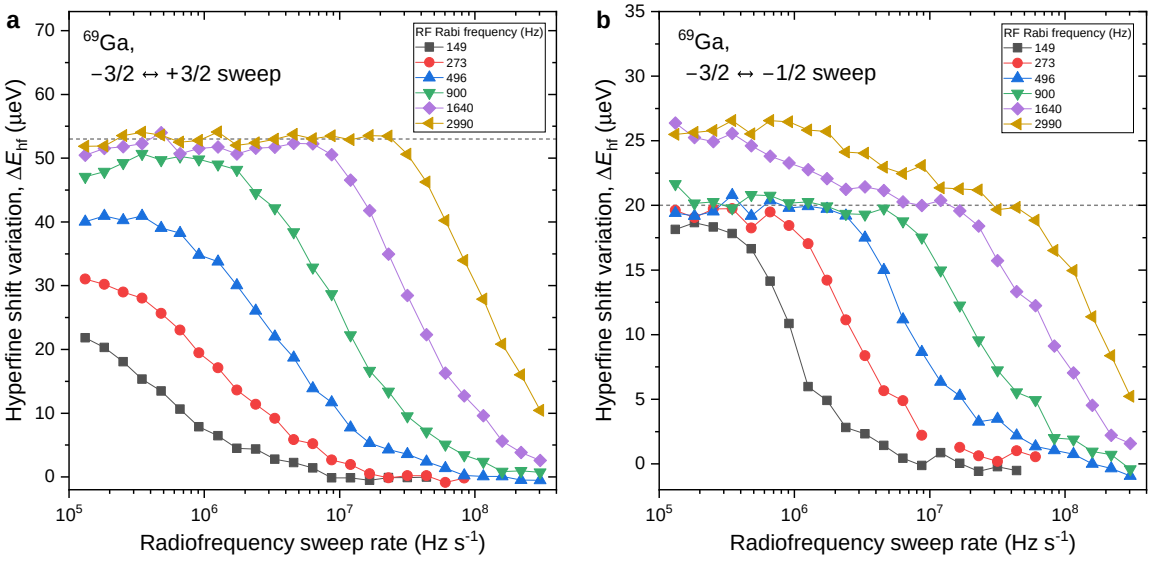

Supplementary Figure 18. **Calibration of the radiofrequency adiabatic sweeps. a,** In these experiments σ^+ optical pumping is first used to produce negative nuclear spin polarization. Optical pumping is followed by a frequency-swept Rf burst and the resulting hyperfine shift variation is plotted as a function of the frequency sweep rate. The radiofrequency field is swept from −50 kHz to +50 kHz with respect to the Larmor frequency of the ^{69}Ga nuclear spins. This range covers all three quadrupolar-split NMR transitions. Results are shown for several amplitudes of the radiofrequency field, expressed in terms of the Rabi frequency ν_1 that such a field produces when tuned in resonance with the satellite NMR transition $-3/2 \leftrightarrow -1/2$. Dashed horizontal line shows the hyperfine shift variation under adiabatic conditions. **b,** Same as (a), but the frequency range of the sweep is from −5 kHz to −50 kHz, covering only the satellite NMR transition $-3/2 \leftrightarrow -1/2$.

$-3/2 \leftrightarrow -1/2$ satellite excites only a small fraction of the nuclei at any given frequency, while the majority of the nuclear spins remain out of resonance and therefore cannot participate in the exchange between the Zeeman and dipolar reservoirs. When the Rf amplitude is increased ($\nu_1 \gtrsim 1.64$ kHz), the magnitude $|\Delta E_{\rm hf}|$ of the hyperfine shift increases further beyond the adiabatic-inversion level. This can be explained by the parasitic driving of the $-1/2 \leftrightarrow +1/2$ transition, which occurs when ν_1 becomes non-negligible compared to the minimal offset (−5 kHz from the $-1/2 \leftrightarrow +1/2$ frequency) during the sweep over the $-3/2 \leftrightarrow -1/2$ transition. Based on these calibrations, we use adiabatic frequency sweeps only on the $\pm 3/2 \leftrightarrow \pm 1/2$ satellites, avoiding any sweeps that involve the $-1/2 \leftrightarrow +1/2$ central transition. For the spin temperature measurements on ^{69}Ga we use $\nu_1 \approx 0.496$ kHz and a sweep rate of 1 MHz s^{-1}. From the data of Supplementary Fig. 18b this combination of parameters is seen to provide good adiabatic inversion of the satellite

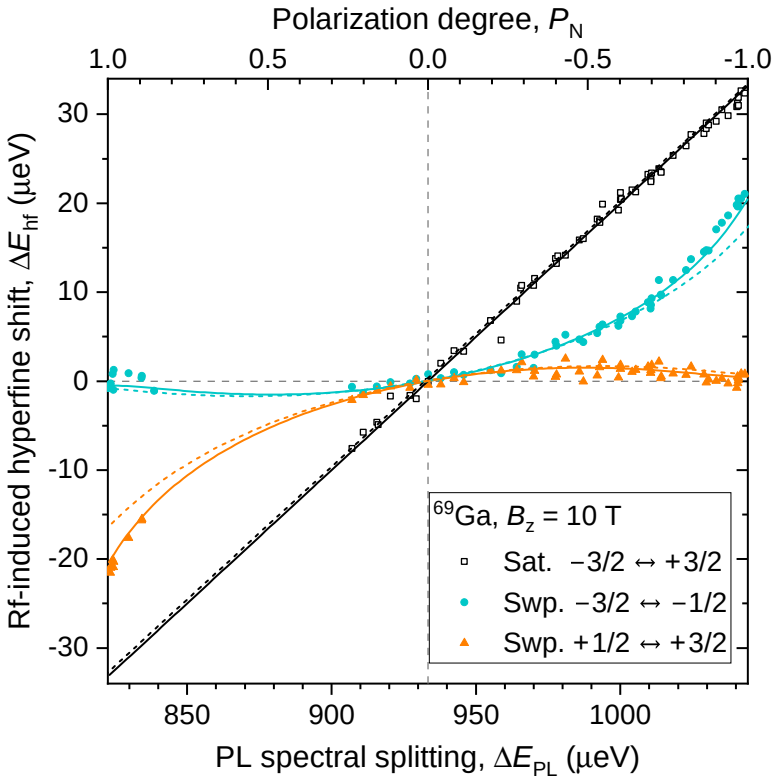

Supplementary Figure 19. **Derivation of nuclear spin polarization from selective NMR excitation.** Spectral splitting ΔE_{PL} of a QD negatively charge trion measured without Rf excitation is plotted on the bottom horizontal axis. Rf-induced hyperfine shift variation ΔE_{hf} is plotted on the vertical axis. Each point is obtained by changing the initial degree of the optically induced nuclear spin polarization and conducting two measurements: with selective Rf excitation and without Rf excitation. ΔE_{hf} is the difference of these two measurements. Several types of ^{69}Ga Rf excitation are employed: non-selective saturation of the entire NMR triplet (squares), adiabatic frequency sweep over the $-3/2 \leftrightarrow -1/2$ satellite (circles) and adiabatic frequency sweep over the $+1/2 \leftrightarrow +3/2$ satellite (triangles). Solid lines show the best fit, whereas dashed lines show a fit constrained by the $|P_{\mathrm{N}}| < 0.9$ hypothesis. The top horizontal scale shows the nuclear spin polarization degree P_{N} evaluated from the best fit. Experiments are conducted on an individual QD1 at $B_z = 10$ T.

transitions without any noticeable parasitic excitation of the central transition. Similar results were obtained from calibrations on the ^{75}As satellite transition resonance – the optimal Rf amplitude was found to be $\nu_1 \approx 0.560$ kHz, with a sweep rate of 0.8 MHz s^{-1}.

E. Model fitting for derivation of the nuclear spin polarization degree

The experimental measurement of the nuclear spin polarization (spin thermometry) uses the Pump-Rf-Probe cycle shown in Supplementary Fig. 3a. The variable parameter is the initial degree of nuclear spin polarization produced by the optical pumping. The steady-state nuclear spin polarization is changed either by detuning the pump laser wavelength away from the optimum or by altering the degree of circular polarization of the pump. For any given initial nuclear polarization the Pump-Rf-Probe measurements are carried out with different types of NMR Rf excitation or with no Rf pulse at all. The spectral splitting of the trion ΔE_{PL} detected in the probe pulse is then used as the horizontal axis for the data plots in Supplementary Fig. 19. On the vertical axis we plot the difference between the trion spectral splitting measured with the Rf pulse (final state) and without the Rf pulse (initial state). This difference yields the change in the hyperfine shift resulting purely from the selective Rf excitation of a certain NMR transition for a chosen isotope, whereas hyperfine shifts arising from other transitions and isotopes remain unaffected. In the experiment we avoid a certain range of positive initial nuclear spin polarizations (characterised by 850 μeV $< \Delta E_{\mathrm{PL}} <$ 900 μeV for QD1 at $B_{\mathrm{z}} = 10$ T) where electron spin energy splitting is close to zero due to the hyperfine shift and the Zeeman effect cancelling each other out. Such cancellation is characterised by accelerated nuclear spin dynamics (observed as a kink in Fig. 4a of the main text), making it difficult to perform non-perturbing optical probing. Therefore, in order to discuss the spin thermometry fitting, we focus on the negative nuclear polarizations, where most of the datapoints are collected (Supplementary Fig. 20).

The splitting in the photoluminescence spectrum of a negatively charged trion X^- (see Supplementary Fig. 2b) can be written as (see Supplementary Eq. S2):

$$\Delta E_{\mathrm{PL}} = \Delta E_{\mathrm{PL},0} - \sum_j F^{(j)} I_j P_{\mathrm{N},j}. \tag{S25}$$

where $\Delta E_{\mathrm{PL},0}$ is the trion splitting corresponding to depolarized nuclei and the summation goes over all isotope species with their individual polarization degrees $P_{\mathrm{N},j}$. The individual proportionality constants can be written as $F^{(j)} = k_j(A^{(j)} - C^{(j)})$, where both the electron ($A^{(j)}$) and the hole ($C^{(j)}$) hyperfine material constants are included since the photoluminescence of the trion is only observed for recombination of an electron and a hole with the opposite spin z projections (see Supplementary Note 2). The factors $0 < k_j \leq 1$ account for the Ga nuclei atoms replaced by Al, resulting in a reduced hyperfine shift experienced by the electron spin. If all $I = 3/2$ isotopes have

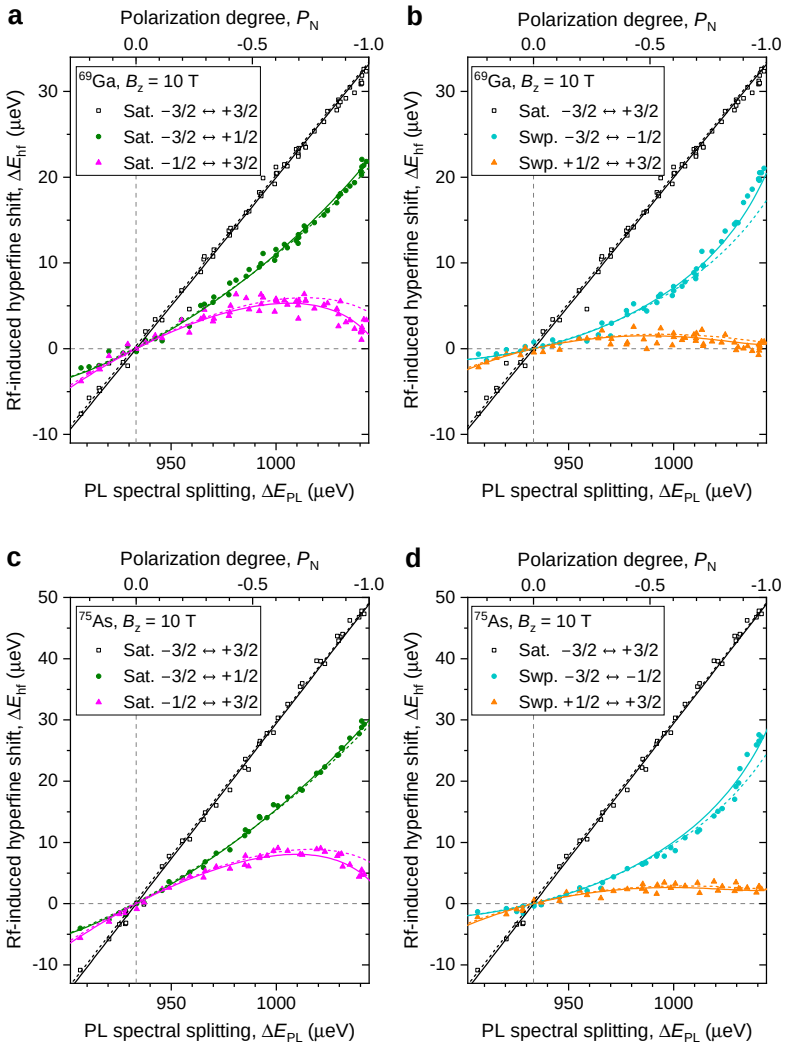

Supplementary Figure 20. **Derivation of nuclear spin polarization from selective NMR measurements.** Same as Supplementary Fig. 19, but focusing on the range of negative nuclear spin polarizations. **a,** Data and fits for ^{69}Ga nuclei. Hyperfine shift variations are shown for saturation of the entire NMR triplet (squares) and selective two-transition saturation (circles for $-3/2 \leftrightarrow +1/2$, triangles for $-1/2 \leftrightarrow +3/2$). **b,** Data for the non-selective saturation (same data as in (a), squares) and selective adiabatic frequency sweeps over NMR satellites (circles for $-3/2 \leftrightarrow -1/2$, triangles for $+1/2 \leftrightarrow +3/2$). **c, d,** Same as (a,b) but for ^{75}As nuclei.

the same polarization degree, Supplementary Eq. S25 simplifies to

$$\Delta E_{\mathrm{PL}} = \Delta E_{\mathrm{PL},0} - I P_{\mathrm{N}} \sum_j F^{(j)}. \tag{S26}$$

Resolving this for P_{N} and substituting into the last of Supplementary Eq. S21, we find that the change in the hyperfine shift (final minus initial) arising from the non-selective saturation of all

three NMR transitions of the j-th isotope is a linear function of the trion spectral splitting:

$$\begin{aligned}\Delta E_{\mathrm{hf},j}^{-I\leftrightarrow+I} &= (\Delta E_{\mathrm{PL}} - \Delta E_{\mathrm{PL},0})\frac{F^{(j)}}{F_{\mathrm{tot}}} = w_j(\Delta E_{\mathrm{PL}} - \Delta E_{\mathrm{PL},0}),\\ F_{\mathrm{tot}} &= \sum_j F^{(j)},\end{aligned} \tag{S27}$$

where w_j is the weight coefficient of the j-th isotope in the total hyperfine shift E_{hf}, and F_{tot} is the total proportionality factor. The measured $\Delta E_{\mathrm{hf},j}^{-I\leftrightarrow+I}$ are shown by the squares in Supplementary Figs. 20a,c for ^{75}As and ^{69}Ga, respectively. The dependence on ΔE_{PL} is indeed seen to be linear. For precise modelling we take the squared differences between the measured $\Delta E_{\mathrm{hf},j}^{-I\leftrightarrow+I}$ and $\Delta E_{\mathrm{hf},j}^{-I\leftrightarrow+I}$ computed from Supplementary Eq. S27 with spectral splitting ΔE_{PL} measured under the same optical pumping but without radiofrequency depolarization.

The same approach is applied to the hyperfine shift variations $\Delta E_{\mathrm{hf},j}^{m\leftrightarrow m+1}$ and $\Delta E_{\mathrm{hf},j}^{m\leftrightarrow m+2}$ arising from selective saturation (or adiabatic inversion) of one or two NMR transitions, respectively. Here, Supplementary Eq. S26 is first resolved to find P_{N} as a function of ΔE_{PL}, and P_{N} is then substituted into Supplementary Eq. S17 to find β. Since there is no explicit form for the inverse of the Brillouin function, this relation is kept in an exact analytical form using the Root[ ] function in Wolfram Mathematica 12.3 software. The inverse temperature β is then inserted into Supplementary Eqs. S21. Finally, the ideal $\Delta E_{\mathrm{hf},j}^{m\leftrightarrow m+1}$ and $\Delta E_{\mathrm{hf},j}^{m\leftrightarrow m+2}$ calculated in this way, are inserted into Supplementary Eqs. S22, S23 using the c coefficients from Supplementary Eq. S24 to account for the small spectral overlaps between the individual components of the quadrupolar NMR triplet. Taking these model hyperfine shifts at the experimentally measured ΔE_{PL}, we calculate the squared differences with respect to the measured Rf-induced hyperfine shifts (triangles and circles in Supplementary Figs. 20a,c for two-transition saturation and in Supplementary Figs. 20b,d for single-transition sweeps). We then sum up the squared differences for all individual Rf types and all isotopes to form the total χ^2 functional.

As a last step, we include in our model the possibility that different isotopes have different polarization degrees $P_{\mathrm{N},j}$. For arbitrary $P_{\mathrm{N},j}$ it is not possible to resolve the trion PL splitting ΔE_{PL} as a function of $P_{\mathrm{N},j}$, requiring some explicit assumptions. As a simplest approximation, we assume that polarization degrees of the three abundant spin-3/2 isotopes (^{75}As, ^{69}Ga and ^{71}Ga) are linearly interdependent. Mathematically, this is equivalent to allowing the total scaling factor F_{tot} to deviate for the different measured isotopes. The introduction of F_{tot} and w_j as model fitting parameters is also convenient in that the data does not have to be collected on all isotopes, in particular on ^{71}Ga, which has not be studied in this work.

The χ^2 is a function of only five fitting parameters: the zero-polarization trion splitting $\Delta E_{\mathrm{PL},0}$,

the total scaling factors F_{tot} of ^{75}As and ^{69}Ga as well as the weight coefficients w_j of ^{75}As and ^{69}Ga. In case of QD1, where the data was measured at two different magnetic fields, we fit these datasets independently in order to account for the different degree to which the probe laser pulse introduces parasitic depolarization in the optically measured hyperfine shifts. The best fits obtained by minimizing the χ^2 functional are plotted by the solid lines in Supplementary Fig. 20 and show a good match to the measured data. The best fit parameters are listed below together with the total number of experimental datapoints N_{data} and the root-mean-square (RMS) residual $R_{\mathrm{min}} = \sqrt{\chi^2_{\mathrm{min}}/N_{\mathrm{data}}}$ derived from the minimized functional value χ^2_{min}. In addition, we quote the residual R'_{min} obtained from a separate linear fit where only the three-transition saturation hyperfine shift $\Delta E^{-I\leftrightarrow+I}_{\mathrm{hf},j}$ is considered:

QD	B_{z}	$w(^{75}\mathrm{As})$	$w(^{69}\mathrm{Ga})$	$IF_{\mathrm{tot}}(^{75}\mathrm{As})$	$IF_{\mathrm{tot}}(^{69}\mathrm{Ga})$	N_{data}	R_{min}	R'_{min}
QD1	4 T	0.416	0.292	112.0 μeV	104.5 μeV	346	0.875 μeV	0.803 μeV
QD1	10 T	0.442	0.300	112.3 μeV	110.7 μeV	510	0.749 μeV	0.778 μeV
QD2	10 T	0.429	0.294	112.3 μeV	110.3 μeV	336	1.108 μeV	0.946 μeV
QD3	10 T	0.424	0.294	113.9 μeV	112.8 μeV	170	0.987 μeV	0.968 μeV

(S28)

As discussed above, the three-transition saturation experiment is the most robust against the errors arising from NMR spectral overlaps. Therefore, the RMS residual R'_{min} obtained from linear fitting of $\Delta E^{-I\leftrightarrow+I}_{\mathrm{hf},j}$ alone characterizes the true random measurement errors. These errors in the optically-detected hyperfine shifts originate mainly from the noise of the CCD detector used to collect the optical photoluminescence spectra of a single quantum dot. Any excess of R_{min} obtained from the nonlinear fit of the entire selective-NMR dataset over R'_{min} is an indicator of systematic deviation between the model and the data. According to the table of Supplementary Eq. S28 such excess is small, confirming the validity of the Boltzmann distribution model (Supplementary Eq. S14). The spread in the isotope-specific weights w_i, and the scaling factor F_{tot} is on the order of 1% for the $B_{\mathrm{z}} = 10$ T data collected from three individual quantum dots, affirming the systematic nature of these results. The fit of the $B_{\mathrm{z}} = 4$ T data shows the most deviation, which is explained by the need for shorter probe pulses T_{Probe}, resulting in more noisy photoluminescence spectra as well as larger systematic deviations arising from the probe-induced nuclear spin depolarization.

In order to derive the nuclear spin polarization degree, we use the highest and the lowest trion spectral splitting ΔE_{PL} detected without any radiofrequency manipulation in a separate measurement. For this measurement we use the timing diagram of Supplementary Fig. 3d, where we allow the nuclear spin polarization to build up over $T_{\mathrm{Buildup}} > 100$ s, giving a closer approach to the

steady state than what can be achieved in the NMR thermometry measurements (Supplementary Fig. 20), where the pumping time $T_{\mathrm{Pump}} \lesssim 30$ s is limited by the maximum duration of the CCD detector exposure. It is worth noting that this approach of using the separately measured steady-state ΔE_{PL} is the reason why we build our fitting model on relating the polarization degree P_{N} to spectral splitting ΔE_{PL} via Supplementary Eq. S25. Otherwise, ΔE_{PL} can be eliminated and polarization degree can be derived purely from the Rf-induced hyperfine shifts of Supplementary Eq. S21. The best fit value of $\Delta E_{\mathrm{PL},0}$ is subtracted from the steady state ΔE_{PL} to derive the lowest negative and the highest positive hyperfine shifts. For QD1 at $B_{\mathrm{z}} = 10$ T we find $E_{\mathrm{hf}} = -109.6$ μeV and $E_{\mathrm{hf}} = +112.3$ μeV. The latter number exceeds the best-fit product $IF_{\mathrm{tot}}(^{69}\mathrm{Ga})$ by $\approx 1\%$. By definition, the IF_{tot} product is the maximum $|E_{\mathrm{hf}}|$ corresponding to full polarization $P_{\mathrm{N}} = \pm 1$. The discrepancy with the measured E_{hf} reveals the scale of errors in the derived polarization degrees P_{N}, both due to the random noise in the raw data and any systematic inaccuracy of the fitting model.

F. Error analysis in model fitting of the nuclear spin polarization data

In order to systematically analyze the fitting errors we construct a multidimensional confidence region (Chapter 9 in Ref.[44]) defined as a collection of all points in the fitting parameter space for which

$$\chi^2 < (1 + Q(\gamma, n)/N_{\mathrm{data}})\chi^2_{\mathrm{min}}, \tag{S29}$$

where we have approximated the standard error in the experimental data by the RMS fit residual $R_{\mathrm{min}} = \sqrt{\chi^2_{\mathrm{min}}/N_{\mathrm{data}}}$. (Note that here we define χ^2 and χ^2_{min} as sums that are not normalized by the standard error.) We define $Q(\gamma, n)$ as a quantile of the χ^2-distribution with n parameters corresponding to the confidence level $1 - \gamma$. We use $1 - \gamma = 0.95$ where the relevant quantile is $Q(1 - 0.95, 5) \approx 11.07$. We implement a Monte-Carlo calculation, where the χ^2 sum is computed for a large number of random sets of the fitting parameters around the best-fit point. For each trial parameter set that satisfies Supplementary Eq. S29 we calculate the polarization degrees P_{N} from the maximum and minimum steady-state spectral splitting ΔE_{PL} measured with long $T_{\mathrm{Buildup}} > 100$ s. Finally, the confidence intervals are derived separately for the maximum positive and the minimum negative polarization degree as maximum and minimum P_{N} values from the random Monte-Carlo set, coerced to satisfy the condition $-1 \leq P_{\mathrm{N}} \leq 1$. The confidence intervals

are shown by the symbols in Fig. 3e of the main text and are tabulated below:

QD	B_z	max ^{75}As P_N	min ^{75}As P_N	max ^{69}Ga P_N	min ^{69}Ga P_N
QD1	4 T	$[0.890, 0.974]$	$[-0.989, -0.903]$	$[0.982, 1]$	$[-1, -0.998]$
QD1	10 T	$[0.969, 1]$	$[-0.994, -0.954]$	$[1, 1]$	$[-1, -0.984]$
QD2	10 T	$[0.956, 1]$	$[-1, -0.962]$	$[0.989, 1]$	$[-1, -0.998]$
QD3	10 T	$[0.954, 1]$	$[-1, -0.951]$	$[0.964, 1]$	$[-1, -0.959]$

(S30)

This systematic evaluation agrees with the rough estimates above, confirming that the accuracy of our P_N estimates is on the other of a few percent. The fit returns similar values for polarization degrees of ^{75}As and ^{69}Ga – this is expected for a spin pumping mechanism [13] where the inverse temperature β of each individual nucleus is independently equilibrated with the β of a spin-polarized electron. The somewhat wider confidence intervals of ^{75}As could be simply due to the larger overlaps of the NMR spectral components, making the fit less sensitive to P_N and more dependent on the accuracy of the c coefficients tabulated in Supplementary Eq. S24. The derived $|P_N|$ values are similarly high at $B_z = 4$ and 10 T, in a sense that their deviation from unity is comparable to the uncertainty of the estimate. For that reason, it is currently not possible to make any conclusion about the dependence of nuclear polarization on the external magnetic field, which is a point of interest for a follow up work.

In order to further evaluate the error estimates we approach the problem of data modelling from the opposite direction. Namely, we start with a hypothesis that the maximum absolute polarization degree $|P_N|$ is no more than a certain value < 1, and then evaluate how well our experimental data can be matched to this hypothesis. In order to demonstrate this approach, we constrain the fit to $|P_N| < 0.9$ and search for the fitting parameter combination that minimizes the χ^2 functional (using the same model as the one used to derive the unconstrained best fit). The resulting constrained best-fit is shown for QD1 by the dashed lines in Supplementary Fig. 20. There are visible systematic deviations from the measured data, already suggesting that the $|P_N| < 0.9$ hypothesis is inadequate, and the actual absolute polarization degree is well above 0.9. Quantitatively, the RMS residual from the fit of the $B_z = 10$ T datasets constrained to $|P_N| < 0.9$ is ≈ 1.73 μeV for QD1, ≈ 2.91 μeV for QD2 and ≈ 2.17 μeV for QD3. These residuals are a factor of $\gtrsim 2$ larger than the best-fit residuals tabulated in Supplementary Eq. S28 – statistically, such deviations are improbable for our datasets containing hundreds of datapoints. It then follows that the $|P_N| < 0.9$ hypothesis should be rejected, leading to a conclusion that polarization is in fact well above 0.9.

Next, we fit the same experimental data but without correcting for the overlaps of the NMR spectral components. This is equivalent to setting $c_{\mathrm{Sat,Ideal}} = c_{\mathrm{Swp,Ideal}} = 1$ with the remaining

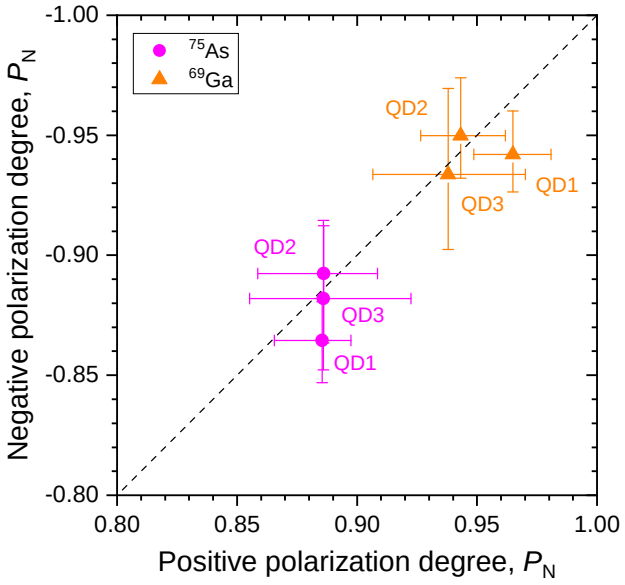

Supplementary Figure 21. **Nuclear spin polarization derived from an uncorrected fit.** Maximum positive (horizontal axis) and minimum negative (vertical axis) nuclear spin polarization degree P_N derived from the measurements on ^{75}As (circles) and ^{69}Ga (triangles) nuclei in individual dots QD1 - QD3. The P_N values in this plot are derived from a fit that ignores the small spectral overlaps between the NMR triplet components. Error bars are 95% confidence intervals.

c coefficients set to 0. Such a fit can be seen as a lower bound estimate for the absolute polarization degree $|P_N|$. Without correction, the RMS fit residual slightly increases from 0.749 μeV to 0.819 μeV for QD1 at $B_z = 10$ T. The resulting uncorrected P_N are shown in Supplementary Fig. 21. The uncorrected polarization degrees for ^{75}As ($P_N \approx 0.88$) are lower than for ^{69}Ga ($P_N \approx 0.94$), contradicting the expectation of equal β across different isotopes. Moreover, the maximum uncorrected $|P_N|$ are very close to the corresponding $c_{Sat,Ideal}$ coefficients. Additional computations confirm that this is to be expected – a naive uncorrected fit of the data affected by NMR spectral overlap returns for fully polarized nuclei a reduced polarization $|P_N|$ which roughly equals the fraction of the "ideal" nuclei that are not affected by the overlap. Nevertheless, even without the corrections, a high polarization degree is derived for ^{69}Ga nuclei, since they are less prone to NMR spectral overlaps than ^{75}As.

Finally, we discuss the different possible sources of systematic errors. Since electron localization in a GaAs quantum dot is not infinitely strong, the electron wavefunction leaks into the AlGaAs barriers where it gradually decays with the increasing distance from the dot. This means that both the nuclear spin pumping efficiency and the sensitivity of the electron hyperfine shift to nuclear

spin polarization are spatially inhomogeneous. The resulting steady-state nuclear spin polarization is also spatially inhomogeneous, if only because the QD layer is sandwiched between the two doped semiconductor layers, where free charge carriers result in $P_N \approx 0$. On the other hand, when considering spins as a quantum resource, a significant role is played only by the nuclei within the QD electron wavefunction. Recent studies of nuclear spin relaxation in the same sample have shown that spin diffusion is the dominant mechanism of nuclear spin decay in a QD [15]. The nuclear spins at the center of the QD are quickly polarized by the optically-pumped electron spin and then transfer their polarization to more distant nuclei via nuclear spin flip-flops. For a sufficiently long pumping the nuclei in the AlGaAs barriers around the dot become gradually polarized. This manifests in a slow-down of the subsequent relaxation without the pump. The relaxation times of the nuclear spins are on the order of hundreds of seconds, much longer than the nuclear spin buildup times, which are less than one second. Such a large ratio of the timescales suggests that competition between spin pumping and polarization leakage would not be a limiting factor for achieving $|P_N|$ up to ≈ 0.99. Moreover, relaxation much slower than pumping means that spin diffusion creates a smooth spatial profile of the nuclear spin polarization – the extent of the polarized volume is larger than the volume of the electron wavefunction. Therefore, we expect that the electron probes a volume with a nearly uniform nuclear spin polarization degree P_N. In other words, the existence of spin diffusion combined with long nuclear spin pumping means that there is no realistic mechanism that would result in abrupt spatial variations of P_N. Under these conditions the selective-NMR thermometry measurements return the average of nuclear polarization, weighted by the electron envelope wavefunction density. Then, observation of a near-unity average polarization itself implies that polarization is very homogeneous for all nuclei within the electron wavefunction volume. For example, if we take the typical leakage of the electron wavefunction into the AlGaAs barriers at ≈ 0.1 (estimated previously in Ref. [13]) and assume full polarization within the GaAs layer ($|P_N| = 1$), then observation of a weighted average of $|P_N| = 0.99$ implies that polarization within the AlGaAs barriers cannot be much smaller than $|P_N| = 0.9$. To summarize, although our present technique is not capable of revealing the spatial profile of the nuclear spin polarization, the most plausible hypothesis is that nuclear spin polarization achieved under steady-state optical pumping is nearly uniform within the volume of the QD electron wavefunction. In practice, this implies the ability to polarize nearly all nuclei whose coupling to the electron is strong enough to have any relevance to electron-nuclear coherent spin dynamics [14]. This also justifies our model, which assumes P_N to be constant within the quantum dot volume and its surrounding. From the ratio of the nuclear spin buildup and decay times we estimate the errors caused by P_N inhomogeneity to

be on the order of 1%.

Although ^{75}As, ^{69}Ga and ^{71}Ga are the three abundant isotopes, the inevitable penetration of the electron into the AlGaAs barriers implies some hyperfine interaction with the spin-5/2 ^{27}Al nuclei. And yet it turns out that ^{27}Al hyperfine shift is too small to be studied quantitatively with our present spin thermometry techniques. As it has been shown previously [13], this is a combined effect of several factors. The small fraction of the wavefunction overlapping with AlGaAs (≈ 0.1), the small fraction of Al atoms (0.33 in our sample) and the small hyperfine constant (≈ 0.3 of that of As and Ga) mean that the ^{27}Al relative contribution to the total electron hyperfine shift is within $\approx 1\%$. In addition to that, the lack of Al at the center of the QD, where the overlap with the electron is the strongest, suggests inhibition of the pumping-through-diffusion mechanism discussed above. The ^{27}Al spins can only be polarized through direct (and weak) contact with the spin-polarized electron, meaning that aluminium polarization can be reduced. In the context of the present work where we focus on polarization of As and Ga, these observations mean that any systematic errors arising from ^{27}Al are small (within $\approx 1\%$). Investigation of ^{27}Al spin polarization would be an interesting subject for future work – this would require more sensitive experimental techniques, such as trigger detection via abundant isotopes [36].

Summarising this analysis, we see that there is a handful of potential error sources, both random and systematic, but all on the order of 1%. Taking a conservative approach we conclude with confidence that nuclear spin polarization degrees well above 0.95 are achieved. In reality, the polarization is likely to be higher, with rigorous confidence-interval analysis returning polarization degrees as high as $|P_\mathrm{N}| \approx 0.99$ (for ^{69}Ga at high magnetic field $B_\mathrm{z} = 10$ T in all three selected individual quantum dots). Achieving even higher polarizations would depend critically on development of more sensitive thermometry techniques. One possibility is to use the dephasing dynamics of the electron spin qubit, since this would gain sensitivity at high polarizations as $\propto 1/\sqrt{1-P_\mathrm{N}^2}$ (Ref. [39]).

Supplementary Note 6. RAW DATA

Raw data is provided in text files using a tab-separated format.

Photoluminescence (PL) spectra (Figs. 2a,b of the main text) are tabulated in files `Fig2a.tsv` and `Fig2b.tsv`, respectively. Each file is a matrix of the measured PL intensity values. There are 787 rows, each row corresponding to a fixed sample gate bias V_Gate. The bias changes linearly from $V_\mathrm{Gate} = +1.43$ V for the first row, to $V_\mathrm{Gate} = -2.5$ V for the last row. There are 1617

columns, each column corresponding to a fixed PL energy E_{PL}. The energy changes linearly from $E_{\mathrm{PL}} = 1.4995$ eV for the first column, to $E_{\mathrm{PL}} = 1.83961$ eV for the last column.

The file `EhfPumpDep(sigma+).txt` contains the data for the dependence of the hyperfine shift E_{hf} on the optical pumping parameters. The data is for σ^+ optical pumping. Each line represents a measurement datapoint. The first column is the sample bias V_{Pump} during the optical pumping in V. The second column is the measured optical pump power P_{Pump} in μW. The third column is the measured optical pump photon energy E_{Pump} in eV. The fourth column is the measured QD hyperfine shift E_{hf} in μeV. This dataset is used to generate subsets of data, such as shown in Fig. 2c of the main text, Supplementary Fig. 4, Supplementary Figs. 8c,d, Supplementary Fig. 10c.

The data of the nuclear spin temperature measurements can be found in several files named `SpinT(QDn,Isotope,Bz=x).txt`, where "QDn" in the filename is the label of the individual quantum dot between QD1 and QD3, "Isotope" is either ^{69}Ga or ^{75}As, and "Bz=x" gives the numeric value x of the static magnetic field, which is either 4 or 10 T. Each file consists of pairs of columns of data. For each pair, the first column is the measured value, while the second column is half of the confidence interval for this value. All data values are in μeV. The column header labels the type of the measurement, which is "NoRf" for a measurement without any radiofrequency excitation, "Comb" for a selective frequency comb saturation, "Swp" for an adiabatic sweep measurement. For the last two types, the type of the measurement is followed by a list of the NMR transitions that are excited by the radiofrequency. The list is given in curly brackets {}, and can include "CT" for the central transition $-1/2 \leftrightarrow +1/2$ and "STL"("STH") for the low-frequency (high-frequency) quadrupolar satellite transition. For ^{69}Ga, the low-frequency satellite corresponds to the $-3/2 \leftrightarrow +1/2$ NMR transition, while for ^{75}As it corresponds to the $+1/2 \leftrightarrow +3/2$ NMR transition. These datasets are used to generate subsets of data, such as shown in Fig. 3d of the main text, Supplementary Fig. 19, and Supplementary Fig. 20.

The data for the maximum positive and minimum negative hyperfine shifts shown for individual dots QD1 - QD12 in Fig. 3f of the main text can be found in file `Fig3f.txt`. Each line corresponds to an individual QD and all values are in μeV.

The data of the nuclear spin buildup dynamics (Fig. 4a of the main text) measured under σ^+ and σ^- optical pumping can be found in files `Fig4a(sigma+).txt` and `Fig4a(sigma+).txt`, respectively. The first column is the pumping time T_{Pump} in s, the second column is the hyperfine shift E_{hf} in μeV.

The data of the nuclear spin relaxation dynamics (Fig. 4b of the main text) can be found in file `Fig4b.txt`. The first column is the dark time T_{Dark} in s. The subsequent columns are the hyperfine

shift E_{hf} in μeV. Each column corresponds to a fixed duration of the second Rf pulse $T_{\mathrm{Rf,2}}$ used to control the degree of the initial nuclear spin polarization. The value of $T_{\mathrm{Rf,2}}$ in s is given in square brackets at the top of each column. Values that are missing for a particular combination of T_{Dark} and $T_{\mathrm{Rf,2}}$ are shown with "-".

Nuclear spin relaxation times $T_{1,\mathrm{N}}$ as a function of the initial hyperfine shift E_{hf} (Fig. 4c of the main text) can be found in files `Fig4c(QD2).txt` and `Fig4c(QD3).txt` for QD2 and QD3, respectively. The first column in each file is the initial E_{hf} in μeV, the second column is half the confidence interval of the initial E_{hf}, also in μeV. The third column is $T_{1,\mathrm{N}}$ in s, with its half confidence interval given in the fourth column.

The calibration data of the optical polarization of the pump (Supplementary Fig. 5) can be found in files `FigS5(sigma+).txt` and `FigS5(sigma-).txt` for optical pumping close to σ^+ and σ^-, respectively. The first column is the rotation angle of the half-wave plate in degrees, the second column is the hyperfine shift E_{hf} in μeV.

---

[1] A. Oshiyama and S. Ohnishi, DX center: Crossover of deep and shallow states in Si-doped $Al_xGa_{1-x}As$, Phys. Rev. B **33**, 4320 (1986).

[2] P. M. Mooney, Deep donor levels (DX centers) in III-V semiconductors, Journal of Applied Physics **67**, R1 (1990).

[3] L. Zhai, M. C. Löbl, G. N. Nguyen, J. Ritzmann, A. Javadi, C. Spinnler, A. D. Wieck, A. Ludwig, and R. J. Warburton, Low-noise GaAs quantum dots for quantum photonics, Nat. Commun. **11**, 4745 (2020).

[4] C. Heyn, A. Stemmann, T. Koppen, C. Strelow, T. Kipp, M. Grave, S. Mendach, and W. Hansen, Highly uniform and strain-free GaAs quantum dots fabricated by filling of self-assembled nanoholes, Appl. Phys. Lett. **94**, 183113 (2009).

[5] P. Atkinson, E. Zallo, and O. G. Schmidt, Independent wavelength and density control of uniform GaAs/AlGaAs quantum dots grown by infilling self-assembled nanoholes, J. Appl. Phys. **112**, 054303 (2012).

[6] B. Urbaszek, X. Marie, T. Amand, O. Krebs, P. Voisin, P. Maletinsky, A. Högele, and A. Imamoğlu, Nuclear spin physics in quantum dots: An optical investigation, Rev. Mod. Phys. **85**, 79 (2013).

[7] Y. El Khalifi, B. Gil, H. Mathieu, T. Fukunaga, and H. Nakashima, Dependence of the light-hole—heavy-hole splitting on layer thickness and substrate orientation in GaAs-(GaAl) As single quantum wells, Phys. Rev. B **39**, 13533 (1989).

[8] V. B. Timofeev, M. Bayer, A. Forchel, and M. Potemski, Mixing of excitonic states containing light and heavy holes in an isolated GaAs/AlGaAs quantum well in a magnetic field, Journal of Experimental

and Theoretical Physics Letters **64**, 57 (1996).

[9] E. A. Chekhovich, M. M. Glazov, A. B. Krysa, M. Hopkinson, P. Senellart, A. Lemaître, M. S. Skolnick, and A. I. Tartakovskii, Element-sensitive measurement of the hole-nuclear spin interaction in quantum dots, Nat. Phys. **9**, 74 (2013).

[10] C. P. Slichter, *Principles of Magnetic Resonance* (Springer, 1990).

[11] C. Bulutay, E. A. Chekhovich, and A. I. Tartakovskii, Nuclear magnetic resonance inverse spectra of InGaAs quantum dots: Atomistic level structural information, Phys. Rev. B **90**, 205425 (2014).

[12] Y. Huang, Y. Puttisong, S. Filippov, I. Buyanova, and W. Chen, Oblique nuclear quadrupole interaction in self-assembled structures based on semiconductor quantum dots, Phys. Rev. Appl. **14**, 044019 (2020).

[13] E. A. Chekhovich, A. Ulhaq, E. Zallo, F. Ding, O. G. Schmidt, and M. S. Skolnick, Measurement of the spin temperature of optically cooled nuclei and GaAs hyperfine constants in GaAs/AlGaAs quantum dots, Nat. Mater. **16**, 982 (2017).

[14] J. M. Taylor, C. M. Marcus, and M. D. Lukin, Long-lived memory for mesoscopic quantum bits, Phys. Rev. Lett. **90**, 206803 (2003).

[15] P. Millington-Hotze, S. Manna, S. F. Covre da Silva, A. Rastelli, and E. A. Chekhovich, Nuclear spin diffusion in the central spin system of a GaAs/AlGaAs quantum dot, Nature Communications **14**, 2677 (2023).

[16] D. Huber, B. U. Lehner, D. Csontosová, M. Reindl, S. Schuler, S. F. Covre da Silva, P. Klenovský, and A. Rastelli, Single-particle-picture breakdown in laterally weakly confining GaAs quantum dots, Phys. Rev. B **100**, 235425 (2019).

[17] X. Yuan, F. Weyhausen-Brinkmann, J. Martín-Sánchez, G. Piredda, V. Křápek, Y. Huo, H. Huang, C. Schimpf, O. G. Schmidt, J. Edlinger, G. Bester, R. Trotta, and A. Rastelli, Uniaxial stress flips the natural quantization axis of a quantum dot for integrated quantum photonics, Nat. Commun. **9**, 3058 (2018).

[18] Y. H. Huo, A. Rastelli, and O. G. Schmidt, Ultra-small excitonic fine structure splitting in highly symmetric quantum dots on GaAs (001) substrate, Appl. Phys. Lett. **102**, 152105 (2013).

[19] A. V. Koudinov, I. A. Akimov, Y. G. Kusrayev, and F. Henneberger, Optical and magnetic anisotropies of the hole states in Stranski-Krastanov quantum dots, Phys. Rev. B **70**, 241305 (2004).

[20] M. Gawełczyk, M. Syperek, A. Maryński, P. Mrowiński, L. Dusanowski, K. Gawarecki, J. Misiewicz, A. Somers, J. P. Reithmaier, S. Höfling, and G. Sek, Exciton lifetime and emission polarization dispersion in strongly in-plane asymmetric nanostructures, Phys. Rev. B **96**, 245425 (2017).

[21] A. M. Waeber, M. Hopkinson, I. Farrer, D. A. Ritchie, J. Nilsson, R. M. Stevenson, A. J. Bennett, A. J. Shields, G. Burkard, A. I. Tartakovskii, M. S. Skolnick, and E. A. Chekhovich, Few-second-long correlation times in a quantum dot nuclear spin bath probed by frequency-comb nuclear magnetic resonance spectroscopy, Nat. Phys. **12**, 688 (2016).

[22] F. Bloch, Nuclear induction, Phys. Rev. **70**, 460 (1946).

[23] E. A. Chekhovich, K. V. Kavokin, J. Puebla, A. B. Krysa, M. Hopkinson, A. D. Andreev, A. M.

Sanchez, R. Beanland, M. S. Skolnick, and A. I. Tartakovskii, Structural analysis of strained quantum dots using nuclear magnetic resonance, Nat. Nanotechnol. **7**, 646 (2012).

[24] B. Urbaszek, P.-F. Braun, T. Amand, O. Krebs, T. Belhadj, A. Lemaítre, P. Voisin, and X. Marie, Efficient dynamical nuclear polarization in quantum dots: Temperature dependence, Phys. Rev. B **76**, 201301 (2007).

[25] C. Schimpf, M. Reindl, P. Klenovský, T. Fromherz, S. F. Covre Da Silva, J. Hofer, C. Schneider, S. Höfling, R. Trotta, and A. Rastelli, Resolving the temporal evolution of line broadening in single quantum emitters, Opt. Express **27**, 35290 (2019).

[26] J. M. Villas-Bôas, S. E. Ulloa, and A. O. Govorov, Decoherence of Rabi oscillations in a single quantum dot, Phys. Rev. Lett. **94**, 057404 (2005).

[27] S. Adachi, *Properties of Semiconductor Alloys: Group-IV, III-V and II-VI Semiconductors* (Wiley, 2009).

[28] A. Imamoğlu, E. Knill, L. Tian, and P. Zoller, Optical pumping of quantum-dot nuclear spins, Phys. Rev. Lett. **91**, 017402 (2003).

[29] H. Christ, J. I. Cirac, and G. Giedke, Quantum description of nuclear spin cooling in a quantum dot, Phys. Rev. B **75**, 155324 (2007).

[30] G. Gillard, E. Clarke, and E. A. Chekhovich, Harnessing many-body spin environment for long coherence storage and high-fidelity single-shot qubit readout, Nature Communications **13**, 4048 (2022).

[31] H. Huang, D. Csontosová, S. Manna, Y. Huo, R. Trotta, A. Rastelli, and P. Klenovský, Electric field induced tuning of electronic correlation in weakly confining quantum dots, Phys. Rev. B **104**, 165401 (2021).

[32] X. Xu, W. Yao, B. Sun, D. G. Steel, A. S. Bracker, D. Gammon, and L. J. Sham, Optically controlled locking of the nuclear field via coherent dark-state spectroscopy, Nature **459**, 1105 (2009).

[33] D. A. Gangloff, L. Zaporski, J. H. Bodey, C. Bachorz, D. M. Jackson, G. Éthier-Majcher, C. Lang, E. Clarke, M. Hugues, C. Le Gall, and M. Atatüre, Witnessing quantum correlations in a nuclear ensemble via an electron spin qubit, Nat. Phys. **17**, 1247 (2021).

[34] D. M. Jackson, U. Haeusler, L. Zaporski, J. H. Bodey, N. Shofer, E. Clarke, M. Hugues, M. Atatüre, C. Le Gall, and D. A. Gangloff, Optimal purification of a spin ensemble by quantum-algorithmic feedback, Phys. Rev. X **12**, 031014 (2022).

[35] A. V. Khaetskii, D. Loss, and L. Glazman, Electron Spin Decoherence in Quantum Dots due to Interaction with Nuclei, Phys. Rev. Lett. **88**, 186802 (2002).

[36] M. Goldman, *Spin temperature and nuclear magnetic resonance in solids* (Oxford University Press, Oxford, 1970).

[37] T. A. Knuuttila, J. T. Tuoriniemi, K. Lefmann, K. I. Juntunen, F. B. Rasmussen, and K. K. Nummila, Polarized nuclei in normal and superconducting rhodium, Journal of Low Temperature Physics **123**, 65 (2001).

[38] W. T. Wenckebach, The solid effect, Applied Magnetic Resonance **34**, 227 (2008).

[39] C. Kloeffel and D. Loss, Prospects for spin-based quantum computing in quantum dots, Annual Review of Cond. Matt. Phys. **4**, 51 (2013).

[40] G. Ragunathan, *Nuclear Spin Phenomena in III-V and II-VI Semiconductor Quantum Dots*, Ph.D. thesis, University of Sheffield (2019).

[41] L. Zaporski, N. Shofer, J. H. Bodey, S. Manna, G. Gillard, M. H. Appel, C. Schimpf, S. F. Covre da Silva, J. Jarman, G. Delamare, G. Park, U. Haeusler, E. A. Chekhovich, A. Rastelli, D. A. Gangloff, M. Atatüre, and C. Le Gall, Ideal refocusing of an optically active spin qubit under strong hyperfine interactions, Nat. Nanotechnol. **18**, 257 (2023).

[42] W. Janzen, Adiabatic rapid passage NMR signal shape and passage conditions in solids, Journal of Magnetic Resonance (1969) **12**, 71 (1973).

[43] M. Goldman, J. Jacquinot, M. Chapellier, and V. H. Chau, Nonlinear effects in spin temperature, Journal of Magnetic Resonance (1969) **18**, 22 (1975).

[44] G. Cowan, *Statistical Data Analysis* (Clarendon Press, 1998).

Chapter 7

Summary and Conclusions

In Chapter 1 the requirements for a viable spin qubit were described. The work in this thesis has been conducted on III-V semiconductor, mainly GaAs/AlGaAs, QDs with the ambition of ultimately attaining an electron spin qubit. For this to be achieved, multiple avenues of research are needed to progress. Here we have addressed efforts to eliminate decoherence of electron spin qubits and shown a substantial enhancement of nuclear spin polarisation. This was accomplished using optical spectroscopy and NMR techniques to non-invasively probe the nuclear spin bath of nanohole infilled QDs. For the conclusion of this thesis we will summarise each experimental chapter's results and suggest some future pathways of research.

In Chapter 4, the nanoscale strain in various III-V semiconductor QDs was investigated. By combining InvNMR and integral saturation NMR experimental data with Monte-Carlo simulations, we determined the major strain within $Al_xGa_{1-x}As$ QDs to be 0.023%, 0.031%, and 0.039% for the $x = 0\%$, 5%, and 10% dots, respectively. The magnitude of inhomogeneous atomic-scale strain was measured at approximately 0.14%, consistent with the GaAs/AlAs lattice constant difference of 0.138%. Additionally, the inclusion of In within the QD significantly increased the broadening effect observed in the InvNMR/integral saturation NMR spectra, where quadrupolar splitting breadths exceeded 2 MHz. This is consistent with the larger lattice mismatch of InAs/GaAs, which is 7%. Understanding the strain distribution within QDs is crucial, as even though built-in strain in GaAs/AlGaAs QDs is often considered negligible [106], it still significantly effects electron spin coherence times [30, 125, 131, 155, 163, 180–183]. These findings provide valuable insights for guiding future QD sample growth. To minimise nuclear spin transition broadening, it is recommended to use lattice-matched QD systems, such as GaAs/AlGaAs, as well as using nanohole infilling techniques over strain-driven methods such as the Stranski-Krastanov growth mode. Furthermore, reducing contaminants, either through careful control of the growth process or avoiding material mixing with the barriers, is essential, as even small amounts of impurities can induce detectable nanoscale strain.

For Chapter 5, the nuclear spin dynamics of GaAs/AlGaAs QDs were studied. We

addressed the long-standing question of the existence of the Knight-field-gradient diffusion barrier, by demonstrating its absence within this system. It was shown that the addition of an electron spin into a QD accelerates NSR within a large range of external magnetic fields, with the proposed cause being electron spin-flips. In the diffusion-limited QD, the nuclear spin lifetimes were found to be between 1 and 10s, significantly slower than in Stranski-Krastanov-grown InGaAs/GaAs QDs, yet still acceptably long for quantum information processing and storage. To further extend the nuclear spin lifetimes beyond those demonstrated in this study, one could increase the degree of nuclear spin polarisation or extend the optical pumping durations, as explored in greater detail in Chapter 6. Future work could focus on investigating the longevity of multi-electron charged QDs. It would be intriguing to see whether these states exhibit similar behaviour to single electrons in terms of spin dynamics and coherence times.

In the final chapter, we developed an experimental technique to address the long-standing theoretical scepticism surrounding high nuclear spin polarisations in semiconductors, a debate that has persisted for over two decades. It was demonstrated that nuclear spin polarisations well above 95% could be achieved in a statistically significant number of randomly selected GaAs QDs. These near-unity polarisations are crucial for suppressing electron spin qubit dephasing and reducing the entropy of the nuclear spin ensemble. Given the novelty of this discovery, several promising avenues for future research and additional experiments emerge.

A key next step would be to revisit many of the previous measurements to assess how high nuclear polarisation affects the system's properties. For instance, with a highly polarised nuclear spin ensemble, it would be valuable to measure nuclear spin coherence times both in the presence and absence of an electron, as well as to investigate nuclear spin diffusion with an electron present. These experiments would provide deeper insights into nuclear spin lifetimes and diffusion rates, building upon the work described in Chapters 5 and 6. By exploring QDs under conditions of near-unity polarisation, we could connect the findings from these chapters and gain a more comprehensive understanding of spin dynamics in QDs.

Future research could also focus on the impact of strain, particularly through studies on uniaxially or biaxially strained QDs. Strain-induced quadrupolar interactions are known to slow nuclear spin fluctuations, so investigating how different strain configurations influence nuclear spin lifetimes and diffusion under high degrees of nuclear spin polarisation could provide valuable insights. Such studies would contribute to the design of more stable quantum systems by controlling strain in the QDs and fine-tuning their nuclear spin properties.

Another exciting direction for investigation involves the use of specialised RF pulse sequences, such as Combined Hahn and Solid Echo (CHASE) [163]. By combining high nuclear spin polarisation with dynamical decoupling techniques, it would be particularly interesting to see how long a spin-polarised electron can maintain coherence in such an environment. A potential proof of concept for electron spin qubits could involve polarising the

nuclear spins to a high degree, introducing an electron into the QD electrically, applying a CHASE sequence to filter out unwanted interactions, and then reading out the electron's spin state. This experimental setup would not only test the system's ability to store and retrieve quantum information but also help refine methods for preserving electron spin coherence in quantum dot samples.

Bibliography

[1] D. T. Haar. *Old quantum theory*. Pergamon, 1967, pp. 79–81.

[2] M. J. Klein. "Introduction". *Max Planck and the beginnings of the quantum theory*. Archive for history of exact sciences, 1962, pp. 32–32.

[3] D. F. Styer. "Appendix A: A Brief History of Quantum Mechanics". *The Strange World of Quantum Mechanics*. Cambridge Univ. Press, 2004.

[4] I. I. Manin. *Vychislimoe I nevychislimoe [Computable and Uncomputable]*. [In Russian]. Sov. radio, 1980.

[5] P. Benioff. "The computer as a physical system: A microscopic quantum mechanical hamiltonian model of computers as represented by Turing machines". *Journal of Statistical Physics* 22.5 (1980), pp. 563–591. DOI: 10.1007/bf01011339.

[6] P. Benioff. "Quantum mechanical hamiltonian models of Turing machines". *Journal of Statistical Physics* 29.3 (1982), pp. 515–546. DOI: 10.1007/bf01342185.

[7] R. P. Feynman. "Simulating physics with computers". *International Journal of Theoretical Physics* 21.6–7 (1982), pp. 467–488. DOI: 10.1007/bf02650179.

[8] *Proceedings of the Royal Society of London. A. Mathematical and Physical Sciences* 400.1818 (1985), pp. 97–117. DOI: 10.1098/rspa.1985.0070.

[9] R. P. Feynman. "Quantum mechanical computers". *Foundations of Physics* 16.6 (1986), pp. 507–531. DOI: 10.1007/bf01886518.

[10] P. Kok. *Five Lectures on Optical Quantum Computing*. URL: https://www.pieter-kok.staff.shef.ac.uk/docs/LNP787_187.pdf (visited on 13/10/2023).

[11] D. P. DiVincenzo. "The Physical Implementation of Quantum Computation". *Fortschritte der Physik* 48.9-11 (2000), pp. 771–783. DOI: https://doi.org/10.1002/1521-3978(200009)48:9/11<771::AID-PROP771>3.0.CO;2-E.

[12] T. D. Ladd, F. Jelezko, R. Laflamme, Y. Nakamura, C. Monroe, and J. L. O'Brien. "Quantum Computers". *Nature* 464.7285 (2010), pp. 45–53. DOI: 10.1038/nature08812.

[13] J. I. Cirac and P. Zoller. "Quantum computations with cold trapped ions". *Physical Review Letters* 74.20 (1995), pp. 4091–4094. DOI: 10.1103/physrevlett.74.4091.

[14] R. Blatt and D. Wineland. "Entangled states of trapped atomic ions". *Nature* 453.7198 (2008), pp. 1008–1015. DOI: 10.1038/nature07125.

[15] T. Monz, P. Schindler, J. T. Barreiro, M. Chwalla, D. Nigg, W. A. Coish, M. Harlander, W. Hänsel, M. Hennrich, and R. Blatt. "14-Qubit Entanglement: Creation and Coherence". *Phys. Rev. Lett.* 106 (13 2011), p. 130506. DOI: 10.1103/PhysRevLett.106.130506.

[16] C. D. Bruzewicz, J. Chiaverini, R. McConnell, and J. M. Sage. "Trapped-Ion Quantum Computing: Progress and Challenges". *Applied Physics Reviews* 6.2 (2019). DOI: 10.1063/1.5088164.

[17] J. M. Pino, J. M. Dreiling, C. Figgatt, J. P. Gaebler, S. A. Moses, M. S. Allman, C. H. Baldwin, M. Foss-Feig, D. Hayes, K. Mayer, and et al. "Demonstration of the trapped-ion quantum CCD computer architecture". *Nature* 592.7853 (2021), pp. 209–213. DOI: 10.1038/s41586-021-03318-4.

[18] M. H. Abobeih, J. Randall, C. E. Bradley, H. P. Bartling, M. A. Bakker, M. J. Degen, M. Markham, D. J. Twitchen, and T. H. Taminiau. "Atomic-scale imaging of a 27-nuclear-spin cluster using a quantum sensor". *Nature* 576.7787 (2019), pp. 411–415. DOI: 10.1038/s41586-019-1834-7.

[19] J. R. Weber, W. F. Koehl, J. B. Varley, A. Janotti, B. B. Buckley, C. G. Van de Walle, and D. D. Awschalom. "Quantum computing with defects". *Proceedings of the National Academy of Sciences* 107.19 (2010), pp. 8513–8518. DOI: 10.1073/pnas.1003052107.

[20] J. R. Weber, W. F. Koehl, J. B. Varley, A. Janotti, B. B. Buckley, C. G. Van de Walle, and D. D. Awschalom. "Defects in SIC for quantum computing". *Journal of Applied Physics* 109.10 (2011). DOI: 10.1063/1.3578264.

[21] J. Harrison, M. Sellars, and N. Manson. "Measurement of the optically induced spin polarisation of N-V centres in Diamond". *Diamond and Related Materials* 15.4–8 (2006), pp. 586–588. DOI: 10.1016/j.diamond.2005.12.027.

[22] M. V. Dutt, L. Childress, L. Jiang, E. Togan, J. Maze, F. Jelezko, A. S. Zibrov, P. R. Hemmer, and M. D. Lukin. "Quantum register based on individual electronic and nuclear spin qubits in Diamond". *Science* 316.5829 (2007), pp. 1312–1316. DOI: 10.1126/science.1139831.

[23] B. Josephson. "Possible new effects in superconductive tunnelling". *Physics Letters* 1.7 (1962), pp. 251–253. DOI: 10.1016/0031-9163(62)91369-0.

[24] P. W. Anderson and J. M. Rowell. “Probable Observation of the Josephson Superconducting Tunneling Effect”. *Phys. Rev. Lett.* 10 (6 1963), pp. 230–232. DOI: 10.1103/PhysRevLett.10.230.

[25] M. H. Devoret and R. J. Schoelkopf. “Superconducting Circuits for Quantum Information: An Outlook”. *Science* 339.6124 (2013), pp. 1169–1174. DOI: 10.1126/science.1231930.

[26] F. Arute, K. Arya, R. Babbush, D. Bacon, J. C. Bardin, R. Barends, R. Biswas, S. Boixo, F. G. Brandao, D. A. Buell, and et al. “Quantum supremacy using a programmable superconducting processor”. *Nature* 574.7779 (2019), pp. 505–510. DOI: 10.1038/s41586-019-1666-5.

[27] M. Kjaergaard, M. E. Schwartz, J. Braumüller, P. Krantz, J. I.-J. Wang, S. Gustavsson, and W. D. Oliver. “Superconducting qubits: Current State of Play”. *Annual Review of Condensed Matter Physics* 11.1 (2020), pp. 369–395. DOI: 10.1146/annurev-conmatphys-031119-050605.

[28] I. Siddiqi. “Engineering high-coherence superconducting qubits”. *Nature Reviews Materials* 6.10 (2021), pp. 875–891. DOI: 10.1038/s41578-021-00370-4.

[29] K. D. Greve, D. Press, P. L. McMahon, and Y. Yamamoto. “Ultrafast optical control of individual quantum dot spin qubits”. *Reports on Progress in Physics* 76.9 (2013), p. 092501. DOI: 10.1088/0034-4885/76/9/092501.

[30] A. Bechtold, D. Rauch, F. Li, T. Simmet, P.-L. Ardelt, A. Regler, K. Müller, N. A. Sinitsyn, and J. J. Finley. “Three-stage decoherence dynamics of an electron spin qubit in an optically active quantum dot”. *Nature Physics* 11.12 (2015), pp. 1005–1008. DOI: 10.1038/nphys3470.

[31] E. A. Chekhovich, S. F. da Silva, and A. Rastelli. “Nuclear spin quantum register in an optically active semiconductor quantum dot”. *Nature Nanotechnology* 15.12 (2020), pp. 999–1004. DOI: 10.1038/s41565-020-0769-3.

[32] E. Evers, N. E. Kopteva, I. A. Yugova, D. R. Yakovlev, D. Reuter, A. D. Wieck, M. Bayer, and A. Greilich. “Suppression of nuclear spin fluctuations in an InGaAs quantum dot ensemble by GHz-pulsed optical excitation”. *npj Quantum Information* 7.1 (2021). DOI: 10.1038/s41534-021-00395-1.

[33] P. Michler, A. Kiraz, C. Becher, W. V. Schoenfeld, P. M. Petroff, L. Zhang, E. Hu, and A. Imamoglu. “A quantum dot single-photon turnstile device”. *Science* 290.5500 (2000), pp. 2282–2285. DOI: 10.1126/science.290.5500.2282.

[34] C. Santori, D. Fattal, J. Vuckovic, G. S. Solomon, and Y. Yamamoto. “Single-photon generation with InAs quantum dots”. *New Journal of Physics* 6 (2004), pp. 89–89. DOI: 10.1088/1367-2630/6/1/089.

[35] D. Pinotsi and A. Imamoglu. “Single Photon Absorption by a Single Quantum Emitter”. *Phys. Rev. Lett.* 100 (9 2008), p. 093603. DOI: 10.1103/PhysRevLett.100.093603.

[36] F. Liu, A. J. Brash, J. O’Hara, L. M. Martins, C. L. Phillips, R. J. Coles, B. Royall, E. Clarke, C. Bentham, N. Prtljaga, and et al. “High purcell factor generation of indistinguishable on-chip single photons”. *Nature Nanotechnology* 13.9 (2018), pp. 835–840. DOI: 10.1038/s41565-018-0188-x.

[37] D. Hallett, A. P. Foster, D. Whittaker, M. S. Skolnick, and L. R. Wilson. “Engineering chiral light–matter interactions in a waveguide-coupled nanocavity”. *ACS Photonics* 9.2 (2022), pp. 706–713. DOI: 10.1021/acsphotonics.1c01806.

[38] S. J. Sheldon, A. J. Brash, M. S. Skolnick, A. M. Fox, and J. Iles-Smith. “Optical Spin Initialisation and Readout with a Cavity-Coupled Quantum Dot in an In-Plane Magnetic Field” (2022). arXiv: 2206.11008 [quant-ph].

[39] M. J. Mehrabad, A. P. Foster, N. J. Martin, R. Dost, E. Clarke, P. K. Patil, M. S. Skolnick, and L. R. Wilson. “Chiral topological add-drop filter for integrated quantum photonic circuits”. *Optica* 10.3 (2023), p. 415. DOI: 10.1364/optica.481684.

[40] H. Siampour, C. O’Rourke, A. J. Brash, M. N. Makhonin, R. Dost, D. J. Hallett, E. Clarke, P. K. Patil, M. S. Skolnick, and A. M. Fox. “Observation of large spontaneous emission rate enhancement of quantum dots in a broken-symmetry slow-light waveguide”. *npj Quantum Information* 9.1 (2023). DOI: 10.1038/s41534-023-00686-9.

[41] N. J. Martin, M. J. Mehrabad, X. Chen, R. Dost, E. Nussbaum, D. Hallett, L. Hallacy, A. Foster, E. Clarke, P. K. Patil, S. Hughes, M. Hafezi, A. M. Fox, M. S. Skolnick, and L. R. Wilson. “Topological and conventional nano-photonic waveguides for chiral integrated quantum optics” (2023). arXiv: 2305.11082 [physics.optics].

[42] C. L. Phillips, A. J. Brash, M. Godsland, N. J. Martin, A. Foster, A. Tomlinson, R. Dost, N. Babazadeh, E. M. Sala, L. Wilson, J. Heffernan, M. S. Skolnick, and A. M. Fox. “Purcell-enhanced single photons at telecom wavelengths from a quantum dot in a photonic crystal cavity”. *Scientific Reports* 14.1 (2024). ISSN: 2045-2322. DOI: 10.1038/s41598-024-55024-6.

[43] A. J. Ramsay, A. V. Gopal, E. M. Gauger, A. Nazir, B. W. Lovett, A. M. Fox, and M. S. Skolnick. “Damping of exciton Rabi rotations by acoustic phonons in optically excited InGaAs/GaAs quantum dots”. *Physical Review Letters* 104.1 (2010). DOI: 10.1103/physrevlett.104.017402.

[44] D. Brunner, B. D. Gerardot, P. A. Dalgarno, G. Wüst, K. Karrai, N. G. Stoltz, P. M. Petroff, and R. J. Warburton. “A Coherent Single-Hole Spin in a Semiconductor”. *Science* 325.5936 (2009), pp. 70–72. ISSN: 1095-9203. DOI: 10.1126/science.1173684.

[45] X. Xu, W. Yao, B. Sun, D. G. Steel, A. S. Bracker, D. Gammon, and L. J. Sham. "Optically controlled locking of the nuclear field via coherent dark-state spectroscopy". *Nature* 459.7250 (2009), pp. 1105–1109. ISSN: 1476-4687. DOI: 10.1038/nature08120.

[46] K. Heshami, D. G. England, P. C. Humphreys, P. J. Bustard, V. M. Acosta, J. Nunn, and B. J. Sussman. "Quantum memories: emerging applications and recent advances". *Journal of Modern Optics* 63.20 (2016), pp. 2005–2028. ISSN: 1362-3044. DOI: 10.1080/09500340.2016.1148212.

[47] E. V. Denning, D. A. Gangloff, M. Atatüre, J. Mørk, and C. Le Gall. "Collective Quantum Memory Activated by a Driven Central Spin". *Phys. Rev. Lett.* 123 (14 2019), p. 140502. DOI: 10.1103/PhysRevLett.123.140502.

[48] S. Adachi. "Energy-Band Structure: Effective Masses". *Properties of semiconductor alloys: Group-IV, III-V and II-VI semiconductors*. Wiley, 2009.

[49] Nobel Prize Outreach. *Nobel Prize press release*. URL: https://www.nobelprize.org/prizes/chemistry/2023/press-release/ (visited on 23/10/2023).

[50] R. Rossetti and L. Brus. "Electron-hole recombination emission as a probe of surface chemistry in aqueous cadmium sulfide colloids". *The Journal of Physical Chemistry* 86.23 (1982), pp. 4470–4472. DOI: 10.1021/j100220a003.

[51] C. B. Murray, D. J. Norris, and M. G. Bawendi. "Synthesis and characterization of nearly monodisperse CdE (E = sulfur, selenium, tellurium) semiconductor nanocrystallites". *Journal of the American Chemical Society* 115.19 (1993), pp. 8706–8715. DOI: 10.1021/ja00072a025.

[52] A. I. Ekimov and A. A. Onushchehko. "Quantum size effect in three-dimensional microscopic semiconductor crystals". *JETP Lett.* 34 (1981), p. 345.

[53] O. Gywat, J. Berezovsky, and H. J. Krenner. "Optically Active Quantum Dots: Single and Coupled Structures". *Spins in optically active quantum dots concepts and methods*. Wiley-VCH, 2010, pp. IX & 15–37 & 105.

[54] T. Edvinsson. "Optical quantum confinement and photocatalytic properties in two-, one- and zero-dimensional nanostructures". *Royal Society Open Science* 5.9 (2018), p. 180387. DOI: 10.1098/rsos.180387.

[55] K. G. Günther. "Aufdampfschichten aus halbleitenden III-V-verbindungen". *Die Naturwissenschaften* 45.17 (1958), pp. 415–416. DOI: 10.1007/bf00603228.

[56] J. E. Davey and T. Pankey. "Epitaxial GaAs films deposited by Vacuum Evaporation". *Journal of Applied Physics* 39.4 (1968), pp. 1941–1948. DOI: 10.1063/1.1656467.

[57] A. Cho and J. Arthur. "Molecular beam epitaxy". *Progress in Solid State Chemistry* 10 (1975), pp. 157–191. DOI: 10.1016/0079-6786(75)90005-9.

[58] I. Griffiths. "Nuclear magnetic resonance studies of spin and strain phenomena in nanohole GaAs/AlGaAs Quantum Dots". PhD thesis. University of Sheffield, 2021. URL: https://etheses.whiterose.ac.uk/30763/.

[59] F. C. Frank and J. H. Van der Merwe. "One-dimensional dislocations. II. Misfitting monolayers and oriented overgrowth". *Proceedings of the Royal Society of London. Series A. Mathematical and Physical Sciences* 198.1053 (1949), pp. 216–225. DOI: 10.1098/rspa.1949.0096.

[60] M. Volmer and Weber. "Keimbildung in übersättigten Gebilden". *Zeitschrift für Physikalische Chemie* 119U.1 (1926), pp. 277–301. DOI: 10.1515/zpch-1926-11927.

[61] I. N. Stranski and L. Krastanow. "Zur Theorie der Orientierten Ausscheidung von Ionenkristallen Aufeinander". *Monatshefte für Chemie* 71.1 (1937), pp. 351–364. DOI: 10.1007/bf01798103.

[62] S. Baker. *3. Quantum Dots, (3.1 Self-Assembled Quantum Dots)*. Lecture at the University of Leicester. 2018.

[63] Q. Q. Wang, A. Muller, P. Bianucci, E. Rossi, Q. K. Xue, T. Takagahara, C. Piermarocchi, A. H. MacDonald, and C. K. Shih. "Decoherence processes during optical manipulation of excitonic qubits in semiconductor quantum dots". *Phys. Rev. B* 72 (3 2005), p. 035306. DOI: 10.1103/PhysRevB.72.035306.

[64] A. K. Rai, S. Gordon, A. Ludwig, A. D. Wieck, A. Zrenner, and D. Reuter. "Spatially indirect transitions in electric field tunable quantum dot diodes". *physica status solidi (b)* 253.3 (2015), pp. 437–441. DOI: 10.1002/pssb.201552591.

[65] Z. M. Wang, B. L. Liang, K. A. Sablon, and G. J. Salamo. "Nanoholes fabricated by self-assembled gallium nanodrill on GaAs(100)". *Applied Physics Letters* 90.11 (2007). DOI: 10.1063/1.2713745.

[66] C. Heyn, A. Stemmann, T. Köppen, C. Strelow, T. Kipp, M. Grave, S. Mendach, and W. Hansen. "Highly uniform and strain-free GaAs quantum dots fabricated by filling of self-assembled nanoholes". *Applied Physics Letters* 94.18 (2009). DOI: 10.1063/1.3133338.

[67] C. Heyn, A. Stemmann, T. Köppen, C. Strelow, T. Kipp, M. Grave, S. Mendach, and W. Hansen. "Optical properties of GaAs quantum dots fabricated by filling of self-assembled nanoholes". *Nanoscale Research Letters* 5.3 (2009), pp. 576–580. DOI: 10.1007/s11671-009-9507-3.

[68] C. Heyn, A. Stemmann, and W. Hansen. "Nanohole formation on AlGaAs surfaces by local droplet etching with gallium". *Journal of Crystal Growth* 311.7 (2009), pp. 1839–1842. DOI: 10.1016/j.jcrysgro.2008.11.001.

[69] J. D. Plumhof, V. Křápek, L. Wang, A. Schliwa, D. Bimberg, A. Rastelli, and O. G. Schmidt. "Experimental investigation and modeling of the fine structure splitting of neutral excitons in strain-free GaAs/$Al_xGa_{1-x}As$ quantum dots". *Phys. Rev. B* 81 (12 2010). DOI: 10.1103/PhysRevB.81.121309.

[70] C. J. Sheppard. "Approximate calculation of the reflection coefficient from a stratified medium". *Pure and Applied Optics: Journal of the European Optical Society Part A* 4.5 (1995), pp. 665–669. DOI: 10.1088/0963-9659/4/5/018.

[71] R. E. Fern and A. Onton. "Refractive index of alas". *Journal of Applied Physics* 42.9 (1971), pp. 3499–3500. DOI: 10.1063/1.1660760.

[72] G.-Q. Jiang, Q.-H. Zhang, J.-Y. Zhao, Y.-K. Qiao, Z.-X. Ge, R.-Z. Liu, T.-H. Chung, C.-Y. Lu, and Y.-H. Huo. "Comprehensive measurement of the near-infrared refractive index of GaAs at cryogenic temperatures". *Optics Letters* 48.13 (2023), p. 3507. DOI: 10.1364/ol.491357.

[73] S. A. Lourenço, I. F. Dias, J. L. Duarte, E. Laureto, E. A. Meneses, J. R. Leite, and I. Mazzaro. "Temperature dependence of optical transitions in AlGaAs". *Journal of Applied Physics* 89.11 (2001), pp. 6159–6164. DOI: 10.1063/1.1367875.

[74] S.-T. Hwang, S. Kim, H. Cheun, H. Lee, B. Lee, T. Hwang, S. Lee, W. Yoon, H.-M. Lee, and B. Park. "Bandgap grading and $Al_{0.3}Ga_{0.7}As$ heterojunction emitter for highly efficient GaAs-based solar cells". *Solar Energy Materials and Solar Cells* 155 (2016), pp. 264–272. ISSN: 0927-0248. DOI: 10.1016/j.solmat.2016.06.009.

[75] J. S. Blakemore. "Semiconducting and other major properties of gallium arsenide". *Journal of Applied Physics* 53.10 (1982). DOI: 10.1063/1.331665.

[76] C Kittel. *Introduction to solid state physics*. 8th ed. Wiley, 2005, p. 190.

[77] C. Hartwigsen, S. Goedecker, and J. Hutter. "Relativistic separable dual-space Gaussian pseudopotentials from H to Rn". *Phys. Rev. B* 58 (7 1998), pp. 3641–3662. DOI: 10.1103/PhysRevB.58.3641.

[78] M. I. Dyakonov. *Spin Physics in Semiconductors*. 2nd ed. Springer, 2008.

[79] I. Vurgaftman, J. R. Meyer, and L. R. Ram-Mohan. "Band parameters for III-V compound semiconductors and their alloys". *Journal of Applied Physics* 89.11 (2001), pp. 5815–5875. DOI: 10.1063/1.1368156.

[80] P. Harrison. "Numerical Solutions". *Quantum Wells, Wires and Dots*. John Wiley & Sons, Ltd, 2005. Chap. 3, pp. 73–118. ISBN: 9780470010822. DOI: https://doi.org/10.1002/0470010827.ch3.

[81] A. Wojs, P. Hawrylak, S. Fafard, and L. Jacak. "Electronic structure and magneto-optics of self-assembled quantum dots". *Phys. Rev. B* 54 (8 1996), pp. 5604–5608. DOI: 10.1103/PhysRevB.54.5604.

[82] A. H. Rodríguez, C. Trallero-Giner, S. E. Ulloa, and J. Marín-Antuña. "Electronic states in a quantum lens". *Phys. Rev. B* 63 (12 2001), p. 125319. DOI: 10.1103/PhysRevB.63.125319.

[83] F. M. Peeters and V. A. Schweigert. "Two-electron quantum disks". *Phys. Rev. B* 53 (3 1996), pp. 1468–1474. DOI: 10.1103/PhysRevB.53.1468.

[84] C. Pryor. "Eight-band calculations of strained InAs/GaAs quantum dots compared with one-, four-, and six-band approximations". *Phys. Rev. B* 57 (12 1998), pp. 7190–7195. DOI: 10.1103/PhysRevB.57.7190.

[85] O. Stier, M. Grundmann, and D. Bimberg. "Electronic and optical properties of strained quantum dots modeled by 8-band k·p theory". *Phys. Rev. B* 59 (8 1999), pp. 5688–5701. DOI: 10.1103/PhysRevB.59.5688.

[86] A. M. Waeber. PhD thesis. University of Sheffield, 2016. URL: https://etheses.whiterose.ac.uk/13614/.

[87] D. Smirnov, S. Raymond, S. Studenikin, A. Babinski, J. Leotin, P. Frings, M. Potemski, and A. Sachrajda. "Electronic structure of InAs/GaAs self-assembled Quantum Dots studied by high-excitation luminescence in magnetic fields up to 73 T". *Physica B: Condensed Matter* 346–347 (2004), pp. 432–436. DOI: 10.1016/j.physb.2004.01.121.

[88] W. Wang. "On the band offsets of AlGaAs/GaAs and beyond". *Solid-State Electronics* 29.2 (1986), pp. 133–139. DOI: 10.1016/0038-1101(86)90031-6.

[89] T. Sogabe, T. Kaizu, Y. Okada, and S. Tomić. "Theoretical analysis of GaAs/AlAaAs Quantum Dots in quantum wire array for intermediate band Solar Cell". *Journal of Renewable and Sustainable Energy* 6.1 (2013). DOI: 10.1063/1.4828359.

[90] L. P. Kouwenhoven, D. G. Austing, and S Tarucha. "Few-electron quantum dots". *Reports on Progress in Physics* 64.6 (2001), pp. 701–736. DOI: 10.1088/0034-4885/64/6/201.

[91] R. J. Warburton. "Single spins in self-assembled quantum dots". *Nature Materials* 12.6 (2013), pp. 483–493. DOI: 10.1038/nmat3585.

[92] P. Millington-Hotze, S. Manna, S. F. Covre da Silva, A. Rastelli, and E. A. Chekhovich. "Nuclear spin diffusion in the Central Spin System of a GaAs/AlGaAs quantum dot". *Nature Communications* 14.1 (2023). DOI: 10.1038/s41467-023-38349-0.

[93] M. El Allali, C. B. Sørensen, E. Veje, and P. Tidemand-Petersson. "Experimental determination of the GaAs and $Ga_{1-x}Al_xAs$ band-gap energy dependence on temperature and aluminum mole fraction in the direct band-gap region". *Physical Review B* 48.7 (1993), pp. 4398–4404. DOI: 10.1103/physrevb.48.4398.

[94] M. Bayer, S. N. Walck, T. L. Reinecke, and A. Forchel. "Exciton binding energies and diamagnetic shifts in semiconductor quantum wires and quantum dots". *Phys. Rev. B* 57 (11 1998), pp. 6584–6591. DOI: 10.1103/PhysRevB.57.6584.

[95] R. J. Warburton, B. T. Miller, C. S. Dürr, C. Bödefeld, K. Karrai, J. P. Kotthaus, G. Medeiros-Ribeiro, P. M. Petroff, and S. Huant. "Coulomb interactions in small charge-tunable quantum dots: A simple model". *Phys. Rev. B* 58 (24 1998), pp. 16221–16231. DOI: 10.1103/PhysRevB.58.16221.

[96] S. B. Nam, D. C. Reynolds, C. W. Litton, R. J. Almassy, T. C. Collins, and C. M. Wolfe. "Free-exciton energy spectrum in GaAs". *Phys. Rev. B* 13 (2 1976), pp. 761–767. DOI: 10.1103/PhysRevB.13.761.

[97] P. A. Dalgarno, J. M. Smith, J. McFarlane, B. D. Gerardot, K. Karrai, A. Badolato, P. M. Petroff, and R. J. Warburton. "Coulomb interactions in single charged self-assembled quantum dots: Radiative lifetime and recombination energy". *Phys. Rev. B* 77 (24 2008), p. 245311. DOI: 10.1103/PhysRevB.77.245311.

[98] E Dekel, D. Regelman, D Gershoni, E Ehrenfreund, W. Schoenfeld, and P. Petroff. "Radiative lifetimes of single excitons in semiconductor quantum dots - manifestation of the spatial coherence effect". *Solid State Communications* 117.7 (2001), pp. 395–400. DOI: 10.1016/s0038-1098(00)00483-x.

[99] E. Schöll, L. Hanschke, L. Schweickert, K. D. Zeuner, M. Reindl, S. F. Covre da Silva, T. Lettner, R. Trotta, J. J. Finley, K. Müller, A. Rastelli, V. Zwiller, and K. D. Jöns. "Resonance Fluorescence of GaAs Quantum Dots with Near-Unity Photon Indistinguishability". *Nano Letters* 19.4 (2019). PMID: 30862165, pp. 2404–2410. DOI: 10.1021/acs.nanolett.8b05132.

[100] L. D Landau and E. M Lifshitz. *A shorter course of theoretical physics*. Vol. 2. Oxford, 1974.

[101] E. Poem, Y. Kodriano, C. Tradonsky, N. H. Lindner, B. D. Gerardot, P. M. Petroff, and D. Gershoni. "Accessing the dark exciton with light". *Nature Physics* 6.12 (2010), pp. 993–997. DOI: 10.1038/nphys1812.

[102] J. McFarlane, P. A. Dalgarno, B. D. Gerardot, R. H. Hadfield, R. J. Warburton, K. Karrai, A. Badolato, and P. M. Petroff. "Gigahertz bandwidth electrical control over a dark exciton-based memory bit in a single quantum dot". *Applied Physics Letters* 94.9 (2009). DOI: 10.1063/1.3086461.

[103] M. Zieliński, Y. Don, and D. Gershoni. "Atomistic theory of dark excitons in self-assembled quantum dots of reduced symmetry". *Phys. Rev. B* 91 (8 2015), p. 085403. DOI: 10.1103/PhysRevB.91.085403.

[104] E. A. Chekhovich, M. N. Makhonin, K. V. Kavokin, A. B. Krysa, M. S. Skolnick, and A. I. Tartakovskii. "Pumping of Nuclear Spins by Optical Excitation of Spin-Forbidden Transitions in a Quantum Dot". *Physical Review Letters* 104.6 (2010). DOI: 10.1103/physrevlett.104.066804.

[105] T. Belhadj, T. Amand, A. Kunold, C.-M. Simon, T. Kuroda, M. Abbarchi, T. Mano, K. Sakoda, S. Kunz, X. Marie, and B. Urbaszek. "Impact of heavy hole-light hole coupling on optical selection rules in GaAs Quantum Dots". *Applied Physics Letters* 97.5 (2010). DOI: 10.1063/1.3473824.

[106] X. Yuan, S. F. Covre da Silva, D. Csontosová, H. Huang, C. Schimpf, M. Reindl, J. Lu, Z. Ni, A. Rastelli, and P. Klenovský. "GaAs quantum dots under quasiuniaxial stress: Experiment and theory". *Physical Review B* 107.23 (2023). ISSN: 2469-9969. DOI: 10.1103/physrevb.107.235412.

[107] P. Millington-Hotze, H. E. Dyte, S. Manna, S. F. Covre da Silva, A. Rastelli, and E. A. Chekhovich. "Approaching a fully-polarized state of nuclear spins in a solid". *Nature Communications* 15.1 (2024). ISSN: 2041-1723. DOI: 10.1038/s41467-024-45364-2.

[108] H. Mekni, A. Pankratov, S. Ben Radhia, K. Boujdaria, M. Chamarro, and C. Testelin. "Fine structure of bright and dark excitons in asymmetric droplet epitaxy GaAs/AlGaAs Quantum Dots". *Physical Review B* 103.7 (2021). DOI: 10.1103/physrevb.103.075302.

[109] D. Fuster, Y. González, and L. González. "Fundamental role of arsenic flux in nanohole formation by Ga droplet etching on GaAs(001)". *Nanoscale Research Letters* 9.1 (2014). DOI: 10.1186/1556-276x-9-309.

[110] P. Michler. "Quantum Dot Single-Photon Sources". *Single Semiconductor Quantum Dots* (2009), pp. 185–225. DOI: 10.1007/978-3-540-87446-1_6.

[111] H. W. van Kesteren, E. C. Cosman, W. A. van der Poel, and C. T. Foxon. "Fine structure of excitons in type-II GaAs/AlAs quantum wells". *Physical Review B* 41.8 (1990), pp. 5283–5292. DOI: 10.1103/physrevb.41.5283.

[112] M. Bayer, G. Ortner, O. Stern, A. Kuther, A. A. Gorbunov, A. Forchel, P. Hawrylak, S. Fafard, K. Hinzer, T. L. Reinecke, and et al. "Fine structure of neutral and charged excitons in self-assembled In(Ga)As/(Al)GaAs quantum dots". *Physical Review B* 65.19 (2002). DOI: 10.1103/physrevb.65.195315.

[113] Y. H. Huo, V. Křápek, A. Rastelli, and O. G. Schmidt. "Volume dependence of excitonic fine structure splitting in geometrically similar quantum dots". *Phys. Rev. B* 90 (4 2014), p. 041304. DOI: 10.1103/PhysRevB.90.041304.

[114] D. A. Miller, D. S. Chemla, T. C. Damen, A. C. Gossard, W. Wiegmann, T. H. Wood, and C. A. Burrus. "Electric field dependence of optical absorption near the band gap of quantum-well structures". *Physical Review B* 32.2 (1985), pp. 1043–1060. DOI: 10.1103/physrevb.32.1043.

[115] M. M. Vogel, S. M. Ulrich, R. Hafenbrak, P. Michler, L. Wang, A. Rastelli, and O. G. Schmidt. "Influence of lateral electric fields on multiexcitonic transitions and fine structure of Single Quantum Dots". *Applied Physics Letters* 91.5 (2007), p. 051904. DOI: 10.1063/1.2761522.

[116] R. B. Patel, A. J. Bennett, I. Farrer, C. A. Nicoll, D. A. Ritchie, and A. J. Shields. "Two-photon interference of the emission from electrically tunable remote quantum dots". *Nature Photonics* 4.9 (2010), pp. 632–635. DOI: 10.1038/nphoton.2010.161.

[117] A Laucht, F Hofbauer, N Hauke, J Angele, S Stobbe, M Kaniber, G Böhm, P Lodahl, M.-C. Amann, and J. J. Finley. "Electrical control of spontaneous emission and strong coupling for a single quantum dot". *New Journal of Physics* 11.2 (2009), p. 023034. DOI: 10.1088/1367-2630/11/2/023034.

[118] A. M. Bonch-Bruevich and V. A. Khodovoĭ. "Current methods for the study of the Stark Effect In atoms". *Soviet Physics Uspekhi* 10.5 (1968), pp. 637–657. DOI: 10.1070/pu1968v010n05abeh005850.

[119] A. Muller, W. Fang, J. Lawall, and G. S. Solomon. "Creating polarization-entangled photon pairs from a semiconductor quantum dot using the optical stark effect". *Physical Review Letters* 103.21 (2009). DOI: 10.1103/physrevlett.103.217402.

[120] M. Fox. "Experimental observations of Rabi oscillations". *Quantum Optics: An introduction*. Oxford University Press, 2012, pp. 182–187.

[121] S. L. Portalupi and P. Michler. "Resonantly excited Quantum Dots: Superior non-classical light sources for quantum information". *Quantum Dots for Quantum Information Technologies* (2017), pp. 77–121. DOI: 10.1007/978-3-319-56378-7_3.

[122] C. L. Phillips. "Solid state Quantum Optics with a quantum dot in a nano-photonic cavity". PhD thesis. 2021. URL: https://etheses.whiterose.ac.uk/28600/.

[123] E. Blackwood, M. J. Snelling, R. T. Harley, S. R. Andrews, and C. T. B. Foxon. "Exchange interaction of excitons in GaAs heterostructures". *Physical Review B* 50.19 (1994), pp. 14246–14254. DOI: 10.1103/physrevb.50.14246.

[124] A. Kuther, M. Bayer, A. Forchel, A. Gorbunov, V. B. Timofeev, F. Schäfer, and J. P. Reithmaier. "Zeeman splitting of excitons and biexcitons in single $In_{0.60}Ga_{0.40}As$/GaAs self-assembled quantum dots". *Phys. Rev. B* 58 (12 1998), R7508–R7511. DOI: 10.1103/PhysRevB.58.R7508.

[125] B. Urbaszek, X. Marie, T. Amand, O. Krebs, P. Voisin, P. Maletinsky, A. Högele, and A. Imamoglu. "Nuclear spin physics in quantum dots: An optical investigation". *Rev. Mod. Phys.* 85 (1 2013), pp. 79–133. DOI: 10.1103/RevModPhys.85.79.

[126] W. A. Coish and J. Baugh. "Nuclear spins in nanostructures". *physica status solidi (b)* 246.10 (2009), pp. 2203–2215. DOI: https://doi.org/10.1002/pssb.200945229.

[127] A. Abragam. *The principles of nuclear magnetism*. Clarendon Press, 1961.

[128] M. Dyakonov and V. Perel. "Theory of optical spin orientation of electrons and nuclei in semiconductors". *Optical Orientation* (1984), pp. 11–71. DOI: 10.1016/b978-0-444-86741-4.50007-x.

[129] D. Gammon, A. L. Efros, T. A. Kennedy, M. Rosen, D. S. Katzer, D. Park, S. W. Brown, V. L. Korenev, and I. A. Merkulov. "Electron and Nuclear Spin Interactions in the Optical Spectra of Single GaAs Quantum Dots". *Physical Review Letters* 86.22 (2001), pp. 5176–5179. DOI: 10.1103/physrevlett.86.5176.

[130] C. Latta, A. Srivastava, and A. Imamoğlu. "Hyperfine Interaction-Dominated Dynamics of Nuclear Spins in Self-Assembled InGaAs Quantum Dots". *Phys. Rev. Lett.* 107 (16 2011), p. 167401. DOI: 10.1103/PhysRevLett.107.167401.

[131] E. A. Chekhovich, A. Ulhaq, E. Zallo, F. Ding, O. G. Schmidt, and M. S. Skolnick. "Measurement of the spin temperature of optically cooled nuclei and GaAs hyperfine constants in GaAs/AlGaAs quantum dots". *Nature Materials* 16.10 (2017), pp. 982–986. DOI: 10.1038/nmat4959.

[132] D. Joseph Klauser. "Hyperfine interaction and spin decoherence in quantum dots". PhD thesis. University of Basel, 2008. URL: https://edoc.unibas.ch/761/1/DissB_8302.pdf.

[133] R. K. Harris, E. D. Becker, S. M. Cabral de Menezes, R. Goodfellow, and P. Granger. "NMR Nomenclature: Nuclear Spin Properties and Conventions for Chemical Shifts". *Solid State Nuclear Magnetic Resonance* 22.4 (2002), pp. 458–483. DOI: 10.1006/snmr.2002.0063.

[134] A. Ulhaq, Q. Duan, E. Zallo, F. Ding, O. G. Schmidt, A. I. Tartakovskii, M. S. Skolnick, and E. A. Chekhovich. "Vanishing electron g factor and long-lived nuclear spin polarization in weakly strained nanohole-filled GaAs/AlGaAs quantum dots". *Physical Review B* 93.16 (2016). DOI: 10.1103/physrevb.93.165306.

[135] T. Flissikowski, I. A. Akimov, A. Hundt, and F. Henneberger. "Single-hole spin relaxation in a quantum dot". *Physical Review B* 68.16 (2003). DOI: 10.1103/physrevb.68.161309.

[136] D. Heiss, S. Schaeck, H. Huebl, M. Bichler, G. Abstreiter, J. J. Finley, D. V. Bulaev, and D. Loss. "Observation of extremely slow hole spin relaxation in self-assembled quantum dots". *Physical Review B* 76.24 (2007). DOI: 10.1103/physrevb.76.241306.

[137] S. Laurent, B. Eble, O. Krebs, A. Lemaître, B. Urbaszek, X. Marie, T. Amand, and P. Voisin. "Electrical Control of Hole Spin Relaxation in Charge Tunable InAs/GaAs Quantum Dots". *Physical Review Letters* 94.14 (2005). DOI: 10.1103/physrevlett.94.147401.

[138] D. N. Krizhanovskii, A. Ebbens, A. I. Tartakovskii, F. Pulizzi, T. Wright, M. S. Skolnick, and M. Hopkinson. "Individual neutral and charged $In_xGa_{1-x}As$-GaAs quantum dots with strong in-plane optical anisotropy". *Phys. Rev. B* 72 (16 2005), p. 161312. DOI: 10.1103/PhysRevB.72.161312.

[139] T. Hughbanks. *Electron Paramagnetic Resonance: Hyperfine Interactions*. 2021. URL: https://www.chem.tamu.edu/rgroup/hughbanks/courses/634/lecturenotes/EPR_notes_1.pdf (visited on 17/11/2021).

[140] J. Fischer, W. A. Coish, D. V. Bulaev, and D. Loss. "Spin decoherence of a heavy hole coupled to nuclear spins in a quantum dot". *Physical Review B* 78.15 (2008). DOI: 10.1103/physrevb.78.155329.

[141] B. Eble, C. Testelin, P. Desfonds, F. Bernardot, A. Balocchi, T. Amand, A. Miard, A. Lemaître, X. Marie, and M. Chamarro. "Hole–Nuclear Spin Interaction in Quantum Dots". *Phys. Rev. Lett.* 102 (14 2009), p. 146601. DOI: 10.1103/PhysRevLett.102.146601.

[142] J. W. Peng, C. A. Lepre, J. Fejzo, N. Abdul-Manan, and J. M. Moore. "Nuclear Magnetic Resonance-Based Approaches for Lead Generation in Drug Discovery". *Nuclear Magnetic Resonance of Biological Macromolecules Part A*. Ed. by T. L. James, V. Dötsch, and U. Schmitz. Vol. 338. Methods in Enzymology. Academic Press, 2002, pp. 202–230. DOI: 10.1016/S0076-6879(02)38221-1.

[143] H. Dyson and A. Palmer. *1.9 Introduction to Solution State NMR Spectroscopy*. Comprehensive Biophysics, 2012, pp. 136–159.

[144] Z.-X. Gong, Z.-q. Yin, and L.-M. Duan. "Dynamics of the Overhauser field under nuclear spin diffusion in a quantum dot". *New Journal of Physics* 13.3 (2011), p. 033036. DOI: 10.1088/1367-2630/13/3/033036.

[145] E. D. Commins. "Electric Dipole Moments of Elementary Particles, Nuclei, Atoms, and Molecules". *Journal of the Physical Society of Japan* 76.11 (2007), p. 111010. DOI: 10.1143/JPSJ.76.111010.

[146] W. S. C. Williams. *Springer series in nuclear and particle physics*. Clarendon Press, 1991.

[147] C. Bulutay. "Quadrupolar spectra of nuclear spins in strained $In_xGa_{1-x}As$ quantum dots". *Physical Review B* 85.11 (2012). DOI: 10.1103/physrevb.85.115313.

[148] C. Bulutay, E. A. Chekhovich, and A. I. Tartakovskii. "Nuclear magnetic resonance inverse spectra of InGaAs quantum dots: Atomistic level structural information". *Physical Review B* 90.20 (2014). DOI: 10.1103/physrevb.90.205425.

[149] C. P. Slichter. *Principles of magnetic resonance*. 3rd ed. Springer, 1996.

[150] E. A. Chekhovich, M. N. Makhonin, A. I. Tartakovskii, A. Yacoby, H. Bluhm, K. C. Nowack, and L. M. Vandersypen. "Nuclear spin effects in semiconductor Quantum Dots". *Nature Materials* 12.6 (2013), pp. 494–504. DOI: 10.1038/nmat3652.

[151] E. A. Chekhovich, K. V. Kavokin, J. Puebla, A. B. Krysa, M. Hopkinson, A. D. Andreev, A. M. Sanchez, R. Beanland, M. S. Skolnick, and A. I. Tartakovskii. "Structural analysis of strained quantum dots using nuclear magnetic resonance". *Nature Nanotechnology* 7.10 (2012), pp. 646–650. DOI: 10.1038/nnano.2012.142.

[152] E. A. Chekhovich, M. N. Makhonin, J. Skiba-Szymanska, A. B. Krysa, V. D. Kulakovskii, M. S. Skolnick, and A. I. Tartakovskii. "Dynamics of optically induced nuclear spin polarization in individual InP/$Ga_xIn_{1-x}P$ quantum dots". *Physical Review B* 81.24 (2010). DOI: 10.1103/physrevb.81.245308.

[153] D. Paget, G. Lampel, B. Sapoval, and V. I. Safarov. "Low field electron-nuclear spin coupling in gallium arsenide under optical pumping conditions". *Physical Review B* 15.12 (1977), pp. 5780–5796. DOI: 10.1103/physrevb.15.5780.

[154] J. Puebla, E. A. Chekhovich, M. Hopkinson, P. Senellart, A. Lemaitre, M. S. Skolnick, and A. I. Tartakovskii. "Dynamic nuclear polarization in InGaAs/GaAs and GaAs/AlGaAs Quantum Dots under nonresonant ultralow-power optical excitation". *Physical Review B* 88.4 (2013). DOI: 10.1103/physrevb.88.045306.

[155] A. V. Khaetskii, D. Loss, and L. Glazman. "Electron Spin Decoherence in Quantum Dots due to Interaction with Nuclei". *Phys. Rev. Lett.* 88 (18 2002), p. 186802. DOI: 10.1103/PhysRevLett.88.186802.

[156] C. Deng and X. Hu. "Electron-spin dephasing via hyperfine interaction in a quantum dot: An equation-of-motion calculation of electron-spin correlation functions". *Phys. Rev. B* 78 (24 2008), p. 245301. DOI: 10.1103/PhysRevB.78.245301.

[157] G. Giedke, J. M. Taylor, D. D'Alessandro, M. D. Lukin, and A. Imamoğlu. "Quantum measurement of a mesoscopic spin ensemble". *Phys. Rev. A* 74 (3 2006), p. 032316. DOI: 10.1103/PhysRevA.74.032316.

[158] M. Kelly. *MRI: Principles of Magnetic Resonance and Relaxation*. Lecture at the University of Leicester. 2018.

[159] F. Bloch. "Nuclear Induction". *Physical Review* 70.7-8 (1946), pp. 460–474. DOI: 10.1103/physrev.70.460.

[160] G. Sallen, S. Kunz, T. Amand, L. Bouet, T. Kuroda, T. Mano, D. Paget, O. Krebs, X. Marie, K. Sakoda, and B. Urbaszek. "Nuclear magnetization in gallium arsenide quantum dots at zero magnetic field". *Nature Communications* 5.1 (2014). DOI: 10.1038/ncomms4268.

[161] B. P Cowan. *Nuclear magnetic resonance and relaxation*. Cambridge University Press, 1997.

[162] J. R. Petta, A. C. Johnson, J. M. Taylor, E. A. Laird, A. Yacoby, M. D. Lukin, C. M. Marcus, M. P. Hanson, and A. C. Gossard. "Coherent Manipulation of Coupled Electron Spins in Semiconductor Quantum Dots". *Science* 309.5744 (2005), pp. 2180–2184. DOI: 10.1126/science.1116955.

[163] A. M. Waeber, G. Gillard, G. Ragunathan, M. Hopkinson, P. Spencer, D. A. Ritchie, M. S. Skolnick, and E. A. Chekhovich. "Pulse control protocols for preserving coherence in dipolar-coupled nuclear spin baths". *Nature Communications* 10.1 (2019). DOI: 10.1038/s41467-019-11160-6.

[164] M. Holmes, S. Kako, K. Choi, P. Podemski, M. Arita, and Y. Arakawa. "Measurement of an Exciton Rabi Rotation in a Single GaN/$Al_xGa_{1-x}N$ Nanowire-Quantum Dot Using Photoluminescence Spectroscopy: Evidence for Coherent Control". *Physical Review Letters* 111.5 (2013). DOI: 10.1103/physrevlett.111.057401.

[165] A. Franzen. *ComponentLibrary*. Accessed: 2022-11-25. Used under Creative Commons Attribution-NonCommercial 3.0 Unported License. URL: https://www.gwoptics.org/ComponentLibrary/.

[166] M. Atatüre, J. Dreiser, A. Badolato, A. Högele, K. Karrai, and A. Imamoglu. "Quantum-Dot Spin-State Preparation with Near-Unity Fidelity". *Science* 312.5773 (2006), pp. 551–553. DOI: 10.1126/science.1126074.

[167] G. Dresselhaus. "Spin-Orbit Coupling Effects in Zinc Blende Structures". *Physical Review* 100.2 (1955), pp. 580–586. DOI: 10.1103/physrev.100.580.

[168] A. Manchon, H. C. Koo, J. Nitta, S. M. Frolov, and R. A. Duine. "New Perspectives for Rashba Spin-Orbit Coupling". *Nature Materials* 14.9 (2015), pp. 871–882. DOI: 10.1038/nmat4360.

[169] A. V. Koudinov, I. A. Akimov, Y. G. Kusrayev, and F. Henneberger. "Optical and magnetic anisotropies of the hole states in Stranski-Krastanov quantum dots". *Phys. Rev. B* 70 (24 2004), p. 241305. DOI: 10.1103/PhysRevB.70.241305.

[170] Y. Léger, L. Besombes, L. Maingault, and H. Mariette. "Valence-band mixing in neutral, charged, and Mn-doped self-assembled quantum dots". *Phys. Rev. B* 76 (4 2007), p. 045331. DOI: 10.1103/PhysRevB.76.045331.

[171] C. Heyn, C. Strelow, and W Hansen. "Excitonic lifetimes in single GaAs quantum dots fabricated by local droplet etching". *New Journal of Physics* 14.5 (2012), p. 053004. ISSN: 1367-2630. DOI: 10.1088/1367-2630/14/5/053004.

[172] C. Schimpf, M. Reindl, P. Klenovský, T. Fromherz, S. F. Covre Da Silva, J. Hofer, C. Schneider, S. Höfling, R. Trotta, and A. Rastelli. "Resolving the temporal evolution of line broadening in single quantum emitters". *Optics Express* 27.24 (2019), p. 35290. ISSN: 1094-4087. DOI: 10.1364/oe.27.035290.

[173] A. I. Tartakovskii, T. Wright, A. Russell, V. I. Fal'ko, A. B. Van'kov, J. Skiba-Szymanska, I. Drouzas, R. S. Kolodka, M. S. Skolnick, P. W. Fry, and et al. "Nuclear spin switch in semiconductor Quantum Dots". *Physical Review Letters* 98.2 (2007). DOI: 10.1103/physrevlett.98.026806.

[174] P. Maletinsky, C. W. Lai, A. Badolato, and A. Imamoglu. "Nonlinear Dynamics of Quantum Dot Nuclear Spins". *Physical Review B* 75.3 (2007). DOI: 10.1103/physrevb.75.035409.

[175] P.-F. Braun, B. Urbaszek, T. Amand, X. Marie, O. Krebs, B. Eble, A. Lemaitre, and P. Voisin. "Bistability of the nuclear polarization created through optical pumping in $In_{1-x}Ga_x$ As quantum dots". *Physical Review B* 74.24 (2006). DOI: 10.1103/physrevb.74.245306.

[176] G. Gillard. "Lifetime and Coherence of the Coupled Electron and Nuclear Spin Systems in Semiconductor Quantum Dots". PhD thesis. University of Sheffield, 2022. URL: https://etheses.whiterose.ac.uk/30563/.

[177] H. E. Dyte, G. Gillard, S. Manna, S. F. C. da Silva, A. Rastelli, and E. A. Chekhovich. "Quantum non-demolition measurement of an electron spin qubit through its low-energy many-body spin environment" (2023). DOI: 10.48550/ARXIV.2307.00308.

[178] A. Waeber, M. Hopkinson, I. Farrer, D. Ritchie, J. Nilsson, R. Stevenson, A. Bennett, A. Shields, G. Burkard, A. Tartakovskii, and et al. "Few-second-long correlation times in a quantum dot nuclear spin bath probed by frequency-comb nuclear magnetic resonance spectroscopy". *Nature Physics* 12.7 (2016), pp. 688–693. DOI: 10.1038/nphys3686.

[179] D. M. Pozar. "Impedance Matching And Tuning". *Microwave engineering*. John Wiley & Sons, 2021, pp. 228–245.

[180] E. Chekhovich, M. Hopkinson, M. Skolnick, and A. Tartakovskii. "Suppression of nuclear spin bath fluctuations in self-assembled quantum dots induced by inhomogeneous strain". *Nature Communications* 6.1 (2015). DOI: 10.1038/ncomms7348.

[181] R. Stockill, C. Le Gall, C. Matthiesen, L. Huthmacher, E. Clarke, M. Hugues, and M. Atatüre. "Quantum dot spin coherence governed by a strained nuclear environment". *Nature Communications* 7.1 (2016). DOI: 10.1038/ncomms12745.

[182] T. Lettner, S. Gyger, K. D. Zeuner, L. Schweickert, S. Steinhauer, C. Reuterskiöld Hedlund, S. Stroj, A. Rastelli, M. Hammar, R. Trotta, and et al. "Strain-controlled quantum dot fine structure for entangled photon generation at 1550 nm". *Nano Letters* 21.24 (2021), pp. 10501–10506. DOI: 10.1021/acs.nanolett.1c04024.

[183] L. Zaporski, N. Shofer, J. H. Bodey, S. Manna, G. Gillard, M. H. Appel, C. Schimpf, S. F. Covre da Silva, J. Jarman, G. Delamare, G. Park, U. Haeusler, E. A. Chekhovich, A. Rastelli, D. A. Gangloff, M. Atatüre, and C. Le Gall. "Ideal refocusing of an optically active spin qubit under strong hyperfine interactions". *Nature Nanotechnology* 18.3 (2023), pp. 257–263. DOI: 10.1038/s41565-022-01282-2.

[184] D. J. Reilly, J. M. Taylor, J. R. Petta, C. M. Marcus, M. P. Hanson, and A. C. Gossard. "Exchange Control of Nuclear Spin Diffusion in a Double Quantum Dot". *Phys. Rev. Lett.* 104 (23 2010), p. 236802. DOI: 10.1103/PhysRevLett.104.236802. URL: https://link.aps.org/doi/10.1103/PhysRevLett.104.236802.

[185] D. Klauser, W. A. Coish, and D. Loss. "Nuclear spin dynamics and Zeno effect in quantum dots and defect centers". *Phys. Rev. B* 78 (20 2008), p. 205301. DOI: 10.1103/PhysRevB.78.205301. URL: https://link.aps.org/doi/10.1103/PhysRevB.78.205301.

[186] J. Lu, M. J. R. Hoch, P. L. Kuhns, W. G. Moulton, Z. Gan, and A. P. Reyes. "Nuclear spin-lattice relaxation in n-type insulating and metallic GaAs single crystals". *Phys. Rev. B* 74 (12 2006), p. 125208. DOI: 10.1103/PhysRevB.74.125208.

[187] C. Deng and X. Hu. "Nuclear spin diffusion in quantum dots: Effects of inhomogeneous hyperfine interaction". *Phys. Rev. B* 72 (16 2005), p. 165333. DOI: 10.1103/PhysRevB.72.165333.

[188] C. W. Lai, P. Maletinsky, A. Badolato, and A. Imamoglu. "Knight-Field-Enabled Nuclear Spin Polarization in Single Quantum Dots". *Phys. Rev. Lett.* 96 (16 2006), p. 167403. DOI: 10.1103/PhysRevLett.96.167403.

[189] C. Ramanathan. "Dynamic nuclear polarization and spin diffusion in nonconducting solids". *Applied Magnetic Resonance* 34.3–4 (2008). DOI: 10.1007/s00723-008-0123-7.

[190] G. Burkard, D. Loss, and D. P. DiVincenzo. "Coupled quantum dots as quantum gates". *Phys. Rev. B* 59 (3 1999), pp. 2070–2078. DOI: 10.1103/PhysRevB.59.2070.

[191] C. Kloeffel and D. Loss. "Prospects for Spin-Based Quantum Computing in Quantum Dots". *Annual Review of Condensed Matter Physics* 4.1 (2013), pp. 51–81. ISSN: 1947-5462. DOI: 10.1146/annurev-conmatphys-030212-184248.

[192] A. Imamoğlu, E. Knill, L. Tian, and P. Zoller. "Optical pumping of quantum-dot nuclear spins". *Physical Review Letters* 91.1 (2003). DOI: 10.1103/physrevlett.91.017402.

[193] H. Christ, J. I. Cirac, and G. Giedke. "Quantum description of nuclear spin cooling in a quantum dot". *Physical Review B* 75.15 (2007). DOI: 10.1103/physrevb.75.155324.

[194] H. Ribeiro and G. Burkard. "Nuclear state preparation via Landau-Zener-Stückelberg transitions in double quantum dots". *Physical Review Letters* 102.21 (2009). DOI: 10.1103/physrevlett.102.216802.

[195] J. Hildmann, E. Kavousanaki, G. Burkard, and H. Ribeiro. "Quantum limit for nuclear spin polarization in semiconductor quantum dots". *Phys. Rev. B* 89 (20 2014), p. 205302. DOI: 10.1103/PhysRevB.89.205302.

[196] T. A. Knuuttila, J. T. Tuoriniemi, K. Lefmann, K. I. Juntunen, F. B. Rasmussen, and K. K. Nummila. *Journal of Low Temperature Physics* 123.1/2 (2001), pp. 65–102. DOI: 10.1023/a:1017545531677.

[197] A. M. Steane. "Efficient fault-tolerant quantum computing". *Nature* 399.6732 (1999), pp. 124–126. ISSN: 1476-4687. DOI: 10.1038/20127.

[198] L.-M. Duan, M. D. Lukin, J. I. Cirac, and P. Zoller. "Long-distance quantum communication with atomic ensembles and linear optics". *Nature* 414.6862 (2001), pp. 413–418. ISSN: 1476-4687. DOI: 10.1038/35106500.

[199] J. M. Taylor, C. M. Marcus, and M. D. Lukin. "Long-Lived Memory for Mesoscopic Quantum Bits". *Physical Review Letters* 90.20 (2003). ISSN: 1079-7114. DOI: 10.1103/physrevlett.90.206803.